THE FLORIDA STATE UNIVERSITY

COLLEGE OF ARTS AND SCIENCES

HIGGS BOSON PRODUCTION WITH HEAVY QUARKS AT
HADRON COLLIDERS

By

CHRISTOPHER B. JACKSON

A Dissertation submitted to the
Department of Physics
in partial fulfillment of the
requirements for the degree of
Doctorate of Philosophy

Degree Awarded:
Summer Semester, 2005

The members of the Committee approve the dissertation of Christopher B. Jackson defended on June 29, 2005.

Laura Reina
Professor Directing Dissertation

Philip L. Bowers
Outside Committee Member

Joseph F. Owens, III
Committee Member

Harrison B. Prosper
Committee Member

Jorge Piekarewicz
Committee Member

The Office of Graduate Studies has verified and approved the above named committee members.

To my grandparents, George and Charlene Shadburne.

ACKNOWLEDGEMENTS

First and foremost, I would like to thank my wife, Jennifer, for the support and encouragement she has given me over the last five years. I could never repay her for the sacrifices she has made and everything she has done for our family during these *lean* years of graduate school. To my sons, Jake and Henry, I say thanks for reminding me what life is really all about.

I would also like to thank two members of my thesis committee who have provided help and support along the way. First, to Jeff Owens, who has given me guidance in many QCD-related topics. Second, to Jorge Piekarewicz, who has been my mentor in all areas of physics over the past five years and, more importantly, a good friend.

Lastly, I would like to say a special "thank you" to my thesis adviser, Laura Reina. No matter how discouraging NLO QCD calculations can be sometimes, we have always been able to have a good laugh.

TABLE OF CONTENTS

LIST OF TABLES

LIST OF FIGURES

xii

ABSTRACT

One of the remaining puzzles in particle physics is the origin of electroweak symmetry breaking. In the Standard Model (SM), a single doublet of complex scalar fields is responsible for breaking the $SU(2)_L \times U(1)_Y$ gauge symmetry, thus giving mass to the electroweak gauge bosons via the *Higgs mechanism* and to the fermions via Yukawa couplings. The remnant of the process is a yet to be discovered scalar particle, the Higgs boson (h). Current and future experiments at hadron colliders hold great promise. The Fermilab Tevatron proton-antiproton ($p\bar{p}$) collider, which is currently running, has the potential to discover a light Higgs boson with mass between 100 and 200 GeV. Starting in 2007, the CERN proton-proton (pp) Large Hadron Collider (LHC) will be able to produce a Higgs boson over its full mass range (up to 1 TeV) through *multiple* processes.

Of particular interest is the production of a Higgs boson in association with a pair of heavy quarks, $p\bar{p}(pp) \rightarrow Q\bar{Q}h$, where Q can be either a top or a bottom quark. Indeed, the production of a Higgs boson with a pair of top quarks provides a very distinctive signal in hadronic collisions where background processes are formidable, and it will be instrumental in the discovery of a Higgs boson below about 130 GeV at the LHC. Also, since the Higgs boson is radiated from a top quark, this channel provides a unique opportunity to directly measure the top quark Yukawa coupling. On the other hand, the production of a Higgs boson with bottom quarks can be strongly enhanced in models of new physics beyond the SM, e.g. supersymmetric models. If this is the case, $b\bar{b}h$ production will play a crucial role at the Tevatron where it could provide the first signal of new physics.

Given the prominent role that Higgs production with heavy quarks can play at hadron colliders, it becomes imperative to have precise theoretical predictions for total and differential cross sections. Hadronic cross sections are mainly affected by strong interaction effects which, at high energy, are described by perturbative Quantum Chromodynamics (QCD). Lowest-order predictions in perturbative QCD are often severely plagued by renormalization and factorization scale dependence. Therefore, to obtain precise results, it becomes mandatory to calculate cross sections beyond the LO. In this thesis, we report on the next-to-leading order (NLO) QCD calculation for the total and differential cross sections of $p\bar{p}(pp) \rightarrow Q\bar{Q}h$. The NLO cross sections exhibit drastically reduced dependence on renormalization and factorization scales and, thus, lead to increased confidence in predictions based on these results. In fact, the results presented in this thesis are currently being used in experimental simulations at both the Tevatron and the LHC.

In the first part of this thesis, we outline and present detailed results for the NLO QCD calculation of $t\bar{t}h$ production at both the Tevatron and the LHC. This calculation involves several difficult issues due to the three massive particles in the final state, a situation which is at the frontier of radiative correction calculations in quantum field theory. For instance, the virtual one-loop corrections contain pentagon Feynman diagrams with several massive internal and external particles that pose both analytic and numerical challenges. Another difficulty arises in the calculation of the real gluon emission contribution, where one must compute a four-body phase space containing three massive particles. In this thesis, we will detail the novel techniques we have developed to deal with these challenges.

In the second part of this thesis, we focus on the production of Higgs bosons with bottom quarks. The calculation of $p\bar{p}(pp) \rightarrow b\bar{b}h$ at NLO in QCD involves several subtle issues not encountered in the case of $p\bar{p}(pp) \rightarrow t\bar{t}h$. Both from an experimental and theoretical standpoint, it is important to distinguish between *inclusive* and *exclusive* $b\bar{b}h$ production. In fact, the production of a Higgs boson

with a pair of b quarks can be detected via: (i) a fully *exclusive* measurement, when both b jets are identified; (ii) a fully *inclusive* measurement, when no b jet is identified; or (iii) a *semi-inclusive* measurement, when at least one of the two b jets is identified. Theoretically, different calculational approaches may be adopted when a final state b quark is treated either exclusively or inclusively. In this thesis, we present results for both exclusive and inclusive production of Higgs bosons with bottom quarks, and we devote particular care to clarifying some outstanding issues concerning the inclusive production modes. Indeed, when a final state b quark is not identified, the corresponding integration over its phase space gives rise to large collinear logarithms originating from the region of low transverse momentum. These collinear logarithms appear at every order in the strong coupling α_s and, hence, could hinder the convergence of the perturbative expansion. Currently, there are two approaches to the calculation of inclusive Higgs production with bottom quarks: one can (i) calculate the partonic processes $gg, q\bar{q} \rightarrow b\bar{b}h$ at fixed order in α_s with no special treatment of the collinear logarithms (the so-called *Four Flavor Number Scheme*) or (ii) introduce a bottom quark Parton Distribution Function, in which case the semi-inclusive process becomes $gb \rightarrow bh$ and the inclusive one $b\bar{b} \rightarrow h$, and resum leading and sub-leading logarithms through the Altarelli-Parisi equation (the so-called *Five Flavor Number Scheme*). Here, we compare these two seemingly different schemes and show that they produce compatible results for the total and differential cross sections in the cases of Higgs production with zero tagged b jets and one tagged b jet. This comparison is made possible by having computed the NLO QCD cross section for $b\bar{b}h$ production.

CHAPTER 1

BREAKING THE ELECTROWEAK SYMMETRY

1.1   The Standard Model

The Standard Model (SM) of particle physics is the theoretical framework which best describes all of the experimentally observed properties of elementary particles and their interactions [2, 3, 4]. It is a quantum field theory based on the (local) gauge symmetry $SU(2)_L \times U(1)_Y$ for the electroweak interactions and $SU(3)_C$ for the strong interactions. The matter sector of the SM consists of fermionic fields called *quarks* and *leptons*, which are organized into three *families* or *generations*. Each generation has identical properties except for mass. The fermions all carry a *hypercharge* quantum number (Y of $U(1)_Y$) and transform either as left-handed doublets or right-handed singlets under the weak isospin gauge group, $SU(2)_L$. Quarks also carry a *color* quantum number and transform as triplets of $SU(3)_C$. The gauge vector boson sector of the SM is composed of the massive weak interaction bosons, $W^\pm$ and Z^0, the massless electromagnetic photon, and eight massless, colored gluons. Since the $W^\pm$ and Z^0 are known to be massive, the $SU(2)_L \times U(1)_Y$ gauge symmetry of the electroweak interaction must be broken. In fact, the SM Lagrangian which describes the theory cannot contain explicit mass terms for either the gauge fields or the fermion fields, since such terms would destroy gauge invariance. Therefore, there are two distinct problems concerning mass: (*i*) explaining the masses of the gauge bosons, which requires an understanding of electroweak symmetry breaking (EWSB)

and (*ii*) accounting for the masses of the fermion fields, which requires not only an understanding of EWSB but also explaining how the breaking of gauge symmetry is communicated to the fermionic sector.

1.1.1 The Higgs mechanism

First of all, to give the $W^\pm$ and Z^0 bosons mass, while leaving the photon massless, the $SU(2)_L \times U(1)_Y$ gauge symmetry of the SM is assumed to be *spontaneously* broken, i.e. the Lagrangian is symmetric under gauge transformations (or *gauge invariant*), but the vacuum state and spectrum of particles are not. The simplest way to induce spontaneous symmetry breaking (SSB) is the *Higgs mechanism* [5, 6, 7, 8]. In the SM, this is achieved by introducing an $SU(2)$ doublet of complex scalar fields:

$$\Phi = \begin{pmatrix} \phi^+ \\ \phi^0 \end{pmatrix}, \tag{1.1}$$

with the Lagrangian:

$$\mathcal{L} = (D_\mu \Phi)^\dagger (D^\mu \Phi) - [\mu^2 \Phi^\dagger \Phi + \lambda (\Phi^\dagger \Phi)^2] \equiv (D_\mu \Phi)^\dagger (D^\mu \Phi) - V(\Phi), \tag{1.2}$$

where $D_\mu = (\partial_\mu - ig A^a_\mu \tau^a - ig' Y_\phi B_\mu)$ is the covariant derivative associated with the $SU(2)_L \times U(1)_Y$ gauge symmetry. A^a_μ is the gauge field of the $SU(2)_L$ gauge group, B_μ is the gauge field of the $U(1)_Y$, while g and g' are the couplings of the $SU(2)_L$ and $U(1)_Y$ gauge groups respectively. The matrices $\tau^a = \sigma^a/2$ (for $a = 1, 2, 3$) are the $SU(2)$ Lie algebra generators, proportional to the Pauli matrices σ^a, and Y_ϕ is the generator of the $U(1)_Y$ group.

In the scalar potential $V(\Phi)$, λ and μ^2 are arbitrary parameters, with $\lambda > 0$ in order for $V(\Phi)$ to be bounded from below. To achieve spontaneous symmetry breaking, one chooses $\mu^2 < 0$, in which case $V(\Phi)$ is minimized by field configurations that satisfy the condition:

$$\Phi^\dagger \Phi = \frac{-\mu^2}{\lambda} \equiv v^2, \tag{1.3}$$

2

instead of $\Phi^\dagger \Phi = 0$ as is the case when $\mu^2 > 0$. Equivalently, we can say that the Higgs potential $V(\Phi)$ is minimized for a *non-zero* vacuum expectation value (vev). In particular, to be identified with the electromagnetic $U(1)_{em}$, the $SU(2)_L \times U(1)_Y$ gauge symmetry of the Lagrangian is broken when the vev $\langle \Phi \rangle$ is chosen to be:

$$\langle \Phi \rangle = \Phi_0 = \frac{1}{\sqrt{2}} \begin{pmatrix} 0 \\ v \end{pmatrix} . \tag{1.4}$$

When expanded about the chosen minimum of $V(\Phi)$, parameterizing the fields in terms of the shifted field Φ' ($\Phi \rightarrow \Phi_0 + \Phi'$), the kinetic term of the Lagrangian (Eq. (1.2)) becomes:

$$(D^\mu \phi)^\dagger D_\mu \phi \longrightarrow \cdots + \frac{1}{8}(0 \ v)\left(gA_\mu^a \sigma^a + g'B_\mu\right)\left(gA^{b\mu}\sigma^b + g'B^\mu\right)\begin{pmatrix} 0 \\ v \end{pmatrix} + \cdots$$

$$\longrightarrow \cdots + \frac{1}{2}\frac{v^2}{4}\left[g^2(A_\mu^1)^2 + g^2(A_\mu^2)^2 + (-gA_\mu^3 + g'B_\mu)^2\right] + \cdots$$

$$\tag{1.5}$$

In Eq. (1.5), one can then recognize the mass terms for the $W_\mu^\pm$:

$$W_\mu^\pm = \frac{1}{\sqrt{2}}(A_\mu^1 \pm A_\mu^2) \quad \longrightarrow \quad M_W = g\frac{v}{2} , \tag{1.6}$$

and for the neutral Z_μ^0 gauge boson:

$$Z_\mu^0 = \frac{1}{\sqrt{g^2 + g'^2}}(gA_\mu^3 - g'B_\mu) \quad \longrightarrow \quad M_Z = \sqrt{g^2 + g'^2}\frac{v}{2} , \tag{1.7}$$

while the orthogonal linear combination of A_μ^3 and B_μ remains massless and corresponds to the photon (A_μ):

$$A_\mu = \frac{1}{\sqrt{g^2 + g'^2}}(g'A_\mu^3 + gB_\mu) \quad \longrightarrow \quad M_A = 0 , \tag{1.8}$$

the gauge boson of the residual $U(1)_{em}$ gauge symmetry.

The content of the scalar sector of the theory becomes more transparent if one works in the unitary gauge and uses gauge invariance to eliminate any unphysical

degrees of freedom. This amounts to parameterizing and rotating the $\Phi(x)$ complex scalar field as follows:

$$\phi(x) = \frac{e^{\frac{i}{v}\vec{\chi}(x)\cdot\vec{\tau}}}{\sqrt{2}}\begin{pmatrix} 0 \\ v + h(x) \end{pmatrix} \xrightarrow{SU(2)} \phi(x) = \frac{1}{\sqrt{2}}\begin{pmatrix} 0 \\ v + h(x) \end{pmatrix} \ , \qquad (1.9)$$

where the χ degrees of freedom have been *rotated away*, as indicated in Eq. (1.9), by enforcing the $SU(2)$ gauge invariance of the original Lagrangian. With this gauge choice (or the so-called *unitary gauge*), the scalar Lagrangian becomes:

$$\mathcal{L}_\phi = \mu^2 h^2 - \lambda v h^3 - \frac{1}{4}h^4 = -\frac{1}{2}M_h^2 h^2 - \sqrt{\frac{\lambda}{2}}M_h h^3 - \frac{1}{4}\lambda h^4 \ . \qquad (1.10)$$

Three degrees of freedom $(\chi^a(x))$ have been reabsorbed into the longitudinal components of the $W_\mu^\pm$ and Z_μ^0 weak gauge bosons making them massive. One real scalar field remains, the *Higgs boson h*, with mass $M_h^2 = -2\mu^2 = 2\lambda v^2$ and self-couplings which are given by:

$$g_{hhh} = -3i\frac{M_h^2}{v} \quad \text{and} \quad g_{hhhh} = -3i\frac{M_h^2}{v^2} \ . \qquad (1.11)$$

Furthermore, some of the terms omitted in Eq. (1.5), the terms linear in the gauge bosons $W_\mu^\pm$ and Z_μ^0, give rise to couplings between the massive vector gauge bosons, V ($V = W^\pm$ or Z^0), and the Higgs boson of the form:

$$g_{VVh} = 2i\frac{M_V^2}{v}g^{\mu\nu} \ . \qquad (1.12)$$

1.1.2 Yukawa interactions and fermion masses

Let us now turn to the problem of fermion masses. The only possibility of giving mass to the quarks and leptons, while respecting the $SU(2)_L \times U(1)_Y$ symmetry of the theory, is by adding to the SM Lagrangian a gauge-invariant, renormalizable Yukawa interaction of the form:

$$\mathcal{L}_{Yukawa} = -\Gamma_u^{ij}\bar{Q}_L^i\Phi^c u_R^j - \Gamma_d^{ij}\bar{Q}_L^i\Phi d_R^j - \Gamma_e^{ij}\bar{L}_L^i\Phi l_R^j + h.c. \qquad (1.13)$$

where $\Phi^c = -i\sigma^2\Phi^\dagger$, and Γ_f ($f = u, d, l$) are matrices of couplings arbitrarily introduced to realize the Yukawa coupling between the field Φ and the fermionic

4

fields of the SM. Q_L^i and L_L^i (where $i = 1, 2, 3$ is a generation index) represent quark and lepton left handed doublets of $SU(2)_L$, while u_R^i, d_R^i and l_R^i are the corresponding right handed singlets. Once the Higgs mechanism is invoked to give the weak gauge bosons mass, these Yukawa terms in the Lagrangian *communicate* SSB to the fermionic sector. Actually, when the Higgs doublet is expanded about its vev, the Yukawa Lagrangian gives rise to fermion mass terms:

$$m_f = \Gamma_f \frac{v}{\sqrt{2}} \ , \tag{1.14}$$

where the process of diagonalization from the current eigenstates in Eq. (1.13) to the mass fermionic eigenstates is understood and Γ_f are therefore the elements of the diagonalized Yukawa matrices corresponding to a given fermion f. The Yukawa couplings of the f fermion to the Higgs boson ($g_{f\bar{f}h}$) is proportional to Γ_f:

$$g_{f\bar{f}h} = \frac{\Gamma_f}{\sqrt{2}} = \frac{m_f}{v}. \tag{1.15}$$

Hence, given Eqs. (1.12) and (1.15), we expect that the dominant production and decay modes of the SM Higgs boson are those in which the Higgs boson couples directly or indirectly to heavy particles, i.e. the weak bosons $W^\pm$ and Z^0 , the top quark and, to a lesser extent, the bottom quark.

1.1.3 Theoretical constraints on the SM Higgs boson mass

Despite the success of the SM in describing physics at energy scales of $\mathcal{O}(100\,\mathrm{GeV})$ and below, it is generally believed that the SM is an effective theory which breaks down at some large scale Λ. That is, the SM ceases to be adequate to describe physics above Λ, and effects associated with new physics become relevant. In particular, we know that Λ must be less than the Planck scale ($M_{\mathrm{PL}} \simeq 10^{19}$ GeV), since above M_{PL} quantum gravitational effects become significant and the SM must be replaced by a more fundamental theory which incorporates gravity. In this context, the scale of new physics Λ can be related through several theoretical arguments to the SM Higgs
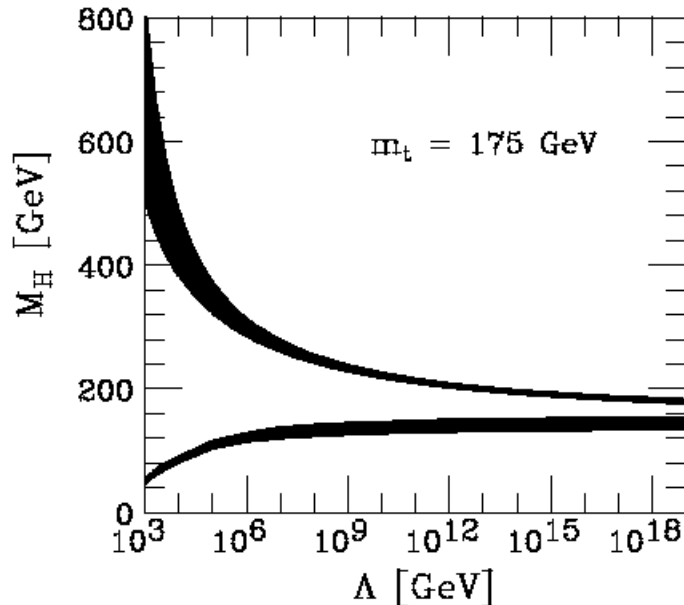
Figure 1.1. The upper [11] and lower [12] Higgs mass bounds as a function of the energy scale Λ at which the SM breaks down. See Ref. [9] and references within.

boson mass, M_h, and a lower and upper bound on M_h can be derived as a function of Λ. Several discussions can be found in the literature and we refer the reader in particular to Refs. [9] and [10]. For the purpose of this thesis, we can explain Fig. 1.1. First, if M_h is too small, the Higgs potential develops a second minimum at a large value of the scalar field of order Λ [12]. Thus, new physics must enter at some scale less than Λ in order to ensure that the global minimum of the theory correspond to the observed $SU(2)_L \times U(1)_Y$ broken vacuum with $v = 246$ GeV. Second, if M_h is too large, then the Higgs self-coupling λ blows up at some scale below the Planck scale [11]. Thus, given a scale Λ, one can compute the minimum and maximum Higgs masses allowed. In Fig. 1.1, we see that a Higgs mass in the range 130 GeV $\leq M_h \leq$ 180 GeV is consistent with an effective SM that survives all the way to the Planck scale [9].

6
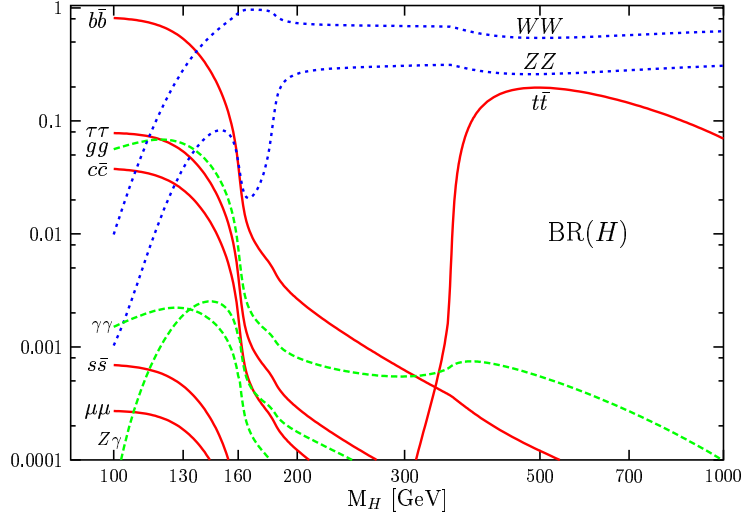
Figure 1.2. SM Higgs decay branching ratios as a function of M_h. The blue curves represent tree-level decays into electroweak gauge bosons, while the red curves represent tree-level decays into quarks and leptons. The green curves represent the one-loop induced decays. From Ref. [10].

1.1.4 SM Higgs boson decays

The preference of the SM Higgs boson to couple to heavy particles also plays a role in its decay pattern. As can be seen in Fig. 1.2 [10], a light SM Higgs boson ($M_h \leq 130 - 140$ GeV) mainly decays into a pair of bottom quarks, $b\bar{b}$, while a heavier SM Higgs boson mainly decays into W^+W^-, Z^0Z^0 and $t\bar{t}$ pairs. Actually, the overall behavior of a light SM Higgs boson differs substantially from a heavier one. In this mass range, loop-induced decays also play a role. $h \rightarrow gg$, which proceeds through a loop of top quarks, is the the most dominant among these. Unfortunately, at hadron colliders, this decay channel is buried by hadronic background processes. Between the rare decays $h \rightarrow \gamma\gamma$ and $h \rightarrow \gamma Z^0$ decays, $h \rightarrow \gamma\gamma$ which proceeds through loops of $W^\pm$'s and top quarks, has the larger branching ratio and provides the cleaner signal, because of the very neat two photon signal.

On the other hand, for larger Higgs masses, it becomes kinematically favorable for the SM Higgs boson to decay into weak gauge bosons (W^+W^- and Z^0Z^0). In this region, all decays into fermions or loop-induced decays vanish, except for $h \to t\bar{t}$ for Higgs masses above the $t\bar{t}$ production threshold. In the intermediate Higgs mass range (around $M_h \approx 160$ GeV), i.e. below the W^+W^- and Z^0Z^0 mass thresholds, the Higgs boson can still decay into a pair of heavy gauge bosons, although one of the gauge bosons is now off-shell, $h \to WW^*, ZZ^*$. These three-body decays (since the off-shell gauge boson quickly decays) start to dominate over the $b\bar{b}$ decay channel because the largeness of the gauge boson couplings to the Higgs boson compensates for their phase space suppression. As we will see in the next chapter, the different decay patterns for light and heavy Higgs bosons will influence the role played, in each mass region, by different Higgs production processes at hadron colliders.

1.2 The Minimal Supersymmetric Standard Model

The way in which EWSB is realized through the SM Higgs mechanism is, however, not entirely satisfactory and the Higgs mechanism itself is rather *ad hoc*. Both the Higgs boson mass and the Yukawa couplings remain arbitrary. In addition, the renormalized Higgs boson mass depends quadratically on the scale at which the SM ceases to be the effective theory of Nature and a satisfactory value of M_h at the EW scale can be obtained only at the price of *extreme* fine tuning of parameters. The quadratic growth in the Higgs boson mass beyond lowest order in perturbation theory is one of the driving motivations for alternatives (or extensions) to the SM.

Among the most interesting and successful attempts at going beyond the SM is *supersymmetry* (SUSY), in particular, the Minimal Supersymmetric Standard Model (MSSM). In any supersymmetric theory, EWSB is still realized via the Higgs mechanism, but, in order to give masses to both up- and down-type fermions, two Higgs doublets must be introduced. The quadratic divergences encountered in the

perturbative calculation of the Higgs boson mass vanish in the SUSY limit (i.e. where SUSY is an unbroken symmetry) due to the existence of equal numbers of bosons and fermions which contribute with opposite signs to loop corrections. Therefore, no extreme fine-tuning seems to be required to ensure that M_h stays around the electroweak scale. Moreover, SUSY theories contain a dynamic mechanism which drives EWSB, known as radiative electroweak symmetry breaking (REWSB) [13, 14, 15, 16]. In this mechanism, renormalization effects drive the Higgs boson squared mass parameters to negative values, resulting in the observed EWSB pattern.

Before discussing the Higgs sector of the MSSM, let us first explain how the MSSM is constructed. The MSSM is built upon four basic assumptions:

Minimal gauge group: the MSSM is assumed to possess the *same* gauge group as the SM, i.e. $SU(3)_C \times SU(2)_L \times U(1)_Y$.

Minimal particle content: in the MSSM, the particle content is that of the SM *plus* a new fermion (boson) partner field for each boson (fermion) field of the SM. However, to avoid reintroducing gauge anomalies (which cancel in the SM) and to give masses to both up- and down-type fermions, two Higgs doublets must be introduced along with their fermion superpartners.

Conservation of R parity: in order to avoid baryon and lepton number violation, a discrete symmetry called R parity is introduced. The conservation of R parity results in consequences which are important for searches at collider experiments, mainly that: SUSY particles are always produced in pairs, their decay products always contain an odd number of SUSY particles and the lightest SUSY particle (LSP) is absolutely stable.

Minimal set of soft SUSY-breaking terms: we know that supersymmetry is a broken symmetry since, for example, no bosonic particle has been observed with mass equal to that of the electron. Unfortunately, the mechanism behind this breaking is yet unknown. Therefore, to break supersymmetry in the MSSM, one must add to the Lagrangian a (minimal) set of terms to break it explicitly. As a

9

consequence, the MSSM contains a large number (105) of new parameters in addition to the 19 from the SM. However, most of these parameters have no impact on Higgs boson phenomenology and we will not concern ourselves with them here. Below, we identify and discuss the parameters that govern the main properties of the MSSM Higgs bosons.

1.2.1 Higgs sector of the MSSM

Due to restrictions on the form of the *superpotential* in any SUSY theory, the Higgs sector of the MSSM must contain two Higgs doublets in order to give masses to both up- and down-type fermions: one complex $Y = $ -1 doublet, $\mathbf{\Phi_d} = (\Phi_d^0, \Phi_d^-)$, and one complex $Y = $ +1 doublet, $\mathbf{\Phi_u} = (\Phi_u^+, \Phi_u^0)$. Where, $\mathbf{\Phi_d}$ ($\mathbf{\Phi_u}$) couples exclusively (at tree level) to up- (down-)type fermions. Similar to the SM, when the Higgs potential is minimized, the neutral components of the Higgs fields develop vevs, thus breaking the electroweak symmetry. The minima of the scalar potential are usually chosen to be:

$$\langle \mathbf{\Phi_d} \rangle = \frac{1}{\sqrt{2}} \begin{pmatrix} v_d \\ 0 \end{pmatrix}, \qquad \langle \mathbf{\Phi_u} \rangle = \frac{1}{\sqrt{2}} \begin{pmatrix} 0 \\ v_u \end{pmatrix}, \qquad (1.16)$$

where v_u and v_d satisfy the normalization condition: $v^2 \equiv v_d^2 + v_u^2 = (246 \text{ GeV})^2$. As in the SM, three of the original degrees of freedom become the longitudinal components of the $W^\pm$ and Z^0 gauge bosons, thus giving them mass. This results in five left-over scalar degrees of freedom which are identified with the five physical Higgs bosons of the MSSM. They consist of two CP-even scalars:

$$h^0 = -(\sqrt{2} \operatorname{Re} \Phi_d^0 - v_d) \sin \alpha + (\sqrt{2} \operatorname{Re} \Phi_u^0 - v_u) \cos \alpha \,,$$
$$H^0 = (\sqrt{2} \operatorname{Re} \Phi_d^0 - v_d) \cos \alpha + (\sqrt{2} \operatorname{Re} \Phi_u^0 - v_u) \sin \alpha \,, \qquad (1.17)$$

one CP-odd scalar (or pseudoscalar)

$$A^0 = \sqrt{2} \left(\operatorname{Im} \Phi_d^0 \sin \beta + \operatorname{Im} \Phi_u^0 \cos \beta \right) \,, \qquad (1.18)$$

10

and a pair of charged Higgs bosons

$$H^{\pm} = \Phi_d^{\pm} \sin\beta + \Phi_u^{\pm} \cos\beta \, , \tag{1.19}$$

where α is the angle that diagonalizes the CP-even Higgs mass matrix to obtain the physical Higgs bosons h^0 and H^0, while the angle β serves to parameterize the ratio of the two Higgs vevs as:

$$\tan\beta \equiv \frac{v_u}{v_d} \, . \tag{1.20}$$

The Higgs sector of the MSSM is fully described in terms of six parameters: the four Higgs masses ($M_{h^0}, M_{H^0}, M_{A^0}$ and $M_{H^{\pm}}$) and the two angles (α and β). However, in contrast to the Higgs sector of the SM, the SUSY structure of the MSSM imposes very strong constraints on the properties of the Higgs bosons. Consequently, the tree-level Higgs sector of the MSSM can be fully described by only *two* free parameters, which are conveniently chosen to be $\tan\beta$ and the mass of the pseudoscalar (M_{A^0}). The masses of the four remaining Higgs bosons can be written in terms of these two parameters as:

$$M_{H^{\pm}}^2 = M_{A^0}^2 + M_W^2 \, , \tag{1.21}$$

and

$$M_{H^0,h^0}^2 = \frac{1}{2}\left(M_{A^0}^2 + M_Z^2 \pm \sqrt{(M_{A^0}^2 + M_Z^2)^2 - 4M_Z^2 M_{A^0}^2 \cos^2 2\beta} \right) \, . \tag{1.22}$$

By definition, h^0 is chosen to be the lighter of the two CP-even scalars. In addition, one can obtain a condition to determine the angle α, namely:

$$\cos^2(\beta - \alpha) = \frac{M_{h^0}^2(M_Z^2 - M_{h^0}^2)}{M_{A^0}^2(M_{H^0}^2 - M_{h^0}^2)} \, . \tag{1.23}$$

An important consequence of Eq. (1.22) is that the MSSM provides an upper bound to the mass of the light CP-even Higgs boson, h^0, given by:

$$M_{h^0} \leq M_Z |\cos 2\beta| \leq M_Z \, . \tag{1.24}$$

This (tree-level) condition implies that h^0 should be lighter than the Z^0 boson and, thus, should have been detected at past experiments. However, it turns out that

11

SUSY radiative corrections to M_{h^0} are large and, in fact, significantly shift the upper limit to the range $M_{h^0}^{\text{max}} \simeq 130$ GeV (depending on the value of $\tan\beta$ and on the amount of mixing between the superpartners of the top quark). The fact that the MSSM predicts an upper limit is in sharp contrast to the SM, where the mass of the Higgs is only mildly constrained as seen in Sec. 1.1.3. However, it is interesting to note that the MSSM prediction $M_{h^0}^{\text{max}} \simeq 130$ GeV is consistent with the predictions shown in Fig. 1.1 at $\Lambda \simeq 1$ TeV, where SUSY effects are predicted to appear. Finally, both the Tevatron and the LHC will be able to test this important prediction of the MSSM.

1.2.2 Higgs-fermion interactions in the MSSM

The other aspect of the MSSM Higgs sector that is of importance to the work done for this thesis concerns the interactions between the neutral Higgs bosons and the fermions. In the MSSM, the tree-level Higgs couplings to the fermions are given by the Lagrangian (using third generation notation):

$$-\mathcal{L}_{\text{Yukawa}} = h_t \left[\bar{t} P_L t \Phi_u^0 - \bar{t} P_L b \Phi_u^+ \right] + h_b \left[\bar{b} P_L b \Phi_d^0 - \bar{b} P_L t \Phi_d^- \right] + \text{h.c.}, \qquad (1.25)$$

where $P_L \equiv \frac{1}{2}(1-\gamma_5)$ is the left-handed projection operator. Using Eqs. (1.17)-(1.19) along with Eq. (1.25), one can extract the couplings of the neutral Higgs bosons to $f\bar{f}$ pairs relative to the SM values:

$$h^0 b\bar{b} \quad (\text{or } h^0 \tau^+ \tau^-): \quad -\frac{\sin\alpha}{\cos\beta} g_{b\bar{b}h} = [\sin(\beta-\alpha) - \tan\beta \cos(\beta-\alpha)] \, g_{b\bar{b}h}, \quad (1.26)$$

$$h^0 t\bar{t}: \quad \frac{\cos\alpha}{\sin\beta} g_{t\bar{t}h} = [\sin(\beta-\alpha) + \cot\beta \cos(\beta-\alpha)] \, g_{t\bar{t}h}, \quad (1.27)$$

$$H^0 b\bar{b} \quad (\text{or } H^0 \tau^+ \tau^-): \quad \frac{\cos\alpha}{\cos\beta} g_{b\bar{b}h} = [\cos(\beta-\alpha) + \tan\beta \sin(\beta-\alpha)] \, g_{b\bar{b}h}, \quad (1.28)$$

$$H^0 t\bar{t}: \quad \frac{\sin\alpha}{\sin\beta} g_{t\bar{t}h} = [\cos(\beta-\alpha) - \cot\beta \sin(\beta-\alpha)] \, g_{t\bar{t}h}, \quad (1.29)$$

$$A^0 b\bar{b} \quad (\text{or } A^0 \tau^+ \tau^-): \qquad \gamma_5 \tan \beta \, g_{b\bar{b}h} , \qquad (1.30)$$

$$A^0 t\bar{t}: \qquad \gamma_5 \cot \beta \, g_{t\bar{t}h} , \qquad (1.31)$$

where $g_{b\bar{b}h}$ and $g_{t\bar{t}h}$ are the SM Yukawa couplings of the bottom and top quarks respectively (see Section 1.1.2). In particular, we see that for large $\tan \beta$ ($\sin \beta \to 1$ and $\cos \beta \to 0$), the neutral Higgs bosons couplings to down-type quarks become strongly enhanced, while the couplings to up-type quarks are suppressed.

Recently, it has been shown that, for large $\tan \beta$, the SUSY radiative corrections to the MSSM Yukawa couplings can also be quite significant [17]. As an example, consider the situation for the bottom quark in the MSSM. At tree level and in the supersymmetric limit, the bottom quark only couples to the down-type Higgs doublet ($\mathbf{\Phi_d}$). However, SUSY is broken and the bottom quark develops a small (loop-induced) coupling to the up-type Higgs doublet ($\mathbf{\Phi_u}$), such that the effective Lagrangian for the bottom Yukawa couplings becomes:

$$\mathcal{L} = h_b \mathbf{\Phi_d} b\bar{b} + \Delta h_b \mathbf{\Phi_u} b\bar{b} . \qquad (1.32)$$

The second term is loop-suppressed compared to the first, but when the Higgs doublets acquire vacuum expectation values, the bottom quark mass receives corrections proportional to $\Delta h_b v_u$. In the limit of large $\tan \beta$ ($v_u \gg v_d$), the two terms in Eq. (1.32) become comparable in size and, thus, the bottom quark mass can be significantly modified from the (SUSY) tree-level value, namely

$$m_b = h_b v_d (1 + \Delta(m_b)) , \qquad (1.33)$$

where $\Delta(m_b) = \Delta h_b \tan \beta / h_b$. Using Eq. (1.33), one can extract the corrections to the bottom quark Yukawa coupling of the physical Higgs bosons. For the neutral Higgs, we have:

$$g_{b\bar{b}h^0} = -\frac{m_b}{v} \frac{\sin \alpha}{\cos \beta} \left[1 - \frac{\Delta(m_b)}{1 + \Delta(m_b)} \left(1 + \frac{1}{\tan \alpha \tan \beta} \right) \right] g_{b\bar{b}h} , \qquad (1.34)$$

13

$$g_{b\bar{b}H^0} = \frac{m_b}{v}\frac{\cos\alpha}{\cos\beta}\left[1 - \frac{\Delta(m_b)}{1+\Delta(m_b)}\left(1 - \frac{\tan\alpha}{\tan\beta}\right)\right]g_{b\bar{b}h} , \qquad (1.35)$$

$$g_{b\bar{b}A^0} = \frac{m_b}{v}\tan\beta\left[1 - \frac{\Delta(m_b)}{(1+\Delta(m_b))\sin^2\beta}\right]g_{b\bar{b}h} . \qquad (1.36)$$

1.2.3 Regimes of the MSSM Higgs sector

Although fully determined by only two free parameters, the phenomenology of the MSSM Higgs sector can be quite diverse, depending on the values of M_{A^0} and $\tan\beta$. For simplicity and since it is important to the study performed here, i.e. Higgs boson production with bottom quarks, we focus on the large $\tan\beta$ ($\gtrsim 10$) region where the Yukawa couplings to down-type fermions can become enhanced for the neutral Higgs bosons. In this region, the $M_{A^0} - \tan\beta$ plane divides into three distinct regimes which we briefly describe below.

Decoupling regime: in the case where M_{A^0} is large compared to the maximal mass of h^0, $M_{A^0} \gg M_{h^0}^{\max}$, we immediately see from Eq. (1.22) that the H^0 becomes degenerate in mass with the pseudoscalar, $M_{H^0} \approx M_{A^0}$. Additionally, the inequality in Eq. (1.24) saturates and the light CP-even Higgs boson reaches its maximal mass, $M_{h^0} \approx M_{h^0}^{\max}$. Using Eqs. (1.23) and (1.26)-(1.31), we also see that the Yukawa couplings to down-type fermions of the heavy CP-even Higgs and the pseudoscalar Higgs become nearly equal in strength and, thus, highly enhanced for large $\tan\beta$. However, the couplings of the light CP-even Higgs bosons become equal to those corresponding to the SM Higgs boson, i.e. h^0 becomes *SM-like*.

Anti-decoupling regime: when M_{A^0} is small, i.e. $M_{A^0} \ll M_{h^0}^{\max}$, the situation is exactly the opposite of that in the decoupling regime. Namely, the h^0 and A^0 become nearly degenerate in mass, while the mass of the heavy CP-even Higgs approaches $M_{h^0}^{\max}$. Thus, in this regime, all three scalar Higgs bosons are light. Additionally, the Yukawa couplings to down-type fermions of the h^0 become nearly equal in strength

to that of the pseudoscalar and are greatly enhanced for large $\tan\beta$. In contrast, the couplings of the heavy CP-even Higgs boson become SM-like.

Intense-coupling regime: finally, when $M_{A^0} \approx M_{h^0}^{\mathrm{max}}$, all three neutral Higgs bosons become nearly degenerate in mass, $M_{A^0} \approx M_{h^0} \approx M_{H^0} \approx M_{h^0}^{\mathrm{max}}$. In this regime, which serves as a transition between the decoupling and anti-decoupling regimes, *both h^0 and H^0* have enhanced couplings to down-type fermions. However, given the mass degeneracy in this region, distinguishing the three different scalar Higgs bosons will be extremely difficult.

1.2.4 MSSM Higgs boson decays

As can be expected from the above discussion, the decay patterns of the MSSM Higgs bosons can be quite different from those of the SM Higgs boson. In particular, the hierarchy of decay modes strongly depends on the values of M_{A^0} and $\tan\beta$ and is clearly sensitive to the choice of the SUSY masses since these determine the possibility for the MSSM Higgs bosons to decay into pairs of SUSY particles and for the loop-induced decay channels ($h^0, H^0 \rightarrow gg, \gamma\gamma, etc.$) to receive SUSY loop contributions.

To simplify matters, we will assume that all SUSY masses (excluding the Higgs bosons) are all large enough to prevent the decay of the MSSM Higgs bosons into pairs of SUSY particles. In this scenario, we only need to examine decays into SM particles and compare with the decay patterns of a SM Higgs boson to identify interesting differences (see Figs. 1.3 and 1.4).

From the discussion in Section 1.2.3, we can make several general statements about the decay patters of the MSSM Higgs bosons. First, in the decoupling regime, where $M_{A^0} \gg M_Z$, the properties of the h^0 are almost identical to that of the SM Higgs boson and the decay patterns discussed in Section 1.1.4 apply. On the other hand, in this regime, the H^0 is very heavy ($M_{H^0} \simeq M_{A^0}$) and its couplings to down-type fermions (electroweak gauge bosons) become extremely enhanced

15
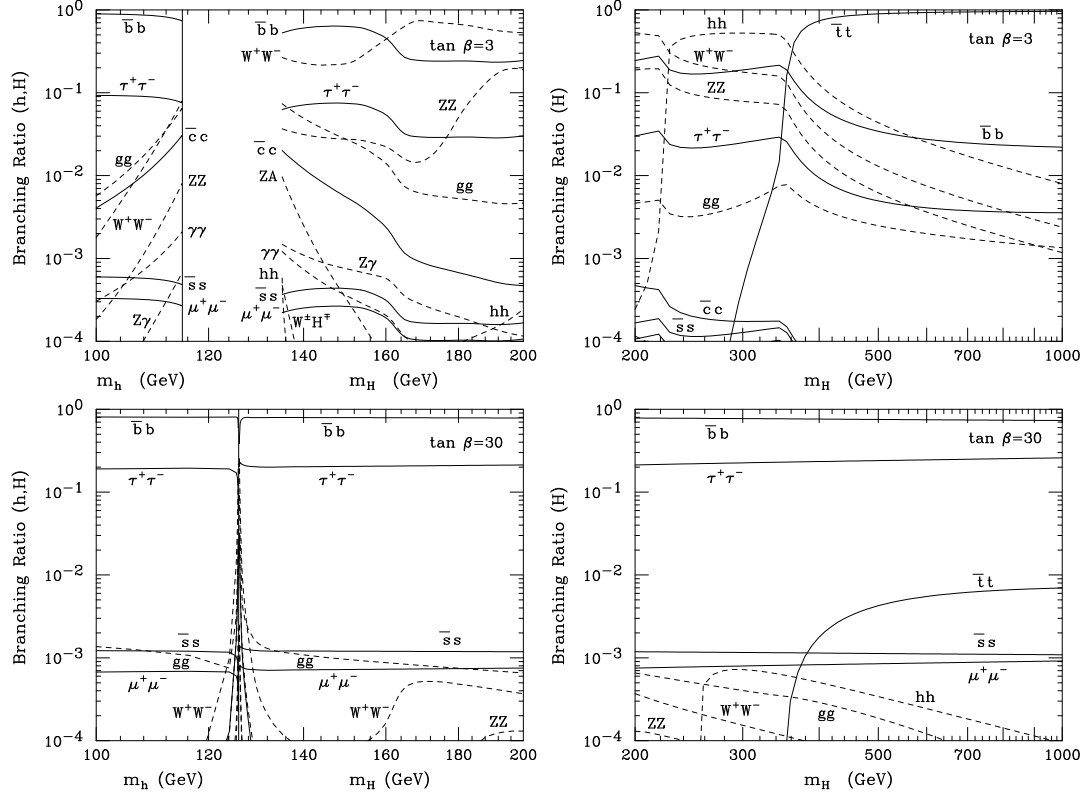
Figure 1.3. Branching ratios for the h^0 and H^0 MSSM Higgs bosons, for $\tan \beta = 3, 30$. The range of M_H corresponds to $M_A = 90\,\text{GeV} - 1\,\text{TeV}$, in the MSSM scenario discussed in the text, with maximal top-squark mixing. The vertical line indicates the upper bound on M_{h^0}, which, for the given scenario is $m_{h^0}^{\max} = 115$ GeV ($\tan \beta = 3$) or $m_{h^0}^{\max} = 125.9$ GeV ($\tan \beta = 30$). From Ref. [9].

(suppressed) such that it decays predominantly into $b\bar{b}, \tau^+\tau^-$ over the full mass range. Away from the decoupling regime, we can expect that the decay rates of the h^0 and H^0 to the electroweak gauge bosons are suppressed in comparison to the SM case. Also, the decays of the pseudoscalar A^0 into vector gauge bosons are absent due to CP-invariance. Finally, in the anti-decoupling and the intense-coupling regimes, the couplings of all neutral MSSM Higgs bosons to $b\bar{b}, \tau^+\tau^-$ pairs are enhanced for large values of $\tan \beta$, thus making these the dominant decay modes.
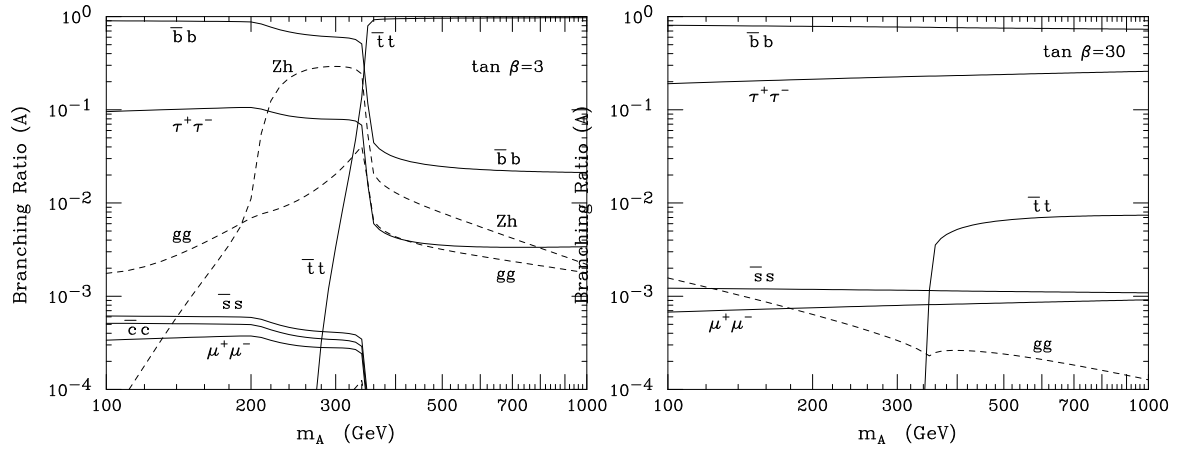
Figure 1.4. Branching ratios for the A^0 MSSM Higgs boson, for $\tan\beta = 3, 30$. From Ref. [9].

1.3 Summary

The Higgs sector of the SM remains the least tested piece of this otherwise extremely successful theory. In particular, discovering the mechanism behind EWSB and the origin of the quark and lepton masses are two of the main challenges facing particle physics and both of these problems are the main goals of present and future colliders. One thing is for sure, both the SM and models of new physics, in particular the MSSM, seem to indicate that the mechanism behind EWSB should *rear its head* around or below the TeV scale. Considering the center of mass energies of present and future colliders (1.96 - 14 TeV), this is a very interesting time for particle physics and, in particular, Higgs physics. A more detailed description of the past, present, and future effort in the search for a Higgs boson is given in the next chapter.

17

CHAPTER 2

IN SEARCH OF A HIGGS BOSON

Even though the SM has been probed to extreme accuracy, the final piece of the puzzle, the Higgs boson, has yet to be discovered. Moreover, had supersymmetry to be realized in Nature, there will be a spectrum of Higgs bosons, one of which at least should be light. Once a Higgs boson *is* discovered, the next task will be to measure its properties, in particular its couplings to SM particles. In this chapter, we review the current bounds on the mass of the SM and MSSM Higgs bosons from both indirect and direct searches. We also summarize the search strategies for SM and MSSM Higgs bosons at hadron colliders.

2.1 Limits on the Higgs mass from precision electroweak data

Over the past few decades, the SM has been tested to extremely high precision. At present, *all* measurements performed on observables of the electroweak sector (e.g. M_W, M_Z, etc.) seem to agree with the predictions of the SM. The theoretical calculations of these observables contain all known orders of radiative corrections, to which the Higgs boson also contributes. The electroweak precision measurements are, in fact, sensitive to these radiative corrections and, therefore, can be used to place indirect constraints on the properties of the Higgs boson, in particular its mass.

With this respect, Fig. 2.1 shows the $\Delta\chi^2$ ($\equiv \chi^2 - \chi^2_{min}$) of the fit to all measurements of the electroweak sector as a function of M_h [18]. Apparently, the data seems to favor a light Higgs boson with a (best fit) mass

18
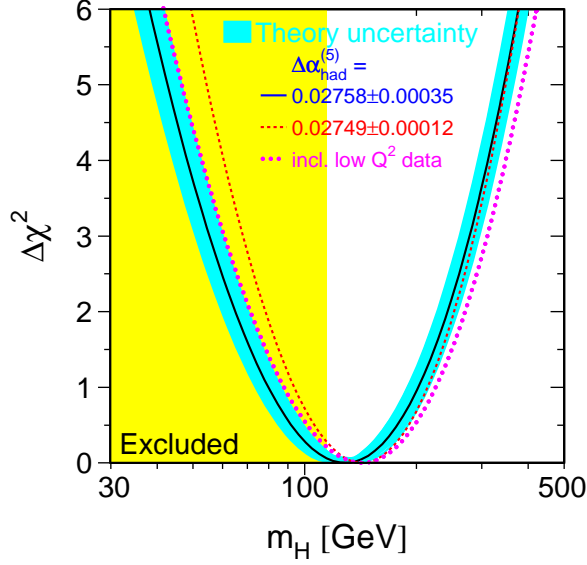
Figure 2.1. The $\Delta\chi^2$ of the fit to electroweak data as a function of M_h (using $m_t = 178$ GeV). The solid line results when all data are included, while the shaded band is the estimated theoretical error from unknown higher-order corrections [18].

$$M_h = 129^{+74}_{-49} \text{ GeV} , \qquad (2.1)$$

with a 95% Confidence Level (C.L.) upper limit of

$$M_h < 285 \text{ GeV}. \qquad (2.2)$$

To conclude, it should be noted that the precise agreement between the electroweak precision data and the SM is not unique. In fact, any extension of the SM which contains an elementary, weakly-coupled Higgs particle generates only small corrections to the electroweak observables, even if these models contain a large number of new particles (e.g. supersymmetric theories).
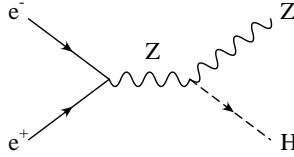
Figure 2.2. Feynman diagram for $e^+e^- \rightarrow Z^0 h$.

2.2   Direct searches

The most recent direct search for Higgs bosons was performed at the LEP2 (CERN) e^+e^- collider which reached a maximum center-of-mass (CM) energy of $\sqrt{s} = 209$ GeV. At this energy, the dominant production mode is $e^+e^- \rightarrow Z^0 h$, where the Higgs boson is radiated from an off-shell Z^0 boson (see Fig. 2.2). The search was performed using two different Higgs decay modes, $h \rightarrow b\bar{b}$ and $h \rightarrow \tau^+\tau^-$, and several decay modes for the Z^0. At present, combining the results for the four LEP collaborations, no significant excess above the SM background has been observed up to an exclusion limit of [19]:

$$M_h > 114.4 \text{ GeV} \tag{2.3}$$

at the 95% C.L. In addition to this limit, the collaborations report a 1.7σ excess of events for a Higgs boson mass of $M_h = 116$ GeV [19].

The non-observation of a Higgs boson signal at LEP can also be used to place limits on the masses of the MSSM Higgs bosons using the search channels $e^+e^- \rightarrow Z^0 h^0(A^0)$ and $e^+e^- \rightarrow h^0 A^0$. Given the complexity of the MSSM parameter space, though, it is difficult to state general exclusion limits on the Higgs boson masses. However, for representative scans of the MSSM parameters, the LEP Higgs Working Group finds that the masses of the lightest scalar and the pseudoscalar MSSM Higgs bosons are excluded below 91.0 GeV and 91.9 GeV, respectively, at the 95% C.L. [20].

20

2.3 Higgs boson production at hadron colliders

The next experiments designed to search for Higgs bosons are at *hadron colliders.* The Tevatron proton-antiproton ($p\bar{p}$) collider is currently running with a center-of-mass (CM) energy of $\sqrt{s_H} = 1.96$ TeV and should be able to provide evidence for a low mass Higgs boson in the range $M_h = 100 - 200$ GeV. The LHC proton-proton (pp) collider is set to turn on in 2007 with a a CM energy of $\sqrt{s_H} = 14$ TeV and will be able to discover a Higgs boson with mass up to ~ 1 TeV. Therefore, regardless of the true structure of the Higgs sector, if it exists, a Higgs boson will be discovered in the near future. In the following, after a brief introduction to the general structure of the theoretical calculation for Higgs production at hadron colliders, we outline the search strategies for SM and MSSM Higgs bosons at both the Tevatron and the LHC.

2.3.1 Theoretical calculations for Higgs production in hadronic collisions

The cross section for pp and $p\bar{p}$ collisions to produce a final state including a Higgs boson can be schematically written as:

$$\sigma(pp, p\bar{p} \to H + X) = \sum_{ij} \int dx_1 dx_2 \mathcal{F}_i^p(x_1) \mathcal{F}_j^{p,\bar{p}}(x_2) \hat{\sigma}(ij \to h + X) \ , \qquad (2.4)$$

where i and j run over the elementary constituents of a proton (antiproton), quarks and gluons, collectively denoted as *partons.* Eq. (2.4) expresses the fact that the hadronic cross section is calculated as the convolution of a *partonic* cross section, $\hat{\sigma}(ij \to h + X)$, with *Parton Distribution Functions* (PDFs), $\mathcal{F}_{i,j}^{p,\bar{p}}(x)$, which can be interpreted as the probability of finding parton i, j in a proton (or antiproton) with a fraction x of the (anti)proton's longitudinal momentum.

In hadronic collisions, the most important effects arise from the strong interactions. Therefore, it is mandatory to have under control the QCD perturbative expansion of the hadronic cross section $\sigma(pp, p\bar{p} \to h + X)$. To accomplish this, the
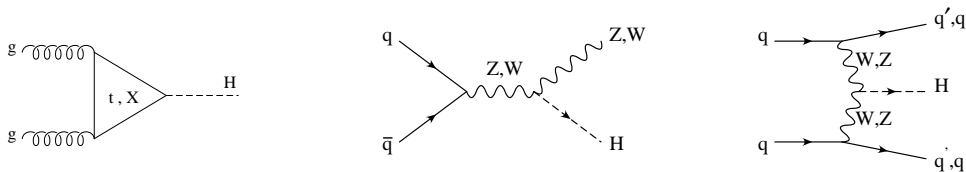
Figure 2.3. Leading Higgs production processes at hadron colliders: $gg \rightarrow h$, $q\bar{q} \rightarrow Wh, Zh$ and $qq \rightarrow qqh$.

partonic cross section and the evolution of the PDFs are calculated perturbatively. At each order in the perturbative expansion, the calculation of $\hat{\sigma}(ij \rightarrow h + X)$ and $\mathcal{F}_{i,j}^{p,\bar{p}}$ contains ultraviolet divergences that are subtracted through a standard renormalization procedure. This, at each finite order, leaves a dependence on the renormalization scale, μ_R, which reflects the fact that the calculation is based on a truncated series. In the same way, when the PDFs are defined in terms of their (experimentally-measured) non-perturbative cores, a factorization scale, μ_F, is introduced in the calculation of $\mathcal{F}_{i,j}^{p,\bar{p}}$ and $\hat{\sigma}(ij \rightarrow h + X)$. In both cases, the dependence on these scales is indicative of the residual theoretical uncertainty present at a given perturbative order. Typically, lowest or leading order (LO) predictions for hadronic cross sections are plagued by very large renormalization/factorization scale dependence. Thus, one is forced to calculate at least next-to-leading order (NLO) QCD corrections to stabilize the theoretical prediction. In fact, for some cases of Higgs production in hadronic collisions, next-to-NLO (NNLO) QCD corrections are required to obtain reliable results.

2.3.2 Higgs bosons at hadron colliders: generalities

The most important partonic processes for Higgs boson production in hadronic collisions are shown in Figs. 2.3 and 2.4. All of these processes have been calculated at NLO in QCD [21, 22, 23, 24, 25, 26, 27, 28, 29, 30, 31], while NNLO corrections have recently been obtained for $gg \rightarrow h$ [32] and $q\bar{q} \rightarrow HV$ (where $V = W^{\pm}, Z^0$) [33].
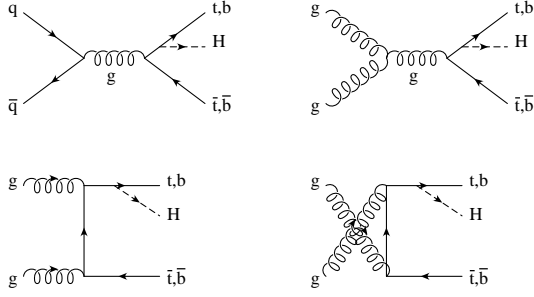
Figure 2.4. Sample Feynman diagrams depicting Higgs production with heavy quarks: $q\bar{q}, gg \to t\bar{t}h, b\bar{b}h$.

Figs. 2.5 and 2.6 summarize the production cross sections for these processes at both the Tevatron and the LHC as a function of the Higgs mass [10].

Due to the large luminosity of gluons at the Tevatron and the LHC, the dominant production mode at both machines is that of *gluon fusion*, $gg \to h$. Although this process is loop-induced, it is greatly enhanced by color structure and the top quark Yukawa coupling, which is of $\mathcal{O}(1)$. However, for light and intermediate Higgs bosons (i.e. below the $h \to WW$ threshold), the Higgs boson decays predominantly to $b\bar{b}$ pairs and the gluon fusion mode must compete with the background process $gg \to b\bar{b}$, which boasts a huge cross section. Thus, extracting a signal from the $gg \to h \to b\bar{b}$ channel is extremely difficult and one must rely on sub-leading decays such as $h \to \gamma\gamma$. On the other hand, for larger Higgs masses (i.e. above the $h \to ZZ$ threshold), gluon fusion together with $h \to ZZ$ produces a very distinctive signal, and makes this a *gold-plated mode* for discovery. For this reason, $gg \to h$ will play a fundamental role at the LHC over the entire Higgs mass range (especially for heavy Higgs bosons), but it is of very limited use at the Tevatron where it can only be considered for Higgs masses close to the upper reach of the machine ($M_h \simeq 200$ GeV).

The most promising detection mode at the Tevatron is the associated production of a Higgs boson with a weak gauge boson, $q\bar{q} \to hW, hZ$ (second diagram in Fig. 2.3). Although this channel plays a smaller role at the LHC, it is extremely important at

the Tevatron where only a light Higgs boson can be discovered. In this range, the Higgs will decay mostly into $b\bar{b}$, but one can use the leptonic decays of the weak gauge bosons to extract a signal.

The channel with the second largest cross section at the LHC is *vector boson fusion* (*VBF*), $qq \rightarrow qqh$, where the initial state quarks both emit weak gauge bosons, which then annihilate into a Higgs boson (third diagram in Fig. 2.3). This process is heavily suppressed at the Tevatron (because of the $p\bar{p}$ initial state), but provides an especially distinct final state (two very forward jets) at the LHC. For low and intermediate Higgs masses, the distinctive final state of VBF has been shown to greatly help in disentangling this signal from the hadronic backgrounds.

Finally, we consider the production of a Higgs boson with a pair of heavy quarks (Fig 2.4). This channel is sub-leading at both the Tevatron and the LHC, but has a great physics potential. Although $t\bar{t}h$ production is too small to be seen at the Tevatron, given the expected luminosities, this channel will be of utmost importance for a light Higgs boson ($M_h \leq 130$ GeV) at the LHC. Despite the small cross section, Higgs production with $t\bar{t}$ pairs, followed by $h \rightarrow b\bar{b}$, displays a spectacular signal ($W^+W^-b\bar{b}b\bar{b}$) which can be easily extracted from backgrounds. Also, given the statistics expected at the LHC, $pp \rightarrow t\bar{t}h$ will provide the only *direct* measurement of the top quark Yukawa coupling. On the other hand, the production of a SM Higgs boson with bottom quarks is suppressed by the smallness of the bottom quark Yukawa coupling. Therefore, the $b\bar{b}h$ ($h \rightarrow b\bar{b}$) channel is the ideal candidate to provide evidence for a non-SM Higgs sector, in particular an extension of the SM like SUSY models where the bottom quark Yukawa coupling is enhanced. In fact, first studies from the two experiments at the Tevatron (CDF [34] and DØ [35]) have already translated the absence of a $b\bar{b} + h^0/H^0/A^0$ signal into an upper bound on the parameter $\tan\beta$ of the MSSM (see Fig. 2.7).
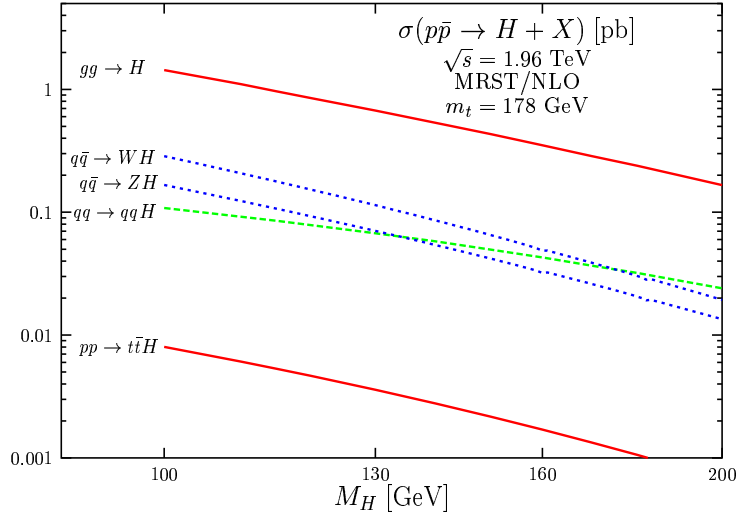
Figure 2.5. The total cross sections for SM Higgs boson production at the Tevatron ($\sqrt{s_H} = 1.96$ TeV) [10].

2.3.3 SM Higgs boson searches at the Tevatron and the LHC

Despite lower luminosities than originally projected, discovering a Higgs boson during Run II of the Tevatron is still among the major goals of the collider. In fact, recent studies have shown that Run II can push the 95% C.L. upper limit much farther than LEP2 (see Sect. 2.2). Also, depending on the integrated luminosity accumulated, the Tevatron could still produce a 3σ or 5σ discovery for a light Higgs boson.

The plot in Fig. 2.8 shows the integrated luminosity estimated to be necessary to reach a 95% C.L. exclusion limit, the 3σ, and the 5σ discovery levels for Higgs masses up to $M_h = 200$ GeV [36]. These curves are produced using $q\bar{q} \to hW, hZ$ with $h \to b\bar{b}$ and $h \to W^+W^-$ over the entire Higgs mass range and $gg \to h$ with $h \to ZZ$ for the upper mass region. From Fig. 2.8, we see that with, e.g., 10 fb^{-1} of integrated luminosity RUN II will be able to put a 95% C.L. exclusion limit on

25
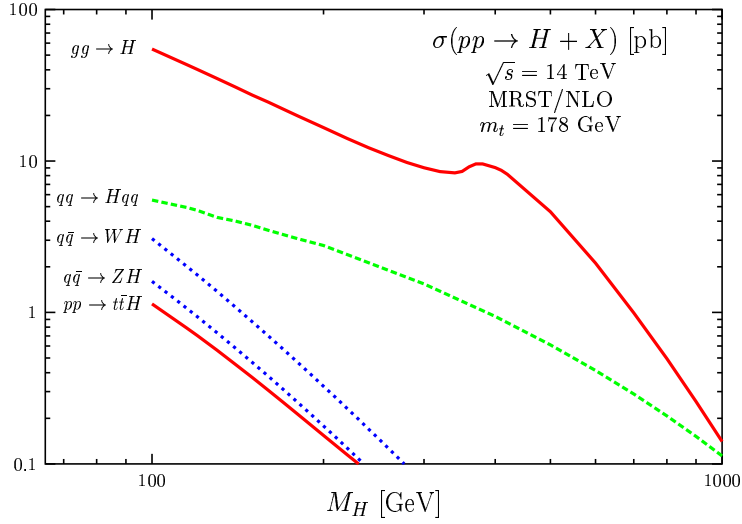
Figure 2.6. The total cross sections for SM Higgs boson production at the LHC ($\sqrt{s_H} = 14$ TeV) as a function of M_h [10].
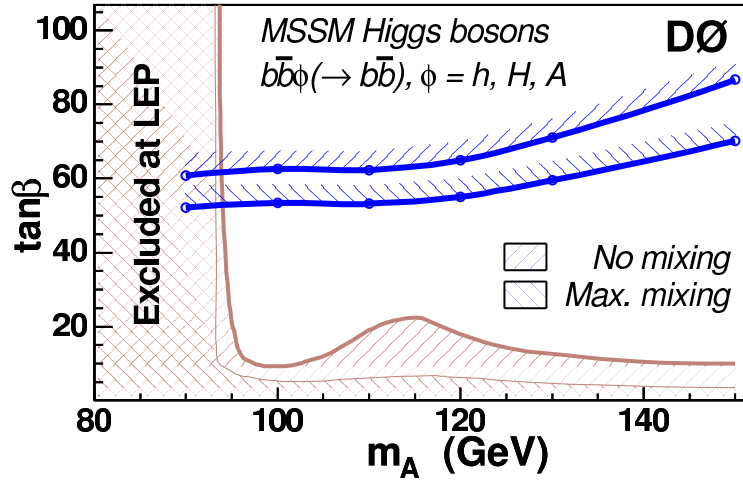
Figure 2.7. The 95% C.L. upper limit on $\tan\beta$ as a function of M_{A^0} from the $b\bar{b}\phi, \phi = h^0, H^0, A^0$ search channel [35].

26
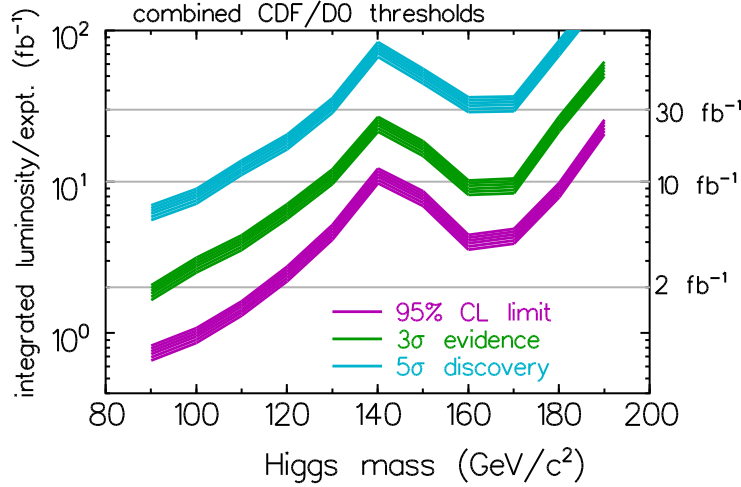
Figure 2.8. Integrated luminosity required for each experiment at the Tevatron Run II to exclude a SM Higgs boson at the 95% C.L. or to observe it at the 3σ or 5σ level [36].

a SM Higgs boson of mass up to 180 GeV, while it could claim a 3σ discovery of a SM Higgs boson with mass up to 125 GeV. A 5σ discovery of a SM Higgs boson up to 130 GeV, i.e. in the region immediately above the LEP2 lower bound, seems to require 30 fb^{-1} of integrated luminosity, well beyond what is currently expected for RUN II.

Even if a SM Higgs boson is not discovered at the Tevatron, the true test of its existence will be provided by the LHC. Due to the larger CM energy, production rates for the SM Higgs boson are significantly larger than those at the Tevatron as shown in Fig. 2.6. In fact, at the LHC, all production modes will be accessible, thanks to the higher statistics, and it becomes natural to distinguish between a light $(M_h < 130 - 140$ GeV) and heavy $(M_h > 130 - 140$ GeV) mass region, as becomes evident by simultaneously looking at both production cross sections (see Fig. 2.6) and decay branching ratios (see Fig. 1.2) over the entire $115 - 1000$ GeV SM Higgs boson mass range. In the region of $M_h < 130 - 140$ GeV the SM Higgs boson at the
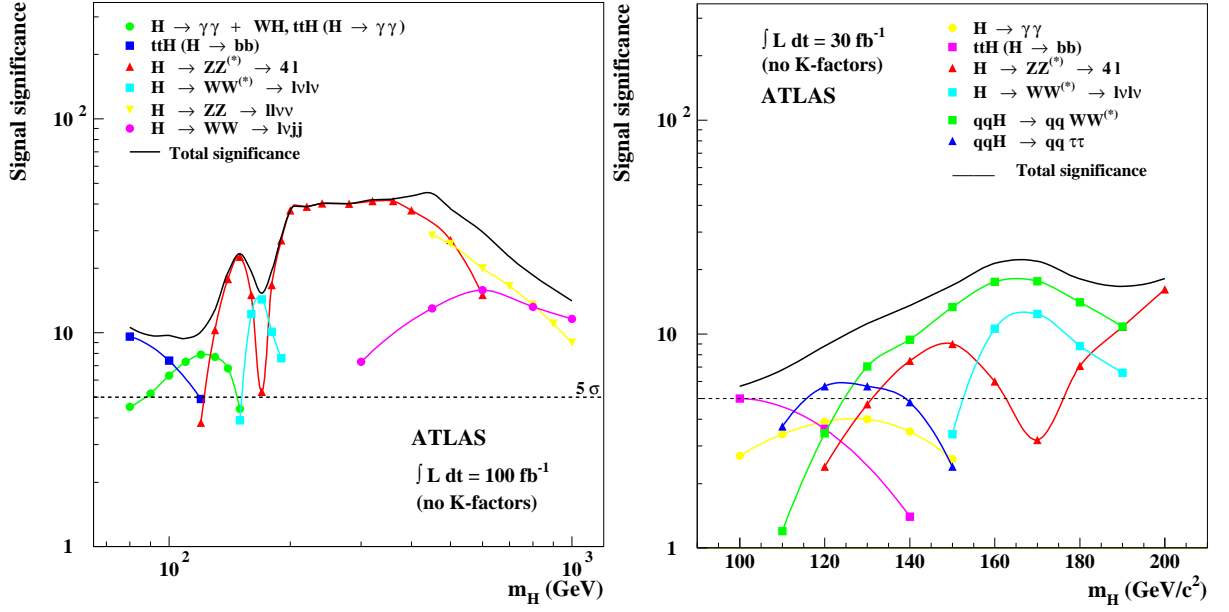
Figure 2.9. The significance for the SM Higgs boson discovery in various channels at ATLAS as a function of the Higgs mass for 100 fb^{-1} data with no vector boson fusion included (left) and 30 fb^{-1} data with vector boson fusion included for $M_h < 200$ GeV [37].

LHC will be searched mainly in the following channels:

$$gg \to h \, , \, h \to \gamma\gamma, W^+W^-, ZZ$$

$$qq \to qqh \, , \, h \to \gamma\gamma, W^+W^-, ZZ, \tau^+\tau^- \qquad (2.5)$$

$$q\bar{q}, gg \to t\bar{t}h \, , \, h \to b\bar{b}, \tau^+\tau^-$$

while above that region, i.e. for $M_h > 130 - 140$ GeV, the discovery modes will be:

$$gg \to h \, , \, h \to W^+W^-, ZZ$$

$$qq \to qqh \, , \, h \to \gamma\gamma, W^+W^-, ZZ \qquad (2.6)$$

$$q\bar{q}, gg \to t\bar{t}h \, , \, h \to W^+W^-$$

The two LHC experiments (ATLAS and CMS) have used these channels to estimate the discovery reach which is shown in Figs. 2.9 and 2.10 [37, 38]. The

28
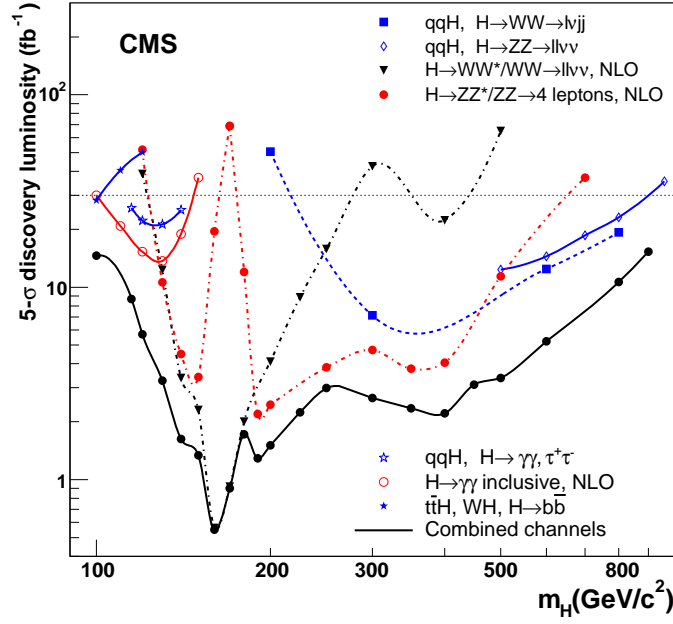
Figure 2.10. Luminosity required to reach a 5σ discovery signal in CMS, using various detection channels, as a function of M_h [38].

ATLAS plots give the signal significance for a total integrated luminosity of 100 fb^{-1} (left plot) and of 30 fb^{-1} (right plot). The high luminosity (upper) plot belongs to the original ATLAS technical design report [39], and the weak boson fusion channels had not been studied in detail at that time. The lower luminosity (lower) plot is taken from a more updated study [37], and the weak boson fusion channels have been included in the low mass region, up to about $M_h \simeq 200$ GeV, where they play an instrumental role towards discovery. Other instrumental channels in the low mass region are the inclusive Higgs production with $h \to \gamma\gamma$ and, below $M_h = 130$ GeV, $t\bar{t}h$ production with $h \to b\bar{b}$. In the high mass region, the inclusive production with $h \to ZZ, WW$ dominates, although CMS has found a substantial contribution coming from weak gauge boson fusion with $h \to ZZ, WW$.

29
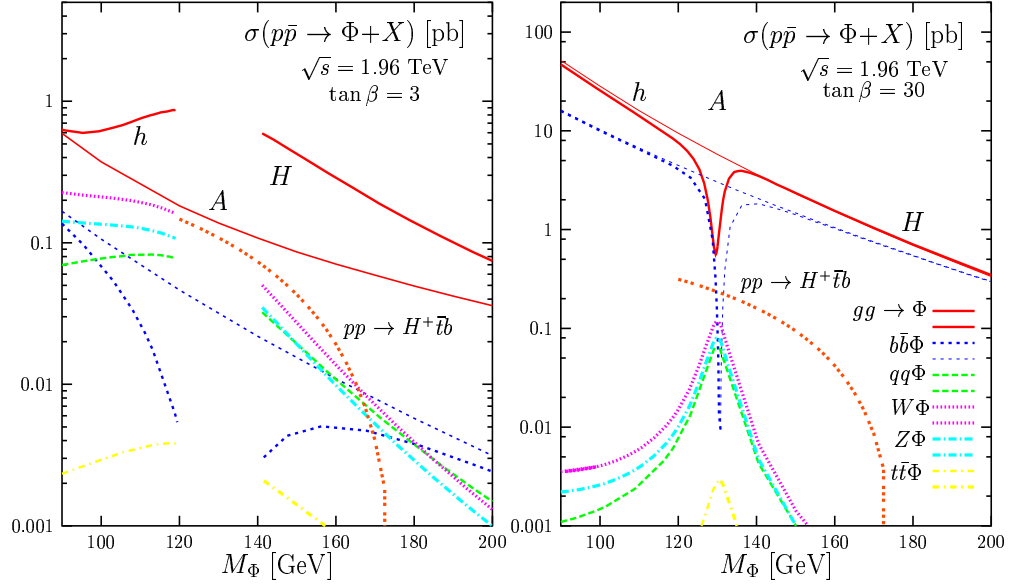
Figure 2.11. The total cross sections for MSSM Higgs boson production at the Tevatron ($\sqrt{s_H} = 1.96$ TeV) [10].

2.3.4 MSSM Higgs boson searches at the Tevatron and the LHC

Figures 2.11 and 2.12 summarize the production cross sections for the MSSM Higgs bosons at the Tevatron and the LHC, for both small and large values of $\tan\beta$. Here, we focus on the large values of $\tan\beta$ (right plots) where the phenomenology can be quite different from that of the SM. Obviously, for large $\tan\beta$, the only relevant processes for $h^0/H^0/A^0$ production are the gluon fusion process (which proceeds mainly through a loop of bottom and, to a lesser extent, top quarks) and the production of $h^0/H^0/A^0$ in association with a pair of bottom quarks.

As discussed in Sect. 1.2.3, the CP-even scalar which has enhanced couplings to $b\bar{b}$ strongly depends on the value of the pseudoscalar mass, M_{A^0}. For convenience, we define Φ_A to be that CP-even scalar which becomes *pseudoscalar-like*, i.e. the Higgs boson which becomes nearly degenerate in mass with A^0 and develops similar

30
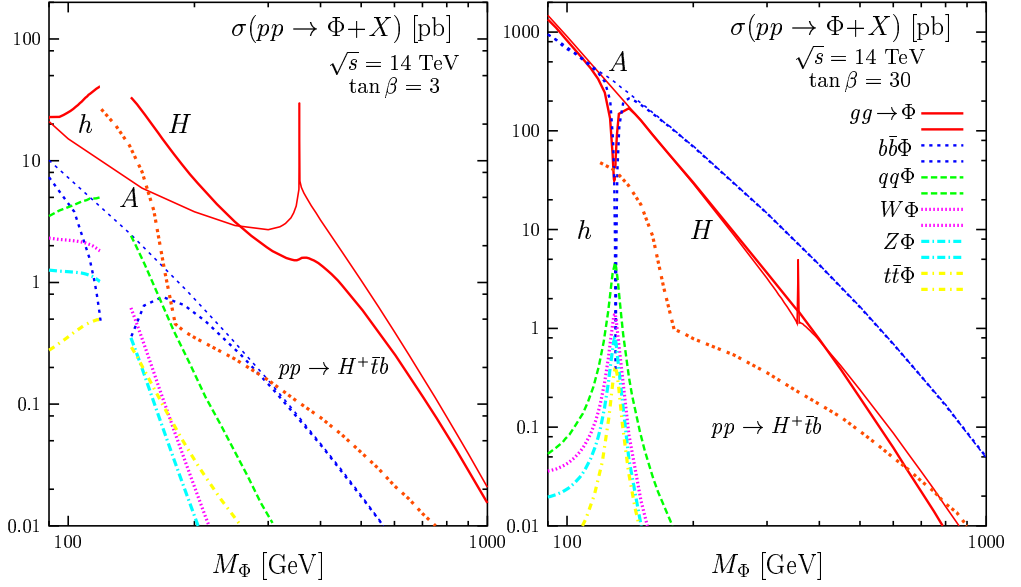
Figure 2.12. The total cross sections for MSSM Higgs boson production at the LHC ($\sqrt{s_H} = 14$ TeV) [10].

(enhanced) couplings to $b\bar{b}$. For example, in the decoupling (anti-decoupling) regime discussed in Sect. 1.2.3, Φ_A is identified with the $H^0(h^0)$. Likewise, we define Φ_H to be the CP-even Higgs boson which becomes SM-like, i.e. $\Phi_H = h^0(H^0)$ in the decoupling (anti-decoupling) regime.

At the Tevatron, for high $\tan\beta$, Φ_A and A^0 are both predominantly produced through $gg \to \Phi_A, A^0$ and $gg, q\bar{q} \to b\bar{b} + \Phi_A/A^0$, followed mostly by the decays $\Phi_A/A^0 \to b\bar{b}, \tau^+\tau^-$. Due to large QCD backgrounds, though, extraction of a signal from the gluon fusion mode may prove difficult. However, $b\bar{b} + \Phi_A/A^0$ followed by $\Phi_A/A^0 \to b\bar{b}$, with bottom quarks identified in the final state (or *tagged*) should be accessible, since the three and four jet backgrounds are not too large at the Tevatron. As mentioned earlier, this channel is presently being utilized in the search for an MSSM Higgs boson at both CDF [34] and D∅ experiments [35] at the Tevatron. Indeed, Fig. 2.7 shows recent results from D∅ in which the $b\bar{b} + \Phi_A/A^0$, $\Phi_A/A^0 \to b\bar{b}$

31

channel is being used to place limits on the value of $\tan\beta$. Finally, detection techniques for the SM-like Higgs (Φ_H) rely heavily on those techniques outlined above for the SM Higgs boson, especially in the mass range below 140 GeV. For example, the dominant process for the production of Φ_H would be $p\bar{p} \to Wh^0 (WH^0)$ in the decoupling (anti-decoupling) regime.

At the LHC, the situation is similar to the Tevatron case where, for large $\tan\beta$, at least two of the MSSM (neutral) Higgs bosons will be produced predominantly through gluon fusion and in association with bottom quarks. As can be seen in the right hand plot of Figure 2.12, these channels dominate over the other production modes by several orders of magnitude. In contrast to the situation at the Tevatron, though, the cross section for production with $b\bar{b}$ pairs becomes larger than that of gluon fusion for H^0 and A^0 above 200 GeV. Unfortunately, the QCD four jet cross section is large at the LHC and $\Phi_A/A^0 \to b\bar{b}$ will not provide a measurable signal if both bottom quarks are at high transverse momentum. Thus, one has to rely on the sub-dominant decays to $\tau^+\tau^-$ and $\mu^+\mu^-$ pairs. Finally, in Fig. 2.13, we show the coverage of the $m_A - \tan\beta$ plane that will be provided by the LHC [40]. Evidently, it may be possible at the LHC to either *exclude* the entire $m_A - \tan\beta$ plane (thereby eliminating the MSSM Higgs sector as a viable model), or achieve 5σ discovery of at least one of the MSSM Higgs bosons, independently of the value of $\tan\beta$ and M_A.
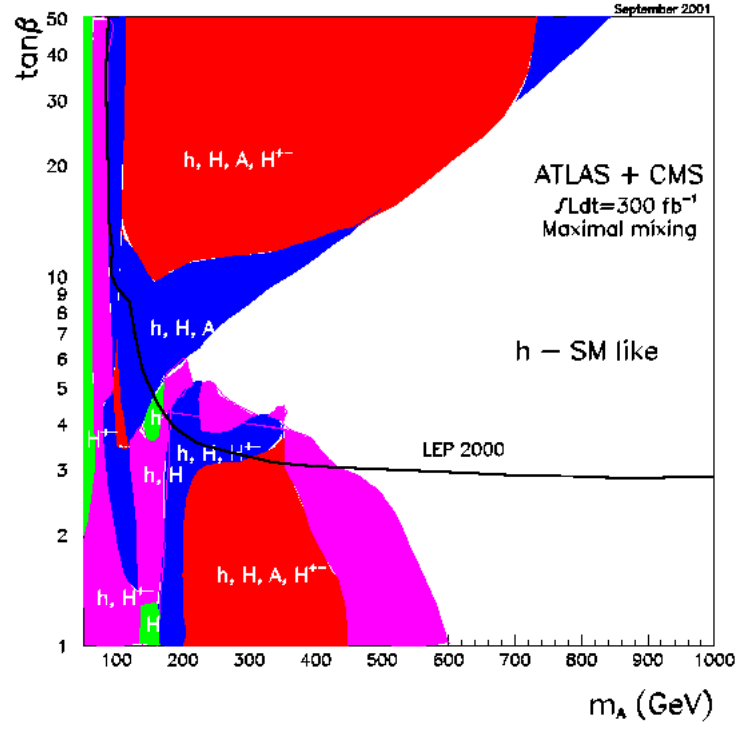
Figure 2.13. Regions in $m_A - \tan\beta$ plane in which up to four Higgs bosons of the MSSM can be discovered at the LHC with 300 fb^{-1} data [40].

CHAPTER 3

ASSOCIATED HIGGS BOSON PRODUCTION
WITH TOP QUARKS

The associated production of a Higgs boson with a $t\bar{t}$ pair can play a very important role at hadron colliders as has been suggested by many studies over the past several years [41, 42, 43, 44]. As we have seen in Section 2.3.2, $t\bar{t}h$ production will play a crucial role in the discovery of a SM-like Higgs boson at the LHC, if $M_h < 130$ GeV. Although the event rate is small, the signature is quite distinctive ($W^+W^-b\bar{b}b\bar{b}$). Most importantly, though, this channel will be instrumental at the LHC in determining the couplings of the Higgs boson to SM particles and would provide the only direct measurement of the top quark Yukawa coupling [45, 46, 47, 48, 49]. Although $t\bar{t}h$ production is probably beyond the reach of the Tevatron, the production of a Higgs boson with bottom quarks will be central to discovering a non-SM Higgs sector. Most of the discussion in this chapter applies also to the case of $b\bar{b}h$ production which we present in Chapter 4.

The leading-order (LO) total cross section for $p\bar{p}(pp) \rightarrow t\bar{t}h$ has been known for quite some time [50, 51]. However, as for any other hadronic process, the LO prediction is plagued by a large dependence on the renormalization and factorization scales (see Figs. 3.3 and 3.4) and, thus, does not provide a reliable result. Next-to-leading order (NLO) QCD corrections are mandatory to reduce the scale dependence and to obtain a precise prediction for the total and differential cross sections.

In this chapter, we present in detail the calculation of the NLO inclusive total cross section for $t\bar{t}h$ production in the SM at both the Tevatron [30] and the LHC [29].

The partonic processes responsible for $t\bar{t}h$ production involve both quark-antiquark $(q\bar{q})$ and gluon-gluon (gg) initial states. At the Tevatron ($\sqrt{s_H} = 1.96$ TeV), the $q\bar{q}$ process dominates, making up more than 95% of the total cross section, and the gg process is effectively negligible. At the LHC ($\sqrt{s_H} = 14$ TeV), the gg initial state becomes dominant, although, the $q\bar{q}$ process is not entirely negligible.

The main challenge in the calculation of the $\mathcal{O}(\alpha_s)$ virtual corrections comes from the presence of pentagon diagrams with several massive external and internal particles. The pentagon scalar and tensor Feynman integrals originating from these diagrams present either analytical (scalar) or numerical (tensor) challenges. We have calculated the pentagon scalar integrals as linear combinations of scalar box integrals using the method of Ref. [52, 53], and cross checked them using the techniques of Ref. [54]. Pentagon tensor integrals have been calculated and cross checked in two ways: numerically, by isolating the numerical instabilities and extrapolating from the numerically safe to the numerically unsafe region using various methods; and analytically, by reducing them to a numerically stable form.

The real corrections (i.e. $p\bar{p}(pp) \to t\bar{t}h + g, q(\bar{q})$) have been computed using the phase space slicing method, in both the double [55] and single [56, 57, 58] cutoff approaches. This is the first application of the single cutoff phase space slicing method to a cross section involving more than one massive particle in the final state and agreement between the two cutoff and the single cutoff approaches is a strong check of the calculation.

The outline of this chapter is as follows. In Section 3.1, we summarize the general structure of the NLO cross section for $p\bar{p}(pp) \to t\bar{t}h$. In Section 3.2, we present the calculation and numerical results for the LO cross sections for $p\bar{p}(pp) \to t\bar{t}h$. Section 3.3 gives a detailed account of the virtual corrections to both $q\bar{q} \to t\bar{t}h$ and $gg \to t\bar{t}h$, where we also discuss the singular structure of the one-loop corrections in the infrared and ultraviolet limits. In Section 3.4, we present the real corrections to $p\bar{p}(pp) \to t\bar{t}h + g, q(\bar{q})$ in both the two-cutoff and the one-cutoff implementations

35

of the Phase Space Slicing method. We proceed in Section 3.5 to present the full analytic structure of the NLO QCD cross sections at the Tevatron and the LHC, while we present our numerical results for both colliders in Section 3.6. We collect most of the technical details, including a list of box and pentagon integrals, in a series of Appendices.

3.1 The calculation: general setup

The inclusive total cross section for $p\bar{p}(pp) \to t\bar{t}h$ at $\mathcal{O}(\alpha_s^3)$ can be written as:

$$\sigma_{NLO}(p\bar{p}(pp) \to t\bar{t}h) =$$
$$\sum_{ij} \frac{1}{1+\delta_{ij}} \int dx_1 dx_2 \left[\mathcal{F}_i^p(x_1, \mu) \mathcal{F}_j^{p(\bar{p})}(x_2, \mu) \hat{\sigma}_{NLO}^{ij}(x_1, x_2, \mu) + (1 \leftrightarrow 2) \right] , \quad (3.1)$$

where $\mathcal{F}_i^{p(\bar{p})}$ are the NLO parton distribution functions (PDFs) for parton i in a proton (or antiproton), defined at a generic factorization scale $\mu_f = \mu$, and $\hat{\sigma}_{NLO}^{ij}$ is the $\mathcal{O}(\alpha_s^3)$ parton-level total cross section for incoming partons i and j, made of the channels $q\bar{q}, gg \to t\bar{t}h$ and $(q, \bar{q})g \to t\bar{t}h(q, \bar{q})$, and renormalized at an arbitrary scale μ_r which we also take to be $\mu_r = \mu$. Throughout this chapter we will always assume the factorization and renormalization scales to be equal, $\mu_r = \mu_f = \mu$, unless differently specified. The δ_{ij} is an identical particle factor which takes the value 0 (1) for the $q\bar{q}$ (gg) initiated process. The partonic center-of-mass energy squared, s, is given in terms of the hadronic center-of-mass energy squared, s_H, by $s = x_1 x_2 s_H$ where x_1 and x_2 are the fractions of the hadron's momenta carried by the partons. As explained above, at the Tevatron, we consider only the $q\bar{q} \to t\bar{t}h$ channel, summed over all light quark flavors, and neglect the $gg \to t\bar{t}h$ channel, since the gg initial state is numerically irrelevant. At the LHC, we include both the $q\bar{q} \to t\bar{t}h$ and $gg \to t\bar{t}h$ channels.

We write the NLO parton-level total cross section $\hat{\sigma}_{NLO}^{ij}(x_1, x_2, \mu)$ as:

$$\hat{\sigma}_{NLO}^{ij}(x_1, x_2, \mu) = \alpha_s^2(\mu) \left\{ f_{LO}^{ij}(x_1, x_2) + \frac{\alpha_s(\mu)}{4\pi} f_{NLO}^{ij}(x_1, x_2, \mu) \right\}$$

$$\equiv \hat{\sigma}_{LO}^{ij}(x_1, x_2, \mu) + \delta\hat{\sigma}_{NLO}^{ij}(x_1, x_2, \mu) \ , \tag{3.2}$$

where $\alpha_s(\mu)$ is the strong coupling constant renormalized at the arbitrary scale $\mu_r = \mu$, $\hat{\sigma}_{LO}^{ij}(x_1, x_2, \mu)$ is the $\mathcal{O}(\alpha_s^2)$ Born cross section, and $\delta\hat{\sigma}_{NLO}^{ij}(x_1, x_2, \mu)$ consists of the $\mathcal{O}(\alpha_s)$ corrections to the Born cross sections for $gg, q\bar{q} \to t\bar{t}h$ and of the tree level $(q, \bar{q})g \to t\bar{t}h(q, \bar{q})$ processes, including the effects of mass factorization (see Section 3.5). $\delta\hat{\sigma}_{NLO}^{ij}(x_1, x_2, \mu)$ can be written as the sum of two terms:

$$\delta\hat{\sigma}_{NLO}^{ij}(x_1, x_2, \mu) = \int d(PS_3) \overline{\sum} |\mathcal{A}_{virt}(ij \to t\bar{t}h)|^2 + \int d(PS_4) \overline{\sum} |\mathcal{A}_{real}(ij \to t\bar{t}h + l)|^2$$

$$\equiv \hat{\sigma}_{virt}^{ij}(x_1, x_2, \mu) + \hat{\sigma}_{real}^{ij}(x_1, x_2, \mu) \ , \tag{3.3}$$

where $|\mathcal{A}_{virt}(ij \to t\bar{t}h)|^2$ and $|\mathcal{A}_{real}(ij \to t\bar{t}h + l)|^2$ (for $ij = q\bar{q}, gg$ and $l = g$, or $ij = qg, \bar{q}g$ and $l = q, \bar{q}$) are respectively the $\mathcal{O}(\alpha_s^3)$ terms of the squared matrix elements for the $ij \to t\bar{t}h$ and $ij \to t\bar{t}h + l$ processes, and $\overline{\sum}$ indicates that they have been averaged over the initial state degrees of freedom and summed over the final state ones. Moreover, $d(PS_3)$ and $d(PS_4)$ in Eq. (3.3) denote the integration over the corresponding three and four-particle phase spaces respectively. The first term in Eq. (3.3) represents the contribution of the virtual one gluon corrections to $q\bar{q} \to t\bar{t}h$ and $gg \to t\bar{t}h$, while the second one is due to the real one gluon and real one quark/antiquark emission, i.e. $q\bar{q}, gg \to t\bar{t}h + g$ and $qg(\bar{q}g) \to t\bar{t}h + q(\bar{q})$.

We observe that the scale dependence of the total cross section at NLO is dictated by renormalization group arguments, and $f_{NLO}^{ij}(x_1, x_2, \mu)$ in Eq. (3.2) must be of the form:

$$f_{NLO}^{ij}(x_1, x_2, \mu) = f_1^{ij}(x_1, x_2) + \tilde{f}_1^{ij}(x_1, x_2) \ln\left(\frac{\mu^2}{s}\right) \ , \tag{3.4}$$

with $\tilde{f}_1^{ij}(x_1, x_2)$ given by:

$$\tilde{f}_1^{ij}(x_1, x_2) = 2 \left\{ 4\pi b_0 f_{LO}^{ij}(x_1, x_2) - \sum_k \left[\int_\rho^1 dz_1 P_{ik}(z_1) f_{LO}^{kj}(x_1 z_1, x_2) \right. \right.$$

$$\left. \left. + \int_\rho^1 dz_2 P_{jk}(z_2) f_{LO}^{ik}(x_1, x_2 z_2) \right] \right\} \ , \tag{3.5}$$

37

where $\rho = (2m_t + M_h)^2/s$, $P_{ij}(z)$ denotes the lowest-order regulated Altarelli-Parisi splitting function [59] of parton i into parton j, when j carries a fraction z of the momentum of parton i, (see e.g. Section 3.4), and b_0 is determined by the one-loop renormalization group evolution of the strong coupling constant α_s:

$$\frac{d\alpha_s(\mu)}{d\ln(\mu^2)} = -b_0\alpha_s^2 + \mathcal{O}(\alpha_s^3) \quad , \quad b_0 = \frac{1}{4\pi}\left(\frac{11}{3}N - \frac{2}{3}n_{lf}\right) \quad , \tag{3.6}$$

with $N = 3$, the number of colors, and $n_{lf} = 5$, the number of light flavors. The origin of the terms in Eq. (3.5) will become manifest in Sections 3.3, 3.4, and 3.5 when we describe in detail the calculation of both virtual and real $\mathcal{O}(\alpha_s)$ corrections.

In the Sections 3.3 and 3.4 we present the general structure of the $\mathcal{O}(\alpha_s)$ virtual and real corrections to $q\bar{q}, gg \rightarrow t\bar{t}h$. The contribution of the $(q, \bar{q})g$ initiated process will be considered in Section 3.4, when dealing with the real part of the $\mathcal{O}(\alpha_s^3)$ cross section. The results presented in the following sections have been obtained by two completely independent calculations, based on a combination of FORM [60] and *Maple* codes in one case, and on the *Mathematica* based code Tracer [61] in the other. The matrix elements squared for the tree level processes $gg \rightarrow t\bar{t}h$, $gg \rightarrow t\bar{t}h + g$, and $(q, \bar{q})g \rightarrow t\bar{t}h + (q, \bar{q})$ have been checked with Madgraph [62]. The numerical results presented in Section 3.6 have been obtained with two independent *Fortran* codes.

3.2 The tree level cross sections

3.2.1 LO cross section for $q\bar{q} \rightarrow t\bar{t}h$

The Feynman diagrams contributing to the process

$$q(q_1) + \bar{q}(q_2) \rightarrow t(p_t) + \bar{t}(p_t') + h(p_h) \ ,$$

where $q_1 + q_2 = p_t + p_t' + p_h$ are shown in Fig. 3.1. Using these diagrams, the tree-level amplitude can be written as:
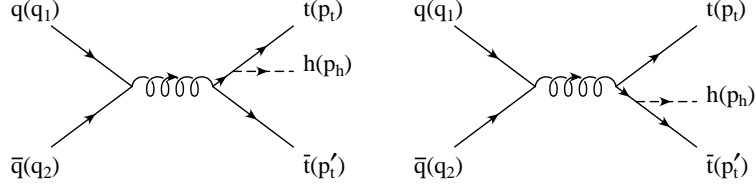
Figure 3.1. Feynman diagrams contributing to the lowest order process, $q\bar{q} \to t\bar{t}h$. The arrows indicate the momentum flow.

$$\mathcal{A}_0^{q\bar{q}} = -ig_s^2\, g_{t\bar{t}h}\, T^a T^a\, \frac{1}{s}\, \bar{v}(q_2)\, \gamma_\mu\, u(q_1)\, \bar{u}(p_t) \left[\mathcal{A}_0^{(1),q\bar{q},\mu} + \mathcal{A}_0^{(2),q\bar{q},\mu} \right] v(p_t') \,, \tag{3.7}$$

where $u(\bar{u})$, $v(\bar{v})$ are the initial and final state spinors, g_s is the strong coupling constant, $g_{t\bar{t}h} = m_t/v$ is the top quark Yukawa coupling, and s is the partonic CM energy squared, i.e. $s = (q_1 + q_2)^2$. The subamplitudes $\mathcal{A}_0^{(1,2),q\bar{q}}$ are given by:

$$\mathcal{A}_0^{(1),q\bar{q},\mu} = \frac{(\slashed{p}_t + \slashed{p}_h + m_t)\gamma^\mu}{(p_t + p_h)^2 - m_t^2} \tag{3.8}$$

and

$$\mathcal{A}_0^{(2),q\bar{q},\mu} = \frac{\gamma^\mu(-\slashed{p}_t' - \slashed{p}_h + m_t)}{(p_t' + p_h)^2 - m_t^2} \,, \tag{3.9}$$

where m_t is the top quark mass. Finally, using Eqs. (3.7)-(3.9) the Born cross section to $q\bar{q} \to t\bar{t}h$ can be written in a closed analytic form given by [63]:

$$\hat{\sigma}_{LO}^{q\bar{q}}(x_1, x_2, \mu) = \frac{\alpha_s^2(\mu)}{27\pi s} g_{t\bar{t}h}^2 \int_{x_h^{min}}^{x_h^{max}} dx_h \left[\frac{4\hat{\beta}}{x_h^2 - \hat{\beta}^2} \left(1 + \frac{2m_t^2}{s} \right) \left(\frac{4m_t^2 - M_h^2}{s} \right) + \right. \tag{3.10}$$

$$\left. \left[x_h + 2\left(\frac{4m_t^2 - M_h^2}{s} \right) + \frac{2}{x_h} \frac{(4m_t^2 - M_h^2)(2m_t^2 - M_h^2)}{s^2} + \frac{8m_t^2}{sx_h} \right] \ln\left(\frac{x_h + \hat{\beta}}{x_h - \hat{\beta}} \right) \right] \,,$$

where $x_h = 2E_h/\sqrt{s}$, E_h is the Higgs boson energy in the $q\bar{q}$ center-of-mass frame, $x_h^{min} = 2M_h/\sqrt{s}$, $x_h^{max} = 1 - 4m_t^2/s + M_h^2/s$, and we have introduced:

$$\hat{\beta} = \left\{ \frac{[x_h^2 - (x_h^{min})^2][x_h^{max} - x_h]}{x_h^{max} - x_h + 4m_t^2/s} \right\}^{1/2} \,. \tag{3.11}$$

39

3.2.2 LO cross section for $gg \to t\bar{t}h$

The tree level amplitude for the process

$$g^A(q_1) + g^B(q_2) \to t(p_t) + \bar{t}(p'_t) + h(p_h) \; ,$$

where $q_1 + q_2 = p_t + p'_t + p_h$ and A, B denote the color of the incoming gluons, is obtained from the three classes of Feynman diagrams represented in Fig. 3.2, identified as $s-$channel, $t-$channel, and $u-$channel diagrams respectively. We find it convenient to organize the color structure of both the tree level amplitude and the one-loop virtual amplitude for $gg \to t\bar{t}h$ in terms of only two color factors, one symmetric and one antisymmetric in the color indices of the initial gluons. Following this prescription, the tree level amplitude for $gg \to t\bar{t}h$ can be written as:

$$\mathcal{A}_0^{gg} = \mathcal{A}_0^{nab}[T^A, T^B] + \mathcal{A}_0^{ab}\{T^A, T^B\} \; , \tag{3.12}$$

where $T^{A,B} = \lambda^{A,B}/2$ in terms of the Gell-Mann matrices $\lambda^{A,B}$ [1]. $\mathcal{A}_0^{ab}$ and $\mathcal{A}_0^{nab}$ correspond to the terms in the amplitude that are proportional respectively to the *abelian* (or symmetric) and *non-abelian* (or antisymmetric) color factors and are explicitly given by:

$$\mathcal{A}_0^{ab} = \frac{1}{2}(\mathcal{A}_{0,t}^{gg} + \mathcal{A}_{0,u}^{gg}) \; , \quad \mathcal{A}_0^{nab} = \mathcal{A}_{0,s}^{gg} + \frac{1}{2}(\mathcal{A}_{0,t}^{gg} - \mathcal{A}_{0,u}^{gg}) \; , \tag{3.13}$$

where $\mathcal{A}_{0,s}^{gg}$, $\mathcal{A}_{0,t}^{gg}$, and $\mathcal{A}_{0,u}^{gg}$ are the amplitudes corresponding to the sum of the $s-$channel, $t-$channel, and $u-$channel tree level diagrams:

$$\mathcal{A}_{0,s}^{gg} = ig_s^2 \, g_{t\bar{t}h} \, \epsilon_\mu(q_1) \, \epsilon_\nu(q_2) \, \bar{u}_t(p_t)\mathcal{A}_{0,s}^{gg,\mu\nu}v_{\bar{t}}(p'_t) \; ,$$

$$\mathcal{A}_{0,t}^{gg} = ig_s^2 \, g_{t\bar{t}h} \, \epsilon_\mu(q_1) \, \epsilon_\nu(q_2) \, \bar{u}_t(p_t)\mathcal{A}_{0,t}^{gg,\mu\nu}v_{\bar{t}}(p'_t) \; ,$$

$$\mathcal{A}_{0,u}^{gg} = ig_s^2 \, g_{t\bar{t}h} \, \epsilon_\mu(q_1) \, \epsilon_\nu(q_2) \, \bar{u}_t(p_t)\mathcal{A}_{0,u}^{gg,\mu\nu}v_{\bar{t}}(p'_t) \; . \tag{3.14}$$

---

[1]We note that the one-loop virtual amplitude can be expressed in terms of the same antisymmetric color factor $[T^A, T^B]$ and a symmetric color factor made of $\{T^A, T^B\}$ and δ^{AB}.

where $\epsilon^{\mu,\nu}$ are the polarization vectors of the initial-state gluons. The subamplitudes $\mathcal{A}_{0,s}^{gg,\mu\nu}$, $\mathcal{A}_{0,t}^{gg,\mu\nu}$, and $\mathcal{A}_{0,u}^{gg,\mu\nu}$ are given by:

$$\mathcal{A}_{0,s}^{gg,\mu\nu} = \mathcal{A}_{0,s}^{(1),gg,\mu\nu} + \mathcal{A}_{0,s}^{(2),gg,\mu\nu} \ ,$$

$$\mathcal{A}_{0,t}^{gg,\mu\nu} = \mathcal{A}_{0,t}^{(1),gg,\mu\nu} + \mathcal{A}_{0,t}^{(2),gg,\mu\nu} + \mathcal{A}_{0,t}^{(3),gg,\mu\nu} \ ,$$

$$\mathcal{A}_{0,u}^{gg,\mu\nu} = \mathcal{A}_{0,u}^{(1),gg,\mu\nu} + \mathcal{A}_{0,u}^{(2),gg,\mu\nu} + \mathcal{A}_{0,u}^{(3),gg,\mu\nu} \ , \tag{3.15}$$

where the individual amplitudes for the $s-$channel, $t-$channel, and $u-$channel diagrams in Fig. 3.2 are:

$$\mathcal{A}_{0,s}^{(1),gg,\mu\nu} = \frac{1}{s}\frac{\not{p}_t + \not{p}_h + m_t}{[(p_t + p_h)^2 - m_t^2]}\gamma_\alpha V^{\mu\nu\alpha} \ ,$$

$$\mathcal{A}_{0,s}^{(2),gg,\mu\nu} = \frac{1}{s}\gamma_\alpha \frac{-\not{p}_t' - \not{p}_h + m_t}{[(p_t' + p_h)^2 - m_t^2]}V^{\mu\nu\alpha} \ ,$$

$$\mathcal{A}_{0,t}^{(1),gg,\mu\nu} = \frac{\not{p}_t + \not{p}_h + m_t}{[(p_t + p_h)^2 - m_t^2]}\gamma^\mu \frac{\not{q}_2 - \not{p}_t' + m_t}{[(q_2 - p_t')^2 - m_t^2]}\gamma^\nu \ ,$$

$$\mathcal{A}_{0,t}^{(2),gg,\mu\nu} = \gamma_\mu \frac{\not{p}_t - \not{q}_1 + m_t}{[(p_t - q_1)^2 - m_t^2]}\frac{\not{q}_2 - \not{p}_t' + m_t}{[(q_2 - p_t')^2 - m_t^2]}\gamma_\nu \ ,$$

$$\mathcal{A}_{0,t}^{(3),gg,\mu\nu} = \gamma_\mu \frac{\not{p}_t - \not{q}_1 + m_t}{[(p_t - q_1)^2 - m_t^2]}\gamma^\nu \frac{-\not{p}_t' - \not{p}_h + m_t}{[(p_t' + p_h)^2 - m_t^2]} \ ,$$

$$\mathcal{A}_{0,u}^{(1),gg,\mu\nu} = \mathcal{A}_{0,t}^{(1),\mu\nu}(\mu \leftrightarrow \nu, q_1 \leftrightarrow q_2) \ ,$$

$$\mathcal{A}_{0,u}^{(2),gg,\mu\nu} = \mathcal{A}_{0,t}^{(2),\mu\nu}(\mu \leftrightarrow \nu, q_1 \leftrightarrow q_2) \ ,$$

$$\mathcal{A}_{0,u}^{(3),gg,\mu\nu} = \mathcal{A}_{0,t}^{(3),\mu\nu}(\mu \leftrightarrow \nu, q_1 \leftrightarrow q_2) \ , \tag{3.16}$$

with

$$V^{\mu\nu\alpha} = (q_1 - q_2)^\alpha g^{\mu\nu} + (q_1 + 2q_2)^\mu g^{\nu\alpha} - (2q_1 + q_2)^\nu g^{\mu\alpha} \ .$$

Due to the *orthogonality* between symmetric and antisymmetric color factors, the tree level amplitude squared takes the very simple form:

$$\overline{\sum}|\mathcal{A}_0^{gg}|^2 = \overline{\sum}\left[\frac{N}{2}(N^2 - 1)\left(|\mathcal{A}_0^{nab}|^2 + |\mathcal{A}_0^{ab}|^2\right) - \frac{1}{N}(N^2 - 1)|\mathcal{A}_0^{ab}|^2\right] \ , \tag{3.17}$$

from which we can derive the LO partonic cross section, upon integration over the final state phase space:

$$\hat{\sigma}_{LO}^{gg}(x_1, x_2, \mu) = \int d(PS_3)\overline{\sum}|\mathcal{A}_0^{gg}|^2(x_1, x_2, \mu) \ , \tag{3.18}$$

41
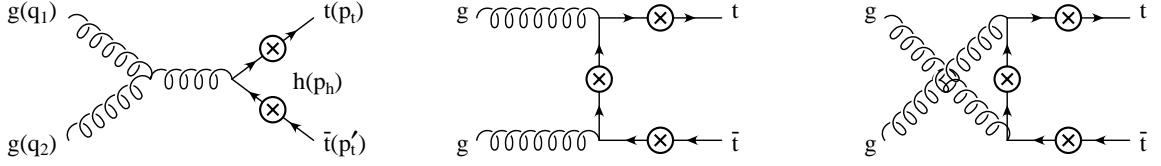
Figure 3.2. Feynman diagrams contributing to the tree level process $gg \to t\bar{t}h$. The circled crosses indicate all possible insertions of the final state Higgs boson leg, each insertion corresponding to a different diagram.

where the dependence of $|\mathcal{A}_0^{gg}|^2$ on x_1 and x_2 (through $s = x_1 x_2 s_H$) and on the renormalization scale μ (through $\alpha_s(\mu)$)) has been made explicit.

When averaging over the polarization states of the initial gluons, the polarization sum of the gluon polarization vectors, $\epsilon_\mu(q_1, \lambda_1)$ and $\epsilon_\nu(q_2, \lambda_2)$, has to be performed in such a way that only the physical (transverse) polarization states of the gluons contribute to the matrix element squared. We adopt the general prescription:

$$\sum_{\lambda_i=1,2} \epsilon_\mu(q_i, \lambda_i)\epsilon_\nu^*(q_i, \lambda_i) = -g_{\mu\nu} + \frac{n_{i\mu}q_{i\nu} + q_{i\mu}n_{i\nu}}{n_i \cdot q_i} - \frac{n_i^2 q_{i\mu}q_{j\nu}}{(n_i \cdot q_i)^2} \quad , \tag{3.19}$$

where $i = 1, 2$ and the arbitrary vectors n_i have to satisfy the relations:

$$n_i^\mu \sum_{\lambda_i=1,2} \epsilon_\mu(q_i, \lambda_i)\epsilon_\nu^*(q_i, \lambda_i) = 0 \quad , \quad n_i^\nu \sum_{\lambda_i=1,2} \epsilon_\mu(q_i, \lambda_i)\epsilon_\nu^*(q_i, \lambda_i) = 0 \quad , \tag{3.20}$$

together with $n_i^2 \neq 0$ and $n_1 \neq n_2$ We choose $n_1 = q_2$ and $n_2 = q_1$, such that:

$$\sum_{\lambda_i=1,2} \epsilon_\mu(q_i, \lambda_i)\epsilon_\nu^*(q_i, \lambda_i) = -g_{\mu\nu} + 2\frac{q_{1\mu}q_{2\nu} + q_{2\mu}q_{1\nu}}{s} \quad . \tag{3.21}$$

Finally, the entire calculation is performed using Feynman gauge for both internal and external gluons.

3.2.3   LO predictions for $p\bar{p}(pp) \to t\bar{t}h$

Figures 3.3 and 3.4 show the LO predictions for $t\bar{t}h$ production at the Tevatron and LHC respectively as a function of the Higgs boson mass. These results are

42
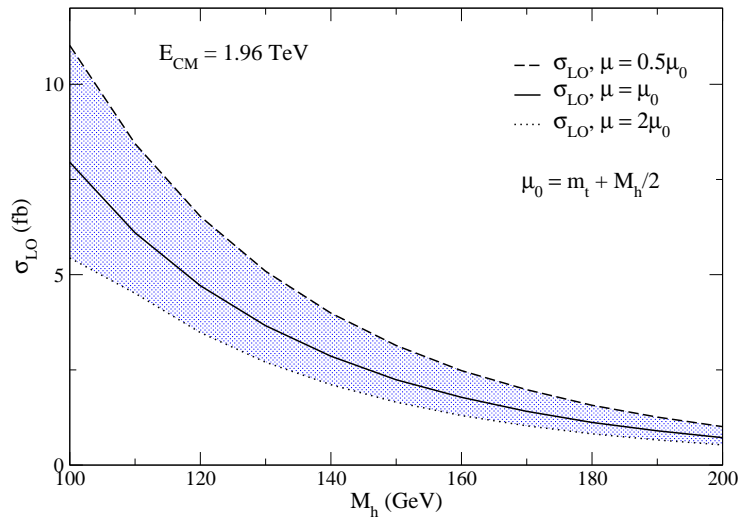
Figure 3.3. LO cross section for $p\bar{p} \rightarrow t\bar{t}h$ at the Tevatron. The band is obtained by varying the renormalization/factorization scale by factors of two around the central value $\mu_0 = m_t + M_h/2$.

obtained using the one-loop evolution of $\alpha_s(\mu)$ and by convoluting the partonic cross sections (Eqs. (3.10) and (3.18)) with the CTEQ6L parton distribution functions. The renormalization and factorization scales are set to a common scale which is then varied by a factor of two in both directions around the central value, $\mu_0 = m_t + M_h/2$, to obtain the *uncertainty bands* shown in Figures 3.3 and 3.4. The dramatic variation of more than a factor of ~ 2 at the Tevatron and a factor ~ 1.5 at the LHC within the small interval $\mu_0/2 < \mu_0 < 2\mu_0$ shows that the LO prediction for the total cross section $p\bar{p}(pp) \rightarrow t\bar{t}h$ is plagued by considerable uncertainties and, therefore, cannot provide a reliable prediction. This underlines the need for NLO QCD corrections.

3.3 Virtual corrections

The $\mathcal{O}(\alpha_s)$ virtual corrections to the tree level processes $q\bar{q}, gg \rightarrow t\bar{t}h$ consist of self-energy, vertex, box, and pentagon diagrams which are shown in Figs. 3.5-3.8 for the $q\bar{q}$-initiated process and in Figs. 3.9-3.12 for the gg-initiated process. The $\mathcal{O}(\alpha_s^3)$ contribution to the virtual amplitude squared of Eq. (3.3) can then be written as:
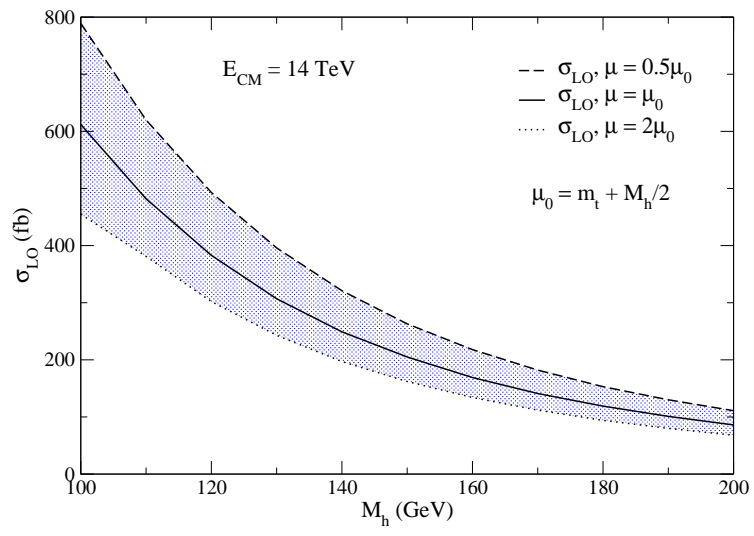
Figure 3.4. LO cross section for $pp \to t\bar{t}h$ at the LHC. The band is obtained by varying the renormalization/factorization scale by factors of two around the central value $\mu_0 = m_t + M_h/2$.
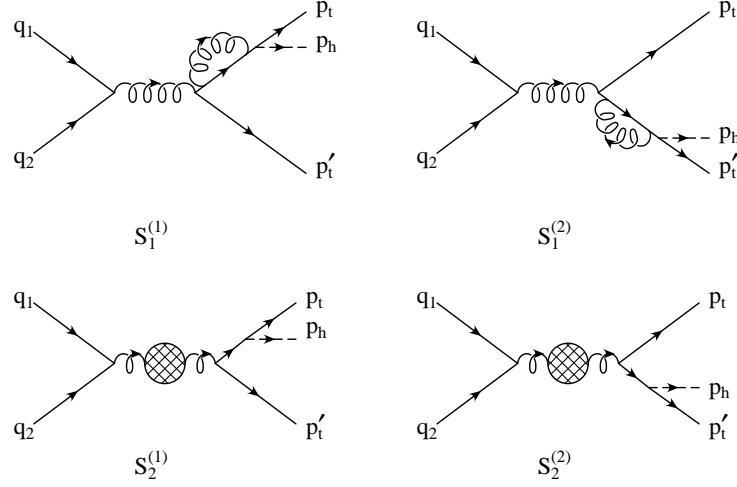
Figure 3.5. $\mathcal{O}(\alpha_s)$ virtual corrections: self-energy diagrams $S_1^{(1,2),q\bar{q}}$ and $S_2^{(1,2),q\bar{q}}$.

$$\overline{\sum}|\mathcal{A}_{virt}(q\bar{q}, gg \to t\bar{t}h)|^2 = \sum_{D_i^{q\bar{q}}}\overline{\sum}\left(\mathcal{A}_0^{q\bar{q}}\mathcal{A}_{D_i}^{q\bar{q}*} + \mathcal{A}_0^{q\bar{q}*}\mathcal{A}_{D_i}^{q\bar{q}}\right) + \sum_{D_{i,j}^{gg}}\overline{\sum}\left(\mathcal{A}_0^{gg}\mathcal{A}_{D_{i,j}}^{gg*} + \mathcal{A}_0^{gg*}\mathcal{A}_{D_{i,j}}^{gg}\right)$$

$$= \sum_{D_i^{q\bar{q}}}\overline{\sum}2\,\mathcal{R}e\left(\mathcal{A}_0^{q\bar{q}}\mathcal{A}_{D_i}^{q\bar{q}*}\right) + \sum_{D_{i,j}^{gg}}\overline{\sum}2\,\mathcal{R}e\left(\mathcal{A}_0^{gg}\mathcal{A}_{D_{i,j}}^{gg*}\right) , \qquad (3.22)$$
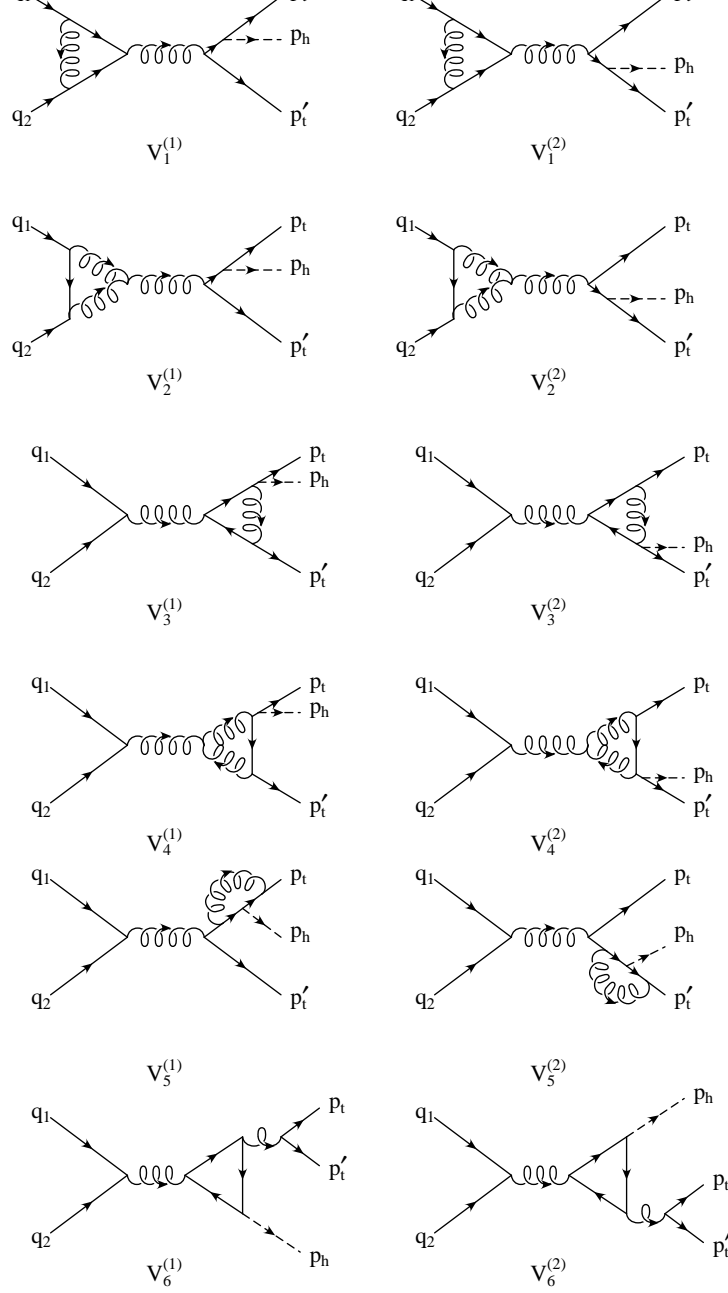
Figure 3.6. $\mathcal{O}(\alpha_s)$ virtual corrections: vertex diagrams $V_1^{(1,2),q\bar{q}}$-$V_6^{(1,2),q\bar{q}}$.

where $\mathcal{A}_0^{q\bar{q},gg}$ are the tree level amplitudes for the $q\bar{q}$- and gg-initiated processes respectively, while $\mathcal{A}_{D_i}^{q\bar{q}}$ and $\mathcal{A}_{D_{i,j}}^{gg}$ denote the amplitudes for classes of virtual diagrams that only differ by the insertion of the final state Higgs boson leg, i.e.
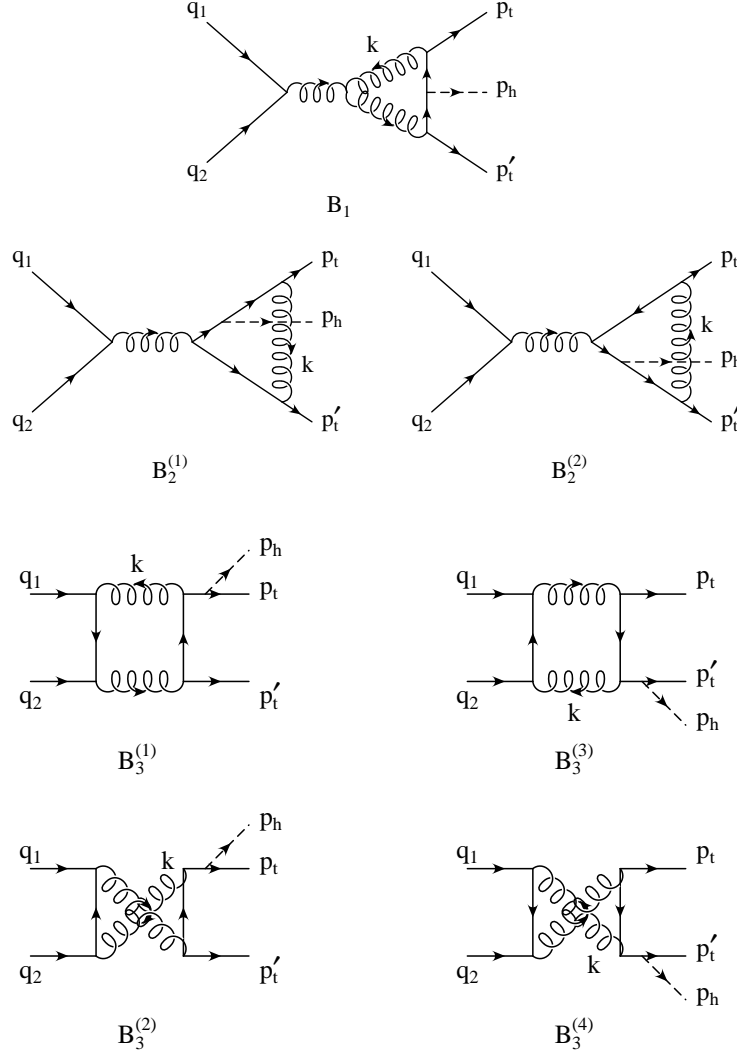
Figure 3.7. $\mathcal{O}(\alpha_s)$ virtual corrections: box diagrams $B_1^{q\bar{q}}$, $B_2^{(1,2),q\bar{q}}$ and $B_3^{(1-4),q\bar{q}}$.

$D_i^{q\bar{q}} = \sum_k D_i^{(k),q\bar{q}}$ and $D_{i,j}^{gg} = \sum_k D_{i,j}^{(k),gg}$ with $D_i^{q\bar{q},gg} = S_i^{q\bar{q},gg}, V_i^{q\bar{q},gg}, B_i^{q\bar{q},gg}, P_i^{q\bar{q},gg}$, $j = s, t, u$, and k running over all possible Higgs boson insertions, as illustrated in Figs. 3.5-3.12. The symbols S, V, B and P represent, respectively, the diagrams containing self-energy, vertex, box and pentagon loops, while the index i labels a particular diagram in these subsets.

46
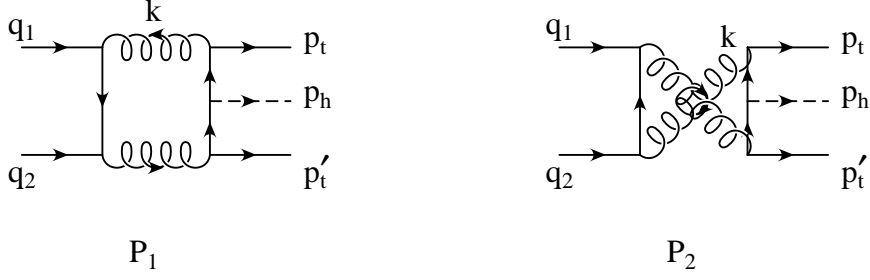
Figure 3.8. $\mathcal{O}(\alpha_s)$ virtual corrections: pentagon diagrams $P_1^{q\bar{q}}$ and $P_2^{q\bar{q}}$.
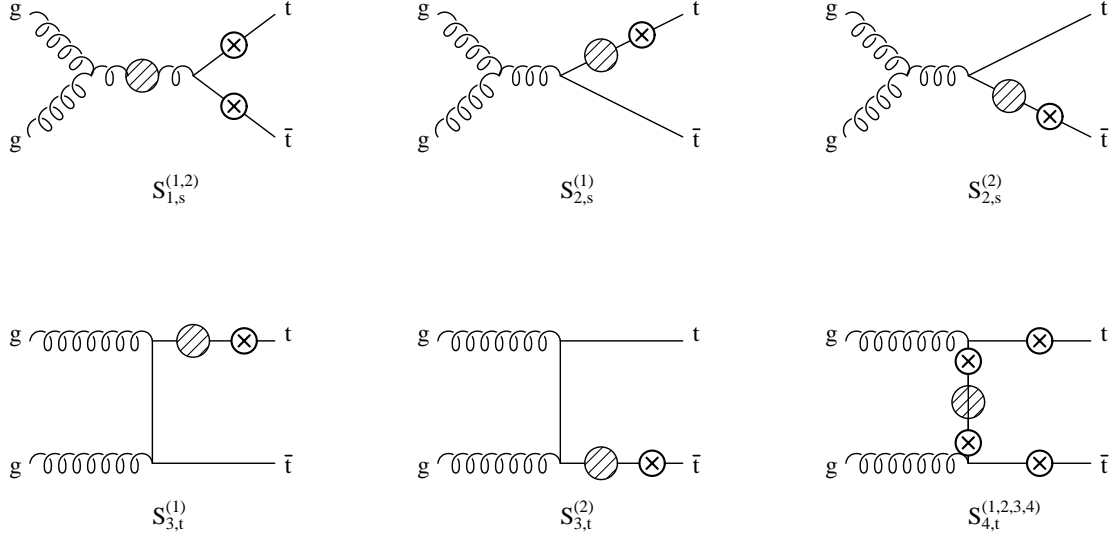
Figure 3.9. $\mathcal{O}(\alpha_s)$ virtual corrections to $gg \rightarrow t\bar{t}h$: self-energy diagrams. The shaded blobs denote standard one-loop QCD corrections to the gluon and top quark propagators respectively. The circled crosses denote all possible insertions of the final state Higgs boson leg, each insertion corresponding to a different diagram. All t-channel diagrams (labeled as $S_{i,t}^{(j),gg}$) have corresponding u-channel diagrams.

The amplitude of each virtual diagram ($\mathcal{A}_{D_i}^{q\bar{q}}$ and $\mathcal{A}_{D_{i,j}}^{gg}$) is calculated as a linear combination of fundamental Dirac structures with coefficients that depend on both
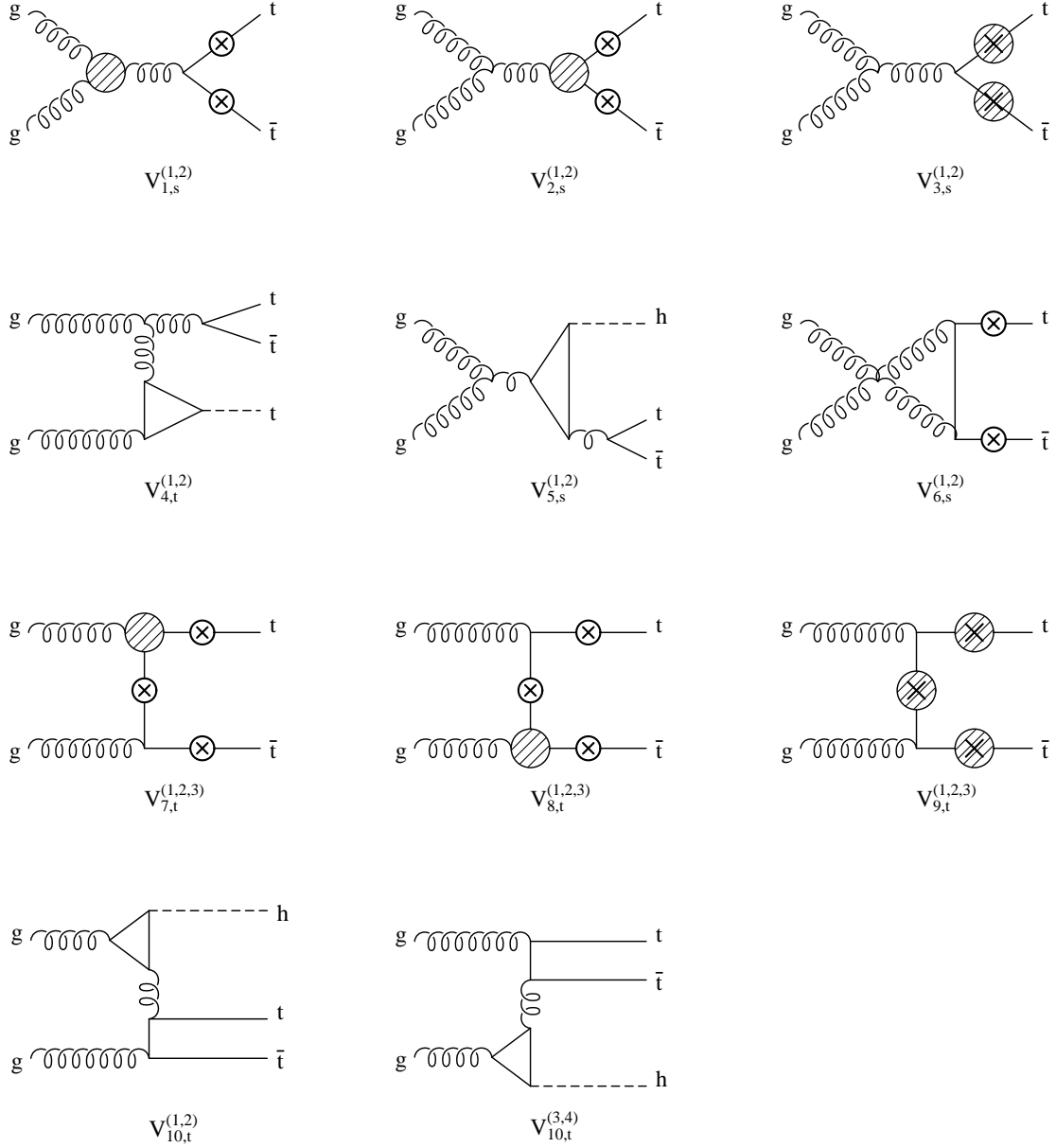
Figure 3.10. $\mathcal{O}(\alpha_s)$ virtual corrections to $gg \to t\bar{t}h$: vertex diagrams. The shaded blobs denote standard one-loop QCD corrections to the ggg, $gt\bar{t}$, or $ht\bar{t}$ vertices respectively. The circled crosses denote all possible insertions of the final Higgs boson leg, each insertion corresponding to a different diagram. Diagrams with a closed fermion loop have to be counted twice, once for each orientation of the loop fermion line. All t-channel diagrams (labeled as $V_{i,t}^{(j),gg}$) have corresponding u-channel diagrams.

48
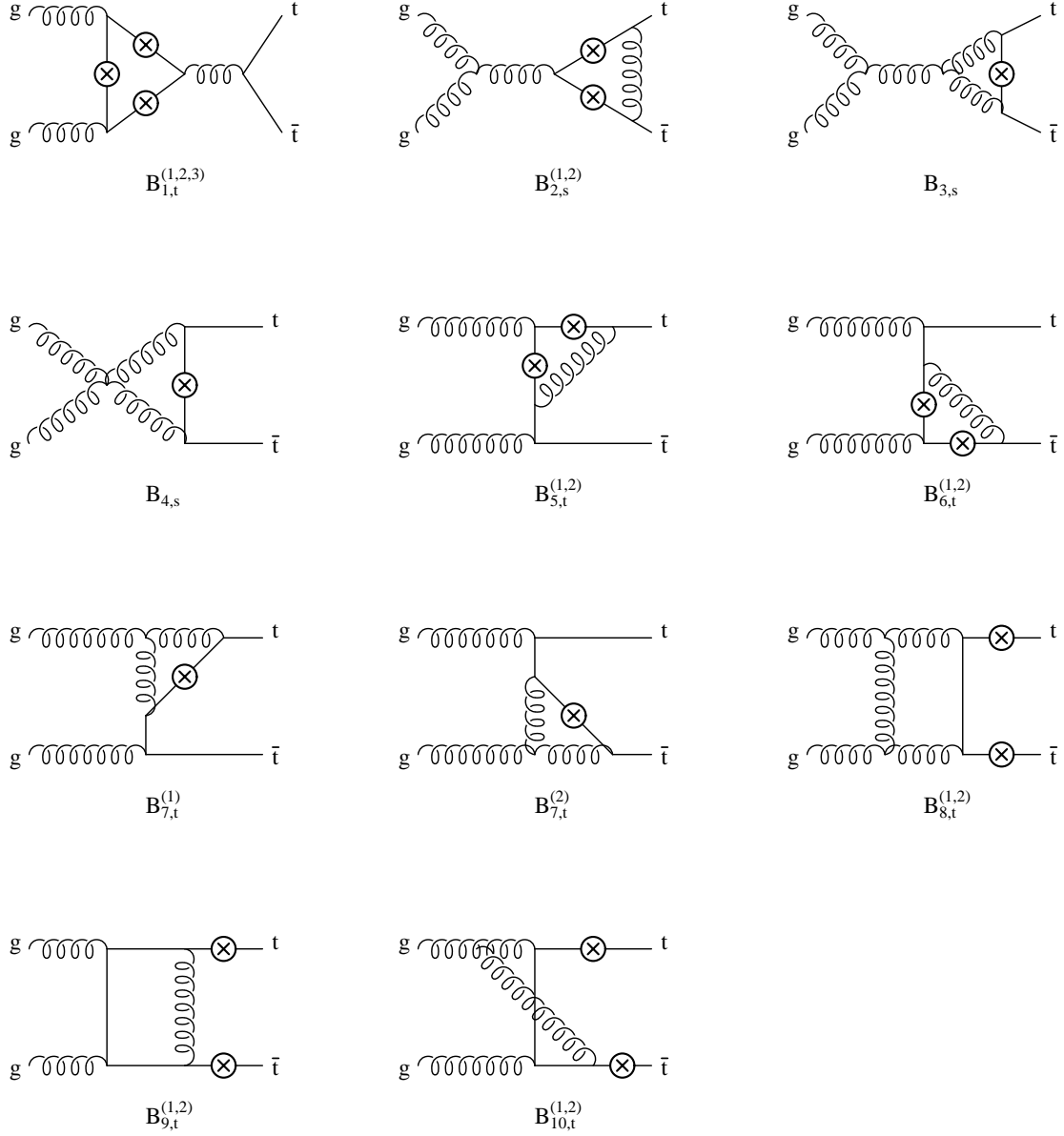
Figure 3.11. $\mathcal{O}(\alpha_s)$ virtual corrections to $gg \to t\bar{t}h$: box diagrams. The circled crosses denote all possible insertions of the final Higgs boson leg, each insertion corresponding to a different diagram. Diagrams with a closed fermion loop have to be counted twice, once for each orientation of the loop fermion line. All t-channel diagrams (labeled as $B_{i,t}^{(j),gg}$) have corresponding u-channel diagrams.
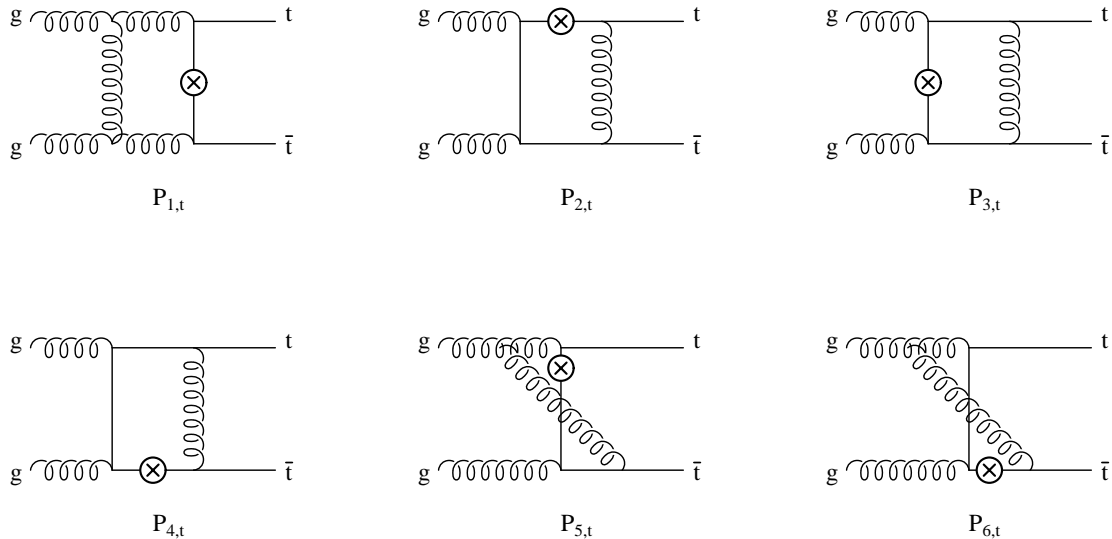
Figure 3.12. $\mathcal{O}(\alpha_s)$ virtual corrections to $gg \to t\bar{t}h$: pentagon diagrams. The circled crosses denote all possible insertions of the final Higgs boson leg, each insertion corresponding to a different diagram. All t-channel diagrams (labeled as $P_{i,t}^{gg}$) have corresponding u-channel diagrams.

tensor and scalar one-loop Feynman integrals with up to five denominators. The tensor integrals are further reduced in terms of scalar one-loop integrals using standard techniques [64, 65]. A simple example of this reduction technique is given in Appendix B. After the tensor integral reduction is performed, the fundamental building blocks are one-loop scalar integrals with up to five denominators. They may be finite or contain both ultraviolet (UV) and infrared (IR) divergences. The finite scalar integrals are evaluated using the method described in Ref. [54] and cross checked with the numerical package FF [66]. The singular scalar integrals are calculated analytically by using dimensional regularization in $d = 4 - 2\epsilon$ dimensions. The most difficult integrals arise from IR divergent pentagon diagrams with several external and internal massive particles. We calculate them as linear combination of box integrals using the method of Ref. [52, 53] and of Ref. [54] generalized to the case of several massive particles. Details of the box and pentagon scalar integrals

used in this calculation are given in Appendix A. All other scalar integrals, with two or three denominators, are commonly found in the literature.

In the tensor integral reduction, numerical problems can arise for higher rank integrals with several denominators. In particular, the $\mathcal{O}(\alpha_s)$ virtual corrections to $gg \rightarrow t\bar{t}h$ involve pentagon tensor integrals of rank higher than one, i.e. Feynman integrals with five denominators and more than one Lorentz tensor index. These pentagon tensor integrals are not present in the corresponding corrections for $q\bar{q} \rightarrow t\bar{t}h$. This introduces a new difficulty in the calculation, due to the numerical instabilities that may arise as a consequence of the proportionality of the tensor integral coefficients to higher powers of the inverse Gram determinant (GD) of the full $gg \rightarrow t\bar{t}h$ phase space (see Appendix B).

The coefficients of the linearly independent tensor structures can be found by solving a system of linear equations, one for each independent tensor structure. As a result, they are proportional to inverse powers of the so called Gram determinant (GD), of the form $\text{GD} = \det(p_i \cdot p_j)$ with p_i and p_j generic independent external momenta (for $i, j = 1, \ldots, 4$, since only four out of the five external momenta are independent). The higher the rank of the original tensor integral, the higher the inverse power of GD that appears in the coefficients of its tensor decomposition.

To briefly illustrate the problem, we parameterize the Gram determinant in terms of the $t\bar{t}h$ phase space variables as

$$\text{GD} = -\frac{[s - (2m_t + M_h)^2]}{64}[M_h^4 + (s - \bar{s}_{t\bar{t}})^2 - 2M_h^2(s + \bar{s}_{t\bar{t}})] \, s \, \bar{s}_{t\bar{t}} \sin^2 \theta_{t\bar{t}} \sin^2 \phi_{t\bar{t}} \sin^2 \theta \ ,$$

(3.23)

where $s = x_1 x_2 s_H$ is the partonic center-of-mass energy squared, and the $t\bar{t}h$ phase space has been expressed in terms of a time-like invariant $\bar{s}_{t\bar{t}} = (p_t + p_t')^2$, polar angles $(\theta, \theta_{t\bar{t}})$ and azimuthal angles $(\phi, \phi_{t\bar{t}})$ in the center-of-mass frames of the incoming gluons and of the $t\bar{t}$ pair, respectively. As can be seen in Eq. (3.23), the Gram determinant vanishes when two momenta become degenerate, i.e. at the boundaries

51

of phase space. Near the boundary of phase space it can become arbitrary small, giving rise to spurious divergences which cause serious numerical difficulties, since they appear in various parts of the calculation that are normally numerically, not analytically, combined. In the case of a $2 \to 3$ process, this problem arises for pentagon tensor integrals, when all the independent external momenta are involved, and it becomes more serious for higher rank tensor integrals. The probability that the Monte Carlo integration hits a point close to the boundary of phase space is not negligible and these points cannot just be discarded.

We use two methods to overcome this problem and find agreement within the statistical uncertainty of the Monte Carlo phase space integration. In the first method, we impose kinematic cuts to avoid the phase space regions where the Gram determinant vanishes, and then extrapolate from the numerically safe to the numerically unsafe region using different algorithms. We have used extrapolations based on polynomial or trigonometric functions. We have also reproduced the analytic dependence of each pentagon diagram on the Gram determinant, tested it in the safe region of phase space, and used it to extrapolate to the unsafe region. A phase space point is kept only if the true and the extrapolated results come very close to each other, after repeated iterations. Each extrapolation has been repeated imposing cuts on different kinematic variables, until a stable answer, independent of the kinematic cuts, can be found. The details of the extrapolation procedure are very technical and we do not think they can be of interest to this discussion. In the second method, after having interfered the pentagon amplitudes with the Born matrix element, we eliminate all pentagon tensor integrals by simplifying scalar products of the loop momentum in the numerator against the propagators in the denominator wherever possible. The resulting expressions are very large, but numerically very stable, and we have used them to confirm the results obtained using the extrapolation methods explained above.

Inserting all diagram contributions from $q\bar{q}, gg \rightarrow t\bar{t}h$ into Eq. (3.22), we obtain the complete $\mathcal{O}(\alpha_s^3)$ contribution to the virtual amplitude squared, and integrating over the final state phase space we calculate $\hat{\sigma}_{virt}^{q\bar{q}}$ and $\hat{\sigma}_{virt}^{gg}$ in Eq. (3.3). The UV singularities of the virtual cross section are regularized in $d = 4 - 2\epsilon_{UV}$ dimensions and renormalized by introducing a suitable set of counterterms, while the residual renormalization scale dependence is checked from first principles using renormalization group arguments. The detailed renormalization procedure adopted in this calculation is explained in Section 3.3.1.2. The IR singularities of the virtual cross section are extracted in $d = 4 - 2\epsilon_{IR}$ dimensions and are canceled by analogous singularities in the $\mathcal{O}(\alpha_s^3)$ real cross section. The structure of the IR singular part of the virtual cross section is presented in Sections 3.3.1.3 and 3.3.2.2, while the IR singularities of the real cross section are discussed in Section 3.4. The explicit cancellation of IR singularities in the total inclusive NLO cross section for $q\bar{q}, gg \rightarrow t\bar{t}h$ is outlined in Sections 3.4 and 3.5.

Finally, we note that the tree level amplitudes $\mathcal{A}_0^{q\bar{q},gg}$ in Eq. (3.22) have to generically be considered as the d-dimensional tree level amplitudes. This matters when the $\mathcal{A}_{D_i}^{q\bar{q}}$, $\mathcal{A}_{D_{i,j}}^{gg}$ amplitudes in Eq. (3.22) are UV or IR divergent. Actually, as will be shown in the following, both UV and IR divergences are always proportional to the tree level amplitudes or parts of it and they can be formally canceled without having to explicitly specify the dimensionality of the tree level amplitude(s). After UV and IR singularities have been canceled, everything is calculated in $d = 4$ dimensions.

3.3.1 One-loop corrections to $q\bar{q} \rightarrow t\bar{t}h$

3.3.1.1 UV singularities

The UV singularities of the $\mathcal{O}(\alpha_s^3)$ $q\bar{q} \rightarrow t\bar{t}h$ total cross section originate from self-energy and vertex virtual corrections. These singularities are renormalized by introducing counterterms for the wave function of the external fields $(\delta Z_2^{(q)}, \delta Z_2^{(t)})$, the top-quark mass (δm_t), and the coupling constants $(\delta g_{t\bar{t}h}, \delta Z_{\alpha_s})$. The explicit forms

53

of the counterterms will be given in Section 3.3.1.2. If we denote by $\Delta_{UV}(S_i^{(1,2),q\bar{q}})\mathcal{A}_0^{q\bar{q}}$ and $\Delta_{UV}(V_i^{(1,2),q\bar{q}})\mathcal{A}_0^{q\bar{q}}$ the UV-divergent contribution of each self-energy $(S_i^{(1,2),q\bar{q}})$ or vertex diagram $(V_i^{(1,2),q\bar{q}})$ to the virtual amplitude squared (see Eq. (3.22)), we can write the UV-singular part of the total virtual amplitude squared as:

$$(\hat{\sigma}_{virt}^{q\bar{q}})_{UV-pole} = \int d(PS_3) \, \overline{\sum} |\mathcal{A}_0^{q\bar{q}}|^2 \left\{ \sum_{i=1}^{2} \Delta_{UV}(S_i^{(1),q\bar{q}} + S_i^{(2),q\bar{q}}) + \sum_{i=1}^{6} \Delta_{UV}(V_i^{(1),q\bar{q}} + V_i^{(2),q\bar{q}}) \right.$$
$$\left. + 2 \left[\left(\delta Z_2^{(q)}\right)_{UV} + \left(\delta Z_2^{(t)}\right)_{UV} + \frac{\delta m_t}{m_t} + \delta Z_{\alpha_s} \right] \right\} \ . \tag{3.24}$$

As described earlier, we denote by $|\mathcal{A}_0^{q\bar{q}}|^2$ the matrix element squared of the tree-level amplitude for $q\bar{q} \to t\bar{t}h$ which can be computed in $d = 4$ dimensions since the quantity in the curly brackets is free of UV singularities. We also notice that, in writing Eq. (3.24), we have included in the top-quark self-energy the top-mass counterterm, and we have used the fact that the Yukawa-coupling counterterm coincides with the top-mass counterterm.

The UV-divergent contributions due to the individual diagrams are explicitly given by:

$$\Delta_{UV}\left(S_1^{(1),q\bar{q}} + S_1^{(2),q\bar{q}}\right) = \frac{\alpha_s}{2\pi}\mathcal{N}_t\left(\frac{N}{2} - \frac{1}{2N}\right)\left(-\frac{1}{\epsilon_{UV}}\right) \ ,$$

$$\Delta_{UV}\left(S_2^{(1),q\bar{q}} + S_2^{(2),q\bar{q}}\right) = \frac{\alpha_s}{2\pi}\left[\mathcal{N}_s\left(\frac{5}{3}N - \frac{2}{3}n_{lf}\right) - \mathcal{N}_t\frac{2}{3}\right]\left(\frac{1}{\epsilon_{UV}}\right) \ ,$$

$$\Delta_{UV}\left(V_1^{(1),q\bar{q}} + V_1^{(2),q\bar{q}}\right) = \frac{\alpha_s}{2\pi}\mathcal{N}_s\left(-\frac{1}{2N}\right)\left(\frac{1}{\epsilon_{UV}}\right) \ ,$$

$$\Delta_{UV}\left(V_2^{(1),q\bar{q}} + V_2^{(2),q\bar{q}}\right) = \frac{\alpha_s}{2\pi}\mathcal{N}_s\left(\frac{N}{2}\right)\left(\frac{3}{\epsilon_{UV}}\right) \ , \tag{3.25}$$

$$\Delta_{UV}\left(V_3^{(1),q\bar{q}} + V_3^{(2),q\bar{q}}\right) = \frac{\alpha_s}{2\pi}\mathcal{N}_t\left(-\frac{1}{2N}\right)\left(\frac{1}{\epsilon_{UV}}\right) \ ,$$

$$\Delta_{UV}\left(V_4^{(1),q\bar{q}} + V_4^{(2),q\bar{q}}\right) = \frac{\alpha_s}{2\pi}\mathcal{N}_t\left(\frac{N}{2}\right)\left(\frac{3}{\epsilon_{UV}}\right) \ ,$$

$$\Delta_{UV}\left(V_5^{(1),q\bar{q}} + V_5^{(2),q\bar{q}}\right) = \frac{\alpha_s}{2\pi}\mathcal{N}_t\left(\frac{N}{2} - \frac{1}{2N}\right)\left(\frac{4}{\epsilon_{UV}}\right) \ ,$$

$$\Delta_{UV}\left(V_6^{(1),q\bar{q}} + V_6^{(2),q\bar{q}}\right) = 0 \ ,$$

where $\mathcal{N}_s$ and $\mathcal{N}_t$ are standard normalization factors defined as:

$$\mathcal{N}_s = \left(\frac{4\pi\mu^2}{s}\right)^\epsilon \Gamma(1+\epsilon) \quad , \quad \mathcal{N}_t = \left(\frac{4\pi\mu^2}{m_t^2}\right)^\epsilon \Gamma(1+\epsilon) \quad . \tag{3.26}$$

In this section we limit the discussion to the UV singularities only, while the IR structure of the individual diagrams and counterterms will be considered in Section 3.3.1.3. To this purpose we have explicitly denoted by ϵ_{UV} the pole parameter.

3.3.1.2 Counterterms

The counterterms needed to cancel the UV singularities described above are defined as follows. Although, some counterterms contain IR divergences in addition to the UV divergences discussed below, we wait until Section 3.3.1.3 to present the IR structures.

For the external fields, we fix the wave-function renormalization constants of the external light quark (q) and the top (t) quark fields using the on-shell subtraction scheme:

$$\left(\delta Z_2^{(q)}\right)_{UV} = -\frac{\alpha_s}{4\pi}\mathcal{N}_s \left(\frac{N}{2} - \frac{1}{2N}\right)\left(\frac{1}{\epsilon_{UV}}\right) \quad , \tag{3.27}$$

$$\left(\delta Z_2^{(t)}\right)_{UV} = -\frac{\alpha_s}{4\pi}\mathcal{N}_t \left(\frac{N}{2} - \frac{1}{2N}\right)\left(\frac{1}{\epsilon_{UV}} + 4\right) \quad , \tag{3.28}$$

while we renormalize the wave-function of external gluons in the $\overline{MS}$ subtraction scheme:

$$(\delta Z_3)_{UV} = \frac{\alpha_s}{4\pi}(4\pi)^\epsilon \Gamma(1+\epsilon)\left\{\left(\frac{5}{3}N - \frac{2}{3}n_{lf}\right)\frac{1}{\epsilon_{UV}} - \frac{2}{3}\left[\frac{1}{\epsilon_{UV}} + \ln\left(\frac{\mu^2}{m_t^2}\right)\right]\right\} \quad , \tag{3.29}$$

according to which we also need to consider for $gg \to t\bar{t}h$ the insertion of a finite self-energy correction on the external gluon legs. This amounts to an extra contribution

$$\delta_{UV} = \frac{\alpha_s}{4\pi}(4\pi)^\epsilon \Gamma(1+\epsilon)\left(\frac{5}{3}N - \frac{2}{3}n_{lf}\right)\ln\left(\frac{\mu^2}{m_t^2}\right) \quad , \tag{3.30}$$

which is important in order to obtain the correct scale dependence of the NLO cross section.

We define the subtraction condition for the top-quark mass m_t in such a way that m_t is the pole mass, in which case the top-mass counterterm is given by:

$$\frac{\delta m_t}{m_t} = -\frac{\alpha_s}{4\pi}\mathcal{N}_t \left(\frac{N}{2} - \frac{1}{2N}\right)\left(\frac{3}{\epsilon_{UV}} + 4\right) \quad . \tag{3.31}$$

This counterterm has to be used twice: to renormalize the top-quark mass, in all diagrams that contain a top quark self-energy insertion, and to renormalize the top quark Yukawa coupling. As previously noted, the expressions in Eqs. (3.25) and ((3.41)) already include the top-mass counterterm.

Finally, for the renormalization of α_s we use the $\overline{MS}$ scheme, modified to decouple the top quark [67, 68]. The first n_{lf} light flavors are subtracted using the $\overline{MS}$ scheme, while the divergences associated with the top-quark loop are subtracted at zero momentum:

$$\delta Z_{\alpha_s} = \frac{\alpha_s}{4\pi}(4\pi)^\epsilon \Gamma(1+\epsilon)\left\{\left(\frac{2}{3}n_{lf} - \frac{11}{3}N\right)\frac{1}{\epsilon_{UV}} + \frac{2}{3}\left[\frac{1}{\epsilon_{UV}} + \ln\left(\frac{\mu^2}{m_t^2}\right)\right]\right\} \quad , \tag{3.32}$$

such that, in this scheme, the renormalized strong coupling constant $\alpha_s(\mu)$ evolves with $n_{lf} = 5$ light flavors.

Using the results in Eqs. (3.25)-(3.32), it is easy to verify that $(\hat{\sigma}_{virt}^{q\bar{q}})_{UV-pole}$ (Eq. (3.24)) is free of UV singularities and has a residual renormalization scale dependence of the form:

$$\hat{\sigma}_{LO}^{q\bar{q},gg}\frac{\alpha_s(\mu)}{2\pi}\left(-\frac{2}{3}n_{lf} + \frac{11}{3}N\right)\ln\left(\frac{\mu^2}{s}\right) \quad , \tag{3.33}$$

as expected by renormalization group arguments (see the first term of Eq. (3.5)). We note that the presence of s in the argument of the logarithm of Eq. (3.33) has no particular relevance. Choosing a different argument would amount to reabsorbing some μ-independent logarithms in f_1^{ij} of Eq. (3.4).

3.3.1.3 IR singularities

This section describes the structure of the IR singularities originating from the $\mathcal{O}(\alpha_s)$ virtual corrections to $q\bar{q} \rightarrow t\bar{t}h$. The virtual IR singularities come from

56

the following set of diagrams: vertex diagrams $V_1^{(1,2),q\bar{q}}$ and $V_2^{(1,2),q\bar{q}}$, box diagrams $B_2^{(1,2),q\bar{q}}$, box diagrams $B_3^{(1-4),q\bar{q}}$, pentagon diagrams $P_1^{q\bar{q}}$ and $P_2^{q\bar{q}}$, and from the wave function renormalization of the external fields, $\delta Z_2^{(q)}$ and $\delta Z_2^{(t)}$. The IR-singular $\mathcal{O}(\alpha_s^3)$ virtual cross section for $q\bar{q} \to t\bar{t}h$ can then be written as:

$$(\hat{\sigma}_{virt}^{q\bar{q}})_{IR-pole} = \int d(PS_3) \overline{\sum} |\mathcal{A}_{LO}^{q\bar{q}}|^2 \left\{ \Delta_{IR}\left(V_1^{(1),q\bar{q}} + V_1^{(2),q\bar{q}}\right) + \Delta_{IR}\left(V_2^{(1),q\bar{q}} + V_2^{(2),q\bar{q}}\right) \right.$$
$$+ \left(\delta Z_2^{(q)}\right)_{IR} + \left(\delta Z_2^{(q)}\right)_{IR} + \Delta_{IR}\left(B_2^{(1),q\bar{q}} + B_2^{(2),q\bar{q}}\right) +$$
$$\left. + \Delta_{IR}\left(B_3^{(1),q\bar{q}} + B_3^{(3),q\bar{q}} + P_1^{q\bar{q}}\right) + \Delta_{IR}\left(B_3^{(2),q\bar{q}} + B_3^{(4),q\bar{q}} + P_1^{q\bar{q}}\right) \right\} \quad , \quad (3.34)$$

where, as before, $|\mathcal{A}_{LO}^{q\bar{q}}|^2$ denotes the matrix element squared of the tree-level amplitude for $q\bar{q} \to t\bar{t}h$, in $d = 4$ dimensions. The IR-divergent contributions of the various diagrams to the virtual amplitude squared are of the form $\Delta_{IR}(D_i^{q\bar{q}})\mathcal{A}_0^{q\bar{q}}$:

$$\Delta_{IR}\left(V_1^{(1),q\bar{q}} + V_1^{(2),q\bar{q}}\right) = \left(\frac{\alpha_s}{2\pi}\right)\mathcal{N}_s\left(-\frac{1}{2N}\right)\left(-\frac{2}{\epsilon_{IR}^2} - \frac{4}{\epsilon_{IR}}\right) \quad ,$$

$$\Delta_{IR}\left(V_2^{(1),q\bar{q}} + V_2^{(2),q\bar{q}}\right) = \left(\frac{\alpha_s}{2\pi}\right)\mathcal{N}_s\left(\frac{N}{2}\right)\left(-\frac{4}{\epsilon_{IR}}\right) \quad ,$$

$$\left(\delta Z_2^{(q)}\right)_{IR} = \left(\frac{\alpha_s}{2\pi}\right)\mathcal{N}_s\left(\frac{N}{2} - \frac{1}{2N}\right)\left(\frac{1}{\epsilon_{IR}}\right) \quad , \qquad (3.35)$$

$$\left(\delta Z_2^{(t)}\right)_{IR} = \left(\frac{\alpha_s}{2\pi}\right)\mathcal{N}_t\left(\frac{N}{2} - \frac{1}{2N}\right)\left(-\frac{2}{\epsilon_{IR}}\right) \quad ,$$

$$\Delta_{IR}\left(B_2^{(1),q\bar{q}} + B_2^{(2),q\bar{q}}\right) = \left(\frac{\alpha_s}{2\pi}\right)\mathcal{N}_t\left(-\frac{1}{N}\right)\left(\frac{1}{\epsilon_{IR}}\frac{s_{t\bar{t}}}{(2m_t^2 + s_{t\bar{t}})\beta_{t\bar{t}}}\Lambda_{t\bar{t}}\right) \quad ,$$

$$\Delta_{IR}\left(B_3^{(1),q\bar{q}} + B_3^{(3),q\bar{q}} + P_1\right) = \left(\frac{\alpha_s}{2\pi}\right)\mathcal{N}_t\left(\frac{N}{2} - \frac{1}{N}\right)\left[-\frac{2}{\epsilon_{IR}^2} + \frac{2}{\epsilon_{IR}}\left(\ln\left(\frac{\tau_1}{m_t^2}\right) + \ln\left(\frac{\tau_2}{m_t^2}\right)\right)\right] \quad ,$$

$$\Delta_{IR}\left(B_3^{(2),q\bar{q}} + B_3^{(4),q\bar{q}} + P_2\right) = \left(\frac{\alpha_s}{2\pi}\right)\mathcal{N}_t\left(-\frac{1}{N}\right)\left[\frac{2}{\epsilon_{IR}^2} - \frac{2}{\epsilon_{IR}}\left(\ln\left(\frac{\tau_4}{m_t^2}\right) + \ln\left(\frac{\tau_3}{m_t^2}\right)\right)\right] \quad ,$$

where $\mathcal{N}_s$ and $\mathcal{N}_t$ are given in Eq. (3.26), while ϵ_{IR} denotes that we are now considering only singularities of IR origin. Moreover, we have introduced the following kinematic invariants:

$$s = s_{q\bar{q}} = 2q_1 \cdot q_2 \quad , \quad s_{t\bar{t}} = 2p_t \cdot p_t' \quad , \quad \tau_1 = 2q_1 \cdot p_t \quad , \quad \tau_2 = 2q_2 \cdot p_t' \quad , \quad \tau_3 = 2q_2 \cdot p_t \quad , \quad \tau_4 = 2q_1 \cdot p_t' \quad ,$$

$$(3.36)$$

and we have defined

$$\beta_{t\bar{t}} = \sqrt{1 - \frac{4m_t^2}{(p_t + p'_t)^2}} \quad , \tag{3.37}$$

$$\Lambda_{t\bar{t}} = \ln\left(\frac{1 + \beta_{t\bar{t}}}{1 - \beta_{t\bar{t}}}\right) \quad .$$

Substituting the explicit expression for the IR-divergent contributions given in Eq. (3.35) into Eq. (3.34) yields:

$$(\hat{\sigma}^{q\bar{q}}_{virt})_{IR-pole} = \int d(PS_3) \left(\frac{\alpha_s}{2\pi}\right) \mathcal{N}_t \overline{\sum} |\mathcal{A}^{q\bar{q}}_{LO}|^2 \left\{ \frac{X^{q\bar{q},virt}_{-2}}{\epsilon_{IR}^2} + \frac{X^{q\bar{q},virt}_{-1}}{\epsilon_{IR}} + \delta^{q\bar{q},IR}_{virt} \right\} \quad , \tag{3.38}$$

where

$$X^{q\bar{q},virt}_{-2} = -\left(N - \frac{1}{N}\right) \quad , \tag{3.39}$$

$$X^{q\bar{q},virt}_{-1} = N \left[-\frac{5}{2} + \ln\left(\frac{\tau_1}{m_t^2}\right) + \ln\left(\frac{\tau_2}{m_t^2}\right) \right]$$

$$+ \frac{1}{N} \left[-\ln\left(\frac{s}{m_t^2}\right) + \frac{5}{2} - \frac{s_{t\bar{t}}}{(2m_t^2 + s_{t\bar{t}})\beta_{t\bar{t}}} \Lambda_{t\bar{t}} - 2\ln\left(\frac{\tau_1\tau_2}{\tau_4\tau_3}\right) \right] \quad ,$$

while $\delta^{q\bar{q},IR}_{virt}$ is a finite term that derives from having factored out a common factor $\mathcal{N}_t$, and is given by:

$$\delta^{q\bar{q},IR}_{virt} = \left(N - \frac{1}{N}\right) \left[\frac{3}{2} \ln\left(\frac{s}{m_t^2}\right) \right] + \frac{1}{N} \left[\frac{1}{2} \ln^2\left(\frac{s}{m_t^2}\right) \right] \quad . \tag{3.40}$$

Finally, we note that the IR singularities of $\sigma^{q\bar{q}}_{virt}$ will be canceled by the corresponding IR singularities of $\sigma^{q\bar{q}}_{real}$.

3.3.2 One-loop corrections to $gg \rightarrow t\bar{t}h$

3.3.2.1 UV singularities

Self-energy and vertex one loop corrections to the tree level $gg \rightarrow t\bar{t}h$ process also give rise to UV divergences. These singularities are canceled by the same set of counterterms introduced in Section 3.3.1.2.

By carefully grouping subsets of self-energy and vertex diagrams, we can factor out the UV singularities of the $\mathcal{O}(\alpha_s^3)$ virtual amplitude and write them in terms of the tree level partial amplitudes $\mathcal{A}_{0,s}^{gg}$, $\mathcal{A}_{0,t}^{gg}$, and $\mathcal{A}_{0,u}^{gg}$ introduced in Eq. (3.14). According to the notation introduced in Figs. 3.9-3.12, we denote by $D_{i,j}^{gg}$ (with $D^{gg} = S^{gg}, V^{gg}$, $i = 1, 2, \ldots$, and $j = s, t, u$) a class of diagrams with a given self-energy or vertex correction insertion, summed over all possible insertions of the external Higgs field, one for each different diagram. We now define $\Delta_{UV}(\mathcal{A}_{D_{i,j}}^{gg})$ to be the UV pole part of the corresponding amplitude. Using this notation, we find

$$\Delta_{UV}(\mathcal{A}_{S_{1,s}}^{gg}) = \frac{\alpha_s}{4\pi}\left[\mathcal{N}_s\left(\frac{5}{3}N - \frac{2}{3}n_{lf}\right) - \mathcal{N}_t\frac{2}{3}\right]\left(\frac{1}{\epsilon_{UV}}\right)[T^A, T^B]\mathcal{A}_{0,s}^{gg} ,$$

$$\Delta_{UV}(\mathcal{A}_{V_{1,s}}^{gg}) = \frac{\alpha_s}{4\pi}\left[\mathcal{N}_s\left(-\frac{2}{3}N + \frac{2}{3}n_{lf}\right) + \mathcal{N}_t\frac{2}{3}\right]\left(\frac{1}{\epsilon_{UV}}\right)[T^A, T^B]\mathcal{A}_{0,s}^{gg} ,$$

$$\Delta_{UV}(\mathcal{A}_{V_{2,s}}^{gg} + \mathcal{A}_{V_{7,t}}^{gg} + \mathcal{A}_{V_{7,u}}^{gg}) = \frac{\alpha_s}{4\pi}\mathcal{N}_t\left(\frac{3}{2}N - \frac{1}{2N}\right)\left(\frac{1}{\epsilon_{UV}}\right)\mathcal{A}_0^{gg} ,$$

$$\Delta_{UV}(\mathcal{A}_{V_{8,t}}^{gg} + \mathcal{A}_{V_{8,u}}^{gg}) = \frac{\alpha_s}{4\pi}\mathcal{N}_t\left(\frac{3}{2}N - \frac{1}{2N}\right)\left(\frac{1}{\epsilon_{UV}}\right) \times$$
$$\left(\frac{1}{2}(\mathcal{A}_{0,t}^{gg} - \mathcal{A}_{0,u}^{gg})[T^A, T^B] + \frac{1}{2}(\mathcal{A}_{0,t}^{gg} + \mathcal{A}_{0,u}^{gg})\{T^A, T^B\}\right) ,$$

$$\Delta_{UV}(\mathcal{A}_{V_{3,s}}^{gg} + \mathcal{A}_{V_{9,t}}^{gg} + \mathcal{A}_{V_{9,u}}^{gg}) = \frac{\alpha_s}{4\pi}\mathcal{N}_t\left(\frac{N}{2} - \frac{1}{2N}\right)\left(\frac{4}{\epsilon_{UV}}\right)\mathcal{A}_0 ,$$

$$\Delta_{UV}(\mathcal{A}_{S_{2,s}}^{gg} + \mathcal{A}_{S_{3,t}}^{gg} + \mathcal{A}_{S_{3,u}}^{gg} + \mathcal{A}_{S_{4,t}}^{gg} + \mathcal{A}_{S_{4,u}}^{gg}) = \frac{\alpha_s}{4\pi}\mathcal{N}_t\left(\frac{N}{2} - \frac{1}{2N}\right)\left(-\frac{1}{\epsilon_{UV}}\right) \times$$
$$\left(\mathcal{A}_0^{gg} + \frac{1}{2}(\mathcal{A}_{0,t}^{gg} - \mathcal{A}_{0,u}^{gg})[T^A, T^B] + \frac{1}{2}(\mathcal{A}_{0,t}^{gg} + \mathcal{A}_{0,u}^{gg})\{T^A, T^B\}\right) ,$$
(3.41)

where $n_{lf} = 5$ corresponds to the number of light quark flavors, $N = 3$ is the number of colors, $\mathcal{N}_s$ and $\mathcal{N}_t$ are given in Eq.(3.26) and we have already included in the top quark self-energy diagrams the top mass counterterm. Using these expressions, we find that the UV-singular part of the total virtual amplitude squared for $gg \rightarrow t\bar{t}h$ can be written as:

$$(\hat{\sigma}^{gg}_{virt})_{UV-pole} = \int d(PS_3) \sum_{D_{i,j}} \overline{\sum} \overline{\sum} 2\,\mathcal{R}e\left(\mathcal{A}^{gg}_0 \, \Delta_{UV}(\mathcal{A}^{gg*}_{D_{i,j}})\right) +$$

$$2\hat{\sigma}^{gg}_{LO}\left[\left(\delta Z^{(t)}_2\right)_{UV} + \left(\delta Z_3\right)_{UV} + \delta_{UV} + \frac{\delta m_t}{m_t} + \delta Z_{\alpha_s}\right] \qquad (3.42)$$

We again notice that some of the UV divergent virtual corrections ($V^{gg}_{1,s}$, $V^{gg}_{7,(t,u)}$, and $V^{gg}_{8,(t,u)}$), as well as $\delta Z^{(t)}_2$ and δZ_3 in Eqs. (3.28) and (3.29) above, also have IR singularities. Again, in this section we limit the discussion to the UV singularities only, while the IR structure of these terms will be considered in Section 3.3.2.2. To this purpose we have explicitly denoted by ϵ_{UV} the pole parameter.

Using the above results and the results from Section 3.3.1.2 , it is easy to verify that $(\hat{\sigma}^{gg}_{virt})_{UV-pole}$ (Eq. (3.42)) is free of UV singularities and has a residual renormalization scale dependence of the form:

$$\hat{\sigma}^{q\bar{q},gg}_{LO} \frac{\alpha_s(\mu)}{2\pi}\left(-\frac{2}{3}n_{lf} + \frac{11}{3}N\right)\ln\left(\frac{\mu^2}{s}\right) \quad , \qquad (3.43)$$

as expected by renormalization group arguments (see the first term of Eq. (3.5)).

3.3.2.2 IR singularities

The structure of the IR singularities originating from the $\mathcal{O}(\alpha_s)$ virtual corrections to the tree level amplitude for $gg \to t\bar{t}h$ is more involved than for the UV singularities. However, it simplifies considerably when given at the level of the amplitude squared, and this is what we present in this section.

The IR divergent part of the $\mathcal{O}(\alpha^3_s)$ virtual amplitude squared for $gg \to t\bar{t}h$ can be written in the following compact form:

$$\sum_{D^{gg}_{i,j}} \overline{\sum}\,\overline{\sum} 2\mathcal{R}e\left(\mathcal{A}^{gg}_0 \, \Delta_{IR}(\mathcal{A}^{gg*}_{D_{i,j}})\right) = \frac{\alpha_s}{2\pi}\mathcal{N}_t \overline{\sum}\left(C_1 \mathcal{M}^{(1),gg}_{V,\epsilon} + C_2 \mathcal{M}^{(2),gg}_{V,\epsilon} + C_3 \mathcal{M}^{(3),gg}_{V,\epsilon}\right) \quad ,$$

$$(3.44)$$

where $\mathcal{N}_t$ is defined in Eq. (3.26) and we denote by $\Delta_{IR}(\mathcal{A}^{gg}_{D_{i,j}})$ the IR pole part of the amplitude of a given $D^{gg}_{i,j}$ class of diagrams. The result is organized in terms of leading and subleading color factors:

60

$$C_1 = \frac{N^2}{4}(N^2 - 1) \ ,$$

$$C_2 = -\frac{1}{4}(N^2 - 1) \ ,$$

$$C_3 = \left(1 + \frac{1}{N^2}\right)(N^2 - 1) \ , \tag{3.45}$$

and the corresponding matrix elements squared $M_{V,\epsilon}^{(1),gg}$, $M_{V,\epsilon}^{(2),gg}$, and $M_{V,\epsilon}^{(3),gg}$ are given by:

$$
\begin{aligned}
\mathcal{M}_{V,\epsilon}^{(1),gg} &= \left[-\frac{4}{\epsilon_{IR}^2} + \frac{2}{\epsilon_{IR}}(-2 + \Lambda_\sigma)\right]\left(|\mathcal{A}_0^{nab}|^2 + |\mathcal{A}_0^{ab}|^2\right) \\
&\quad + \frac{1}{\epsilon_{IR}}\left[(\Lambda_{\tau_1} + \Lambda_{\tau_2})|\mathcal{A}_{0,s}^{gg} + \mathcal{A}_{0,t}^{gg}|^2 + (\Lambda_{\tau_3} + \Lambda_{\tau_4})|\mathcal{A}_{0,u}^{gg} - \mathcal{A}_{0,s}^{gg}|^2\right] \ , \\
\mathcal{M}_{V,\epsilon}^{(2),gg} &= \left[-\frac{8}{\epsilon_{IR}^2} + \frac{4}{\epsilon_{IR}}(-2 + \Lambda_{\tau_1} + \Lambda_{\tau_2} + \Lambda_{\tau_3} + \Lambda_{\tau_4})\right]|\mathcal{A}_0^{ab}|^2 \\
&\quad + \frac{2}{\epsilon_{IR}}\frac{\bar{s}_{t\bar{t}} - 2m_t^2}{\bar{s}_{t\bar{t}}\beta_{t\bar{t}}}\Lambda_{t\bar{t}}\left(|\mathcal{A}_0^{nab}|^2 + |\mathcal{A}_0^{ab}|^2\right) \ , \\
\mathcal{M}_{V,\epsilon}^{(3),gg} &= \frac{1}{\epsilon_{IR}}\frac{\bar{s}_{t\bar{t}} - 2m_t^2}{\bar{s}_{t\bar{t}}\beta_{t\bar{t}}}\Lambda_{t\bar{t}}|\mathcal{A}_0^{ab}|^2 \ , \tag{3.46}
\end{aligned}
$$

where the IR nature of the pole terms has been made explicit. $\mathcal{A}_0^{ab}$ and $\mathcal{A}_0^{nab}$ are defined in Eq. (3.13), while $\mathcal{A}_{0,s}^{gg}$, $\mathcal{A}_{0,t}^{gg}$, and $\mathcal{A}_{0,u}^{gg}$ are given explicitly in Eq. (3.14). Moreover, $\beta_{t\bar{t}}$ and $\Lambda_{t\bar{t}}$ are given in Eq. (3.37) and we have defined:

$$\bar{s}_{t\bar{t}} = (p_t + p_t')^2 \ , \tag{3.47}$$

and we have introduced the notation: $\Lambda_\sigma = \ln(\sigma/m_t^2)$ and $\Lambda_{\tau_i} = \ln(\tau_i/m_t^2)$ where

$$\sigma = (q_1 + q_2)^2 \ , \tag{3.48}$$

and the τ_i's are given in Eq. (3.36). When we add the IR singularities coming from the counterterms given in Eq. (3.35), we can write the complete pole part of the IR singular $\mathcal{O}(\alpha_s^3)$ virtual cross section for $gg \to t\bar{t}h$ as:

$$(\hat{\sigma}_{virt}^{gg})_{IR-pole} = \int d(PS_3)\sum_{D_{i,j}^{gg}}\overline{\sum}2\mathcal{R}e\left(\mathcal{A}_0^{gg}\,\Delta_{IR}(\mathcal{A}_{D_{i,j}}^{gg*})\right) + 2\hat{\sigma}_{LO}^{gg}\left(\left(\delta Z_2^{(t)}\right)_{IR} + (\delta Z_3)_{IR}\right)$$

61

$$
= \int d(PS_3) \frac{\alpha_s}{2\pi} \mathcal{N}_t \overline{\sum} \left(C_1 \mathcal{M}_{V,\epsilon}^{(1),gg} + C_2 \mathcal{M}_{V,\epsilon}^{(2),gg} + C_3 \mathcal{M}_{V,\epsilon}^{(3),gg} \right)
$$

$$
+ \frac{\alpha_s}{2\pi} \mathcal{N}_t \left(\frac{2}{3} n_{lf} - \frac{8}{3} N + \frac{1}{N} \right) \frac{1}{\epsilon_{IR}} \hat{\sigma}_{LO}^{gg} \quad . \tag{3.49}
$$

As will be demonstrated in Section 3.4, the IR singularities of $\hat{\sigma}_{virt}^{gg}$ are canceled by the corresponding IR singularities of $\hat{\sigma}_{real}^{gg}$.

3.4 Real-emission corrections
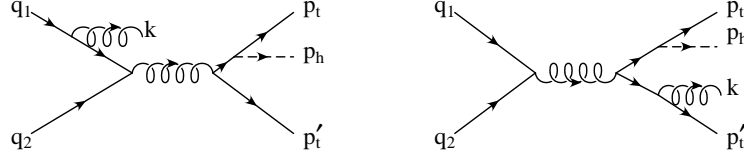
Figure 3.13. $\mathcal{O}(\alpha_s)$ real corrections to $q\bar{q} \to t\bar{t}h$: examples of initial and final state real gluon emission.

The NLO real cross sections $\hat{\sigma}_{real}^{q\bar{q},gg}$ in Eq. (3.3) correspond to the $\mathcal{O}(\alpha_s)$ corrections to $q\bar{q}, gg \to t\bar{t}h$ due to the emission of a real gluon, i.e. to the processes $q\bar{q}, gg \to t\bar{t}h + g$, examples of which are illustrated in Figs. 3.13 and 3.14. These cross sections contain IR singularities which cancel the analogous singularities present in the $\mathcal{O}(\alpha_s)$ virtual corrections (see Sections 3.3.1.3 and 3.3.2.2) and in the NLO parton distribution functions. These singularities can be either *soft*, when the energy of the emitted gluon becomes very small, or *collinear*, when the final state gluon is emitted collinear to one of the initial gluons. There is no collinear radiation from the final t and $\bar{t}$ quarks because they are massive and their mass effectively regulates any collinear divergences. At the same order in α_s, the $\hat{\sigma}_{real}^{qg}$ cross section corresponds to the tree level processes $(q, \bar{q})g \to t\bar{t}h + (q, \bar{q})$, an example of which is also illustrated in Fig. 3.14. This part of the NLO cross section develops IR singularities entirely due
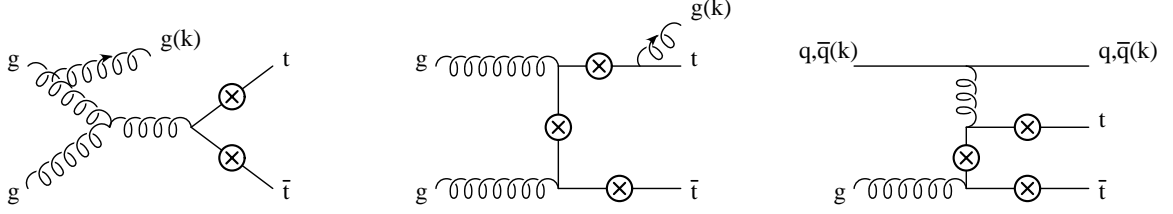
Figure 3.14. Examples of $\mathcal{O}(\alpha_s)$ real corrections to $gg \to t\bar{t}h$ (first two diagrams) and of the tree level $(q,\bar{q})g \to t\bar{t}h(q,\bar{q})$ processes (third diagram). The circled crosses denote all possible insertions of an external Higgs boson leg, each insertion corresponding to a different diagram.

to the collinear emission of a final state quark or antiquark from one of the initial state massless partons.

The IR singularities encountered in the calculation of the real cross section can be conveniently isolated by *slicing* the $q\bar{q}, gg \to t\bar{t}h + g$ and $(q,\bar{q})g \to t\bar{t}h + (q,\bar{q})$ phase spaces into different regions defined by suitable cutoffs, a method which goes under the general name of *Phase Space Slicing* (PSS). The dependence on the arbitrary cutoff(s) introduced in *slicing* the phase space of the final state particles is not physical, and cancels at the level of the total real hadronic cross section, i.e. in σ_{real}, as well as at the level of the real cross section for each separate channel, i.e. in $\sigma_{real}^{q\bar{q}}$, σ_{real}^{gg}, and σ_{real}^{qg}. This cancellation constitutes an important check of the calculation and will be discussed in detail in Section 3.5.

We have calculated the cross section for the processes

$$q(q_1) + \bar{q}(q_2) \to t(p_t) + \bar{t}(p'_t) + h(p_h) + g(k) \ ,$$

$$g(q_1) + g(q_2) \to t(p_t) + \bar{t}(p'_t) + h(p_h) + g(k) \ ,$$

and

$$(q,\bar{q})(q_1) + g(q_2) \to t(p_t) + \bar{t}(p'_t) + h(p_h) + (q,\bar{q})(k) \ ,$$

63

with $q_1 + q_2 = p_t + p'_t + p_h + k$, using two different implementations of the PSS method which we call the *two-cutoff* and *one-cutoff* methods respectively, depending on the number of cutoffs introduced. The *two-cutoff* implementation of the PSS method was originally developed to study QCD corrections to dihadron production [69] and has since then been applied to a variety of processes (for a review see, e.g. [55]). The *one-cutoff* PSS method was developed for massless quarks in Ref. [56, 57] and extended to the case of massive quarks in Ref. [58].

In the following sections we discuss the application of the PSS method to the $q\bar{q}$-, gg and $(q\bar{q})g$-initiated process separately, using the *two-cutoff* implementation in Section 3.4.1 and the *one-cutoff* implementation in Section 3.4.2. The results for σ_{real} obtained using PSS with one or two cutoffs agree within the statistical errors of the Monte Carlo integration. In spite of the fact that both methods are realizations of the general idea of phase space slicing, they have very different characteristics and finding agreement between the two represents an important check of our calculation.

3.4.1 Phase Space Slicing method with two cutoffs

The general implementation of the PSS method using two cutoffs proceeds in two steps. First, by introducing an arbitrary small *soft* cutoff δ_s, we separate the overall integration of the $q\bar{q}, gg \rightarrow t\bar{t}h + g$ phase space into two regions according to whether the energy of the final state gluon ($k^0 = E_g$) is *soft*, i.e. $E_g \leq \delta_s \sqrt{s}/2$, or *hard*, i.e. $E_g > \delta_s \sqrt{s}/2$. The partonic real cross section of Eq. (3.3) can then be written as:

$$\hat{\sigma}_{real}^{q\bar{q},gg} = \hat{\sigma}_{soft}^{q\bar{q},gg} + \hat{\sigma}_{hard}^{q\bar{q},gg} \ , \tag{3.50}$$

where $\hat{\sigma}_{soft}^{q\bar{q},gg}$ is obtained by integrating over the *soft* region of the gluon phase space, and contains all the IR soft divergences of $\hat{\sigma}_{real}^{q\bar{q},gg}$. To isolate the remaining collinear divergences from $\hat{\sigma}_{hard}^{q\bar{q},gg}$, we further split the integration over the gluon phase space according to whether the final state gluon is ($\hat{\sigma}_{hard/coll}^{q\bar{q},gg}$) or is not

64

$(\hat{\sigma}_{hard/non-coll}^{q\bar{q},gg})$ emitted within an angle θ from the initial state quarks or gluons such that $(1 - \cos\theta) < \delta_c$, for an arbitrary small *collinear* cutoff δ_c:

$$\hat{\sigma}_{hard}^{q\bar{q},gg} = \hat{\sigma}_{hard/coll}^{q\bar{q},gg} + \hat{\sigma}_{hard/non-coll}^{q\bar{q},gg} \ . \tag{3.51}$$

In the same way, we isolate the collinear divergences in the cross section for the $(q,\bar{q})g$ initiated processes and write the corresponding cross section as:

$$\hat{\sigma}_{real}^{qg} = \hat{\sigma}_{coll}^{qg} + \hat{\sigma}_{non-coll}^{qg} \ . \tag{3.52}$$

The hard non-collinear part of the real $q\bar{q}$- and gg-initiated cross sections, $\hat{\sigma}_{hard/non-coll}^{q\bar{q}}$ and $\hat{\sigma}_{hard/non-coll}^{gg}$, and the non-collinear part of the $(q,\bar{q})g$-initiated cross section, $\hat{\sigma}_{non-coll}^{qg}$, are finite and can be computed numerically.

On the other hand, in the soft and collinear regions the integration over the phase space of the emitted gluon or quark can be performed analytically, thus allowing us to isolate and extract the IR divergences of $\hat{\sigma}_{real}^{q\bar{q},gg}$ and $\hat{\sigma}_{real}^{qg}$. More details on the calculations of $\hat{\sigma}_{soft}^{q\bar{q}}$ and $\hat{\sigma}_{soft}^{gg}$ are given in Sections 3.4.1.1 and 3.4.1.2, respectively, while details of the calculations of $\hat{\sigma}_{hard}^{q\bar{q}}$ and $\hat{\sigma}_{hard}^{gg}$ are given in Section 3.4.1.3. The calculation of $\hat{\sigma}_{real}^{qg}$ is described in Section 3.4.1.4.

3.4.1.1 Soft gluon emission: $q\bar{q} \rightarrow t\bar{t}h + g$

The soft region of the $q\bar{q} \rightarrow t\bar{t}h + g$ phase space is defined by requiring that the energy of the gluon satisfies:

$$E_g < \delta_s \frac{\sqrt{s}}{2} \ , \tag{3.53}$$

for an arbitrary small value of the *soft* cutoff δ_s. In the limit when the energy of the gluon becomes small, i.e. in the *soft limit*, the matrix element squared for the real gluon emission, $\overline{\sum}|\mathcal{A}_{real}^{q\bar{q}}|^2$, assumes a very simple form, i.e. it factorizes into the Born matrix element squared times an eikonal factor $\Phi_{eik}^{q\bar{q}}$:

$$\overline{\sum}|\mathcal{A}_{real}(q\bar{q} \rightarrow t\bar{t}h + g)|^2 \xrightarrow{soft} (4\pi\alpha_s)\overline{\sum}|\mathcal{A}_{LO}^{q\bar{q}}|^2 \ \Phi_{eik}^{q\bar{q}} \ , \tag{3.54}$$

65

where the eikonal factor is given by:

$$\Phi_{eik}^{q\bar{q}} = \frac{N}{2}\left[-\frac{m_t^2}{(p_t\cdot k)^2} - \frac{m_t^2}{(p_t'\cdot k)^2} + \frac{\tau_1}{(q_1\cdot k)(p_t\cdot k)} + \frac{\tau_2}{(q_2\cdot k)(p_t'\cdot k)}\right]$$

$$+\frac{1}{2N}\left[\frac{m_t^2}{(p_t\cdot k)^2} + \frac{m_t^2}{(p_t'\cdot k)^2} - \frac{s}{(q_1\cdot k)(q_2\cdot k)} - \frac{s_{t\bar{t}}}{(p_t\cdot k)(p_t'\cdot k)}\right.$$

$$\left.+2\left(-\frac{\tau_1}{(q_1\cdot k)(p_t\cdot k)} + \frac{\tau_4}{(q_1\cdot k)(p_t'\cdot k)} + \frac{\tau_3}{(q_2\cdot k)(p_t\cdot k)} - \frac{\tau_2}{(q_2\cdot k)(p_t'\cdot k)}\right)\right] \quad . \tag{3.55}$$

Moreover, in the soft region the $q\bar{q} \to t\bar{t}h + g$ phase space also factorizes as:

$$d(PS_4)(q\bar{q} \to t\bar{t}h + g) \xrightarrow{soft} d(PS_3)(q\bar{q} \to t\bar{t}h)d(PS_g)_{soft} \tag{3.56}$$

$$= d(PS_3)(q\bar{q} \to t\bar{t}h)\frac{d^{(d-1)}k}{(2\pi)^{(d-1)}2E_g}\theta(\delta_s\frac{\sqrt{s}}{2} - E_g) \ ,$$

where $d(PS_g)_{soft}$ denotes the integration over the phase space of the soft gluon. The parton level soft cross section can then be written as:

$$\hat{\sigma}_{soft}^{q\bar{q}} = (4\pi\alpha_s)\,\mu^{2\epsilon}\int d(PS_3)\overline{\sum}|\mathcal{A}_{LO}^{q\bar{q}}|^2\int d(PS_g)_{soft}\Phi_{eik}^{q\bar{q}} \ . \tag{3.57}$$

Since the contribution of the soft gluon is now completely factorized, we can perform the integration over $d(PS_g)_{soft}$ in Eq. (3.57) analytically, and extract the soft poles that will have to cancel $X_{-2}^{q\bar{q},virt}$ and $X_{-1}^{q\bar{q},virt}$ of Eq. (3.39). The integration over the gluon phase space in Eq. (3.57) can be performed using standard techniques and we refer to Refs. [55, 70] for more details. For sake of completeness, in Appendix C we give explicit results for the soft integrals used in our calculation.

Finally, the soft gluon contribution to $\hat{\sigma}_{real}^{q\bar{q}}$ can be written as follows:

$$\hat{\sigma}_{soft}^{q\bar{q}} = \frac{\alpha_s}{2\pi}\mathcal{N}_t\int d(PS_3)\overline{\sum}|\mathcal{A}_{LO}^{q\bar{q}}|^2\left\{\frac{X_{-2}^{q\bar{q},s}}{\epsilon^2} + \frac{X_{-1}^{q\bar{q},s}}{\epsilon} + NC_1^{q\bar{q},s} + \frac{C_2^{q\bar{q},s}}{N}\right\} \ , \tag{3.58}$$

where

$$X_{-2}^{q\bar{q},s} = -X_{-2}^{virt} \ , \tag{3.59}$$

$$X_{-1}^{q\bar{q},s} = -X_{-1}^{virt} - \left(N - \frac{1}{N}\right)\left[\frac{3}{2} + 2\ln(\delta_s)\right] \ ,$$

$$C_1^{q\bar{q},s} = \frac{3}{2}\ln\left(\frac{s}{\mu^2}\right) + 2\ln^2(\delta_s) - 2\ln(\delta_s)\left[1 + \ln\left(\frac{m_t^2\mu^2}{\tau_1\tau_2}\right)\right]$$
$$+ \frac{1}{2}\ln^2\left(\frac{s}{m_t^2}\right) - \frac{\pi^2}{3} - \ln\left(\frac{s}{m_t^2}\right)\left[\frac{5}{2} + \ln\left(\frac{sm_t^2}{\tau_1\tau_2}\right)\right]$$
$$+ \frac{1}{2}\frac{1}{\beta_t}\ln\left(\frac{1+\beta_t}{1-\beta_t}\right) + \frac{1}{2}\frac{1}{\beta_{\bar{t}}}\ln\left(\frac{1+\beta_{\bar{t}}}{1-\beta_{\bar{t}}}\right)$$
$$+ \frac{1}{2}\left(F(q_1,p_t) + F(q_2,p_t')\right) + \left[\frac{3}{2} + 2\ln(\delta_s)\right]\ln\left(\frac{\mu^2}{m_t^2}\right) \ ,$$

$$C_2^{q\bar{q},s} = -\frac{3}{2}\ln\left(\frac{s}{\mu^2}\right) - 2\ln^2(\delta_s)$$
$$- 2\ln(\delta_s)\left[-1 + \frac{s_{t\bar{t}}}{(2m_t^2 + s_{t\bar{t}})\beta_{t\bar{t}}}\Lambda_{t\bar{t}} + \ln\left(\frac{s}{\mu^2}\right) + 2\ln\left(\frac{\tau_1\tau_2}{\tau_4\tau_3}\right)\right]$$
$$- \frac{1}{2}\ln^2\left(\frac{s}{m_t^2}\right) + \frac{\pi^2}{3} - \ln\left(\frac{s}{m_t^2}\right)\left[-\frac{5}{2} + \frac{s_{t\bar{t}}}{(2m_t^2 + s_{t\bar{t}})\beta_{t\bar{t}}}\Lambda_{t\bar{t}} + 2\ln\left(\frac{\tau_1\tau_2}{\tau_4\tau_3}\right)\right]$$
$$- \frac{1}{2}\frac{1}{\beta_t}\ln\left(\frac{1+\beta_t}{1-\beta_t}\right) - \frac{1}{2}\frac{1}{\beta_{\bar{t}}}\ln\left(\frac{1+\beta_{\bar{t}}}{1-\beta_{\bar{t}}}\right)$$
$$+ \frac{s_{t\bar{t}}}{(2m_t^2 + s_{t\bar{t}})\beta_{t\bar{t}}}\left[-\frac{1}{4}\ln^2\left(\frac{1+\beta_t}{1-\beta_t}\right) + \frac{1}{4}\ln^2\left(\frac{1+\beta_{\bar{t}}}{1-\beta_{\bar{t}}}\right)\right.$$
$$-\mathrm{Li}\left(1 - \frac{\alpha_{t\bar{t}}}{v_{t\bar{t}}}p_t^0(1+\beta_t)\right) - \mathrm{Li}\left(1 - \frac{\alpha_{t\bar{t}}}{v_{t\bar{t}}}p_t^0(1-\beta_t)\right)$$
$$\left.+\mathrm{Li}\left(1 - \frac{1}{v_{t\bar{t}}}p_t'^0(1+\beta_{\bar{t}})\right) + \mathrm{Li}\left(1 - \frac{1}{v_{t\bar{t}}}p_t'^0(1-\beta_{\bar{t}})\right)\right]$$
$$+ -F(q_1,p_t) + F(q_1,p_t') + F(q_2,p_t) - F(q_2,p_t')$$
$$- \left[\frac{3}{2} + 2\ln(\delta_s)\right]\ln\left(\frac{\mu^2}{m_t^2}\right) \ ,$$

where

$$\beta_i = \sqrt{1 - \frac{m_t^2}{(p_i^0)^2}} \ , \tag{3.60}$$

while

$$\alpha_{t\bar{t}} = \frac{1+\beta_{t\bar{t}}}{1-\beta_{t\bar{t}}} \ \text{and} \ v_{t\bar{t}} = \frac{m_t^2(\alpha_{t\bar{t}}^2 - 1)}{2(\alpha_{t\bar{t}}p_t^0 - p_t'^0)} \ . \tag{3.61}$$

The factor $\mathcal{N}_t$ is defined in Eq. (3.26), and Li_2 denotes the dilogarithm function. $\beta_{t\bar{t}}$ and $\Lambda_{t\bar{t}}$ are defined in Eq. (3.37), while, for any initial parton i and final parton f, and the function $F^{q\bar{q}}(p_i,p_f)$ can is given explicitly in Appendix C

After adding Eqs. (3.39) and (3.59), the IR poles of the virtual corrections are exactly canceled by the corresponding singularities in the soft gluon contribution and we are left with:

$$\hat{\sigma}_{s+v}^{q\bar{q}} \equiv (\hat{\sigma}_{soft}^{q\bar{q}})_{pole} + (\hat{\sigma}_{virt}^{q\bar{q}})_{IR-pole} = \frac{\alpha_s}{2\pi}\left(N - \frac{1}{N}\right)\left[-\frac{3}{2} - 2\ln(\delta_s)\right]\frac{1}{\epsilon}\hat{\sigma}_{LO}^{gg} \;,$$

(3.62)

Note that, in this section and below, we do not explicitly denote the IR poles as poles in ϵ_{IR}, since it is understood that all singularities present in $\sigma_{real}^{gg,qg}$ are of IR origin. These remaining IR poles will be canceled by the PDF counterterms as described in detail in Sec. 3.5.

3.4.1.2 Soft gluon emission: $gg \rightarrow t\bar{t}h + g$

The soft region of the $gg \rightarrow t\bar{t}h + g$ phase space is also defined by requiring that the energy of the emitted gluon satisfies Eq. (3.53). In the *soft limit* $(E_g \rightarrow 0)$, the amplitude for this process can be written as:

$$\mathcal{A}_{soft}(gg \rightarrow t\bar{t}h + g) =$$
$$T^C T^A T^B \left(\frac{p_t \cdot \epsilon^*}{p_t \cdot k} - \frac{q_1 \cdot \epsilon^*}{q_1 \cdot k}\right)\left(\mathcal{A}_{0,t}^{gg} + \mathcal{A}_{0,s}^{gg}\right) + T^C T^B T^A \left(\frac{p_t \cdot \epsilon^*}{p_t \cdot k} - \frac{q_2 \cdot \epsilon^*}{q_2 \cdot k}\right)\left(\mathcal{A}_{0,u}^{gg} - \mathcal{A}_{0,s}^{gg}\right)$$
$$- T^A T^B T^C \left(\frac{p_t' \cdot \epsilon^*}{p_t' \cdot k} - \frac{q_2 \cdot \epsilon^*}{q_2 \cdot k}\right)\left(\mathcal{A}_{0,t}^{gg} + \mathcal{A}_{0,s}^{gg}\right) - T^B T^A T^C \left(\frac{p_t' \cdot \epsilon^*}{p_t' \cdot k} - \frac{q_1 \cdot \epsilon^*}{q_1 \cdot k}\right)\left(\mathcal{A}_{0,u}^{gg} - \mathcal{A}_{0,s}^{gg}\right)$$
$$+ T^A T^C T^B \left(\frac{q_1 \cdot \epsilon^*}{q_1 \cdot k} - \frac{q_2 \cdot \epsilon^*}{q_2 \cdot k}\right)\left(\mathcal{A}_{0,t}^{gg} + \mathcal{A}_{0,s}^{gg}\right) + T^B T^C T^A \left(\frac{q_2 \cdot \epsilon^*}{q_2 \cdot k} - \frac{q_1 \cdot \epsilon^*}{q_1 \cdot k}\right)\left(\mathcal{A}_{0,u}^{gg} - \mathcal{A}_{0,s}^{gg}\right) \;,$$

(3.63)

where A, B, and C are the color indices of the external gluons, while $\epsilon^\mu(k, \lambda)$ (for $\lambda = 1, 2$) is the polarization vector of the emitted soft gluon. Moreover, in the soft region the $gg \rightarrow t\bar{t}h + g$ phase space factorizes identically to Eq. (3.56), i.e:

$$d(PS_4)(gg \rightarrow t\bar{t}h + g) \xrightarrow{soft} d(PS_3)(gg \rightarrow t\bar{t}h)d(PS_g)_{soft}$$
$$= d(PS_3)(gg \rightarrow t\bar{t}h)\frac{d^{(d-1)}k}{(2\pi)^{(d-1)}2E_g}\theta\left(\delta_s\frac{\sqrt{s}}{2} - E_g\right) \;,$$

(3.64)

68

where $d(PS_4)$ and $d(PS_3)$ have been defined in Section 3.1, while $d(PS_g)_{soft}$ denotes the integration over the phase space of the soft gluon. Since the contribution of the soft gluon is now completely factorized, we can perform the integration over $d(PS_g)_{soft}$ analytically, using dimensional regularization in $d = 4 - 2\epsilon$ to extract the soft poles that will have to cancel the corresponding singularities in Eqs. (3.49) and (3.46). The integrals that we have used to perform the integration over the phase space of the soft gluon are collected in Appendix C.

After squaring the soft amplitude $\mathcal{A}_{soft}^{gg}$, summing over the polarization of the radiated soft gluon, and integrating over the soft gluon momentum, the pole part of the parton level soft cross section reads

$$(\hat{\sigma}_{soft}^{gg})_{pole} = \int d(PS_3) \left(\int d(PS_g)_{soft} \overline{\sum} |\mathcal{A}_{soft}(gg \to t\bar{t}h + g)|^2 \right)_{pole}$$
$$= \int d(PS_3) \frac{\alpha_s}{2\pi} \mathcal{N}_t \overline{\sum} \left(C_1 \mathcal{M}_{S,\epsilon}^{(1),gg} + C_2 \mathcal{M}_{S,\epsilon}^{(2),gg} + C_3 \mathcal{M}_{S,\epsilon}^{(3),gg} \right) \quad , (3.65)$$

where C_1, C_2, and C_3 are defined in Eq. (3.45), while $\mathcal{M}_{S,\epsilon}^{(1),gg}$, $\mathcal{M}_{S,\epsilon}^{(2),gg}$, and $\mathcal{M}_{S,\epsilon}^{(3),gg}$ represent the IR pole parts of the corresponding matrix elements squared, and can be written as:

$$\mathcal{M}_{S,\epsilon}^{(1),gg} = -\mathcal{M}_{V,\epsilon}^{(1),gg} - \frac{2}{\epsilon}(1 + 4\ln(\delta_s)) \left(|\mathcal{A}_0^{nab}|^2 + |\mathcal{A}_0^{ab}|^2 \right) \quad ,$$
$$\mathcal{M}_{S,\epsilon}^{(2),gg} = -\mathcal{M}_{V,\epsilon}^{(2),gg} - \frac{16}{\epsilon}\ln(\delta_s)|\mathcal{A}_0^{ab}|^2 + \frac{2}{\epsilon} \left(|\mathcal{A}_0^{nab}|^2 + |\mathcal{A}_0^{ab}|^2 \right) \quad ,$$
$$\mathcal{M}_{S,\epsilon}^{(3),gg} = -\mathcal{M}_{V,\epsilon}^{(3),gg} + \frac{1}{\epsilon}|\mathcal{A}_0^{ab}|^2 \quad . \tag{3.66}$$

After adding the IR divergent part of the parton level virtual cross section of Eq. (3.49) we obtain:

$$\hat{\sigma}_{s+v}^{gg} \equiv (\hat{\sigma}_{soft}^{gg})_{pole} + (\hat{\sigma}_{virt}^{gg})_{IR-pole} = \frac{\alpha_s}{2\pi} \mathcal{N}_t \left[-4N\ln(\delta_s) - \frac{1}{3}(11N - 2n_{lf}) \right] \frac{1}{\epsilon}\hat{\sigma}_{LO}^{gg} \quad ,$$
$$\tag{3.67}$$

where we can see that the IR poles of the parton level virtual cross section are exactly canceled by the corresponding singularities in the parton level soft gluon emission

69

cross section. The residual divergences will be canceled by the soft+virtual part of the PDF counterterm when convoluting with the gluon PDFs as will be demonstrated in Section 3.5. The finite contribution to the parton level soft cross section is finally given by

$$(\hat{\sigma}^{gg}_{soft})_{finite} = \int d(PS_3) \left(\int d(PS_g)_{soft} \overline{\sum} |\mathcal{A}_{soft}(gg \to t\bar{t}h + g)|^2 \right)_{finite}$$

$$= \int d(PS_3) \frac{\alpha_s}{2\pi} \mathcal{N}_t \overline{\sum} \left(C_1 \mathcal{M}^{(1),gg}_S + C_2 \mathcal{M}^{(2),gg}_S + C_3 \mathcal{M}^{(3),gg}_S \right) \quad (3.68)$$

where the finite parts of the $\mathcal{M}^{(1),gg}_S$, $\mathcal{M}^{(2),gg}_S$, and $\mathcal{M}^{(3),gg}_S$ matrix element squared are explicitly given by:

$$\mathcal{M}^{(1),gg}_S = \left[-\frac{4}{3}\pi^2 + 4\Lambda_\sigma \ln(\delta_s) + 8\ln^2(\delta_s) - 2\Lambda_\sigma - 4\ln(\delta_s) \right.$$

$$\left. + \frac{1}{\beta_t} \ln\left(\frac{1+\beta_t}{1-\beta_t}\right) + \frac{1}{\beta_{\bar{t}}} \ln\left(\frac{1+\beta_{\bar{t}}}{1-\beta_{\bar{t}}}\right) \right] \left(|\mathcal{A}^{nab}_0|^2 + |\mathcal{A}^{ab}_0|^2 \right)$$

$$+ \left[(\Lambda_\sigma + 2\ln(\delta_s))(\Lambda_{\tau_1} + \Lambda_{\tau_2}) + \frac{1}{2}F(q_1, p_t) + \frac{1}{2}F(q_2, p'_t) \right] |\mathcal{A}^{nab}_0 + \mathcal{A}^{ab}_0|^2$$

$$+ \left[(\Lambda_\sigma + 2\ln(\delta_s))(\Lambda_{\tau_3} + \Lambda_{\tau_4}) + \frac{1}{2}F(q_2, p_t) + \frac{1}{2}F(q_1, p'_t) \right] |\mathcal{A}^{nab}_0 - \mathcal{A}^{ab}_0|^2 \quad,$$

$$\mathcal{M}^{(2),gg}_S = \left\{ \frac{\bar{s}_{t\bar{t}} - 2m_t^2}{\bar{s}_{t\bar{t}}} \left[(2\Lambda_\sigma + 4\ln(\delta_s)) \frac{1}{\beta_{t\bar{t}}}\Lambda_{t\bar{t}} + \frac{1}{2}\ln^2\left(\frac{1+\beta_t}{1-\beta_t}\right) - \frac{1}{2}\ln^2\left(\frac{1+\beta_{\bar{t}}}{1-\beta_{\bar{t}}}\right) \right. \right.$$

$$+ 2\text{Li}\left(1 - \frac{\alpha_{t\bar{t}}}{v_{t\bar{t}}}p_t^0(1+\beta_t)\right) + 2\text{Li}\left(1 - \frac{\alpha_{t\bar{t}}}{v_{t\bar{t}}}p_t^0(1-\beta_t)\right)$$

$$\left. - 2\text{Li}\left(1 - \frac{1}{v_{t\bar{t}}}p_t'^0(1+\beta_{\bar{t}})\right) - 2\text{Li}\left(1 - \frac{1}{v_{t\bar{t}}}p_t'^0(1-\beta_{\bar{t}})\right) \right]$$

$$\left. - 2\Lambda_\sigma - 4\ln(\delta_s) + \frac{2}{\beta_{t\bar{t}}}\Lambda_{t\bar{t}} \right\} \left(|\mathcal{A}^{nab}_0|^2 + |\mathcal{A}^{ab}_0|^2 \right)$$

$$+ 2\left[-\frac{4}{3}\pi^2 - 2\Lambda_\sigma^2 + 8\ln^2(\delta_s) + 2(\Lambda_\sigma + 2\ln(\delta_s))(\Lambda_{\tau_1} + \Lambda_{\tau_2} + \Lambda_{\tau_3} + \Lambda_{\tau_4}) \right.$$

$$+ F(q_1, p_t) + F(q_2, p'_t) + F(q_2, p_t) + F(q_1, p'_t)$$

$$\left. - 4\Lambda_\sigma - 8\ln(\delta_s) + +\frac{2}{\beta_t}\ln\left(\frac{1+\beta_t}{1-\beta_t}\right) + \frac{2}{\beta_{\bar{t}}}\ln\left(\frac{1+\beta_{\bar{t}}}{1-\beta_{\bar{t}}}\right) \right] |\mathcal{A}^{ab}_0|^2 \quad,$$

$$\mathcal{M}^{(3),gg}_S = \frac{1}{2}\left\{ \frac{\bar{s}_{t\bar{t}} - 2m_t^2}{\bar{s}_{t\bar{t}}} \left[(2\Lambda_\sigma + 4\ln(\delta_s)) \frac{1}{\beta_{t\bar{t}}}\Lambda_{t\bar{t}} + \frac{1}{2}\ln^2\left(\frac{1+\beta_t}{1-\beta_t}\right) - \frac{1}{2}\ln^2\left(\frac{1+\beta_{\bar{t}}}{1-\beta_{\bar{t}}}\right) \right. \right.$$

$$+ 2\text{Li}\left(1 - \frac{\alpha_{t\bar{t}}}{v_{t\bar{t}}}p_t^0(1+\beta_t)\right) + 2\text{Li}\left(1 - \frac{\alpha_{t\bar{t}}}{v_{t\bar{t}}}p_t^0(1-\beta_t)\right)$$

70

$$-2\text{Li}\left(1 - \frac{1}{v_{t\bar{t}}}p_t'^0(1+\beta_{\bar{t}})\right) - 2\text{Li}\left(1 - \frac{1}{v_{t\bar{t}}}p_t'^0(1-\beta_{\bar{t}})\right)\Bigg]$$

$$- 2\Lambda_\sigma - 4\ln(\delta_s) + + \frac{1}{\beta_t}\ln\left(\frac{1+\beta_t}{1-\beta_t}\right) + \frac{1}{\beta_{\bar{t}}}\ln\left(\frac{1+\beta_{\bar{t}}}{1-\beta_{\bar{t}}}\right)\Bigg\}|\mathcal{A}_0^{ab}|^2 \quad . \qquad (3.69)$$

We note that β_i is defined in Eq. (3.60), while $\beta_{t\bar{t}}$ and $\Lambda_{t\bar{t}}$ are defined in Eq. (3.37). $\bar{s}_{t\bar{t}}$ is given in Eq. (3.47), and finally the function $F^{gg}(p_i, p_f)$ can be found in Appendix C (Eq. (C.9)).

3.4.1.3 Hard gluon emission: $q\bar{q}, gg \to t\bar{t}h + g$

The hard region of the final state gluon phase space is defined by requiring that the energy of the emitted gluon is above a given threshold. As we discussed earlier, this is expressed by the condition that

$$E_g > \delta_s \frac{\sqrt{s}}{2} \quad , \qquad (3.70)$$

for an arbitrary small *soft* cutoff δ_s, which automatically assures that $\hat{\sigma}_{hard}^{q\bar{q},gg}$ does not contain soft singularities. However, a hard gluon can still give rise to singularities when it is emitted at a small angle, i.e. *collinear*, to a massless incoming or outgoing parton. In order to isolate these divergences and compute them analytically, we further divide the hard region of the $q\bar{q}, gg \to t\bar{t}h+g$ phase space into a *hard/collinear* and a *hard/non-collinear* region, by introducing a second small *collinear* cutoff δ_c. The *hard/non-collinear* region is defined by the condition that both

$$\frac{2q_1 \cdot k}{E_g\sqrt{s}} > \delta_c \quad \text{and} \quad \frac{2q_2 \cdot k}{E_g\sqrt{s}} > \delta_c \qquad (3.71)$$

are true. The contribution from the *hard/non-collinear* region, $\hat{\sigma}_{hard/non-coll}^{q\bar{q},gg}$, is finite and we compute it numerically by using standard Monte Carlo integration techniques.

In the *hard/collinear* region, one of the conditions in Eq. (3.71) is not satisfied and the hard gluon is emitted collinear to one of the incoming partons. In this region, the initial state parton i with momentum q_i is considered to split into a hard parton i' and a collinear gluon g, $i \to i'g$, with $q_{i'} = zq_i$ and $k = (1-z)q_i$. The matrix element

71

squared for $ij \to t\bar{t}h + g$ factorizes into the Born matrix element squared and the unregulated Altarelli-Parisi splitting function $P_{ii'} = P_{ii'}^4 + \epsilon P_{ii'}'$ for $i \to i'g$, i.e.:

$$\overline{\sum}|\mathcal{A}_{real}(ij \to t\bar{t}h + g)|^2 \xrightarrow{collinear} (4\pi\alpha_s)\overline{\sum}|\mathcal{A}_0(i'j \to t\bar{t}h)|^2 \frac{2P_{ii'}(z)}{z\,s_{ig}} \quad, \tag{3.72}$$

where $P_{ii'}^4$ and $P_{ii'}'$ denote the coefficients of the $\mathcal{O}(1)$ and $\mathcal{O}(\epsilon)$ parts of $P_{ii'}$, while $s_{ig} = 2q_i \cdot k$. In the case of $q\bar{q} \to t\bar{t}h + g$, the unregulated splitting function in d dimensions is

$$P_{ii'}(z) = P_{qq}(z) = C_F\left(\frac{1 + z^2}{1 - z} - \epsilon(1 - z)\right) \tag{3.73}$$

while for the case of $gg \to t\bar{t}h + g$ the initial partons are gluons and the unregulated splitting function in d dimensions is ($P_{gg}' = 0$):

$$P_{ii'}(z) = P_{gg}(z) = 2N\left(\frac{z}{1 - z} + \frac{1 - z}{z} + z(1 - z)\right) \quad. \tag{3.74}$$

Moreover, in the collinear limit, the $ij \to t\bar{t}h + g$ phase space also factorizes as:

$$d(PS_4)(ij \to t\bar{t}h + g) \xrightarrow{collinear} d(PS_3)(i'j \to t\bar{t}h)\frac{z\,d^{(d-1)}k}{(2\pi)^{(d-1)}2E_g}\theta\left(E_g - \delta_s\frac{\sqrt{s}}{2}\right) \times$$

$$\theta\left(\cos\theta_{ig} - (1 - \delta_c)\right)$$

$$\stackrel{d=4-2\epsilon}{=} d(PS_3)(i'j \to t\bar{t}h)\frac{1}{\Gamma(1 - \epsilon)}\frac{(4\pi)^\epsilon}{16\pi^2}z\,dz\,ds_{ig}\left[(1 - z)s_{ig}\right]^{-\epsilon} \times$$

$$\theta\left(\frac{(1 - z)}{z}s'\frac{\delta_c}{2} - s_{ig}\right) \quad, \tag{3.75}$$

where $d(PS_4)$ and $d(PS_3)$ have been defined in Section 3.1, while the integration range for s_{ig} in the collinear region is given in terms of the collinear cutoff, and we have defined $s' = 2q_{i'} \cdot q_j$. The integral over the collinear gluon degrees of freedom can then be performed analytically, and this allows us to explicitly extract the collinear singularities of $\hat{\sigma}_{hard}^{q\bar{q},gg}$ [55, 71] as:

$$\hat{\sigma}_{hard/coll}^{q\bar{q},gg} = \left[\frac{\alpha_s}{2\pi}\frac{1}{\Gamma(1 - \epsilon)}\left(\frac{4\pi\mu^2}{m_t^2}\right)^\epsilon\right]\left(-\frac{1}{\epsilon}\right)\delta_c^{-\epsilon} \times$$

$$\left\{\int_0^{1-\delta_s} dz\left[\frac{(1 - z)^2}{2z}\frac{s'}{m_t^2}\right]^{-\epsilon} P_{ii'}(z)\,\hat{\sigma}_{LO}^{q\bar{q},gg}(i'j \to t\bar{t}h) + (i \leftrightarrow j)\right\} \tag{3.76}$$

As usual, these initial state collinear divergences are absorbed into the parton distribution functions as will be described in detail in Section 3.5.

3.4.1.4   The tree level processes $(q, \bar{q})g \to t\bar{t}h + (q, \bar{q})$

The extraction of the collinear singularities of $\hat{\sigma}^{qg}_{real}$ is done in the same way as described in Section 3.4.1.3 for the $q\bar{q}$ and gg initial states. In the collinear region, $\cos\theta_{iq} > 1 - \delta_c$, the initial state parton i with momentum q_i is considered to split into a hard parton i' and a collinear quark q, $i \to i'q$, with $q_{i'} = zq_i$ and $k = (1-z)q_i$. The matrix element squared for $ij \to t\bar{t}h + q$ factorizes into the unregulated Altarelli-Parisi splitting functions in d dimensions: $P_{ii'} = P^4_{ii'} + \epsilon P'_{ii'}$ and the corresponding Born matrix elements squared. The $ij \to t\bar{t}h + q$ phase space factorizes into the $i'j \to t\bar{t}h$ phase space and the phase space of the collinear quark. As a result, after integrating over the phase space of the collinear quark, the collinear singularity of $\hat{\sigma}^{qg}_{real}$ can be extracted as:

$$
\hat{\sigma}^{qg}_{coll} = \left[\frac{\alpha_s}{2\pi}\frac{1}{\Gamma(1-\epsilon)}\left(\frac{4\pi\mu^2}{m_t^2}\right)^\epsilon\right]\left(-\frac{1}{\epsilon}\right)\delta_c^{-\epsilon}\int_0^1 dz \left[\frac{(1-z)^2}{2z}\frac{s'}{m_t^2}\right]^{-\epsilon} \times
$$
$$
[P_{qg}(z)\,\hat{\sigma}^{gg}_{LO}(g(q_{1'})g(q_2) \to t\bar{t}h) + P_{gq}(z)\,\hat{\sigma}^{q\bar{q}}_{LO}(q(q_1)\bar{q}(q_{2'}) \to t\bar{t}h)] \quad . \ (3.77)
$$

The collinear radiation of an antiquark in $\bar{q}g \to t\bar{t}h + \bar{q}$ is treated analogously. In the case of $(q, \bar{q})g \to t\bar{t}h + (q, \bar{q})$ we have two possible splittings: $(q, \bar{q}) \to g(q, \bar{q})$ and $g \to q\bar{q}$. The $O(1)$ and $O(\epsilon)$ parts of the corresponding splitting functions are:

$$
P^4_{gq}(z) = \frac{1}{2}\left(z^2 + (1-z)^2\right) \ ,
$$
$$
P'_{gq}(z) = -z(1-z) \ ,
$$
$$
P^4_{qg}(z) = \frac{N^2-1}{2N}\left(\frac{1+(1-z)^2}{z}\right) \ ,
$$
$$
P'_{qg}(z) = -\frac{N^2-1}{2N}z \ . \tag{3.78}
$$

Again, these initial state collinear divergences are absorbed into the parton distribution functions as will be described in detail in Section 3.5.

73

3.4.2 Phase Space Slicing method with one cutoff

An alternative way of isolating both soft and collinear singularities is to divide the phase space for the radiated parton into only two regions, according to whether all partons can be resolved (the *hard* region) or not (the *infrared* or *ir* region). In the case of $q\bar{q}, gg \to t\bar{t}h + g$, the *hard* and *ir* regions are defined according to whether the final state gluon can be resolved. The emitted gluon is considered as not resolved, and therefore part of the *ir* cross section, when

$$s_{ig} = 2p_i \cdot k < s_{min} \quad (p_i = q_1, q_2, p_t, p'_t) \ , \tag{3.79}$$

for an arbitrary small cutoff s_{min}, with k the final state gluon momentum which becomes soft or collinear. In the case of $(q, \bar{q})g \to t\bar{t}h + (q, \bar{q})$, the emitted (anti)quark is considered as not resolved, and therefore part of the *ir* cross section, when

$$s_{iq} = 2p_i \cdot k < s_{min} \quad (p_i = q_1, q_2, p_t, p'_t) \ , \tag{3.80}$$

with k the final state (anti)quark momentum which becomes collinear. The partonic real cross sections can then be written as the sum of two terms ($ij = q\bar{q}, gg, qg$):

$$\hat{\sigma}^{ij}_{real} = \hat{\sigma}^{ij}_{ir} + \hat{\sigma}^{ij}_{hard} \ , \tag{3.81}$$

where $\hat{\sigma}^{ij}_{ir}$ includes the IR singularities, both soft and collinear, while $\hat{\sigma}^{ij}_{hard}$ is finite. Following the general idea of PSS, we calculate $\hat{\sigma}^{ij}_{ir}$ analytically, while we evaluate $\hat{\sigma}^{ij}_{hard}$ numerically, using standard Monte Carlo integration techniques. Both $\hat{\sigma}^{ij}_{ir}$ and $\hat{\sigma}^{ij}_{hard}$ depend on the cutoff s_{min}, but the hadronic real cross section, σ_{real}, is cutoff independent after mass factorization, as will be shown in Section 3.5.

3.4.2.1 Real corrections to $q\bar{q} \to t\bar{t}h + g$

In order to calculate $\hat{\sigma}^{q\bar{q}}_{ir}$ we apply and generalize the formalism developed in Refs. [56, 57, 58, 30] as follows.

(a) We consider the crossed process $h \rightarrow q\bar{q}t\bar{t}+g$ which is obtained from $q\bar{q} \rightarrow t\bar{t}h+g$ by crossing all the initial state colored partons to the final state, while crossing the Higgs boson to the initial state. For a systematic extraction of the IR singularities within the one-cutoff method, we organize the amplitude for $h \rightarrow q\bar{q}t\bar{t} + g$, $\mathcal{A}^{h \rightarrow q\bar{q}t\bar{t}g}$, in terms of colored ordered amplitudes [72]. Using the color decomposition:

$$T^a_{c_1c_2} T^a_{c_3c_4} = \frac{1}{2}\left(\delta_{c_1c_4}\delta_{c_3c_2} - \frac{1}{N}\delta_{c_1c_2}\delta_{c_3c_4} \right) , \tag{3.82}$$

we write $\mathcal{A}^{h \rightarrow q\bar{q}t\bar{t}g}$ as the sum of four color ordered amplitudes $\mathcal{A}_1^{q\bar{q}}, \ldots, \mathcal{A}_4^{q\bar{q}}$ as follows:

$$\mathcal{A}^{h \rightarrow q\bar{q}t\bar{t}g} = ig_s\delta_{f_q f_{\bar{q}}}\delta_{f_t f_{\bar{t}}}\frac{1}{2}\left(\delta_{c_t c_{\bar{q}}} T^a_{c_q c_{\bar{t}}} \mathcal{A}_1^{q\bar{q}}(p_t, p_t', q_1, q_2, k) + T^a_{c_t c_{\bar{q}}}\delta_{c_q c_{\bar{t}}} \mathcal{A}_2^{q\bar{q}}(p_t, p_t', q_1, q_2, k) \right.$$
$$\left. - \frac{1}{N}\delta_{c_t c_{\bar{t}}} T^a_{c_q c_{\bar{q}}} \mathcal{A}_3^{q\bar{q}}(p_t, p_t', q_1, q_2, k) - \frac{1}{N} T^a_{c_t c_{\bar{t}}}\delta_{c_q c_{\bar{q}}} \mathcal{A}_4^{q\bar{q}}(p_t, p_t', q_1, q_2, k) \right) , \tag{3.83}$$

where $g_s = \sqrt{4\pi\alpha_s}$, while $(f_q, f_{\bar{q}}, f_t, f_{\bar{t}})$ and $(c_q, c_{\bar{q}}, c_t, c_{\bar{t}})$ denote the flavor and color indices of the various outgoing quarks. The amplitudes $\mathcal{A}_i^{q\bar{q}}(p_t, p_t', q_1, q_2, k)$ (for $i = 1, 2, 3, 4$) correspond to the four possible independent color structures that arise in the $h \rightarrow q\bar{q}t\bar{t} + g$ process, and each $\mathcal{A}_i^{q\bar{q}}$ contains terms describing the emission of the gluon from a different pair of external quarks. We give the explicit expressions for the $\mathcal{A}_i^{q\bar{q}}$ amplitudes in Appendix D. Due to this decomposition, the partonic cross section for $h \rightarrow q\bar{q}t\bar{t} + g$ can be written in a very compact form:

$$\hat{\sigma}^{h \rightarrow q\bar{q}t\bar{t}g} = \int d(PS_5)\overline{\sum}|\mathcal{A}^{h \rightarrow q\bar{q}t\bar{t}g}|^2 , \tag{3.84}$$

with

$$\overline{\sum}|\mathcal{A}^{h \rightarrow q\bar{q}t\bar{t}g}|^2 = \left(\frac{g_s^2 N}{2}\right)\left(\frac{N^2 - 1}{4}\right)\overline{\sum}\left\{|\mathcal{A}_1^{q\bar{q}}|^2 + |\mathcal{A}_2^{q\bar{q}}|^2 + \right. \tag{3.85}$$
$$\left. \frac{1}{N^2}\left[-2|\mathcal{A}_3^{q\bar{q}} + \mathcal{A}_4^{q\bar{q}}|^2 + |\mathcal{A}_3^{q\bar{q}}|^2 + |\mathcal{A}_4^{q\bar{q}}|^2\right]\right\} .$$

75

(b) Using the one-cutoff PSS method and the factorization properties of both the color ordered amplitudes $\mathcal{A}_i^{q\bar{q}}$ and the gluon phase space in the soft/collinear limit, we extract the IR singularities of $\hat{\sigma}^{h \to q\bar{q}t\bar{t}g}$ into $\hat{\sigma}_{soft}^{h \to q\bar{q}t\bar{t}g}$ and $\hat{\sigma}_{coll}^{h \to q\bar{q}t\bar{t}g}$ as follows:

$$\hat{\sigma}^{h \to q\bar{q}t\bar{t}g} \xrightarrow{soft} \hat{\sigma}_{soft}^{h \to q\bar{q}t\bar{t}g} = \int d(PS_4) d(PS_g)_{soft} \overline{\sum} |\mathcal{A}_{soft}^{h \to q\bar{q}t\bar{t}g}|^2 \quad , \quad (3.86)$$

$$\hat{\sigma}^{h \to q\bar{q}t\bar{t}g} \xrightarrow{collinear} \hat{\sigma}_{coll}^{h \to q\bar{q}t\bar{t}g} = \int d(PS_4) d(PS_g)_{coll} \overline{\sum} |\mathcal{A}_{coll}^{h \to q\bar{q}t\bar{t}g}|^2 \quad , \quad (3.87)$$

where we denote by $d(PS_g)_{soft}$ $(d(PS_g)_{coll})$ the phase space of the gluon in the soft (collinear) limit, while $\overline{\sum} |\mathcal{A}_{soft}^{h \to q\bar{q}t\bar{t}g}|^2$ $(\overline{\sum} |\mathcal{A}_{coll}^{h \to q\bar{q}t\bar{t}g}|^2)$ represents the soft (collinear) limit of Eq.(3.85). The explicit calculation of $\hat{\sigma}_{soft,coll}^{h \to q\bar{q}t\bar{t}g}$ is described in detail below. The factorization of soft and collinear singularities for color ordered amplitudes has been discussed in the literature mainly for the leading color terms $(\mathcal{O}(N))$. For our application of the one-cutoff PSS method, we will have to extend these results to the subleading color terms $(\mathcal{O}(1/N))$.

(c) Finally, the IR singular contribution $\hat{\sigma}_{ir}$ in Eq. (3.81) consists of two terms:

$$\hat{\sigma}_{ir} = \hat{\bar{\sigma}}_{ir}^{q\bar{q}} + \hat{\sigma}_{crossing}^{q\bar{q}} \ . \quad (3.88)$$

As described in detail below, $\hat{\bar{\sigma}}_{ir}^{q\bar{q}}$ is obtained by crossing q and $\bar{q}$ to the initial state and h to the final state in the sum of $\hat{\sigma}_{soft}^{h \to q\bar{q}t\bar{t}g}$ and $\hat{\sigma}_{coll}^{h \to q\bar{q}t\bar{t}g}$, while $\hat{\sigma}_{crossing}^{q\bar{q}}$ corrects for the difference between the collinear gluon radiation from initial and final state partons [57], as will be discussed in detail in Sec. 3.5. As explicitly shown below, the IR singularities of $\hat{\sigma}_{virt}^{q\bar{q}}$ of Sec. 3.3.1.3 are exactly canceled by the corresponding singularities in $\hat{\bar{\sigma}}_{ir}^{q\bar{q}}$. On the other hand, $\hat{\sigma}_{crossing}^{q\bar{q}}$ still contains collinear divergences that will be canceled by the PDF counterterms when the parton cross section is convoluted with the PDFs (see Sec. 3.5).

Soft gluon emission: $\boldsymbol{h \to q\bar{q}t\bar{t} + g}$

76

We first consider the case of soft singularities, when, in the limit of $E_g \to 0$ (soft limit), one or more $s_{ig} < s_{min}$ $(i = q, \bar{q}, t, \bar{t})$. Using the factorization properties of the color ordered amplitudes $\mathcal{A}_i^{q\bar{q}}$ in the soft limit, the amplitude squared for $h \to q\bar{q}t\bar{t} + g$ can be written as:

$$\overline{\sum}|\mathcal{A}^{h \to q\bar{q}t\bar{t}g}|^2 \xrightarrow{soft} \overline{\sum}|\mathcal{A}_{soft}^{h \to q\bar{q}t\bar{t}g}|^2 = \left(\frac{g_s^2 N}{2}\right) \overline{\sum}|\mathcal{A}_{LO}^{h \to q\bar{q}t\bar{t}}|^2 \left\{ f_{q\bar{t}}(g) + f_{\bar{q}t}(g) \right. \quad (3.89)$$

$$\left. \frac{1}{N^2} \left[f_{t\bar{t}}(g) + f_{q\bar{q}}(g) - 2\left(f_{qt}(g) - f_{q\bar{t}}(g) - f_{\bar{q}t}(g) + f_{\bar{q}\bar{t}}(g)\right)\right] \right\} ,$$

where, for any pair of partons (a, b) excluding the soft gluon, the soft functions $f_{ab}(g)$ are defined as:

$$f_{ab}(g) \equiv \frac{4s_{ab}}{s_{ag}s_{bg}} - \frac{4m_a^2}{s_{ag}^2} - \frac{4m_b^2}{s_{bg}^2} , \qquad (3.90)$$

and, as before (see Eq. (3.36)),

$$s_{ij} \equiv 2p_i \cdot p_j ,$$

both for massless and massive quarks. $\mathcal{A}_{LO}^{h \to q\bar{q}t\bar{t}}$ is the tree level amplitude for the process $h \to q\bar{q}t\bar{t}$ as given by Eq. (D.1). We note that Eq. (3.89) corresponds to the factorization property expressed in Eq. (3.54). Since, in the soft limit, the $h \to q\bar{q}t\bar{t} + g$ phase space also factorizes, in analogy to Eq. (3.56), we can integrate out the soft gluon degrees of freedom and obtain the soft gluon part of the cross section for $h \to q\bar{q}t\bar{t} + g$ as:

$$\hat{\sigma}_{soft}^{h \to q\bar{q}t\bar{t}g} = \int d(PS_4) \overline{\sum}|\mathcal{A}_{LO}^{h \to q\bar{q}t\bar{t}}|^2 \left\{ \tau_4 + \tau_3 - \frac{1}{N^2} \left[S_{t\bar{t}} + S_{q\bar{q}} - 2\left(\tau_1 - \tau_4 - \tau_3 + \tau_2\right)\right] \right\} ,$$

where, for any pair of quarks (a, b), the integrated soft functions S_{ab} are defined as:

$$S_{ab} = \frac{g_s^2 N}{2} \int d(PS_g)_{soft}(a, b, g) f_{ab}(g) . \qquad (3.91)$$

In the one-cutoff PSS method, the explicit form of the soft gluon phase space integral is given by [58]:

$$d(PS_g)_{soft}(a, b, g) = \frac{(4\pi)^\epsilon}{16\pi^2} \frac{\lambda^{\left(\epsilon - \frac{1}{2}\right)}}{\Gamma(1 - \epsilon)} \left[s_{ag}s_{bg}s_{ab} - m_b^2 s_{ag}^2 - m_a^2 s_{bg}^2\right]^{-\epsilon} ds_{ag}ds_{bg} \times$$

$$\theta(s_{min} - s_{ag})\theta(s_{min} - s_{bg}) , \qquad (3.92)$$

77

where

$$\lambda = s_{ab}^2 - 4m_a^2 m_b^2 \,, \tag{3.93}$$

and the integration boundaries for s_{ag} and s_{bg} vary accordingly to whether a and b are massive or massless quarks (see Ref. [58] for more details).

The explicit form of the integrated soft functions S_{ab} is obtained by carrying out the integration in Eq. (3.91). When both partons a and b are massless S_{ab} is simply given by [56]:

$$S_{ab} = \frac{\alpha_s}{2\pi} N \frac{1}{\Gamma(1-\epsilon)} \left(\frac{4\pi\mu^2}{s_{min}} \right)^\epsilon \left(\frac{s_{ab}}{s_{min}} \right)^\epsilon \frac{1}{\epsilon^2} \,. \tag{3.94}$$

When one parton is massive and the other is massless, the function S_{ab} has the form [58]:

$$
\begin{aligned}
S_{ab} &= \frac{\alpha_s}{2\pi} N \frac{1}{\Gamma(1-\epsilon)} \left(\frac{4\pi\mu^2}{s_{min}} \right)^\epsilon \left(\frac{s_{ab}}{s_{min}} \right)^\epsilon \times \\
&\quad \left\{ \frac{1}{\epsilon^2} \left[1 - \frac{1}{2} \left(\frac{s_{ab}}{m_t^2} \right)^\epsilon \right] + \frac{1}{2\epsilon} \left(\frac{s_{ab}}{m_t^2} \right)^\epsilon - \frac{1}{2}\zeta(2) + \frac{m_t^2}{s_{ab}} \right\} \\
&= \frac{\alpha_s}{2\pi} N \frac{1}{\Gamma(1-\epsilon)} \left(\frac{4\pi\mu^2}{s_{min}} \right)^\epsilon \times \\
&\quad \left\{ \frac{1}{2\epsilon^2} + \frac{1}{2\epsilon} + \frac{1}{2\epsilon} \ln\left(\frac{m_t^2}{s_{min}} \right) \right. \\
&\quad \left. + \frac{1}{4} \ln^2\left(\frac{m_t^2}{s_{min}} \right) - \frac{1}{2} \ln^2\left(\frac{s_{ab}}{m_t^2} \right) + \frac{1}{2} \ln\left(\frac{s_{ab}}{m_t^2} \right) + \frac{1}{2} \ln\left(\frac{s_{ab}}{s_{min}} \right) - \frac{1}{2}\zeta(2) + \frac{m_t^2}{s_{ab}} \right\} \,.
\end{aligned}
\tag{3.95}
$$

Lastly, when both partons are massive, i.e. when $a=t$ and $b=\bar{t}$, the integrated soft function $S_{t\bar{t}}$ is [58]:

$$S_{t\bar{t}} = \frac{\alpha_s}{2\pi} N \frac{1}{\Gamma(1-\epsilon)} \left(\frac{4\pi\mu^2}{s_{min}} \right)^\epsilon \frac{m_t^2}{\sqrt{\lambda_{t\bar{t}}}} \left(J_s \frac{1}{\epsilon} + J_a + J_b \right) \,, \tag{3.96}$$

where we have defined:

$$\frac{m_t^2}{\sqrt{\lambda_{t\bar{t}}}} J_s = 1 - \frac{s_{t\bar{t}}}{(2m_t^2 + s_{t\bar{t}})\beta_{t\bar{t}}} \Lambda_{t\bar{t}} \,,$$

$$J_a = J_s \ln\left(\frac{\tau_+^2 \lambda_{t\bar{t}}}{s_{min} m_t^2} \right) \,,$$

78

$$J_b = (\tau_+ - \tau_-)\left[1 - 2\ln(\tau_+ - \tau_-) - \ln(\tau_+)\right]$$
$$+ \left(\frac{\tau_+ + \tau_-}{2}\right)\left[\ln\left(\frac{\tau_+}{\tau_-}\right)(1 + 2\ln(\tau_+ - \tau_-))\right.$$
$$+ \left.\mathrm{Li}_2\left(1 - \frac{\tau_+}{\tau_-}\right) - \mathrm{Li}_2\left(1 - \frac{\tau_-}{\tau_+}\right)\right] + 1 + \tau_-\tau_+$$
$$+ (\tau_- + \tau_+)\left[-1 - \ln(\tau_+)\ln(\tau_-) + \frac{1}{2}\ln^2(\tau_+)\right] \quad, \tag{3.97}$$

$\beta_{t\bar{t}}$ and $\Lambda_{t\bar{t}}$ are defined in Eq. (3.37) while $\lambda_{t\bar{t}}$ and $\tau_\pm$ are given by:

$$\lambda_{t\bar{t}} \equiv s_{t\bar{t}}^2 - 4m_t^4 \quad,$$
$$\tau_\pm = \frac{s_{t\bar{t}}}{2m_t^2} \pm \sqrt{\left(\frac{s_{t\bar{t}}}{2m_t^2}\right)^2 - 1} \quad. \tag{3.98}$$

Finally, using Eqs. (3.91)-(3.92) and the expressions for the soft integrals, we can derive the complete form of $\hat{\sigma}_{soft}^{h \to q\bar{q}t\bar{t}g}$:

$$\hat{\sigma}_{soft}^{h \to q\bar{q}t\bar{t}g} = \frac{\alpha_s}{2\pi}\frac{1}{\Gamma(1-\epsilon)}\left(\frac{4\pi\mu^2}{m_t^2}\right)^\epsilon \int d(PS_4)\overline{\sum}|\mathcal{A}_{LO}^{h \to q\bar{q}t\bar{t}}|^2\left\{\frac{\tilde{X}_{-2}^{q\bar{q},s}}{\epsilon^2} + \frac{\tilde{X}_{-1}^{q\bar{q},x}}{\epsilon} + N\tilde{C}_1^{q\bar{q},s} + \frac{\tilde{C}_2^{q\bar{q},s}}{N}\right\} \quad, \tag{3.99}$$

where

$$\tilde{X}_{-2}^{q\bar{q},s} = \left(N - \frac{1}{N}\right) \quad,$$
$$\tilde{X}_{-1}^{q\bar{q},s} = N\left[1 + 2\ln\left(\frac{m_t^2}{s_{min}}\right)\right] - \frac{1}{N}\left[\ln\left(\frac{s}{s_{min}}\right) + \ln\left(\frac{m_t^2}{s_{min}}\right) + 1 - \frac{s_{t\bar{t}}}{(2m_t^2 + s_{t\bar{t}})\beta_{t\bar{t}}}\Lambda_{t\bar{t}}\right] \quad,$$
$$\tilde{C}_1^{q\bar{q},s} = 2\ln^2\left(\frac{m_t^2}{s_{min}}\right) + \ln\left(\frac{m_t^2}{s_{min}}\right) - \frac{1}{2}\ln^2\left(\frac{\tau_4}{m_t^2}\right) - \frac{1}{2}\ln^2\left(\frac{\tau_3}{m_t^2}\right) + \ln\left(\frac{\tau_4\tau_3}{m_t^2 s_{min}}\right)$$
$$-\zeta(2) + m_t^2\left(\frac{1}{\tau_4} + \frac{1}{\tau_3}\right) \quad, \tag{3.100}$$
$$\tilde{C}_2^{q\bar{q},s} = -\left[\frac{1}{2}\ln^2\left(\frac{m_t^2}{s_{min}}\right) + \ln\left(\frac{m_t^2}{s_{min}}\right)\left(\ln\left(\frac{s}{s_{min}}\right) + 1 - \frac{s_{t\bar{t}}}{(2m_t^2 + s_{t\bar{t}})\beta_{t\bar{t}}}\Lambda_{t\bar{t}}\right)\right.$$
$$+\frac{1}{2}\ln^2\left(\frac{s}{s_{min}}\right) + \frac{m_t^2}{\sqrt{\lambda_{t\bar{t}}}}(J_a + J_b) + \ln^2\left(\frac{\tau_1}{m_t^2}\right) - \ln^2\left(\frac{\tau_4}{m_t^2}\right) - \ln^2\left(\frac{\tau_3}{m_t^2}\right)$$
$$+\ln^2\left(\frac{\tau_2}{m_t^2}\right) - 2\ln\left(\frac{\tau_1\tau_2}{\tau_3\tau_4}\right) - 2m_t^2\left(\frac{1}{\tau_1} - \frac{1}{\tau_4} - \frac{1}{\tau_3} + \frac{1}{\tau_2}\right)\right] \quad,$$

where $\beta_{t\bar{t}}$ and $\Lambda_{t\bar{t}}$ are defined in Eq. (3.37) and the functions J_a and J_b are given in Eq. (3.97).

<u>Collinear gluon emission: $\boldsymbol{h \to q\bar{q}t\bar{t} + g}$</u>

In the collinear limit when an external massless quark (i) and a hard gluon become collinear and cluster to form a new parton (i') $(i + g \to i'$, with collinear kinematics: $p_i = zp_{i'}$ and $k = (1-z)p_{i'}$), the color ordered amplitudes factorize and the amplitude squared for $h \to q\bar{q}t\bar{t} + g$ can be written as:

$$\overline{\sum}|\mathcal{A}^{h\to q\bar{q}t\bar{t}g}|^2 \overset{collinear}{\longrightarrow} \overline{\sum}|\mathcal{A}_{coll}^{h\to q\bar{q}t\bar{t}g}|^2 = \left(\frac{g_s^2 N}{2}\right)\overline{\sum}|\mathcal{A}_{LO}^{h\to q\bar{q}t\bar{t}}|^2 \left\{ f_{\bar{t}}^{qg\to q} + f_t^{\bar{q}g\to\bar{q}} \right.$$
$$\left. - \frac{1}{N^2}\left[f_{\bar{q}}^{qg\to q} + f_q^{\bar{q}g\to\bar{q}} - 2\left(f_t^{qg\to q} - f_{\bar{t}}^{qg\to q} - f_t^{\bar{q}\to\bar{q}} + f_{\bar{t}}^{\bar{q}g\to\bar{q}}\right)\right] \right\} . \quad (3.101)$$

The collinear functions $f_j^{ig\to i'}$ contain the collinear singularity and are proportional to the Altarelli-Parisi splitting function for $ig \to i'$ (see Eq. (3.73)), i.e.:

$$f_j^{ig\to i'} \equiv \frac{2}{s_{ig}}\left(\frac{1+z^2}{1-z} - \epsilon(1-z)\right) . \quad (3.102)$$

Using this definition, we can see that Eq. (3.101) is equivalent to Eq. (3.72), although q and $\bar{q}$, the massless quarks, are now considered as final state quarks. The reason why we use a more involved expression is because this allows us to match the collinear and soft regions of the gluon phase space in a very natural way, as will be explained in the following. In the same spirit, the lower index j of the collinear functions $f_j^{ig\to i'}$ keeps track of which color ordered amplitude a given collinear pole comes from. Although seemingly useless at this stage, this will be crucial in deriving Eqs. (3.103) and (3.104), where the integration over the collinear region of the gluon phase space is performed in such a way to avoid to overlap with the soft gluon phase space integration in Eqs. (3.91) and (3.91). Finally, we note that there is no $f_{\bar{t}}^{tg\to t}$ or $f_t^{\bar{t}g\to\bar{t}}$ in Eq. (3.101) since the gluon emission from a massive quark does not give origin to collinear singularities.

In the collinear limit, the $h \to q\bar{q}t\bar{t} + g$ phase space also factorizes, in complete analogy to Eq. (3.75), provided the obvious changes between initial and final state partons are taken into account. Therefore, we can integrate out analytically the collinear gluon degrees of freedom and obtain the collinear part of the partonic cross section for $h \to q\bar{q}t\bar{t} + g$ as:

$$\hat{\sigma}_{coll}^{h \to q\bar{q}t\bar{t}g} = \int d(PS_4)\overline{\sum}|\mathcal{A}_{LO}^{h \to q\bar{q}t\bar{t}}|^2 \left\{ C_{q\bar{t}} + C_{\bar{q}t} - \frac{1}{N^2}\left[C_{q\bar{q}} - 2\left(C_{qt} - C_{q\bar{t}} - C_{\bar{q}t} + C_{q\bar{t}}\right)\right] \right\} ,$$
(3.103)

where, for any pair of quarks (i, j), the integrated collinear functions C_{ij} are defined as:

$$C_{ij} = \left(\frac{g_s^2 N}{2}\right)\int d(PS_g)_{coll}(i, j, z)f_j^{ig \to i'}(z) = -\left(\frac{\alpha_s N}{2\pi}\right)\frac{1}{\Gamma(1-\epsilon)}\left(\frac{4\pi\mu^2}{s_{min}}\right)^\epsilon \frac{1}{\epsilon}I_{ig \to i'}(z_1, z_2) .$$
(3.104)

The phase space of the collinear gluon can be written as:

$$d(PS_g)_{coll}(i, j, z) = \frac{(4\pi)^\epsilon}{16\pi^2}\frac{1}{\Gamma(1-\epsilon)}s_{ig}^{-\epsilon}ds_{ig}[z(1-z)]^{-\epsilon}dz\,\theta(s_{min} - s_{ig}) ,$$
(3.105)

and the integration boundaries on z are defined by the requirement that only one s_{ig} verifies the condition $s_{ig} < s_{min}$. This is necessary in order to avoid overlapping with the region of phase space where the gluon is soft (see Eq. (3.91)), and it is easily translated into an upper bound on the z integration, thanks to the structure of Eqs. (3.91) and (3.103). In fact, each term in Eqs. (3.91) and (3.103) depends on only two invariants, s_{ig} and s_{jg}, and each term in $\hat{\sigma}_{coll}^{h \to q\bar{q}t\bar{t}h}$ corresponds to an analogous term in $\hat{\sigma}_{soft}^{h \to q\bar{q}t\bar{t}g}$ (except that $C_{t\bar{t}}$ is missing since there is no collinear emission from t and $\bar{t}$). Therefore, for each C_{ij} we only need to require that when $s_{ig} < s_{min}$:

$$s_{jg} = (1-z)s'_{ij} > s_{min} \longrightarrow z < 1 - \frac{s_{min}}{s'_{ij}} = 1 - z_2 .$$
(3.106)

The lower bound on z is not constrained and the integration starts at $z_1 = 0$. For sake of simplicity, and since this does not give origin to ambiguities, in the following we will denote the s'_{ij} invariants in Eq. (3.106) by s_{ij}. Finally, when the integration over

81

the collinear gluon degrees of freedom is performed, one finds that the $I_{ig \to i'}(z_1, z_2)$ functions in Eq. (3.104) are of the form [56]:

$$I_{ig \to i'}(z_1, z_2) = \left[\left(\frac{z_2^{-\epsilon} - 1}{\epsilon} \right) - \frac{3}{4} + \left(\frac{\pi^2}{6} - \frac{7}{4} \right) \epsilon \right] + O(\epsilon^2) \ . \tag{3.107}$$

When $i = q, \bar{q}$ and $j = t, \bar{t}$, i.e. when one quark is massless and the other is massive, the integrated collinear functions C_{ij} are given by:

$$C_{ij} = - \left(\frac{\alpha_s N}{2\pi} \right) \frac{1}{\Gamma(1-\epsilon)} \left(\frac{4\pi\mu^2}{s_{min}} \right)^\epsilon \left\{ \left[\ln \left(\frac{s_{ij}}{s_{min}} \right) - \frac{3}{4} \right] \frac{1}{\epsilon} + \frac{1}{2} \ln^2 \left(\frac{s_{ij}}{s_{min}} \right) \right. \tag{3.108}$$
$$\left. + \frac{\pi^2}{6} - \frac{7}{4} + O(\epsilon) \right] \ ,$$

while when both $i, j = q, \bar{q}$, i.e. when both quarks are massless,

$$C_{q\bar{q}} = - \left(\frac{\alpha_s N}{2\pi} \right) \frac{1}{\Gamma(1-\epsilon)} \left(\frac{4\pi\mu^2}{s_{min}} \right)^\epsilon \left\{ \left[2 \ln \left(\frac{s}{s_{min}} \right) - \frac{3}{2} \right] \frac{1}{\epsilon} + \ln^2 \left(\frac{s}{s_{min}} \right) \right. \tag{3.109}$$
$$\left. + \frac{\pi^2}{3} - \frac{7}{2} + O(\epsilon) \right] \ .$$

Using these results, we can finally explicitly write the partonic cross section for collinear gluon radiation as follows:

$$\hat{\sigma}_{coll}^{h \to q\bar{q}t\bar{t}g} = \left(\frac{\alpha_s}{2\pi} \right) \frac{1}{\Gamma(1-\epsilon)} \left(\frac{4\pi\mu^2}{m_t^2} \right)^\epsilon \int d(PS_4) \overline{\sum} |\mathcal{A}_{LO}^{h \to q\bar{q}t\bar{t}}|^2$$
$$\times \left\{ \frac{\tilde{X}_{-1}^{q\bar{q},c}}{\epsilon} + N\tilde{C}_1^{q\bar{q},c} + \frac{\tilde{C}_2^{q\bar{q},c}}{N} \right\} \ , \tag{3.110}$$

where

$$\tilde{X}_{-1}^{q\bar{q},c} = N \left[\frac{3}{2} - \ln \left(\frac{\tau_4}{s_{min}} \right) - \ln \left(\frac{\tau_3}{s_{min}} \right) \right] \tag{3.111}$$
$$+ \frac{1}{N} \left[-\frac{3}{2} + 2 \ln \left(\frac{s}{s_{min}} \right) - 2 \ln \left(\frac{\tau_1 \tau_2}{\tau_4 \tau_3} \right) \right] \ ,$$
$$\tilde{C}_1^{q\bar{q},c} = - \ln \left(\frac{m_t^2}{s_{min}} \right) \left(\ln \left(\frac{\tau_4}{s_{min}} \right) + \ln \left(\frac{\tau_3}{s_{min}} \right) - \frac{3}{2} \right)$$
$$- \frac{1}{2} \ln^2 \left(\frac{\tau_4}{s_{min}} \right) - \frac{1}{2} \ln^2 \left(\frac{\tau_3}{s_{min}} \right) + \frac{7}{2} - \frac{\pi^2}{3} \ ,$$
$$\tilde{C}_2^{q\bar{q},c} = \ln^2 \left(\frac{s}{s_{min}} \right) - \ln^2 \left(\frac{\tau_1}{s_{min}} \right) + \ln^2 \left(\frac{\tau_4}{s_{min}} \right) + \ln^2 \left(\frac{\tau_3}{s_{min}} \right) - \ln^2 \left(\frac{\tau_2}{s_{min}} \right)$$
$$+ \ln \left(\frac{m_t^2}{s_{min}} \right) \left(-\frac{3}{2} + 2 \ln \left(\frac{s}{s_{min}} \right) - 2 \ln \left(\frac{\tau_1 \tau_2}{\tau_4 \tau_3} \right) \right) + \frac{\pi^2}{3} - \frac{7}{2} \ .$$

82

IR-singular gluon emission: complete result for $\hat{\boldsymbol{\sigma}}_{ir}^{q\bar{q}}$

As already described in the beginning of Sec. 3.4.2, the partonic cross section for the IR-singular real gluon radiation for the process $q\bar{q} \to t\bar{t}h$ using the one-cutoff PSS method is given by

$$
\begin{aligned}
\hat{\sigma}_{ir}^{q\bar{q}} &= \hat{\bar{\sigma}}_{ir}^{q\bar{q}} + \hat{\sigma}_{crossing}^{q\bar{q}} \\
&= \left[\hat{\sigma}_{soft}^{h\to q\bar{q}t\bar{t}g} + \hat{\sigma}_{coll}^{h\to q\bar{q}t\bar{t}g} \right]_{crossed} + \hat{\sigma}_{crossing}^{q\bar{q}} \ .
\end{aligned} \tag{3.112}
$$

Note that crossing $\hat{\sigma}_{soft}^{h\to q\bar{q}t\bar{t}g}$ and $\hat{\sigma}_{coll}^{h\to q\bar{q}t\bar{t}g}$ only implies the interchange of the momenta of the quark and antiquark, since particle and antiparticle interchange under crossing. In the case of soft gluon emission this can be easily verified by comparing Eq. (3.54) with Eq. (3.89), after flipping helicities and momenta of the crossed particles. For collinear gluon emission, the crossing is complicated by the difference between initial and final state collinear radiation. Using $\hat{\sigma}_{soft,coll}^{h\to q\bar{q}t\bar{t}g}$ in Eqs. (3.99) and (3.110), $\hat{\sigma}_{ir}^{q\bar{q}}$ can be explicitly written as:

$$
\hat{\sigma}_{ir}^{q\bar{q}} = \left(\frac{\alpha_s}{2\pi}\right) \mathcal{N}_t \int d(PS_3) \overline{\sum} |\mathcal{A}_{LO}^{q\bar{q}}|^2 \left\{ \frac{\tilde{X}_{-2}^{q\bar{q},ir}}{\epsilon^2} + \frac{\tilde{X}_{-1}^{q\bar{q},ir}}{\epsilon} + \tilde{C}_1^{q\bar{q},ir} N + \tilde{C}_2^{q\bar{q},ir} \frac{1}{N} \right\} \tag{3.113}
$$

where

$$
\tilde{X}_{-2}^{q\bar{q},ir} = -X_{-2}^{q\bar{q},virt} \ , \tag{3.114}
$$

$$
\tilde{X}_{-1}^{q\bar{q},ir} = -X_{-1}^{q\bar{q},virt} \ ,
$$

$$
\begin{aligned}
\tilde{C}_1^{q\bar{q},ir} = & \ln\left(\frac{m_t^2}{s_{min}}\right) \left[-2\ln\left(\frac{\tau_2}{m_t^2}\right) - 2\ln\left(\frac{\tau_1}{m_t^2}\right) + \frac{7}{2} - \ln\left(\frac{m_t^2}{s_{min}}\right) \right] \\
& + \ln\left(\frac{\tau_2}{m_t^2}\right) + \ln\left(\frac{\tau_1}{m_t^2}\right) - \ln^2\left(\frac{\tau_2}{m_t^2}\right) - \ln^2\left(\frac{\tau_1}{m_t^2}\right) \\
& + \frac{7}{2} - \frac{\pi^2}{2} - \zeta(2) + m_t^2\left(\frac{1}{\tau_2} + \frac{1}{\tau_1}\right) \ ,
\end{aligned}
$$

83

$$\tilde{C}_2^{q\bar{q},ir} = \ln\left(\frac{m_t^2}{s_{min}}\right)\left[2\ln\left(\frac{s}{m_t^2}\right) + 4\ln\left(\frac{\tau_1\tau_2}{\tau_4\tau_3}\right) - \frac{5}{2} + \ln\left(\frac{m_t^2}{s_{min}}\right) + \frac{s_{t\bar{t}}}{(2m_t^2 + s_{t\bar{t}})\beta_{t\bar{t}}}\Lambda_{t\bar{t}}\right]$$

$$+ \frac{1}{2}\ln^2\left(\frac{s}{m_t^2}\right) - 2\ln^2\left(\frac{\tau_3}{m_t^2}\right) + 2\ln^2\left(\frac{\tau_2}{m_t^2}\right) + 2\ln^2\left(\frac{\tau_1}{m_t^2}\right) - 2\ln^2\left(\frac{\tau_4}{m_t^2}\right)$$

$$- 2\ln\left(\frac{\tau_1\tau_2}{\tau_3\tau_4}\right) - 2m_t^2\left(\frac{1}{\tau_1} - \frac{1}{\tau_4} - \frac{1}{\tau_3} + \frac{1}{\tau_2}\right)$$

$$+ \frac{\pi^2}{2} - \frac{7}{2} - \frac{m_t^2}{\sqrt{\lambda_{t\bar{t}}}}\left(J_a + J_b\right) \ .$$

while $\mathcal{N}_t$ is defined in Eq. (3.26), and $\mathcal{A}_{LO}^{q\bar{q}}$ is the tree-level amplitude for $q\bar{q} \to t\bar{t}h$ in $d=4$ dimensions.

As described in detail in Ref. [57], $\hat{\sigma}_{crossing}^{q\bar{q}}$ is given by

$$\hat{\sigma}_{crossing}^{q\bar{q}} = \alpha_s \int_0^1 dz\, \hat{\sigma}_{LO}^{q\bar{q}}\left(X_{q\to q}(z) + X_{\bar{q}\to\bar{q}}(z)\right) \ , \tag{3.115}$$

where $X_{q\to q}(z)$ $(X_{\bar{q}\to\bar{q}}(z))$ is the unrenormalized crossing function of Ref. [57], which accounts for the difference between collinear gluon radiation off an initial or a final state quark (antiquark):

$$X_{q\to q}(z) = -\frac{C_F}{2\pi}\left(\frac{4\pi\mu^2}{s_{min}}\right)^\epsilon \frac{1}{\Gamma(1-\epsilon)}\left(\frac{1}{\epsilon}\right) \times$$

$$\left\{\left[\frac{3}{2} - \epsilon\left(\frac{\pi^2}{3} - \frac{7}{2}\right)\right]\delta(1-z) + \left[\frac{1+z^2}{[(1-z)^{1+\epsilon}]_+} - \epsilon(1-z)^{1-\epsilon}\right]\right\} \tag{3.116}$$

3.4.2.2 Real corrections to $gg \to t\bar{t}h + g$

In order to calculate $\hat{\sigma}_{ir}^{gg}$ we again apply and generalize the formalism developed in Refs. [56, 57, 58, 30] as follows.

(a) We consider the crossed process

$$h(p_h) \to t(p_t) + \bar{t}(p_t') + g^A(q_1) + g^B(q_2) + g^C(k) \ , \tag{3.117}$$

obtained from $gg \to t\bar{t}h + g$ by crossing all the initial state colored partons to the final state, while crossing the Higgs boson to the initial state. All colored partons are hence considered as final state partons. For a systematic extraction

84

of the IR singularities within the one-cutoff method, we organize the amplitude

for $h \to ggt\bar{t} + g$, $\mathcal{A}_{real}^{h \to ggt\bar{t}+g}$, in terms of six colored ordered amplitudes, $\mathcal{A}_{ijk}^{gg}$,

which are the coefficients of all possible permutations of the color matrices

T^A, T^B, T^C, i.e.:

$$\mathcal{A}_{real}^{h \to ggt\bar{t}+g} = \sum_{\substack{i,j,k=A,B,C \\ i \neq j \neq k}} \mathcal{A}_{ijk}^{gg} \, T^i \, T^j \, T^k \, . \tag{3.118}$$

The explicit color ordered amplitudes have very lengthy expressions and we do

not give them in this thesis. Since they are tree level amplitudes, they can

be easily obtained. In the following we will however discuss in detail their

properties in both the soft and collinear regions of the phase space of the extra

emitted gluon. In this respect, we note that decomposing $\mathcal{A}_{real}^{h \to ggt\bar{t}+g}$ in terms of

color ordered amplitudes $\mathcal{A}_{ijk}^{gg}$ allows us to write the partonic real cross section

as:

$$\hat{\sigma}_{real}^{h \to ggt\bar{t}+g} = \int d(PS_5) \overline{\sum} |\mathcal{A}_{real}^{h \to ggt\bar{t}+g}|^2 \, , \tag{3.119}$$

where

$$\overline{\sum} |\mathcal{A}_{real}^{h \to ggt\bar{t}+g}|^2 = \frac{1}{2} \left[C_1 \sum_{\substack{i,j,k=A,B,C \\ i \neq j \neq k}} |\mathcal{A}_{ijk}^{gg}|^2 \right.$$

$$+ C_2 \left(|\mathcal{A}_{ABC}^{gg} + \mathcal{A}_{ACB}^{gg} + \mathcal{A}_{CAB}^{gg}|^2 + |\mathcal{A}_{CBA}^{gg} + \mathcal{A}_{BAC}^{gg} + \mathcal{A}_{BCA}^{gg}|^2 + |\mathcal{A}_{CAB}^{gg} + \mathcal{A}_{CBA}^{gg} + \mathcal{A}_{BCA}^{gg}|^2 + \right.$$

$$\left. |\mathcal{A}_{ABC}^{gg} + \mathcal{A}_{BAC}^{gg} + \mathcal{A}_{ACB}^{gg}|^2 + |\mathcal{A}_{CAB}^{gg} + \mathcal{A}_{CBA}^{gg} + \mathcal{A}_{ACB}^{gg}|^2 + |\mathcal{A}_{ABC}^{gg} + \mathcal{A}_{BAC}^{gg} + \mathcal{A}_{BCA}^{gg}|^2 \right)$$

$$\left. + C_3 \frac{1}{4} \left| \sum_{\substack{i,j,k=A,B,C \\ i \neq j \neq k}} \mathcal{A}_{ijk}^{gg} \right|^2 \right] \tag{3.120}$$

is the full real amplitude squared, including both leading and subleading color

factors (see Eq. (3.45) for a definition of C_1, C_2, and C_3). Each subamplitude

squared in Eq. (3.120) has very definite factorization properties in the soft or

collinear regions of the phase space of the extra emitted gluon.

85

(b) Using the one-cutoff PSS method and the factorization properties of soft and collinear divergences of the various amplitudes squared in Eq. (3.120), we extract the IR singularities from $\hat{\sigma}_{real}^{h\rightarrow ggt\bar{t}+g}$ in $d = 4 - 2\epsilon$ dimensions. In the soft and collinear limits we obtain:

$$\hat{\sigma}_{real}^{h\rightarrow ggt\bar{t}+g} \overset{soft}{\longrightarrow} \hat{\sigma}_{soft}^{h\rightarrow ggt\bar{t}+g} = \int d(PS_4)d(PS_g)_{soft}\overline{\sum}|\mathcal{A}_{soft}^{h\rightarrow ggt\bar{t}+g}|^2 \quad (3.121)$$

$$\hat{\sigma}_{real}^{h\rightarrow ggt\bar{t}+g} \overset{collinear}{\longrightarrow} \hat{\sigma}_{coll}^{h\rightarrow ggt\bar{t}+g} = \int d(PS_4)d(PS_g)_{coll}\overline{\sum}|\mathcal{A}_{coll}^{h\rightarrow ggt\bar{t}+g}|^2 \quad ,(3.122)$$

where we denote by $d(PS_g)_{soft}$ $(d(PS_g)_{coll})$ the phase space of the gluon g^C in the soft (collinear) limit. In both the soft and the collinear limits, the cross section for $h \rightarrow ggt\bar{t} + g$ integrated over the phase space of the IR singular gluon has the form:

$$
\begin{aligned}
\hat{\sigma}_{soft,\,coll}^{h\rightarrow ggt\bar{t}+g} = \int d(PS_4)\frac{1}{N}\overline{\sum} \\
\left\{ C_1 \left[K_{S,C}(t;1,2;\bar{t})\,|\mathcal{A}_{0,s}^{(c),gg} + \mathcal{A}_{0,t}^{(c),gg}|^2 + K_{S,C}(t;2,1;\bar{t})\,|\mathcal{A}_{0,u}^{(c),gg} - \mathcal{A}_{0,s}^{(c),gg}|^2 \right] \right. \\
+ C_2 \left[2\,K_{S,C}(t;\bar{t}) \left(|\mathcal{A}_0^{ab,(c)}|^2 + |\mathcal{A}_0^{nab,(c)}|^2 \right) + \right. \\
\left. 4\,(K_{S,C}(t;1;\bar{t}) + K_{S,C}(t;2;\bar{t}))\,|\mathcal{A}_0^{ab,(c)}|^2 \right] \\
\left. + C_3\,K_{S,C}(t;\bar{t})\,|\mathcal{A}_0^{ab,(c)}|^2 \right\} ,
\end{aligned}
\tag{3.123}
$$

where the tree level amplitudes for the crossed process $h \rightarrow ggt\bar{t}$, denoted by $\mathcal{A}_{0,s}^{(c),gg}$, $\mathcal{A}_{0,t}^{(c),gg}$, and $\mathcal{A}_{0,u}^{(c),gg}$, as well as their linear combinations $\mathcal{A}_0^{ab,(c)}$ and $\mathcal{A}_0^{nab,(c)}$, can be obtained from the corresponding amplitudes for $gg \rightarrow t\bar{t}h$ given explicitly in Eq (3.14) by flipping momenta and helicities of the crossed particles. The functions K are either evaluated in the soft (K_S) or in the collinear limit (K_C), and will be explicitly given in Eqs. (3.125) and (3.129). Moreover, we notice that the arguments of the $K_{S,C}$ functions are indices $i = 1, 2, t, \bar{t}$ denoting the external partons $g^A(q_1)$, $g^B(q_2)$, $t(p_t)$, and $\bar{t}(p'_t)$ respectively. The explicit forms of both the pole and finite parts of $\hat{\sigma}_{soft}^{h\rightarrow ggt\bar{t}+g}$ and $\hat{\sigma}_{coll}^{h\rightarrow ggt\bar{t}+g}$ are given below.

86

(c) Finally, the IR singular contribution $\hat{\sigma}_{ir}^{gg}$ of Eq. (3.81) consists of two terms:

$$\hat{\sigma}_{ir}^{gg} = \hat{\bar{\sigma}}_{ir}^{gg} + \hat{\sigma}_{crossing}^{gg} \ . \tag{3.124}$$

$\hat{\bar{\sigma}}_{ir}^{gg}$ is obtained by crossing g^A, g^B to the initial state and h to the final state in the sum of $\hat{\sigma}_{soft}^{h \to ggt\bar{t}+g}$ and $\hat{\sigma}_{coll}^{h \to ggt\bar{t}+g}$, while $\hat{\sigma}_{crossing}^{gg}$ corrects for the difference between the collinear gluon radiation from initial and final state partons [57, 30]. The IR singularities of $\hat{\sigma}_{virt}^{gg}$ of Section 3.3.2.2 are exactly canceled by the corresponding singularities in $\hat{\bar{\sigma}}_{ir}^{gg}$. On the other hand, $\hat{\sigma}_{crossing}^{gg}$ still contains collinear divergences that will be canceled by the PDF counterterms when the parton cross section is convoluted with the gluon PDFs, as we will show in Section 3.5.

Soft gluon emission: $h \to ggt\bar{t} + g$

In the soft limit, the $h \to ggt\bar{t} + g$ phase space, as well as the full parton level real amplitude squared, factorize the dependence on the degrees of freedom of the soft emitted gluon, as illustrated in Eq. (3.121). The soft part of the parton level cross section can be calculated analytically according to Eq. (3.123). The soft limit of the K functions, K_S, is explicitly given by:

$$K_S(t; i, j; \bar{t}) = \frac{Ng_s^2}{2} \int d(PS_g)_{soft}[f_{ti}(g) + f_{ij}(g) + f_{j\bar{t}}(g)] = S_{ti} + S_{ij} + S_{j\bar{t}} \ ,$$

$$K_S(t; i; \bar{t}) = \frac{Ng_s^2}{2} \int d(PS_g)_{soft}[f_{ti}(g) + f_{i\bar{t}}(g)] = S_{ti} + S_{i\bar{t}} \ ,$$

$$K_S(t; \bar{t}) = \frac{Ng_s^2}{2} \int d(PS_g)_{soft} f_{t\bar{t}}(g) = S_{t\bar{t}} \ , \tag{3.125}$$

where $i, j = 1, 2$ denote the two external hard gluons with momenta q_1 and q_2. The soft functions f_{ab} and S_{ab} are given by Eqs. (3.90) and (3.91), respectively. Additionally, the soft gluon phase space is given by Eq. (3.92). Using these expressions and the

analytic results for the S_{ab} functions in Eqs. (3.95)-(3.96), the pole part of the parton level soft cross section can be written as

$$(\hat{\sigma}_{soft}^{h\to ggt\bar{t}+g})_{pole} = \int d(PS_4)\frac{\alpha_s}{2\pi}\mathcal{N}_t \times$$

$$\overline{\sum}\left\{C_1\left[\frac{4}{\epsilon^2} + \frac{2}{\epsilon} + \frac{2}{\epsilon}\Lambda_\sigma - \frac{8}{\epsilon}\Lambda_{min}\right]\left(|\mathcal{A}_0^{ab,(c)}|^2 + |\mathcal{A}_0^{nab,(c)}|^2\right)\right.$$

$$+2C_2\left[\frac{1}{\epsilon}\left(1 - \frac{\bar{s}_{t\bar{t}} - 2m_t^2}{\bar{s}_{t\bar{t}}\beta_{t\bar{t}}}\Lambda_{t\bar{t}}\right)\left(|\mathcal{A}_0^{ab,(c)}|^2 + |\mathcal{A}_0^{nab,(c)}|^2\right)\right.$$

$$\left.+4\left(\frac{1}{\epsilon^2} + \frac{1}{\epsilon} - \frac{2}{\epsilon}\Lambda_{min}\right)|\mathcal{A}_0^{ab,(c)}|^2\right] + C_3\frac{1}{\epsilon}\left[1 - \frac{\bar{s}_{t\bar{t}} - 2m_t^2}{\bar{s}_{t\bar{t}}\beta_{t\bar{t}}}\Lambda_{t\bar{t}}\right]|\mathcal{A}_0^{ab,(c)}|^2\right\} , \tag{3.126}$$

while the corresponding finite contribution is:

$$(\hat{\sigma}_{soft}^{h\to ggt\bar{t}+g})_{finite} = \int d(PS_4)\frac{\alpha_s}{2\pi}\mathcal{N}_t \times$$

$$\overline{\sum}\left\{C_1\left[\left(\Lambda_\sigma^2 - 4\Lambda_\sigma\Lambda_{min} - 4\Lambda_{min} + 8\Lambda_{min}^2 - \pi^2\right)\left(|\mathcal{A}_0^{ab,(c)}|^2 + |\mathcal{A}_0^{nab,(c)}|^2\right)\right.\right.$$

$$+\left(-\frac{1}{2}\Lambda_{\tau_1}^2 - \frac{1}{2}\Lambda_{\tau_2}^2 + \Lambda_{\tau_1} + \Lambda_{\tau_2} + \frac{m_t^2}{s_{t1}} + \frac{m_t^2}{s_{\bar{t}2}}\right)|\mathcal{A}_{0,s}^{(c),gg} + \mathcal{A}_{0,t}^{(c),gg}|^2$$

$$\left.+\left(-\frac{1}{2}\Lambda_{\tau_3}^2 - \frac{1}{2}\Lambda_{\tau_4}^2 + \Lambda_{\tau_3} + \Lambda_{\tau_4} + \frac{m_t^2}{s_{t2}} + \frac{m_t^2}{s_{\bar{t}1}}\right)|\mathcal{A}_{0,u}^{(c),gg} - \mathcal{A}_{0,s}^{(c),gg}|^2\right]$$

$$+ C_2\left[\left(-2\Lambda_{min}\left(1 - \frac{\bar{s}_{t\bar{t}} - 2m_t^2}{\bar{s}_{t\bar{t}}\beta_{t\bar{t}}}\Lambda_{t\bar{t}}\right) + \frac{2m_t^2}{\sqrt{\lambda_{t\bar{t}}}}(J_a + J_b)\right)\left(|\mathcal{A}_0^{ab,(c)}|^2 + |\mathcal{A}_0^{nab,(c)}|^2\right)\right.$$

$$+4\left(-4\Lambda_{min} + 4\Lambda_{min}^2 - \frac{2}{3}\pi^2 - \frac{1}{2}\Lambda_{\tau_1}^2 - \frac{1}{2}\Lambda_{\tau_2}^2 - \frac{1}{2}\Lambda_{\tau_3}^2 - \frac{1}{2}\Lambda_{\tau_4}^2\right.$$

$$\left.\left.+\Lambda_{\tau_1} + \Lambda_{\tau_2} + \Lambda_{\tau_3} + \Lambda_{\tau_4} + \frac{m_t^2}{s_{t1}} + \frac{m_t^2}{s_{t2}} + \frac{m_t^2}{s_{\bar{t}1}} + \frac{m_t^2}{s_{\bar{t}2}}\right)|\mathcal{A}_0^{ab,(c)}|^2\right]$$

$$+ C_3\left[-\Lambda_{min}\left(1 - \frac{\bar{s}_{t\bar{t}} - 2m_t^2}{\bar{s}_{t\bar{t}}\beta_{t\bar{t}}}\Lambda_{t\bar{t}}\right) + \frac{m_t^2}{\sqrt{\lambda_{t\bar{t}}}}(J_a + J_b)\right]|\mathcal{A}_0^{ab,(c)}|^2\right\} , \tag{3.127}$$

where τ_i is defined in Eq (3.36), σ, Λ_σ, and Λ_{τ_i} are defined in Eq. (3.48) and right before it, $\bar{s}_{t\bar{t}}$ is defined in Eq. (3.47), $\beta_{t\bar{t}}$ and $\Lambda_{t\bar{t}}$ are defined in Eq. (3.37), $\lambda_{t\bar{t}}$ is given in Eq. (3.98), Λ_{min} is:

$$\Lambda_{min} = \ln\left(\frac{s_{min}}{m_t^2}\right) , \tag{3.128}$$

and the functions J_a and J_b are given in Eq. (3.97).

Collinear gluon emission: $\boldsymbol{h \to ggt\bar{t} + g}$

In this case, collinear singularities arise when one of the two final state gluons i ($i=g^A$, g^B) and the hard extra gluon g ($g=g^C$) become collinear and cluster to form a new parton i' (also a gluon), $i + g \to i'$, with the collinear kinematics: $q_i = zq_{i'}$ and $k=(1-z)q_{i'}$. In the collinear limit, the $h \to ggt\bar{t} + g$ phase space as well as the full parton level real amplitude squared factorize the dependence on the degrees of freedom of the collinear emitted gluon, as illustrated in Eq. (3.122). The collinear part of the parton level cross section can be calculated analytically according to Eq. (3.123). The collinear limit of the K functions, K_C, is explicitly given by:

$$
\begin{aligned}
K_C(t;i,j;\bar{t}) &= \int d(PS_g)_{coll} \frac{Ng_s^2}{2} [f_{tj}^{gg\to i} + f_{it}^{gg\to j} + 2n_{lf}f^{q\bar{q}\to g}] \\
&= -\frac{\alpha_s N}{2\pi} \frac{1}{\Gamma(1-\epsilon)} \left(\frac{4\pi\mu^2}{s_{min}}\right)^\epsilon \frac{1}{\epsilon} \left[I_{gg\to g}\left(\frac{s_{min}}{s_{ti}}, \frac{s_{min}}{s_{ij}}\right) + I_{gg\to g}\left(\frac{s_{min}}{s_{ij}}, \frac{s_{min}}{s_{j\bar{t}}}\right) \right. \\
&\quad \left. + 2n_{lf}I_{q\bar{q}\to g}(0,0) \right] , \\
K_C(t;i;\bar{t}) &= \int d(PS_g)_{coll} \frac{Ng_s^2}{2} [f_{t\bar{t}}^{gg\to i} + n_{lf}f^{q\bar{q}\to g}] \\
&= -\frac{\alpha_s N}{2\pi} \frac{1}{\Gamma(1-\epsilon)} \left(\frac{4\pi\mu^2}{s_{min}}\right)^\epsilon \frac{1}{\epsilon} \left[I_{gg\to g}(\frac{s_{min}}{s_{ti}}, \frac{s_{min}}{s_{i\bar{t}}}) + n_{lf}I_{q\bar{q}\to g}(0,0) \right] , \\
K_C(t;\bar{t}) &= 0 ,
\end{aligned}
$$
(3.129)

where $i,j=1,2$ denote the two external hard gluons with momenta q_1 and q_2.

In the one-cutoff PSS method, the collinear gluon phase space factorizes and is given in the previous section (Eq. (3.105)). The collinear functions $f_{ab}^{ig\to i'}$ are proportional to the Altarelli-Parisi splitting function for $ig \to i'$ and explicitly factorize the corresponding collinear pole, i.e. [56, 57]:

$$
f_{ab}^{ig\to i'} = \frac{2}{N} \frac{P_{ig\to i'}(z)}{s_{ig}} ,
$$
(3.130)

where both i and i' are gluons and therefore $P_{ig\to i'}$ corresponds to the $P_{gg}(z)$ splitting function given in Eq. (3.74). The lower indices a and b have been used to specify

89

the integration boundaries on z. In order to avoid double counting between soft and collinear regions of the phase space of g^C, it is crucial to impose that only one s_{ig} at a time becomes singular, i.e. satisfies the condition $s_{ig} < s_{min}$. The advantage of having reorganized the amplitude in terms of color ordered amplitudes, as in Eq. (3.118), is that the $f_{ab}^{ig \to i'}$ collinear functions have a very definite structure: they are all proportional to $(s_{ai} s_{ig} s_{gb})^{-1}$, for $a, b = g^A, g^B, t, \bar{t}$, and the integration boundaries are then found by imposing the conditions given in Eq. (3.106). The terms proportional to $f^{q\bar{q} \to g}$ come from the fact that a pair of collinear final state massless quarks ($n_{lf} = 5$ is the number of massless flavors) can also mimic a gluon. The corresponding collinear function is:

$$f^{q\bar{q} \to g} = \frac{2}{N} \frac{P_{q\bar{q} \to g}(z)}{s_{q\bar{q}}} \quad , \tag{3.131}$$

where both the $\mathcal{O}(1)$ and $\mathcal{O}(\epsilon)$ parts of the splitting function $P_{q\bar{q} \to g}$ are defined in Eq. (3.78). Note that we do not attach any lower index to $f^{q\bar{q} \to g}$ because the integration over z has no singularities and can be performed over the entire range from $z = 0$ to $z = 1$.

The analytic form of the integrated collinear functions $I_{gg \to g}(z_1, z_2)$ and $I_{q\bar{q} \to g}(0, 0)$ is obtained by carrying out the integration in Eq. (3.129), and is explicitly given by [57]:

$$I_{gg \to g}(z_1, z_2) = \frac{1}{\epsilon} \left(z_1^{-\epsilon} + z_2^{-\epsilon} - 2 \right) - \frac{11}{6} + \left(\frac{\pi^2}{3} - \frac{67}{18} \right) \epsilon + \mathcal{O}(\epsilon^2) \quad ,$$

$$I_{q\bar{q} \to g}(0, 0) = \frac{1}{N} \left(\frac{1}{3} + \frac{5}{9} \epsilon \right) + \mathcal{O}(\epsilon^2) \quad . \tag{3.132}$$

Finally, using Eq. (3.123) and Eqs. (3.129)-(3.132), the pole part of the parton level collinear cross section can be written as:

$$(\hat{\sigma}_{coll}^{h \to gg t\bar{t} + g})_{pole} = \int d(PS_4) \frac{\alpha_s}{2\pi} \mathcal{N}_t \frac{1}{\epsilon} \times$$

$$\overline{\sum} \left\{ C_1 \left[\left(-4\Lambda_\sigma + 8\Lambda_{min} + 2 \left(\frac{11}{3} - \frac{2}{3} \frac{n_{lf}}{N} \right) \right) \left(|\mathcal{A}_0^{ab,(c)}|^2 + |\mathcal{A}_0^{nab,(c)}|^2 \right) \right. \right.$$

$$
- (\Lambda_{\tau_1} + \Lambda_{\tau_2}) \, |\mathcal{A}_{0,s}^{(c)} + \mathcal{A}_{0,t}^{(c)}|^2 - (\Lambda_{\tau_3} + \Lambda_{\tau_4}) \, |\mathcal{A}_{0,u}^{(c)} - \mathcal{A}_{0,s}^{(c)}|^2 \Bigg]
$$
$$
+ \, C_2 \left[-4 \left(\Lambda_{\tau_1} + \Lambda_{\tau_2} + \Lambda_{\tau_3} + \Lambda_{\tau_4} \right) + 16 \Lambda_{min} + 4 \left(\frac{11}{3} - \frac{2}{3} \frac{n_{lf}}{N} \right) \right] |\mathcal{A}_0^{ab,(c)}|^2 \Bigg\} \; ,
$$

$$
(3.133)
$$

while the corresponding finite contribution is:

$$
(\hat{\sigma}_{coll}^{h \to ggt\bar{t}+g})_{finite} = \int d(PS_4) \frac{\alpha_s}{2\pi} \mathcal{N}_t \times
$$
$$
\overline{\sum} \Bigg\{ C_1 \left[\left(-2 \Lambda_\sigma^2 - 12 \Lambda_{min}^2 + 8 \Lambda_\sigma \Lambda_{min} - 2 \Lambda_{min} \left(\frac{11}{3} - \frac{2}{3} \frac{n_{lf}}{N} \right) \right) \right.
$$
$$
- 2 \left(\frac{2}{3} \pi^2 - \frac{67}{9} + \frac{10}{9} \frac{n_{lf}}{N} \right) \right) \left(|\mathcal{A}_0^{ab,(c)}|^2 + |\mathcal{A}_0^{nab,(c)}|^2 \right)
$$
$$
+ \left(-\frac{1}{2} \Lambda_{\tau_1}^2 - \frac{1}{2} \Lambda_{\tau_2}^2 + 2 \Lambda_{min} \left(\Lambda_{\tau_1} + \Lambda_{\tau_2} \right) \right) |\mathcal{A}_{0,s}^{(c)} + \mathcal{A}_{0,t}^{(c)}|^2
$$
$$
+ \left(-\frac{1}{2} \Lambda_{\tau_3}^2 - \frac{1}{2} \Lambda_{\tau_4}^2 + 2 \Lambda_{min} \left(\Lambda_{\tau_3} + \Lambda_{\tau_4} \right) \right) |\mathcal{A}_{0,u}^{(c)} - \mathcal{A}_{0,s}^{(c)}|^2 \Bigg]
$$
$$
+ C_2 \Bigg[8 \Lambda_{min} \left(\Lambda_{\tau_1} + \Lambda_{\tau_2} + \Lambda_{\tau_3} + \Lambda_{\tau_4} \right) - 24 \Lambda_{min}^2 - 2 \left(\Lambda_{\tau_1}^2 + \Lambda_{\tau_2}^2 + \Lambda_{\tau_3}^2 + \Lambda_{\tau_4}^2 \right)
$$
$$
- 4 \Lambda_{min} \left(\frac{11}{3} - \frac{2}{3} \frac{n_{lf}}{N} \right) - 4 \left(\frac{2}{3} \pi^2 - \frac{67}{9} + \frac{10}{9} \frac{n_{lf}}{N} \right) \Bigg] |\mathcal{A}_0^{ab,(c)}|^2 \Bigg\} \; ,
$$

$$
(3.134)
$$

where τ_i is defined in Eq (3.36), σ, Λ_σ, and Λ_{τ_i} are defined in Eq. (3.48) and right before it, while Λ_{min} is defined in Eq. (3.128).

IR Singular Gluon Emission: Complete Result for $\hat{\sigma}_{ir}^{gg}$

Summing both soft and collinear contributions to the $h \to ggt\bar{t} + g$ cross section and crossing the final state gluons g^A, g^B to the initial state and the Higgs boson to the final state (which flips both helicities and momenta of these particles), yields $\hat{\sigma}_{ir}^{gg}$ of Eq. (3.124) as

$$
\hat{\sigma}_{ir}^{gg} = (\hat{\sigma}_{soft}^{h \to ggt\bar{t}+g} + \hat{\sigma}_{coll}^{h \to ggt\bar{t}+g})_{crossed} \; .
$$

$$
(3.135)
$$

The IR pole part of $\hat{\bar{\sigma}}^{gg}_{ir}$ is given by

$$(\hat{\bar{\sigma}}^{gg}_{ir})_{pole} = ((\hat{\sigma}^{h\to ggt\bar{t}+g}_{soft})_{pole} + (\hat{\sigma}^{h\to ggt\bar{t}+g}_{coll})_{pole})_{crossed}$$

$$= \int d(PS_3)\frac{\alpha_s}{2\pi}\mathcal{N}_t\overline{\sum}\left(C_1\mathcal{M}^{(1),gg}_{ir,\epsilon} + C_2\mathcal{M}^{(2),gg}_{ir,\epsilon} + C_3\mathcal{M}^{(3),gg}_{ir,\epsilon}\right)$$

$$+\frac{\alpha_s}{2\pi}\mathcal{N}_t\left(-\frac{2}{3}n_{lf} + \frac{8}{3}N - \frac{1}{N}\right)\frac{1}{\epsilon}\hat{\sigma}^{gg}_{LO} \ , \tag{3.136}$$

where $\mathcal{M}^{(i),gg}_{ir,\epsilon} = -\mathcal{M}^{(i),gg}_{V,\epsilon}$ (see Eq. (3.46)) and therefore $(\hat{\bar{\sigma}}^{gg}_{ir})_{pole}$ completely cancels the IR singularities of the virtual cross section $(\hat{\sigma}^{gg}_{virt})_{IR-pole}$ in Eq. (3.49). The IR finite part of $\hat{\bar{\sigma}}^{gg}_{ir}$ is given by

$$(\hat{\bar{\sigma}}^{gg}_{ir})_{finite} = ((\hat{\sigma}^{h\to ggt\bar{t}+g}_{soft})_{finite} + (\hat{\sigma}^{h\to ggt\bar{t}+g}_{coll})_{finite})_{crossed} \ , \tag{3.137}$$

with $(\hat{\sigma}^{h\to ggt\bar{t}+g}_{soft,coll})_{finite}$ given in Eqs. (3.127) and (3.134).

Finally, as described in Section 3.4.2, the partonic cross section for the IR singular real gluon radiation for the process $gg \to t\bar{t}h + g$ using the one-cutoff PSS method, $\hat{\sigma}^{gg}_{ir}$, is obtained from $\hat{\bar{\sigma}}^{gg}_{ir}$ by adding $\hat{\sigma}^{gg}_{crossing}$ (see Eq. (3.124)). The cross section $\hat{\sigma}^{gg}_{crossing}$ accounts for the difference between initial and final state collinear gluon radiation and contributes to the hadronic cross section as

$$\sigma^{gg}_{crossing} = \alpha_s(\mu)\int dx_1 dx_2 f_g(x_1)\int_{x_2}^1 \frac{dz}{z}f_g(\frac{x_2}{z})X_{g\to g}(z)\hat{\sigma}^{gg}_{LO} + (x_1 \leftrightarrow x_2) \ , \tag{3.138}$$

with $X_{g\to g}$ given by [57]:

$$X_{g\to g}(z) = -\frac{N}{2\pi}\left(\frac{4\pi\mu^2}{s_{min}}\right)^{\epsilon}\frac{1}{\Gamma(1-\epsilon)}\left(\frac{1}{\epsilon}\right)\times$$

$$\left\{\left[\frac{11}{6} - \frac{1}{3}\frac{n_{lf}}{N} - \epsilon\left(\frac{\pi^2}{3} - \frac{67}{18} + \frac{5}{9}\frac{n_{lf}}{N}\right)\right]\delta(1-z)\right.$$

$$\left.+2\left[\frac{z}{[(1-z)^{1+\epsilon}]_+} + \frac{(1-z)^{1-\epsilon}}{z} + z(1-z)^{1-\epsilon}\right]\right\} \ , \tag{3.139}$$

in terms of regularized *plus* functions (see Ref. [57] for the exact definition). As will be demonstrated in Section 3.5, these remaining IR singularities will be absorbed into the gluon PDFs when including the effects of mass factorization.

3.4.2.3   The tree-level process $(q, \bar{q})g \to t\bar{t}h + (q, \bar{q})$

When calculating the cross section for $qg \to t\bar{t}h + q$ in the collinear limit using the procedure described above, the resulting IR singular cross section $\hat{\sigma}_{ir}^{qg}$ is simply given by the initial state qg splitting functions of Eq. (3.78) convoluted with the corresponding Born cross sections (see, e.g. Ref. [57])

$$
\hat{\sigma}_{ir}^{qg} = \left[\frac{\alpha_s}{2\pi} \frac{1}{\Gamma(1-\epsilon)} \left(\frac{4\pi\mu^2}{s_{min}} \right)^\epsilon \right] \left(-\frac{1}{\epsilon} \right) \int_0^1 dz (1-z)^{-\epsilon} \times
$$
$$
[P_{qg}(z)\, \hat{\sigma}_{LO}^{gg}(g(q_{1'})g(q_2) \to t\bar{t}h) + P_{gq}(z)\, \hat{\sigma}_{LO}^{q\bar{q}}(q(q_1)\bar{q}(q_{2'}) \to t\bar{t}h)] \quad , (3.140)
$$

where the prime identifies the parton that originates from the splitting of a similar or different parent parton. The cross section for $\bar{q}g \to t\bar{t}h + \bar{q}$ in the collinear limit is obtained in complete analogy with Eq. (3.140).

Finally, the hard part of the parton level cross section, $\hat{\sigma}_{hard}^{ij}$ $(ij = q\bar{q}, gg, qg, \bar{q}g)$, is finite and can be calculated numerically. In this respect we note that, in the one cutoff method, the soft and collinear limits of the real cross section, and consequently $\hat{\sigma}_{hard}^{ij}$, are more sensitive to the smallness of the cutoff. A cut on the full invariant masses s_{ig} is more drastic than two separate cuts on either the energy or the angle of emission of the extra gluon (q or $\bar{q}$), and can be felt even by terms in the amplitude squared that do not contain singularities. These effects are very small, but large enough to affect the results at the level of precision of our calculation. It is therefore crucial, in particular for $\hat{\sigma}_{hard}^{gg}$, to model the Monte Carlo integration for each term in Eqs. (3.119)-(3.120) separately, and to enforce term by term only the cuts on the s_{ig} invariants that are actually present in each term.

3.5   NLO total cross section for $t\bar{t}h$ production

3.5.1   NLO total cross section at the Tevatron: $p\bar{p} \to t\bar{t}h$

As mentioned earlier, at the Tevatron CM energy, the partonic process $q\bar{q} \to t\bar{t}h$ dominates, making up more than 95% of the total cross section. Therefore, in this section we only consider the contribution from the $q\bar{q}$-initiated process.

As described in Sec. 3.1, the observable total cross section at NLO is obtained by convoluting the parton cross section for $q\bar{q} \to t\bar{t}h$ with the NLO quark distribution functions $\mathcal{F}_q^{p,\bar{p}}(x,\mu)$, thereby absorbing the remaining initial-state singularities of $\delta\hat{\sigma}_{NLO}^{q\bar{q}}$ into the quark distribution functions. This can be understood as follows. First the parton cross section is convoluted with the *bare* quark distribution functions $\mathcal{F}_q^{p,\bar{p}}(x)$ and subsequently $\mathcal{F}_q^{p,\bar{p}}(x)$ is replaced by the renormalized quark distribution functions $\mathcal{F}_q^{p,\bar{p}}(x,\mu)$ defined in some subtraction scheme. Using the $\overline{MS}$ scheme, the scale-dependent NLO quark distribution functions are given in terms of $\mathcal{F}_q^{p,\bar{p}}(x)$ and the QCD NLO parton distribution function counterterms [55, 57] as follows:

two-cutoff PSS method

$$\mathcal{F}_q^{p,\bar{p}}(x,\mu) = \mathcal{F}_q^{p,\bar{p}}(x) \left[1 - \frac{\alpha_s}{2\pi} \frac{\Gamma(1-\epsilon)}{\Gamma(1-2\epsilon)} (4\pi)^\epsilon \left(\frac{1}{\epsilon} \right) C_F \left(2\ln(\delta_s) + \frac{3}{2} \right) \right] \tag{3.141}$$
$$+ \left[\frac{\alpha_s}{2\pi} \frac{\Gamma(1-\epsilon)}{\Gamma(1-2\epsilon)} (4\pi)^\epsilon \right] \int_x^{1-\delta_s} \frac{dz}{z} \left(-\frac{1}{\epsilon} \right) P_{qq}(z) \mathcal{F}_j^{p,\bar{p}}(\frac{x}{z}) \ ,$$

one-cutoff PSS method

$$\mathcal{F}_q^{p,\bar{p}}(x,\mu) = \mathcal{F}_q^{p,\bar{p}}(x) \left[1 - \frac{\alpha_s}{2\pi} \frac{(4\pi)^\epsilon}{\Gamma(1-\epsilon)} \left(\frac{1}{\epsilon} \right) C_F \frac{3}{2} \right] \tag{3.142}$$
$$+ \left[\frac{\alpha_s}{2\pi} \frac{(4\pi)^\epsilon}{\Gamma(1-\epsilon)} \right] \int_x^1 \frac{dz}{z} \left(-\frac{1}{\epsilon} \right) C_F \frac{1+z^2}{(1-z)_+} \mathcal{F}_j^{p,\bar{p}}(\frac{x}{z}) \ ,$$

where the $\mathcal{O}(\alpha_s)$ terms in the previous equations are calculated from the $\mathcal{O}(\alpha_s)$ corrections to the $q \to qg$ splitting, in the PSS formalism, and $P_{qq}(z)$ is the Altarelli-Parisi splitting function of Eq. (3.73). Note that, again, we choose the factorization and renormalization scales to be equal. Therefore there is no explicit factorization scale dependence in Eqs. (3.141) and (3.142), and the only μ-dependence in $\mathcal{F}_q^{p,\bar{p}}(x,\mu)$ comes from $\alpha_s(\mu)$. When using the two-cutoff method and convoluting the parton cross section with the renormalized quark distribution function of Eq. (3.141), the IR singular counterterm of Eq. (3.141) exactly cancels the remaining IR poles of $\hat{\sigma}_{virt}^{q\bar{q}} + \hat{\sigma}_{soft}^{q\bar{q}}$ and $\hat{\sigma}_{hard/coll}^{q\bar{q}}$. In case of the one-cutoff PSS method, the IR singular

94

counterterm of Eq. (3.142) exactly cancels the IR poles of $\hat{\sigma}^{q\bar{q}}_{crossing}$. Finally, the complete $\mathcal{O}(\alpha_s^3)$ inclusive total cross section for $p\bar{p} \to t\bar{t}h$ in the $\overline{MS}$ factorization scheme can be written as follows:
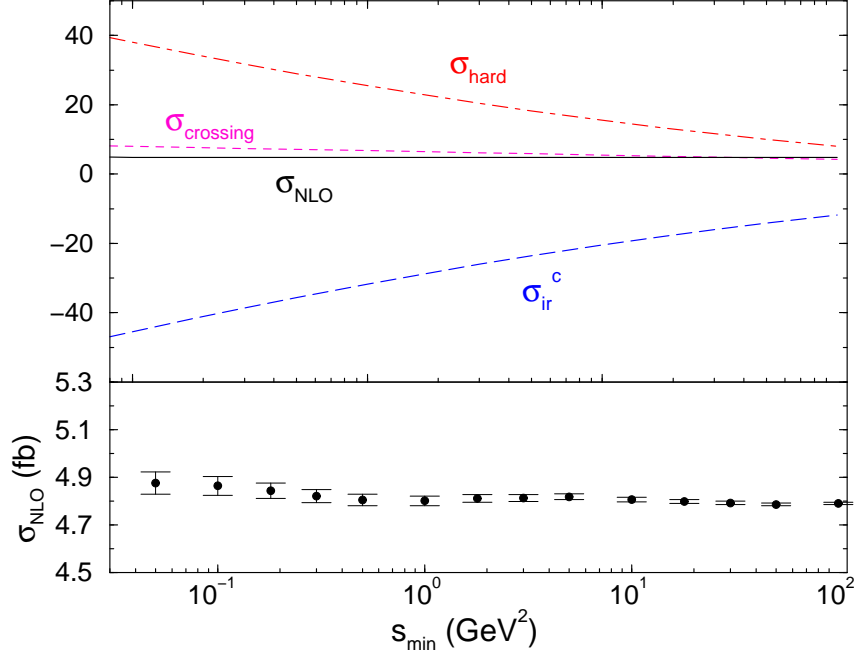
Figure 3.15. Dependence of $\sigma_{NLO}(p\overline{p} \to t\overline{t}h)$ on the arbitrary cutoff of the one-cutoff PSS method, s_{min}, at $\sqrt{s_H} = 2$ TeV, for $M_h = 120$ GeV, and $\mu = m_t$. The upper plot shows the cancellation of the s_{min} dependence between σ^c_{ir}, $\sigma_{crossing}$, and σ_{hard}. The lower plot shows, on an enlarged scale, the dependence of σ_{NLO} on s_{min}, with the corresponding statistical errors.

two-cutoff PSS method

$$\sigma^{q\bar{q}}_{NLO} = \sum_{q\bar{q}} \int dx_1 dx_2 \mathcal{F}^p_q(x_1, \mu) \mathcal{F}^{\bar{p}}_{\bar{q}}(x_2, \mu) \left[\hat{\sigma}^{q\bar{q}}_{LO}(x_1, x_2, \mu) + \hat{\sigma}^{q\bar{q}}_{virt}(x_1, x_2, \mu) + \hat{\sigma}'^{q\bar{q}}_{soft}(x_1, x_2, \mu) \right]$$

$$+ \frac{\alpha_s}{2\pi} C_F \sum_{q\bar{q}} \int dx_1 dx_2 \left\{ \int_{x_1}^{1-\delta_s} \frac{dz}{z} \left[\mathcal{F}^p_q(\frac{x_1}{z}, \mu) \mathcal{F}^{\bar{p}}_{\bar{q}}(x_2, \mu) + \mathcal{F}^{\bar{p}}_{\bar{q}}(x_2, \mu) \mathcal{F}^p_q(\frac{x_1}{z}, \mu) \right] \right. \quad (3.143)$$

95

$$\times \hat{\sigma}_{LO}^{q\bar{q}}(x_1, x_2, \mu) \left[\frac{1+z^2}{1-z} \ln\left(\frac{s}{\mu^2} \frac{(1-z)^2}{z} \frac{\delta_c}{2} \right) + 1 - z \right] + (1 \leftrightarrow 2) \Bigg\}$$

$$+ \sum_{q\bar{q}} \int dx_1 dx_2 \mathcal{F}_q^p(x_1, \mu) \mathcal{F}_{\bar{q}}^{\bar{p}}(x_2, \mu) \, \hat{\sigma}_{hard/non-coll}(x_1, x_2, \mu) \ ,$$

with

$$\hat{\sigma}_{soft}^{'\,q\bar{q}} = \hat{\sigma}_{soft}^{q\bar{q}} + \frac{\alpha_s}{2\pi} \frac{\Gamma(1-\epsilon)}{\Gamma(1-2\epsilon)} (4\pi)^\epsilon \left(\frac{1}{\epsilon} \right) C_F \left[4\ln(\delta_s) + 3 \right] \ , \tag{3.144}$$

<u>one-cutoff PSS method</u>

$$\sigma_{NLO}^{q\bar{q}} = \sum_{q\bar{q}} \int dx_1 dx_2 \mathcal{F}_q^p(x_1, \mu) \mathcal{F}_{\bar{q}}^{\bar{p}}(x_2, \mu) \Bigg\{ \ \hat{\sigma}_{LO}^{q\bar{q}}(x_1, x_2, \mu) + \hat{\sigma}_{virt}^{q\bar{q}}(x_1, x_2, \mu) \tag{3.145}$$

$$+ \hat{\hat{\sigma}}_{ir}^{q\bar{q}}(x_1, x_2, \mu) + \frac{\alpha_s}{2\pi} 2\, C_F \, \hat{\sigma}_{LO}^{q\bar{q}}(x_1, x_2, \mu) \left[\frac{3}{2} \ln\left(\frac{s_{min}}{\mu^2} \right) + \frac{\pi^2}{3} - \frac{7}{2} \right] \Bigg\}$$

$$+ \frac{\alpha_s}{2\pi} C_F \sum_{q\bar{q}} \int dx_1 dx_2 \Bigg\{ \int_{x_1}^1 \frac{dz}{z} \left[\mathcal{F}_q^p(\frac{x_1}{z}, \mu) \mathcal{F}_{\bar{q}}^{\bar{p}}(x_2, \mu) + \mathcal{F}_q^{\bar{p}}(x_2, \mu) \mathcal{F}_{\bar{q}}^p(\frac{x_1}{z}, \mu) \right]$$

$$\times \hat{\sigma}_{LO}^{q\bar{q}}(x_1, x_2, \mu) \left[\frac{1+z^2}{(1-z)_+} \ln\left(\frac{s}{\mu^2} \frac{s_{min}}{s} \right) + 1 - z + (1+z^2) \left(\frac{\ln(1-z)}{1-z} \right)_+ \right]$$

$$+ (1 \leftrightarrow 2) \ \Bigg\} + \sum_{q\bar{q}} \int dx_1 dx_2 \mathcal{F}_q^p(x_1, \mu) \mathcal{F}_{\bar{q}}^{\bar{p}}(x_2, \mu) \, \hat{\sigma}_{hard}^{q\bar{q}}(x_1, x_2, \mu) \ .$$

We note that $\sigma_{NLO}^{q\bar{q}}$ is finite, since, after mass factorization, both soft and collinear singularities have been canceled between $\hat{\sigma}_{virt}^{q\bar{q}} + \hat{\sigma}_{soft}^{'\,q\bar{q}}$ and $\hat{\sigma}_{hard/coll}^{q\bar{q}}$ in the two-cutoff PSS method, and between $\hat{\sigma}_{virt}^{q\bar{q}}$ and $\hat{\hat{\sigma}}_{ir}^{q\bar{q}}$ in the one-cutoff PSS method. The last terms respectively describe the finite real gluon emission of Eq. (3.51) and Eq. (3.81). Note that the second term in Eqs. (3.143) and (3.145), which is proportional to $\ln\left(\frac{s}{\mu^2} \right)$, corresponds exactly to the second and third terms of Eq. (3.5), as predicted by renormalization group arguments. Before we discuss in detail the numerical results for the NLO total cross section for $p\bar{p} \to t\bar{t}h$ we first demonstrate that $\sigma_{NLO}^{q\bar{q}}$ does not depend on the arbitrary cutoffs of the PSS method, i.e. on s_{min} when we use the one-cutoff method, and on the soft and hard/collinear cutoffs δ_s and δ_c when we use the two-cutoff method. We note that the cancellation of the cutoff dependence at the level of the total NLO cross section is a very delicate issue, since it involves

96
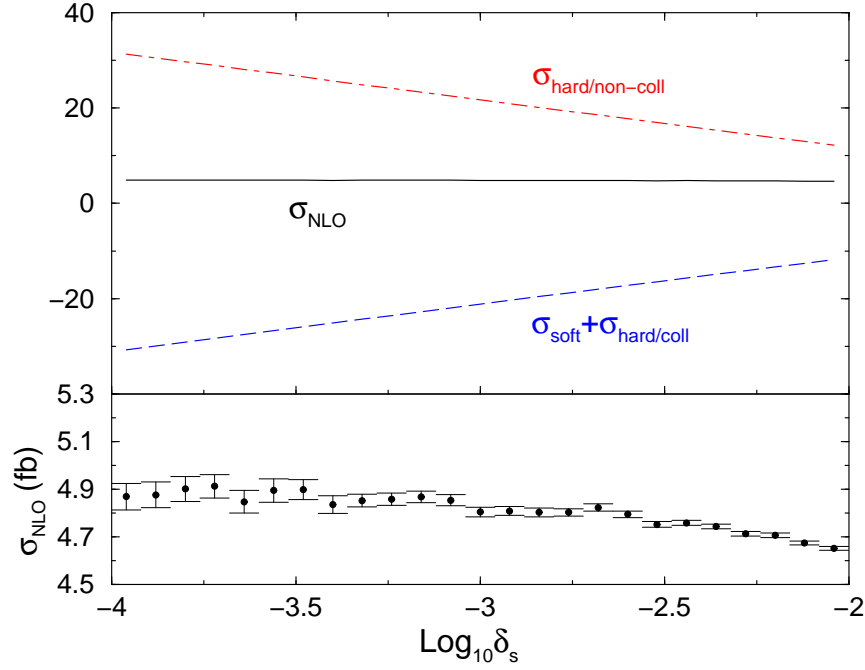
Figure 3.16. Dependence of $\sigma_{NLO}(p\bar{p} \to t\bar{t}h)$ on the soft cutoff δ_s of the two-cutoff PSS method, at $\sqrt{s_H} = 2$ TeV, for $M_h = 120$ GeV, $\mu = m_t$, and $\delta_c = 10^{-4}$. The upper plot shows the cancellation of the δ_s-dependence between $\sigma_{soft} + \sigma_{hard/coll}$ and $\sigma_{hard/non-coll}$. The lower plot shows, on an enlarged scale, the dependence of σ_{NLO} on δ_s with the corresponding statistical errors.

both analytical and numerical contributions. It is crucial to study the behavior of σ_{NLO} in a region where the cutoff(s) are small enough to justify the approximations used in the analytical calculation of the IR-divergent part of $\hat{\sigma}_{real}^{q\bar{q}}$, but not so small to give origin to numerical instabilities.

Fig. 3.15 is about the one-cutoff PSS method and shows the dependence of $\sigma_{NLO}^{q\bar{q}}$ on s_{min}. In the upper window we illustrate the cancellation of the s_{min} dependence between $\sigma_{ir}^{q\bar{q}}$, $\sigma_{crossing}^{q\bar{q}}$, and $\sigma_{hard}^{q\bar{q}}$, while in the lower window we show, on a larger scale, the behavior of σ_{NLO} including the statistical errors from the Monte-Carlo integration. We note that $\sigma_{NLO}^{q\bar{q}}$ also includes the Born cross section and the virtual contribution to the NLO cross section, which are both s_{min}-independent, and are

therefore not shown explicitly in the upper part of Fig. 3.15. Clearly a plateau is reached in the region $0.1\,\mathrm{GeV}^2 < s_{min} < 100\,\mathrm{GeV}^2$.
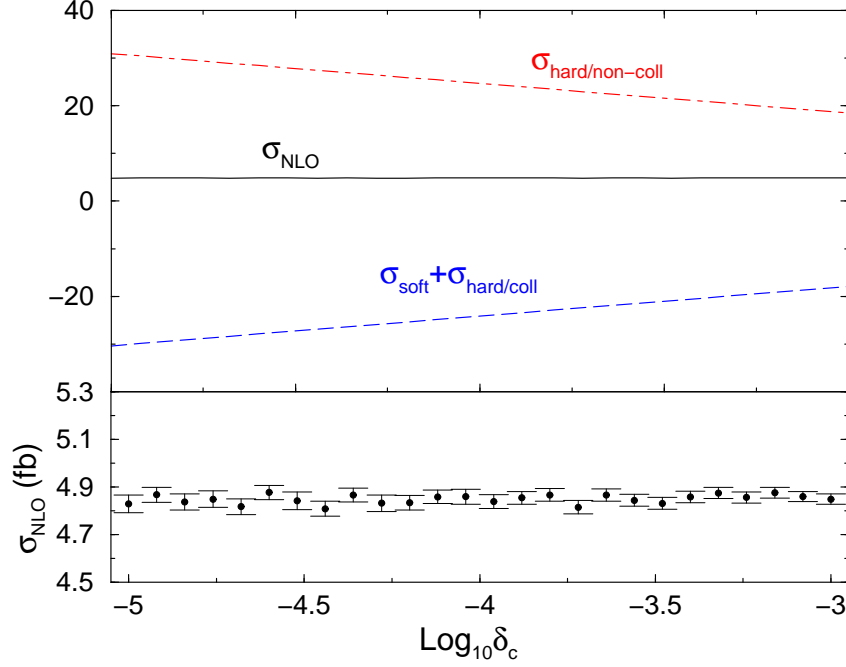
Figure 3.17. Dependence of $\sigma_{NLO}(p\overline{p} \to t\overline{t}h)$ on the collinear cutoff δ_c of the two-cutoff PSS method, at $\sqrt{s_H} = 2$ TeV, for $M_h = 120$ GeV, $\mu = m_t$, and $\delta_s = 5 \times 10^{-4}$. The upper plot shows the cancellation of the δ_c-dependence between $\sigma_{soft} + \sigma_{hard/coll}$ and $\sigma_{hard/non-coll}$. The lower plot shows, on an enlarged scale, the dependence of σ_{NLO} on δ_c with the corresponding statistical errors.

Figs. 3.16 and 3.17 summarize our results using the two-cutoff PSS method. In Fig. 3.16, we show the dependence of $\sigma_{NLO}^{q\bar{q}}$ on the soft cutoff, δ_s, for a fixed value of the hard/collinear cutoff, $\delta_c = 10^{-4}$. In Fig. 3.17, we show the dependence of $\sigma_{NLO}^{q\bar{q}}$ on the hard/collinear cutoff, δ_c, for a fixed value of the soft cutoff, $\delta_s = 5 \times 10^{-4}$. In the upper window of Fig. 3.16 (3.17) we illustrate the cancellation of the δ_s (δ_c) dependence between $\sigma_{soft}^{q\bar{q}} + \sigma_{hard/coll}^{q\bar{q}}$ and $\sigma_{hard/non-coll}^{q\bar{q}}$, while in the lower window we show, on a larger scale, $\sigma_{NLO}^{q\bar{q}}$ with the statistical errors from the Monte-Carlo integration. As before, $\sigma_{NLO}^{q\bar{q}}$ also includes the contribution from the Born and the

virtual cross sections, which are both cutoff-independent and are not shown explicitly in the upper parts of Figs. 3.16,3.17. For δ_s in the range $10^{-4} - 2.5 \times 10^{-3}$ and δ_c in the range $10^{-5} - 10^{-3}$, a clear plateau is reached and the NLO total cross section is independent of the technical cutoffs of the two-cutoff PSS method. All the results presented in the following are obtained using the two-cutoff PSS method with δ_s and δ_c in the range 10^{-4}–10^{-3}. We have confirmed them using the one-cutoff PSS method with $1 \leq s_{min} \leq 10$.

3.5.2   NLO total cross section at the LHC: $pp \rightarrow t\bar{t}h$

The total inclusive hadronic cross section for $pp \rightarrow t\bar{t}h$ is the sum of the contribution from the gg initial state, the $q\bar{q}$ initial state and the $(q,\bar{q})g$ initial states

$$\sigma_{NLO}(pp \rightarrow t\bar{t}h) = \sigma^{gg}_{NLO}(pp \rightarrow t\bar{t}h) + \sigma^{q\bar{q}}_{NLO}(pp \rightarrow t\bar{t}h) + \sigma^{qg}_{NLO}(pp \rightarrow t\bar{t}h) \ . \quad (3.146)$$

As described in Section 3.1, $\sigma^{ij}_{NLO}(pp \rightarrow t\bar{t}h)$ is obtained by convoluting the parton level NLO cross section $\hat{\sigma}^{ij}_{NLO}(pp \rightarrow t\bar{t}h)$ with the NLO PDFs $\mathcal{F}^p_i(x,\mu)$ $(i = q, g)$, thereby absorbing the remaining initial state singularities of $\delta\hat{\sigma}^{ij}_{NLO}$ into the renormalized PDFs. In the following we demonstrate in detail how this cancellation works in the case of the gg and $(q,\bar{q})g$ initiated processes. The case of the $q\bar{q}$ is identical to that presented in Section 3.5.1 and will not be repeated here.

First the parton level cross section is convoluted with the *bare* parton distribution functions $\mathcal{F}^p_i(x)$ and subsequently the $\mathcal{F}^p_i(x)$ are replaced by the renormalized parton distribution functions, $\mathcal{F}^p_i(x,\mu_f)$, defined in some subtraction scheme at a given factorization scale μ_f. Using the $\overline{MS}$ scheme, the scale-dependent NLO parton distribution functions are given in terms of the bare $\mathcal{F}^p_i(x)$ and the QCD NLO parton distribution function counterterms [55, 57] as follows:

(a) For the case where an initial state gluon, quark or antiquark $(b = g, (q,\bar{q}))$ split respectively into a $q\bar{q}$ or $(q,\bar{q})g$ pair $(b' = (q,\bar{q}), g)$:

99

$$\mathcal{F}_{b'}^p(x, \mu_f) = \mathcal{F}_{b'}^p(x) + \left[\frac{\alpha_s}{2\pi} \left(\frac{4\pi\mu_r^2}{\mu_f^2} \right)^\epsilon \frac{1}{\Gamma(1-\epsilon)} \right] \int_x^1 \frac{dz}{z} \left(-\frac{1}{\epsilon} \right) P_{bb'}^4(z) \mathcal{F}_b^p \left(\frac{x}{z} \right) \ ,$$

(3.147)

for both the one-cutoff and two-cutoff PSS methods, where P_{ij}^4 is defined in Eq. (3.78).

(b) For the case of $g \to gg$ splitting:

<u>two-cutoff PSS method</u>

$$\mathcal{F}_g^p(x, \mu_f) = \mathcal{F}_g^p(x) \left[1 - \frac{\alpha_s}{2\pi} \left(\frac{4\pi\mu_r^2}{\mu_f^2} \right)^\epsilon \frac{1}{\Gamma(1-\epsilon)} \left(\frac{1}{\epsilon} \right) N \left(2\ln(\delta_s) + \frac{11}{6} - \frac{1}{3}\frac{n_{lf}}{N} \right) \right]$$
$$+ \left[\frac{\alpha_s}{2\pi} \left(\frac{4\pi\mu_r^2}{\mu_f^2} \right)^\epsilon \frac{1}{\Gamma(1-\epsilon)} \right] \int_x^{1-\delta_s} \frac{dz}{z} \left(-\frac{1}{\epsilon} \right) P_{gg}(z) \mathcal{F}_g^p \left(\frac{x}{z} \right) \ ,$$

(3.148)

where P_{gg} is Altarelli-Parisi splitting function given in Eq. (3.74).

<u>one-cutoff PSS method</u>

$$\mathcal{F}_g^p(x, \mu) = \mathcal{F}_g^p(x) \left[1 - \frac{\alpha_s}{2\pi} \left(\frac{4\pi\mu_r^2}{\mu_f^2} \right)^\epsilon \frac{1}{\Gamma(1-\epsilon)} \left(\frac{1}{\epsilon} \right) N \left(\frac{11}{6} - \frac{1}{3}\frac{n_{lf}}{N} \right) \right]$$
$$+ \left[\frac{\alpha_s}{2\pi} \left(\frac{4\pi\mu_r^2}{\mu_f^2} \right)^\epsilon \frac{1}{\Gamma(1-\epsilon)} \right] \int_x^1 \frac{dz}{z} \left(-\frac{1}{\epsilon} \right) P_{gg}^{(+)}(z) \mathcal{F}_g^p \left(\frac{x}{z} \right) \ ,$$

(3.149)

where $P_{gg}^{(+)}$ is the regulated Altarelli-Parisi splitting function given by:

$$P_{gg}^{(+)}(z) = 2N \left(\frac{z}{(1-z)_+} + \frac{1-z}{z} + z(1-z) \right) \ .$$

(3.150)

The $\mathcal{O}(\alpha_s)$ terms in the previous equations are calculated from the $\mathcal{O}(\alpha_s)$ corrections to the $b \to b'j$ splittings, in the PSS formalism. Moreover, note that in Eqs. (3.147)-(3.149) we have carefully separated the dependence on the factorization (μ_f) and

100

renormalization scale (μ_r). It is understood that $\alpha_s = \alpha_s(\mu_r)$. The definition of the subtracted PDFs is indeed the only place where both scales play a role, and the only place where we have a dependence on μ_f. In the rest of this chapter we have always set $\mu_r = \mu_f = \mu$ and we will also give the master formulas for the total NLO cross section, Eqs. (3.151)-(3.156), using $\mu_r = \mu_f = \mu$. We have checked that this simplifying assumption has a negligible effect on our results and we will comment more about this in Section 3.6.

In the two-cutoff PSS method, when convoluting the parton gg cross section with the renormalized gluon distribution function of Eq. (3.148), the IR singular counterterm of Eq. (3.148) exactly cancels the remaining IR poles of $\hat{\sigma}^{gg}_{virt} + \hat{\sigma}^{gg}_{soft}$ and $\hat{\sigma}^{gg}_{hard/coll}$. In the one-cutoff PSS method, the IR singular counterterm of Eq. (3.149) exactly cancels the IR poles of $\hat{\sigma}^{gg}_{crossing}$. Finally, the complete $\mathcal{O}(\alpha_s^3)$ inclusive total cross section for $pp \to t\bar{t}h$ in the $\overline{MS}$ factorization scheme when only the gg initial state is included, i.e. $\sigma^{gg}_{NLO}(pp \to t\bar{t}h)$ of Eq. (3.146), can be written as follows:

two-cutoff PSS method

$$
\begin{aligned}
\sigma^{gg}_{NLO} = {} & \frac{1}{2} \int dx_1 dx_2 \left\{ \mathcal{F}^p_g(x_1, \mu)\mathcal{F}^p_g(x_2, \mu) \left[\hat{\sigma}^{gg}_{LO}(x_1, x_2, \mu) + (\hat{\sigma}^{gg}_{virt})_{finite}(x_1, x_2, \mu) \right. \right. \\
& \left. \left. + (\hat{\sigma}^{gg}_{soft})_{finite}(x_1, x_2, \mu) + \hat{\sigma}^{gg}_{s+v+ct}(x_1, x_2, \mu) + (1 \leftrightarrow 2) \right] \right\} \\
& + \frac{1}{2} \int dx_1 dx_2 \left\{ \int_{x_1}^{1-\delta_s} \frac{dz}{z} \left[\mathcal{F}^p_g(\frac{x_1}{z}, \mu)\mathcal{F}^p_g(x_2, \mu) + \mathcal{F}^p_g(x_2, \mu)\mathcal{F}^p_g(\frac{x_1}{z}, \mu) \right] \right. \\
& \left. \times \hat{\sigma}^{gg}_{LO}(x_1, x_2, \mu)\frac{\alpha_s}{2\pi} \ln \left(\frac{s}{\mu^2}\frac{(1-z)^2}{z}\frac{\delta_c}{2} \right) P_{gg}(z) + (1 \leftrightarrow 2) \right\} \\
& + \frac{1}{2} \int dx_1 dx_2 \left\{ \mathcal{F}^p_g(x_1, \mu)\mathcal{F}^p_g(x_2, \mu)\, \hat{\sigma}^{gg}_{hard/non-coll}(x_1, x_2, \mu) + (1 \leftrightarrow 2) \right\} \;,
\end{aligned}
$$

$$(3.151)$$

where $\hat{\sigma}^{gg}_{s+v+ct}$ is obtained from the sum of $(\hat{\sigma}^{gg}_{virt})_{UV-pole}$ of Eq. (3.42), $\hat{\sigma}^{gg}_{s+v}$ of Eq. (3.67), and the PDF counterterm in Eq. (3.148) as follows

$$\hat{\sigma}_{s+v+ct}^{gg} = \frac{\alpha_s}{2\pi} \left[4N \ln(\delta_s) \ln\left(\frac{s}{\mu^2}\right) + \left(\frac{11}{3}N - \frac{2n_{lf}}{3} + 4N \ln(\delta_s)\right) \ln\left(\frac{m_t^2}{s}\right) \right] \hat{\sigma}_{LO}^{gg} .$$

(3.152)

one-cutoff PSS method

$$\sigma_{NLO}^{gg} = \frac{1}{2} \int dx_1 dx_2 \left\{ \mathcal{F}_g^p(x_1, \mu) \mathcal{F}_g^p(x_2, \mu) \left[\hat{\sigma}_{LO}^{gg}(x_1, x_2, \mu) + (\hat{\sigma}_{virt}^{gg})_{finite}(x_1, x_2, \mu) \right. \right.$$
$$+ \left. (\hat{\bar{\sigma}}_{ir}^{gg})_{finite}(x_1, x_2, \mu) + \hat{\sigma}_{v+ir+ct}^{gg}(x_1, x_2, \mu) + (1 \leftrightarrow 2) \right] \right\}$$
$$+ \frac{1}{2} \int dx_1 dx_2 \left\{ \int_{x_1}^1 \frac{dz}{z} \left[\mathcal{F}_g^p(\frac{x_1}{z}, \mu) \mathcal{F}_g^p(x_2, \mu) + \mathcal{F}_g^p(x_2, \mu) \mathcal{F}_g^p(\frac{x_1}{z}, \mu) \right] \right.$$
$$\times \hat{\sigma}_{LO}^{gg}(x_1, x_2, \mu) \frac{\alpha_s}{2\pi} 2N \ln\left(\frac{s}{\mu^2} \frac{s_{min}}{s}\right) \left(\frac{z}{(1-z)_+} + \frac{1-z}{z} + z(1-z)\right)$$
$$+ (1 \leftrightarrow 2) \bigg\}$$
$$+ \frac{1}{2} \int dx_1 dx_2 \left\{ \int_{x_1}^1 \frac{dz}{z} \left[\mathcal{F}_g^p(\frac{x_1}{z}, \mu) \mathcal{F}_g^p(x_2, \mu) + \mathcal{F}_g^p(x_2, \mu) \mathcal{F}_g^p(\frac{x_1}{z}, \mu) \right] \right.$$
$$\times \hat{\sigma}_{LO}^{gg}(x_1, x_2, \mu) \frac{\alpha_s}{2\pi} 2N \left[\left(\frac{1-z}{z} + z(1-z)\right) \ln(1-z) + z \left(\frac{\ln(1-z)}{1-z}\right)_+ \right]$$
$$+ (1 \leftrightarrow 2) \bigg\}$$
$$+ \frac{1}{2} \int dx_1 dx_2 \left\{ \mathcal{F}_g^p(x_1, \mu) \mathcal{F}_g^p(x_2, \mu) \hat{\sigma}_{hard}^{gg}(x_1, x_2, \mu) + (1 \leftrightarrow 2) \right\} ,$$

(3.153)

where $\hat{\sigma}_{v+ir+ct}^{gg}$ is obtained from the sum of $(\hat{\sigma}_{virt}^{gg})_{UV-pole}$ of Eq. (3.42), $(\hat{\sigma}_{virt}^{gg})_{IR-pole}$ of Eq. (3.49), $(\hat{\bar{\sigma}}_{ir}^{gg})_{pole}$ of Eq. (3.136), the part proportional to $\delta(1-z)$ of $\hat{\sigma}_{crossing}^{gg}$ of Eq. (3.138), and the PDF counterterm in Eq. (3.149), and can be written as:

$$\hat{\sigma}_{v+ir+ct}^{gg} = \frac{\alpha_s}{2\pi} \left[\left(\frac{11}{3}N - \frac{2n_{lf}}{3}\right) \ln\left(\frac{s_{min}}{s}\right) + 2N \left(\frac{\pi^2}{3} - \frac{67}{18} + \frac{5n_{lf}}{9N}\right) \right] \hat{\sigma}_{LO}^{gg} . \quad (3.154)$$

We note that σ_{NLO}^{gg} is finite, since, after mass factorization, both soft and collinear singularities have been canceled between $\hat{\sigma}_{virt}^{gg} + \hat{\sigma}_{soft}^{gg}$ and $\hat{\sigma}_{hard/coll}^{gg}$ in the two-cutoff PSS method, and between $\hat{\sigma}_{virt}^{gg}$ and $\hat{\bar{\sigma}}_{ir}^{gg}$ in the one-cutoff PSS method. The last terms

102

respectively describe the finite real gluon emission of Eq. (3.51) and (3.81). Note that when collecting all the terms in Eqs. (3.151) and (3.153) that are proportional to $\ln(\mu^2/s)$, one obtains exactly the last two terms in Eq. (3.5), as predicted by renormalization group arguments.

For the $(q, \bar{q})g$ initiated processes we find:

two-cutoff PSS method

$$
\sigma_{NLO}^{qg} = \frac{\alpha_s}{2\pi} \sum_{i=q,\bar{q}} \int dx_1 dx_2 \Bigg\{ \int_{x_1}^{1} \frac{dz}{z} \mathcal{F}_i^p(\frac{x_1}{z}, \mu) \mathcal{F}_g^p(x_2, \mu) \times
$$

$$
\hat{\sigma}_{LO}^{gg}(x_1, x_2, \mu) \left[P_{ig}^4(z) \ln \left(\frac{s}{\mu^2} \frac{(1-z)^2}{z} \frac{\delta_c}{2} \right) - P_{ig}'(z) \right]
$$

$$
+ \int_{x_1}^{1} \frac{dz}{z} \mathcal{F}_g^p(\frac{x_1}{z}, \mu) \mathcal{F}_i^p(x_2, \mu) \times
$$

$$
\hat{\sigma}_{LO}^{q\bar{q}}(x_1, x_2, \mu) \left[P_{gi}^4(z) \ln \left(\frac{s}{\mu^2} \frac{(1-z)^2}{z} \frac{\delta_c}{2} \right) - P_{gi}'(z) \right] + (1 \leftrightarrow 2) \Bigg\}
$$

$$
+ \sum_{i=q,\bar{q}} \int dx_1 dx_2 \left\{ \mathcal{F}_i^p(x_1, \mu) \mathcal{F}_g^p(x_2, \mu) \, \hat{\sigma}_{non-coll}^{qg}(x_1, x_2, \mu) + (1 \leftrightarrow 2) \right\} \;,
$$

$$
(3.155)
$$

one-cutoff PSS method

$$
\sigma_{NLO}^{qg} = \frac{\alpha_s}{2\pi} \sum_{i=q,\bar{q}} \int dx_1 dx_2 \Bigg\{ \int_{x_1}^{1} \frac{dz}{z} \mathcal{F}_g^p(\frac{x_1}{z}, \mu) \mathcal{F}_i^p(x_2, \mu) \times
$$

$$
\hat{\sigma}_{LO}^{gg}(x_1, x_2, \mu) \left[P_{ig}^4(z) \ln \left(\frac{s_{min}(1-z)}{\mu^2} \right) - P_{ig}'(z) \right]
$$

$$
+ \int_{x_1}^{1} \frac{dz}{z} \mathcal{F}_i^p(\frac{x_1}{z}, \mu) \mathcal{F}_g^p(x_2, \mu) \times
$$

$$
\hat{\sigma}_{LO}^{q\bar{q}}(x_1, x_2, \mu) \left[P_{gi}^4(z) \ln \left(\frac{s_{min}(1-z)}{\mu^2} \right) - P_{gi}'(z) \right] + (1 \leftrightarrow 2) \Bigg\}
$$

$$
+ \sum_{i=q,\bar{q}} \int dx_1 dx_2 \left\{ \mathcal{F}_i^p(x_1, \mu) \mathcal{F}_g^{\bar{p}}(x_2, \mu) \, \hat{\sigma}_{hard}^{qg}(x_1, x_2, \mu) + (1 \leftrightarrow 2) \right\} \;,
$$

$$
(3.156)
$$

103

where P_{ij}^4 and P'_{ij} are the $\mathcal{O}(1)$ and $\mathcal{O}(\epsilon)$ contributions to the splitting functions as given in Eq. (3.78). The last terms respectively describe the finite gluon/quark emission of Eqs. (3.52) and (3.81).

We would like to conclude this section by showing explicitly that the total NLO cross section, σ_{NLO}, does not depend on the arbitrary cutoffs introduced by the PSS method, i.e. on s_{min} for the one-cutoff method and on δ_s and δ_c for the two-cutoff method. The cancellation of the PSS cutoff dependence is realized in σ_{real} by matching contributions that are calculated either analytically, in the IR-unsafe region below the cutoff(s), or numerically, in the IR-safe region above the cutoff(s). While the analytical calculation in the IR-unsafe region reproduces the form of the cross section in the soft or collinear limits and is therefore only accurate for small values of the cutoff(s), the numerical integration in the IR-safe region becomes unstable for very small values of the cutoff(s). Therefore, obtaining a convincing cutoff independence involves a delicate balance between the previous antagonistic requirements and ultimately dictates the choice of neither too large nor too small values for the cutoff(s). The Monte Carlo phase space integration has been performed using the adaptive multi-dimensional integration program VEGAS [73] as well as multichannel integration techniques [74, 75, 76].

In Figs. 3.18 and 3.19 we consider the two-cutoff PSS method and study the independence of $\sigma_{NLO}(pp \to t\bar{t}h)$ on δ_s and δ_c separately, by varying only one of the two cutoffs while the other is kept fixed. In Fig. 3.18, δ_s is varied between 10^{-5} and 10^{-3} with $\delta_c = 10^{-5}$, while in Fig. 3.19, δ_c is varied between 10^{-6} and 10^{-4} with $\delta_s = 10^{-4}$. In both plots, we show in the upper window the overall cutoff dependence cancellation between $\sigma_{soft}^{gg} + \sigma_{hard/coll}^{gg}$ and $\sigma_{hard/non-coll}^{gg}$ in σ_{real}^{gg}. We do not include the corresponding contributions from the Born and the virtual cross sections since they are, of course, cutoff independent. Similar plots could be obtained for the other two subchannels, $q\bar{q}$ and $qg + \bar{q}g$. We illustrate the point using just the gg channel, since the $q\bar{q}$ channel has already been presented in Section 3.5.1, while the cutoff

104
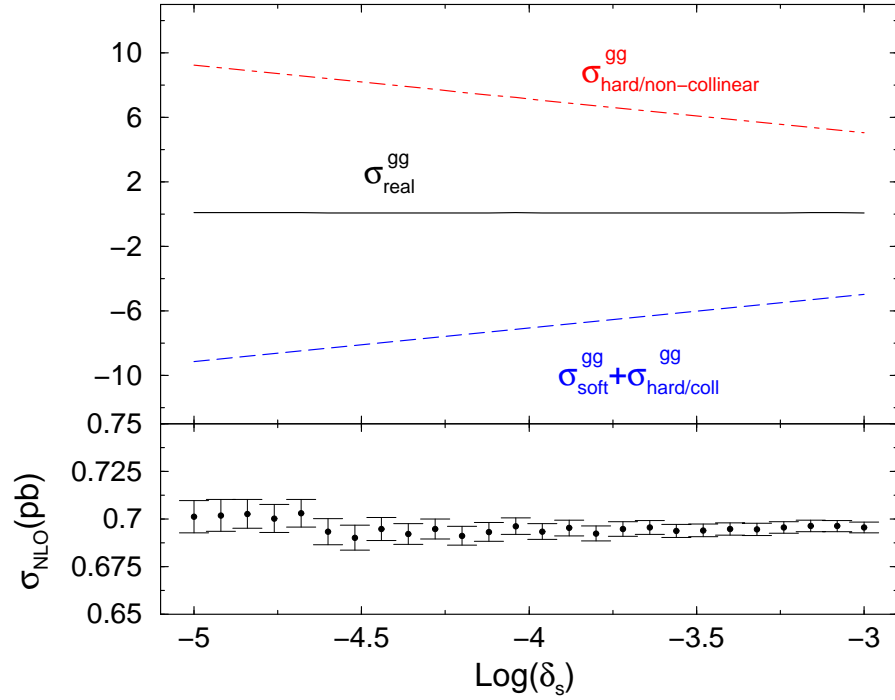
Figure 3.18. Dependence of $\sigma_{NLO}(pp \to t\bar{t}h)$ on the soft cutoff δ_s of the two-cutoff PSS method, at $\sqrt{s_H} = 14$ TeV, for $M_h = 120$ GeV, $\mu = m_t + M_h/2$, and $\delta_c = 10^{-5}$. The upper plot shows the cancellation of the δ_s-dependence between $\sigma_{soft}^{gg} + \sigma_{hard/coll}^{gg}$ and $\sigma_{hard/non-coll}^{gg}$. The lower plot shows, on an enlarged scale, the dependence of the full $\sigma_{NLO} = \sigma_{NLO}^{gg} + \sigma_{NLO}^{q\bar{q}} + \sigma_{NLO}^{qg}$ on δ_s with the corresponding statistical errors.

dependence of the $qg + \bar{q}g$ channel is trivial. In the lower window of the same plots we complement this information by reproducing the full σ_{NLO}, including all channels, on a larger scale that magnifies the details of the cutoff dependence cancellation. The statistical errors from the Monte Carlo phase space integration are also shown. Both Figs. 3.18 and 3.19 show a clear plateau over a wide range of δ_s and δ_c and the NLO cross section is proven to be cutoff independent. The results presented in Section 3.6 have been obtained by using the two-cutoff PSS method with $\delta_s = 10^{-4}$ and $\delta_c = 10^{-5}$.
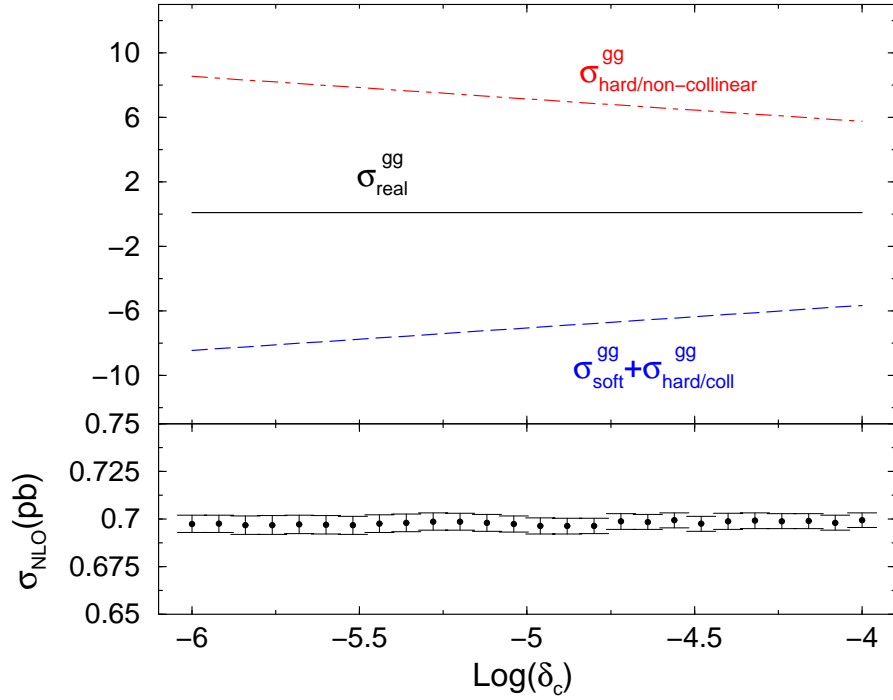
Figure 3.19. Dependence of $\sigma_{NLO}(pp \rightarrow t\bar{t}h)$ on the collinear cutoff δ_c of the two-cutoff PSS method, at $\sqrt{s_H} = 14$ TeV, for $M_h = 120$ GeV, $\mu = m_t + M_h/2$, and $\delta_s = 10^{-4}$. The upper plot shows the cancellation of the δ_s-dependence between $\sigma^{gg}_{soft} + \sigma^{gg}_{hard/coll}$, and $\sigma^{gg}_{hard/non-coll}$. The lower plot shows, on an enlarged scale, the dependence of the full $\sigma_{NLO} = \sigma^{gg}_{NLO} + \sigma^{q\bar{q}}_{NLO} + \sigma^{qg}_{NLO}$ on δ_c with the corresponding statistical errors.

We now turn to the one-cutoff PSS method and, following the same criterion adopted for the case of the two-cutoff PSS method, we summarize in the upper window of Fig. 3.20 the behavior of the different cutoff dependent contributions to the real $gg \rightarrow t\bar{t}h$ cross section, i.e. σ^{gg}_{ir} and σ^{gg}_{hard}, as well as the resulting cutoff independence of σ^{gg}_{real}. The lower window of Fig. 3.20 shows the full σ_{NLO}, where all $t\bar{t}h$ subprocesses are included, on an enlarged scale. The statistical deviations due to the Monte Carlo integration are also shown, and therefore the stability of the integration procedure can be appreciated. In Fig. 3.20 s_{min} is varied over several orders of magnitude and the presence of a clear plateau over most of the s_{min} range

106
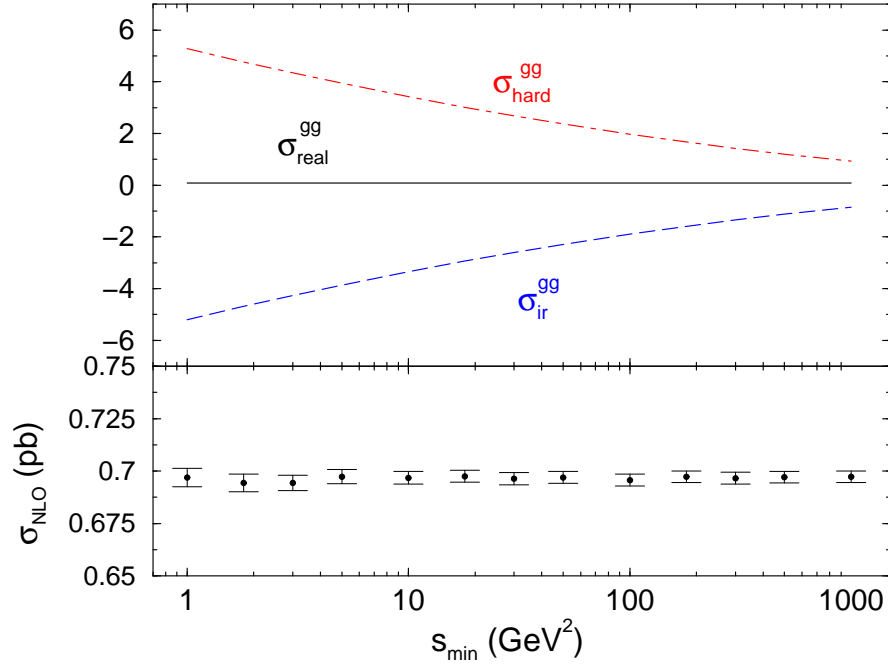
Figure 3.20. Dependence of $\sigma_{NLO}(pp \to t\bar{t}h)$ on the s_{min} cutoff of the one-cutoff PSS method, at $\sqrt{s_H} = 14$ TeV, for $M_h = 120$ GeV, and $\mu = m_t + M_h/2$. The upper plot shows the cancellation of the s_{min}-dependence between σ_{ir}^{gg} and σ_{hard}^{gg}. The lower plot shows, on an enlarged scale, the dependence of the full $\sigma_{NLO} = \sigma_{NLO}^{gg} + \sigma_{NLO}^{q\bar{q}} + \sigma_{NLO}^{qg}$ on s_{min} with the corresponding statistical errors.

is evident. The results presented in Section 3.6 have been cross-checked using the one-cutoff PSS method with $s_{min} = 10$ GeV^2.

3.6 Numerical results

3.6.1 Results for the Tevatron: $p\bar{p} \to t\bar{t}h$

In the following we discuss in detail the results for the NLO inclusive total cross section for $p\bar{p} \to t\bar{t}h$, $\sigma_{NLO}(p\bar{p} \to t\bar{t}h)$, as introduced in Sect. 3.1 and explicitly given by Eqs. (3.143) and (3.145). These numerical results are found using CTEQ4M parton distribution functions [77] and the 2-loop evolution of $\alpha_s(\mu)$ for the calculation

of the NLO cross section, and CTEQ4L parton distribution functions and the 1-loop evolution of $\alpha_s(\mu)$ for the calculation of the lowest order cross section, unless stated otherwise.[2] The top-quark mass is taken to be $m_t = 174$ GeV and $\alpha_s^{NLO}(M_Z) = 0.116$.
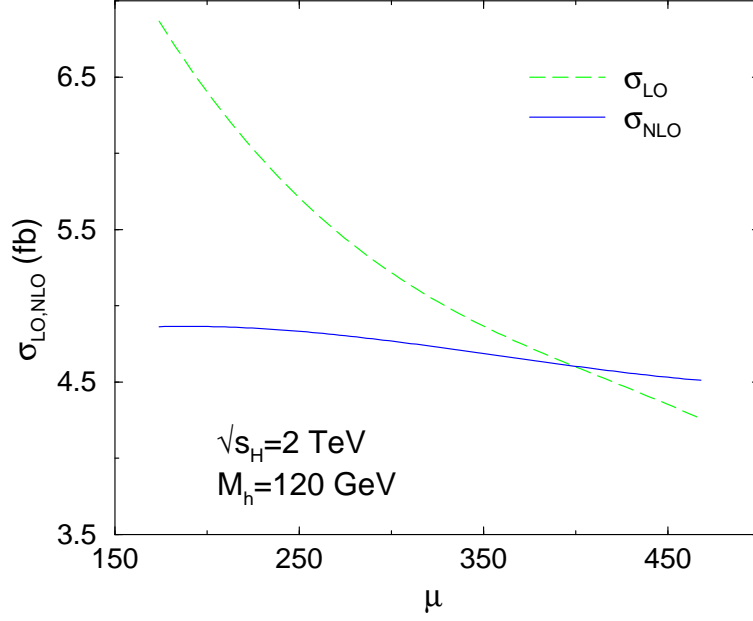
Figure 3.21. Dependence of $\sigma_{LO,NLO}(p\bar{p} \rightarrow t\bar{t}h)$ on the renormalization/factorization scale μ, at $\sqrt{s_H} = 2$ TeV, for $M_h = 120$ GeV.

First of all, in Fig. 3.21 we show how at NLO the dependence on the arbitrary renormalization/factorization scale μ is significantly reduced. We use $M_h = 120$ GeV for illustration purposes. We note that only for scales μ of the order of $2m_t + M_h$ or bigger is the NLO result greater than the lowest order result at $\sqrt{s_H} = 2$ TeV[3].

Fig. 3.22 shows both the LO and the NLO total cross section for $p\bar{p} \rightarrow t\bar{t}h$ as a function of M_h, at $\sqrt{s_H} = 2$ TeV, for two values of the renormalization/factorization

---

[2]Since these PDF sets have been updated after the publication of this investigation, we have checked that using current PDF sets (CTEQ6) does not have a significant effect on the results presented here and hence we have not updated our plots.

[3]Original design CM energy for Run II at the Tevatron
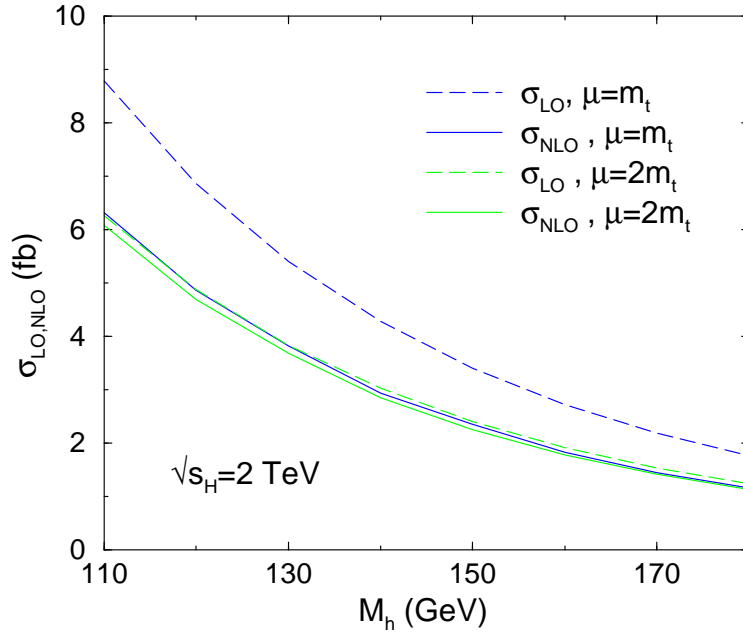
Figure 3.22. σ_{NLO} and σ_{LO} for $p\overline{p} \to t\overline{t}h$ as functions of M_h, at $\sqrt{s_H} = 2$ TeV, for $\mu = m_t$ and $\mu = 2m_t$.

scale, $\mu = m_t$ and $\mu = 2m_t$. Over the entire range of M_h accessible at the Tevatron, the NLO corrections decrease the rate for renormalization/factorization scales $\mu < 2m_t + M_h$. The reduction is much less dramatic at $\mu = 2m_t$ than at $\mu = m_t$, as can be seen from both Fig. 3.21 and Fig. 3.22. An illustrative sample of results is also given in Table 1. The error we quote on our values is the statistical error of the numerical integration involved in evaluating the total cross section. We estimate the remaining theoretical uncertainty on the NLO results to be of the order of 12%. This is mainly due to: the left over μ-dependence (about 8%), the dependence on the PDFs (about 6%), and the error on m_t (about 7%) which particularly plays a role in the Yukawa coupling.

The corresponding K-factor, i.e. the ratio of the NLO cross section to the LO one,
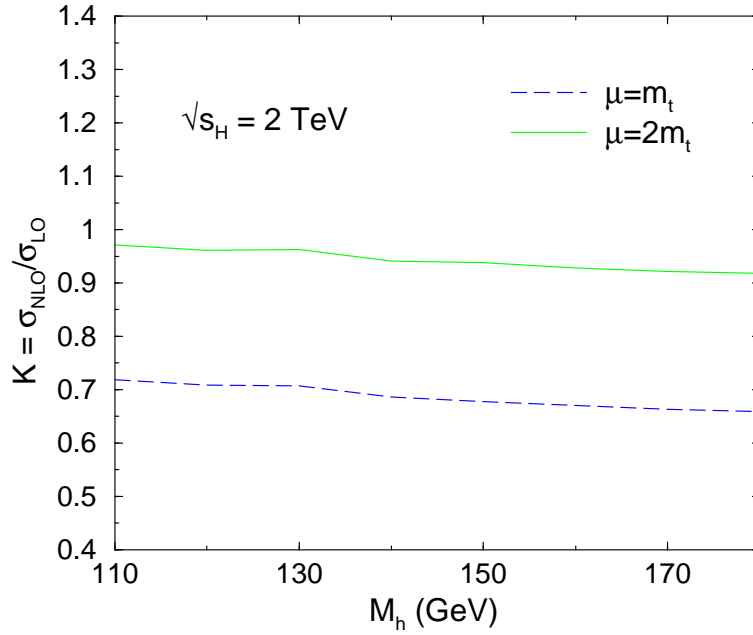
Figure 3.23. K-factor for $p\bar{p} \to t\bar{t}h$ as a function of M_h, at $\sqrt{s_H}=2$ TeV, for $\mu = m_t$ and $\mu = 2m_t$.

$$K = \frac{\sigma_{NLO}}{\sigma_{LO}} \ , \tag{3.157}$$

is shown in Fig. 3.23. For scales μ between $\mu = m_t$ and $\mu = 2m_t$, the K-factor varies roughly between $K = 0.70$ and $K = 0.95$, when M_h varies in the range between 100 and 200 GeV. For scales of the order of $\mu = 2m_t + M_h$ the K-factor is of order one and becomes larger than one for higher scales. Given the strong scale dependence of the LO cross section, the K-factor also shows a significant μ-dependence and therefore is an equally unreliable prediction. Moreover it is important to remember that the K-factor depends on how the LO cross section is calculated. We choose to calculate the LO cross section using both LO $\alpha_s(\mu)$ and LO PDFs, denoted by σ_{LO} in Table 1. An equally valid approach could be to evaluate the LO cross section using NLO $\alpha_s(\mu)$ and NLO PDFs, denoted by $\bar{\sigma}_{LO}$ in Table 1, in which case the K-factor would just represent the impact of the $\mathcal{O}(\alpha_s)$ corrections that do not originate from the

110

Table 3.1. Values of both σ_{LO} (calculated with LO $\alpha_s(\mu)$ and LO PDFs), $\bar{\sigma}_{LO}$ (calculated with NLO $\alpha_s(\mu)$ and NLO PDFs), and σ_{NLO} for different values of M_h and for different renormalization/factorization scales μ.

M_h (GeV)	μ	σ_{LO} (fb)	$\bar{\sigma}_{LO}$ (fb)	σ_{NLO} (fb)
120	m_t	6.8662 ± 0.0013	5.2843 ± 0.0008	4.863 ± 0.029
	$m_t + M_h/2$	5.9085 ± 0.0011	4.5846 ± 0.0007	4.847 ± 0.024
	$2m_t$	4.8789 ± 0.0009	3.8252 ± 0.0006	4.691 ± 0.020
	$2m_t + M_h$	4.2548 ± 0.0008	3.3600 ± 0.0005	4.511 ± 0.017
150	m_t	3.4040 ± 0.0006	2.5811 ± 0.0005	2.355 ± 0.013
	$m_t + M_h/2$	2.8289 ± 0.0005	2.1668 ± 0.0004	2.315 ± 0.011
	$2m_t$	2.4007 ± 0.0004	1.8553 ± 0.0004	2.253 ± 0.010
	$2m_t + M_h$	2.0282 ± 0.0004	1.5813 ± 0.0003	2.147 ± 0.008
180	m_t	1.7605 ± 0.0003	1.3153 ± 0.0002	1.160 ± 0.007
	$m_t + M_h/2$	1.4142 ± 0.0003	1.0693 ± 0.0002	1.158 ± 0.005
	$2m_t$	1.2326 ± 0.0002	0.9390 ± 0.0001	1.132 ± 0.004
	$2m_t + M_h$	1.0096 ± 0.0002	0.7773 ± 0.0001	1.069 ± 0.004

running of $\alpha_s(\mu)$ and the PDFs. Since $\sigma_{LO} > \bar{\sigma}_{LO}$, the K-factor obtained using σ_{LO} is smaller than the one obtained using $\bar{\sigma}_{LO}$, and it is important to match the right K-factor to the right σ_{LO} or $\bar{\sigma}_{LO}$. Therefore we would like to stress once more that we only discuss the K-factor as a qualitative indication of the impact of $\mathcal{O}(\alpha_s)$ QCD corrections, for different processes or when using different approaches. The physical meaningful quantity is the NLO cross section, not the K-factor.

It is interesting to compare our NLO result for $p\bar{p} \to t\bar{t}h$ with the NLO result for $p\bar{p} \to t\bar{t}$. Since the Higgs boson is colorless, one would naively expect the QCD corrections to both processes to be of roughly the same size. Defining the NLO cross section using the NLO evolution of $\alpha_s(\mu)$ and the NLO CTEQ4M PDFs, and the LO cross section using the LO evolution of $\alpha_s(\mu)$ and the LO CTEQ4L PDFs, the K-factor for $t\bar{t}$ production at $\sqrt{s_H} = 2$ TeV, with $\mu = m_t$ and $m_t = 174$ GeV, is:

$$K(p\bar{p} \to t\bar{t})\mid_{q\bar{q}} = 0.98 \ ,$$

$$K(p\bar{p} \to t\bar{t})\mid_{tot} = 1.05 \ , \tag{3.158}$$

111

where the $q\bar{q}$ label indicates that only the $q\bar{q}$ initial state is included. The size of the QCD corrections to $p\bar{p} \to t\bar{t}$ is thus similar in magnitude to the result obtained in Fig. 3.23, taking into account that $p\bar{p} \to t\bar{t}h$ is completely dominated by the $q\bar{q}$ channel. Of course, we do not expect a better agreement, since in $p\bar{p} \to t\bar{t}h$ an additional heavy particle is produced, and new contributions to the virtual corrections arise. Moreover, taking the EHA as an indication, one could naively expect that the radiation of a Higgs boson introduces an additional negative contribution. We also observe that, if we now use as LO cross section the one obtained using NLO $\alpha_s(\mu)$ and NLO CTEQ4M PDFs, the two K-factors in Eq. (3.158) increase, according to the comment we made above, and become:

$$K(p\bar{p} \to t\bar{t})\,|_{q\bar{q}} = 1.18 \ ,$$

$$K(p\bar{p} \to t\bar{t})\,|_{tot} = 1.24 \ , \qquad (3.159)$$

in agreement with the literature [78][4]. Moreover, since the NLO cross section for $p\bar{p} \to t\bar{t}$ is further increased by the resummation of the leading and next-to-leading logarithms arising from the threshold region dynamics, the total K-factor for $p\bar{p} \to t\bar{t}$ can be as high as 1.33 for $\mu = m_t$. With this respect, we also note that, contrary to $p\bar{p} \to t\bar{t}$, in the threshold region for $p\bar{p} \to t\bar{t}h$ there are large negative contributions, mainly from soft gluon radiation, which are largely compensated by large positive contributions from hard gluon radiation at larger $\sqrt{s}$. In the threshold region the Coulomb term, coming from the exchange of virtual gluons between the $t/\bar{t}$ external legs, is important and contributes to decrease the NLO cross section, although it is moderated by the behavior of the three-body phase space. In the strict threshold limit, the Coulomb contribution to $p\bar{p} \to t\bar{t}h$ goes to zero, while for $t\bar{t}$ production it is constant and dominates the NLO cross section.

---

[4]We have compared our results with Fig. 9 of Ref. [78], and we see very good agreement with the LO and the NLO curves, using $m_t = 175$ GeV and $\sqrt{s_H} = 1.8$ TeV.

3.6.2 Results for the LHC: $pp \rightarrow t\bar{t}h$

In this section we summarize the most important numerical results for $\sigma_{NLO}(pp \rightarrow t\bar{t}h)$ and illustrate the impact of NLO QCD corrections on the tree level cross section. In particular, we discuss the renormalization/factorization scale dependence of σ_{NLO} with respect to σ_{LO}, and illustrate the dependence of both LO and NLO cross sections on the Higgs boson mass. Results for σ_{LO} are obtained using the 1-loop evolution of $\alpha_s(\mu)$ and CTEQ5L parton distribution functions [79], while results for σ_{NLO} are obtained using the 2-loop evolution of $\alpha_s(\mu)$ and CTEQ5M parton distribution functions, with $\alpha_s^{NLO}(M_Z) = 0.118$ [5]. According to the renormalization prescription adopted in this chapter and explained in Section 3.3.1.2, throughout our calculation we use for the input parameter m_t the top quark pole mass. Results are presented for $m_t = 174$ GeV, while the uncertainty introduced by varying m_t within its experimental uncertainty is discussed later in this section. We define the top quark Yukawa coupling to be $g_{t\bar{t}h} = m_t/v$ where $v = (G_F\sqrt{2})^{-1/2} = 246$ GeV is the vacuum expectation value of the SM Higgs field, given in terms of the Fermi constant G_F.

In Fig. 3.24, we illustrate the dependence of both σ_{NLO} and σ_{LO} on the renormalization and factorization scales when the two scales are identical, i.e. when $\mu_r = \mu_f = \mu$. We have also studied the behavior of σ_{NLO} when the renormalization and factorization scales are varied independently and noticed no appreciable difference with respect to the case in which the two scales are identical. This justifies our decision to present results only for $\mu_r = \mu_f = \mu$. We also illustrate in Fig. 3.25 the μ dependence of the NLO cross section for each parton level channel independently. We use $M_h = 120$ GeV for the purpose of these plots. As expected, Fig. 3.24 shows that the NLO cross section has a much weaker scale dependence and represents a much more stable theoretical prediction. In Fig. 3.26, we plot $\sigma_{LO}(pp \rightarrow t\bar{t}h)$

---

[5]Again, we have checked our results using the current PDF sets (CTEQ6) and we do not oberve any significant effects.
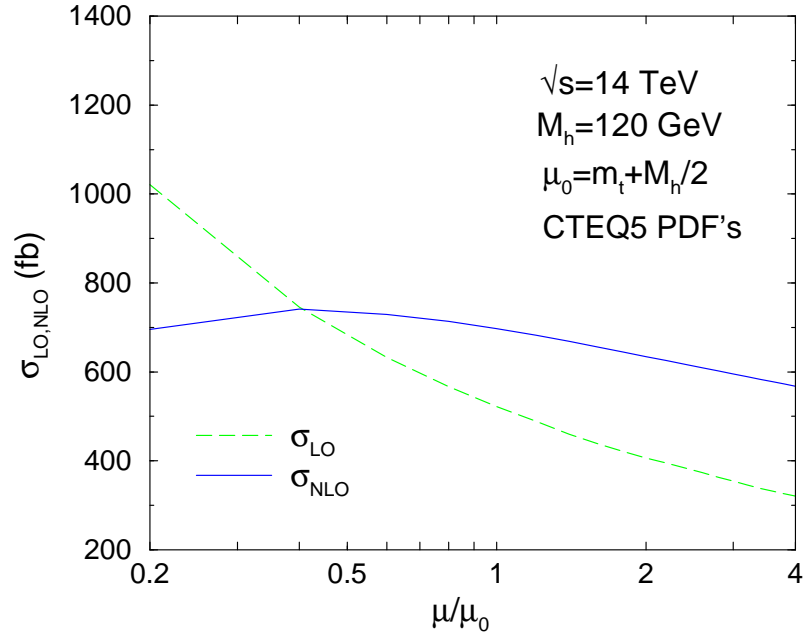
Figure 3.24. Dependence of $\sigma_{LO,NLO}(pp \to t\bar{t}h)$ on the renormalization/factorization scale μ, at $\sqrt{s_H} = 14$ TeV, for $M_h = 120$ GeV.

and $\sigma_{NLO}(pp \to t\bar{t}h)$ as functions of the Higgs boson mass, for $\sqrt{s_H} = 14$ TeV and two values of the common renormalization/factorization scale, $\mu = m_t + M_h/2$ and $\mu = 2m_t + M_h$. We consider $100\,\mathrm{GeV} \leq M_h \leq 200\,\mathrm{GeV}$ since the production of a Higgs boson in association with a pair of top quarks at the LHC will play a crucial role only for relatively light Higgs bosons. The information gathered from this plot nicely complements what has already been shown in Fig. 3.24. We summarize a sample of results from both Figs. 3.24 and 3.26 in Table 3.2, where we also provide the LO cross section, $\bar{\sigma}_{LO}$, calculated using the 2-loop evolution of $\alpha_s(\mu)$ and CTEQ5M PDFs. This can be useful to separately evaluate the impact of the full set of NLO QCD corrections as opposed to the subset of them that mainly correspond to the NLO running of $\alpha_s(\mu)$. The error we quote on our values is the statistical error of the numerical integration involved in evaluating the total cross section. We estimate the

114
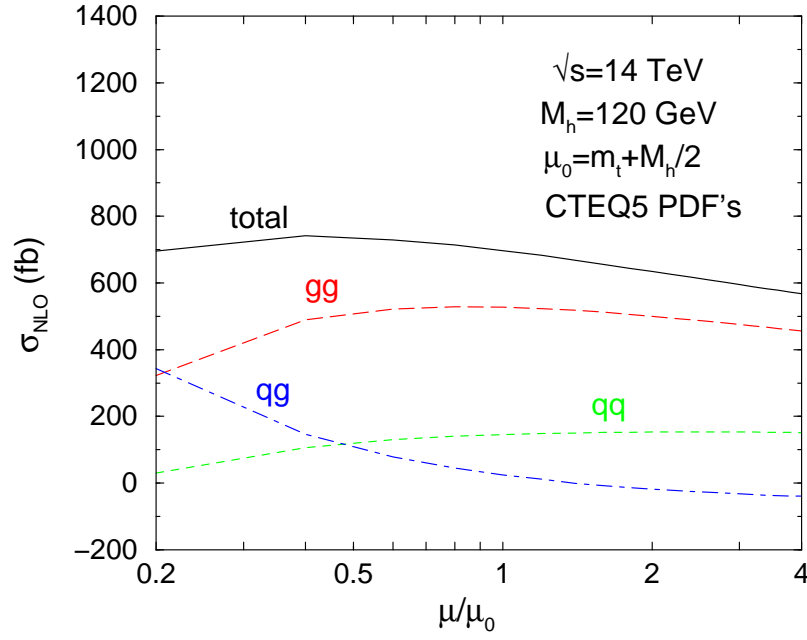
Figure 3.25. Dependence of $\sigma_{NLO}(gg, q\bar{q}, qg + \bar{q}g \rightarrow t\bar{t}h)$ on the renormalization/factorization scale μ, at $\sqrt{s_H} = 14$ TeV, for $M_h = 120$ GeV.

remaining theoretical uncertainty on the NLO results to be of the order of $15-20\%$. This is mainly due to: the left over μ-dependence (about 15%), the dependence on the PDFs (about 6%), and the error on m_t (about 7%) which particularly plays a role in the top quark Yukawa coupling.

It can also be useful to quote the impact of NLO corrections in terms of the K-factor defined in Eq. (3.157). We can see in Fig. 3.24 that, for a SM Higgs boson of mass $M_h = 120$ GeV, the K-factor for $pp \rightarrow t\bar{t}h$ is larger than unity when $\mu \geq 0.4\mu_0$ for $\mu_0 = m_t + M_h/2$. Therefore, over a broad range of the commonly used renormalization/factorization scales, NLO QCD corrections increase the LO cross section. Using the results of Table 3.2, the K-factors for a sample of Higgs boson masses and renormalization/factorization scales can easily be calculated, both using σ_{LO} and $\overline{\sigma}_{LO}$. We notice, however, that the K-factor defined in Eq. (3.157) is
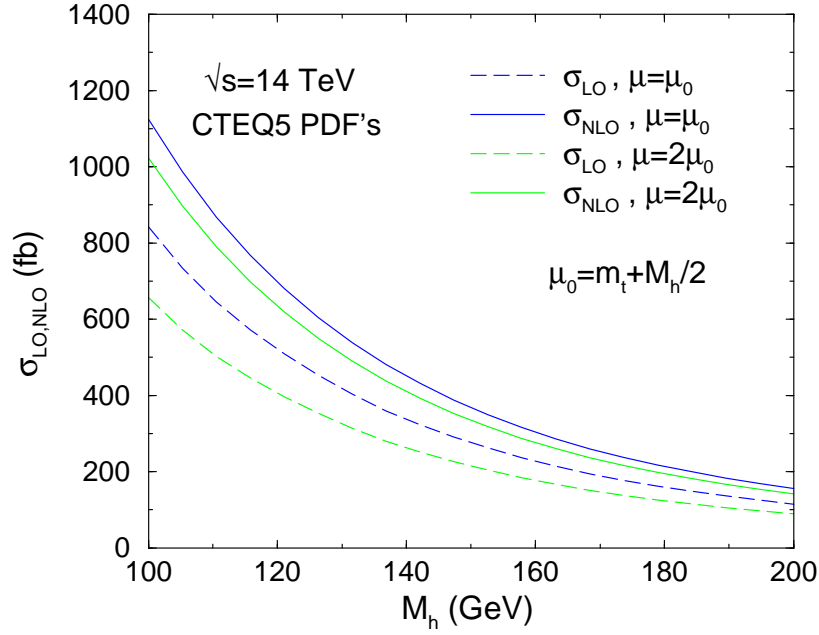
Figure 3.26. $\sigma_{NLO}(pp \rightarrow t\bar{t}h)$ and $\sigma_{LO}(pp \rightarrow t\bar{t}h)$ as functions of M_h, at $\sqrt{s_H} = 14$ TeV, for $\mu = m_t + M_h/2$ and $\mu = 2m_t + M_h$.

affected by a very strong scale dependence, the same as σ_{LO}. Therefore, when the K-factor is used to obtain σ_{NLO} from σ_{LO}, care must be used in matching σ_{LO} and K corresponding to the same μ-scale.

3.7   Summary

The associated production of a Higgs boson with a pair of top quarks will play a crucial role in the discovery of a light SM-like Higgs boson at current and future experiments. Although it is probably at the edge of the machine capabilities of the Tevatron, this channel could be important for discovery of a low mass Higgs boson given enough luminosity. If this channel is not observed at the Tevatron, it will definitely be instrumental in the discovery of a SM-like Higgs boson at the LHC. With the statistics expected at the LHC, $pp \rightarrow t\bar{t}h$, with $h \rightarrow b\bar{b}, \tau^+\tau^-, W^+W^-, \gamma\gamma$

Table 3.2. Values of both $\sigma_{LO}(pp \rightarrow t\bar{t}h)$, $\overline{\sigma}_{LO}(pp \rightarrow t\bar{t}h)$, and $\sigma_{NLO}(pp \rightarrow t\bar{t}h)$, at $\sqrt{s_H} = 14$ TeV, for a sample of different values of M_h and of the renormalization/factorization scales $\mu = \mu_r = \mu_f$.

M_h (GeV)	μ	σ_{LO} (fb)	$\overline{\sigma}_{LO}$ (fb)	σ_{NLO} (fb)
120	m_t	582.92 ± 0.06	616.81 ± 0.07	718.64 ± 3.71
	$m_t + M_h/2$	520.47 ± 0.06	553.25 ± 0.06	697.27 ± 3.20
	$2m_t$	450.09 ± 0.05	480.80 ± 0.05	662.66 ± 2.77
	$2m_t + M_h$	405.54 ± 0.04	434.59 ± 0.05	634.36 ± 2.34
150	m_t	316.27 ± 0.03	336.41 ± 0.04	380.95 ± 1.81
	$m_t + M_h/2$	275.44 ± 0.03	294.35 ± 0.03	367.38 ± 1.52
	$2m_t$	243.47 ± 0.03	261.03 ± 0.03	352.71 ± 1.35
	$2m_t + M_h$	214.43 ± 0.02	230.60 ± 0.02	334.48 ± 1.18
180	m_t	187.44 ± 0.02	200.46 ± 0.02	221.63 ± 1.01
	$m_t + M_h/2$	159.32 ± 0.02	171.15 ± 0.02	214.01 ± 0.85
	$2m_t$	143.77 ± 0.02	154.74 ± 0.02	206.59 ± 0.77
	$2m_t + M_h$	123.85 ± 0.01	133.65 ± 0.02	194.42 ± 0.70

will also play an important part in determining the couplings of the discovered Higgs boson and, in particular, will give the only handle on a direct measurement of the top quark Yukawa coupling.

In this chapter, we have reviewed the calculation of the NLO QCD corrections to the inclusive cross section for $t\bar{t}h$ production at both the Tevatron and the LHC. The corresponding NLO cross sections show drastically reduced renormalization and factorization scale dependence, and lead to increased confidence in predictions based on these results. At the Tevatron, the overall uncertainty on the theoretical prediction, including the errors coming from parton distribution functions and the top quark mass, is reduced to only 10%, while at the LHC the remaining uncertainty is reduced to 15-20%. This is a drastic reduction compared to the 100% uncertainty oberved in the LO predictions (see Section 3.2.3).

At the Tevatron, the NLO QCD corrections slightly decrease or increase the Born level cross section depending on the renormalization/factorization scales used. The

NLO inclusive total cross section for Higgs boson masses in the range accessible at the Tevatron, $120 < M_h < 180$ GeV, is of the order of $1 - 5$ fb.

At the LHC, including NLO QCD corrections increases the LO cross sections for a broad range of commonly used renormalization and factorization scales, and over the entire Higgs boson mass range considered in this chapter. This is summarized by saying that the K-factor for renormalization and factorization scales in the range $m_t < \mu \leq 2m_t + M_h$ and Higgs boson masses in the range $100\,\mathrm{GeV} \leq M_h \leq 200\,\mathrm{GeV}$ is between 1.2 and 1.6. For this mass range, the NLO inclusive total cross section at the LHC is in the range $200 - 700$ fb.

The calculation of the NLO QCD cross section for $p\bar{p}, pp \rightarrow t\bar{t}h$ contains several technical difficulties that have been thoroughly explained in this chapter. The NLO virtual corrections involve pentagon diagrams and consequently require the evaluation of both scalar and tensor pentagon integrals with several external and internal massive particles. Detailed information about the method used as well as explicit results for all the IR singular integrals appearing in the calculation are presented in a series of Appendices. Tensor pentagon integrals are affected by numerical instabilities and we discuss in this chapter how we have calculated them in a numerically stable form. The NLO real corrections are complicated by the presence of IR divergences. We have calculated them in two different variations of the phase space slicing method, involving one or two arbitrary cutoffs respectively. The correspondence between the two Phase Space Slicing methods is made explicit, and the agreement between them constitutes a powerful check of the technicalities used in their implementations. The techniques developed in this chapter can now be applied to similar higher order calculations, in particular to the case of the associated $b\bar{b}h$ production at both the Tevatron and the LHC which we consider in the next chapter.

CHAPTER 4

ASSOCIATED HIGGS BOSON PRODUCTION
WITH BOTTOM QUARKS

As we saw in Chapter 1, the Higgs boson of the SM preferentially couples to the heaviest particles in the spectrum. Hence, the production of a SM Higgs boson with bottom quarks is expected to be suppressed in comparison to other Higgs production modes due to the smallness of the bottom quark Yukawa coupling, $g_{b\bar{b}h} = m_b/v$ where $m_b \approx 4.5$ GeV and $v = (\sqrt{2}G_F)^{-1/2} = 246$ GeV. However, in a two Higgs doublet model , such as the MSSM, the couplings of some Higgs bosons to bottom quarks grows with the ratio of the neutral Higgs boson vacuum expectation values, $\tan\beta$, and can be significantly enhanced over the SM coupling, leading to an observable production rate for a Higgs boson in association with bottom quarks in most regions of the parameter space. Given the relatively light final state, $b\bar{b}h$ production is well within the kinematic reach of the Tevatron and could therefore provide the first signal of new physics from Run II.

Figure 4.1. Sample Feynman diagrams for $gg \to b\bar{b}h$ and $q\bar{q} \to b\bar{b}h$ production at tree level.

For this reason, the production of Higgs bosons in association with bottom quarks has recently received much interest from both the theoretical and experimental communities [35, 80]. At tree level, the cross section is almost entirely dominated by the sub-process $gg \to b\bar{b}h$ (where $h = h_{SM}, h^0, H^0, A^0$) with only a small contribution from $q\bar{q} \to b\bar{b}h$, at both the Tevatron and LHC (see Fig. 4.1). Naively, the calculation of $b\bar{b}h$ production at NLO would follow that of $t\bar{t}h$, outlined in the last chapter, with the universal replacement of the top quark mass with the bottom quark mass, $m_t \leftrightarrow m_b$. However, the theoretical prediction of $b\bar{b}h$ production at hadron colliders involves several subtle issues not encountered in the calculation of $t\bar{t}h$ production.

Both from an experimental and theoretical standpoint, it is important to distinguish between *inclusive* and *exclusive* $b\bar{b}h$ production. More specifically, the production of a Higgs boson with a pair of b quarks can be detected via: (*i*) a fully *exclusive* measurement, where both b jets are observed, (*ii*) a fully *inclusive* measurement, where no b jet is observed, or (*iii*) a *semi-inclusive* measurement, where at least one b jet is observed.

Experimentally, b quarks are identified or *tagged* by imposing selection cuts on their transverse momentum and their angular direction with respect to the beam axis. Inclusive modes have larger cross sections, but also larger background, such that more exclusive modes are preferred experimentally. Moreover, only the exclusive and semi-inclusive modes are unambiguously proportional to the bottom quark Yukawa coupling.

Theoretically, different calculational approaches may be adopted depending on the fact that a final state b quark is either treated inclusively (untagged) or exclusively (tagged). Indeed, when a final state b quark is not identified, the corresponding integration over its phase space gives rise to logarithms of the form:

$$\Lambda_b = \log\left(\frac{\mu_h^2}{m_b^2}\right) , \tag{4.1}$$

120

where m_b and μ_h represent the lower and upper bounds on the integration over the transverse momentum of the final state b quark. μ_h is typically of $\mathcal{O}(M_h)$ and therefore, due to the smallness of the bottom quark mass, these logarithms can be quite large[1]. Additionally, the same logarithms appear at every order in the perturbative expansion of the cross section in the strong coupling, α_s, due to recursive gluon emission from internal bottom quark lines. If the logarithms are large, the convergence of the perturbative expansion of the cross section could be severely hindered and it can be advisable to reorganize the expansion in powers of $\alpha_s^n \Lambda_b^m$, further resumming various orders of logarithms via renormalization group techniques.

Currently, there are two approaches to calculating the inclusive and semi-inclusive cross sections for Higgs production with bottom quarks. Working under certain kinematic approximations, and adopting the so-called *five-flavor-number scheme* (5FNS), the collinear logarithms, Λ_b, can be factored out and resummed by introducing a bottom quark Parton Distribution Function (PDF) [81, 82, 83]. This approach restructures the calculation to be an expansion in both α_s and Λ_b^{-1}. The LO process for the semi-inclusive mode then becomes $gb \rightarrow bh$ shown in Fig. 4.2, while the LO process for the fully-inclusive mode becomes $b\bar{b} \rightarrow h$ shown in Fig. 4.3. Alternatively, working with no kinematic approximations, and adopting the so-called *four-flavor-number scheme* (4FNS), one can compute the cross section for $p\bar{p}, pp \rightarrow b\bar{b}h$ at fixed order in QCD with no special treatment of the collinear logarithms, considering just the parton level processes $q\bar{q}, gg \rightarrow b\bar{b}h$ and their radiative corrections.

The fully exclusive $b\bar{b}h$ production cross section can only be computed in the 4FNS framework. As far as the inclusive and semi-inclusive production cross sections go, the comparison between the the 4FNS and 5FNS needs to consider higher-order

---

[1]The logarithms mentioned here also appear in the $t\bar{t}h$ calculation but, since μ_h is typically of the order of m_t, the logarithms are small and the convergence of the perturbative expansion is preserved.

Figure 4.2. Tree level Feynman diagram for $gb \rightarrow bh$ in the 5FNS.
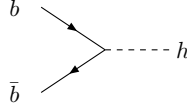
Figure 4.3. Tree level Feynman diagram for $b\bar{b} \rightarrow h$ in the 5FNS.

QCD corrections, in order to work with stable results. For quite some time, the comparison between these two approaches has been hindered by the lack of a NLO QCD calculation for $q\bar{q}, gg \rightarrow b\bar{b}h$. Thanks to our work, this gap has been filled and QCD corrected cross sections for all three final states have now been computed in both the 4FNS and 5FNS. For the inclusive case, the NLO QCD corrected 4FNS [80, 84] and the NNLO QCD corrected 5FNS cross sections [85] have been compared and are found to be in good agreement within theoretical uncertainties. The NLO predictions of the semi-inclusive cross sections for the 4FNS [84, 86] and 5FNS [87] have also been extensively compared and the agreement between the two is spectacular. The compatibility of these two seemingly different calculational schemes in the prediction of Higgs boson production rates is indeed a beautiful check of the theory. Finally, two independent calculations of the NLO QCD corrections for the exclusive mode have been compared and agreement has been found [84, 88].

It should be noted that the above discussion for the production of a *scalar* Higgs boson with bottom quarks applies equally well to the production of a *pseudoscalar*

Higgs boson. In fact, if one neglects the bottom quark mass in the calculation of the NLO corrections, the predictions for $b\bar{b}A^0$ is identical to those for $b\bar{b}h^0(H^0)$ given a rescaling of the Yukawa couplings (see Section 1.2.2). On the other hand, for massive b quarks, the situation becomes more complicated due to the γ_5 matrix appearing in the $b\bar{b}A^0$ Yukawa coupling. The γ_5 Dirac matrix is intrinsically a four-dimensional object and care must be taken in its treatment when regularizing the calculation in dimensional regularization ($d \neq 4$). However, bottom quark mass effects are expected to be small, $\mathcal{O}(\frac{m_b^2}{M_h^2})$, and predictions for $b\bar{b}h^0$, upon rescaling of the Yukawa coupling, are good indicators for $b\bar{b}A^0$ production even in the massive b quark case.

The remainder of this chapter is organized as follows. In Section 4.1, we discuss in detail the framework of the calculations in the 4FNS and 5FNS. Given the importance it plays in the prediction of the cross section through the Yukawa coupling, we also discuss the renormalization of the bottom quark mass. In Section 4.2, we present our results for the inclusive, semi-inclusive and exclusive $b\bar{b}h$ production. In Section 4.3, we investigate the uncertainties arising from the PDFs. These uncertainties, which can be quite significant for hadronic processes, are calculated using the algorithm developed by the CTEQ collaboration [89]. Finally, we summarize our results in Section 4.4.

4.1 Theoretical framework

4.1.1 Four Flavor Number Scheme

In the 4FNS, the NLO QCD corrections to the hadronic processes $p\bar{p}(pp) \rightarrow b\bar{b}h$ consist of the $\mathcal{O}(\alpha_s)$ virtual and real corrections to the tree-level processes $gg, q\bar{q} \rightarrow b\bar{b}h$. In fact, with the interchange of the top and bottom quark masses, the NLO calculation of $b\bar{b}h$ production is identical to that of $t\bar{t}h$ production presented in Chapter 3.

123
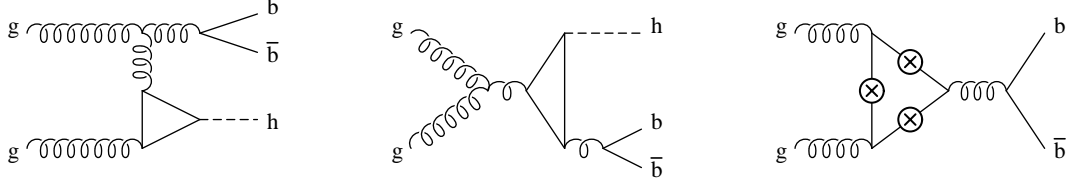
Figure 4.4. Sample of diagrams corresponding to $\mathcal{O}(\alpha_s)$ virtual corrections where the Higgs boson couples to an internal fermion loop and not to the external $b\bar{b}$ pair. The circled cross denotes all possible insertion of the final state Higgs boson leg, each insertion corresponding to a different diagram.

We always first obtain results in the SM and subsequently rescale the Yukawa coupling(s) to produce the corresponding MSSM results. This rescaling must be performed with some care, though, due to virtual diagrams where the Higgs boson is radiated from a closed loop of top quarks as shown in Fig. 4.4. Indeed, the MSSM cross sections are obtained as follows:

$$
\begin{aligned}
\sigma_{MSSM} = & \left(\frac{g_{bbh}^{MSSM}}{g_{bbh}^{SM}} \right)^2 \left(\sigma_{SM} - \sigma_{SM}^t \right) \\
& + \left(\frac{g_{tth}^{MSSM} g_{bbh}^{MSSM}}{g_{tth}^{SM} g_{bbh}^{SM}} \right) \sigma_{SM}^t \quad .
\end{aligned}
\tag{4.2}
$$

where σ_{SM} is the full NLO QCD corrected cross section (including contributions from top-loop diagrams) and σ_{SM}^t is the contribution from top-loop diagrams alone, such that the difference $(\sigma_{SM} - \sigma_{SM}^t)$ is the NLO QCD corrected cross section without top-loop contributions. For the following discussion, we also use the SUSY-corrected Yukawa couplings presented in Section 1.2.2. Numerical values for these corrected couplings have been obtained using input parameters (α, M_A, etc.) from FeynHiggs [1] where higher-order SM and MSSM corrections to masses and couplings have been included.

Finally, to ensure that the b quarks are in a range where experiments can tag the resulting b-quark jet, cuts are placed on the minimum transverse momentum

124

$(p_T^{b,min})$ and the maximum pseudorapidity (η_b^{max}) of the final state b quark(s), where the pseudorapidity is defined as

$$\eta_b = \ln\tan(\theta_b/2) \tag{4.3}$$

and θ_b is the angle of the bottom quark from the beam direction.

4.1.2 Five Flavor Number Scheme

The inclusive and semi-inclusive cross sections have also been computed in the 5FNS, at NNLO [85] and NLO [87] in QCD, respectively.

As mentioned earlier, the idea of using a 5FNS with a bottom quark initial state density is motivated by the possibility of factoring out and, subsequently, resumming large collinear logarithms arising in the perturbative expansion of the cross section when one or both bottom b quarks are treated inclusively.

To clarify this point further, it is instructive to explicitly derive how the form of the bottom quark PDF comes about. In Appendix E, we provide a simple calculation which illustrates the origin of the large logarithms in the case when only one bottom quark is at large p_T. From this calculation, we learn two things. First, the logarithms originating from the integration over the final-state b quark transverse momentum can be factored out into a *b quark density function* or *parton distribution function* given at lowest order in α_s by:

$$b(x,\mu) = \frac{\alpha_s(\mu)}{2\pi}\Lambda_b \int_x^1 \frac{dy}{y} P_{qg}\left(\frac{x}{y}\right) g(y,\mu)\,, \tag{4.4}$$

where $g(y,\mu)$ is the gluon PDF and P_{qg} is the Altarelli-Parisi splitting function for $g \to q\bar{q}$ and is given by

$$P_{qg} = \frac{1}{2}[z^2 + (1-z)^2]. \tag{4.5}$$

The tree-level process then becomes $gb \to bh$ when only one b quark is treated inclusively (or $bb \to h$ when both b quarks are treated inclusively). Second, we see

125

that the 5FNS is based on the approximation that a *spectator* bottom quark (i.e., a b quark which is not tagged in the final state) is at small transverse momentum (the calculation in Appendix E is performed with small p_T). At lowest order, these spectator quarks are produced with zero p_T, and a transverse momentum spectrum for the outgoing bottom quarks is generated at higher orders [81, 82]. Finally, the resummation of the leading Λ_b collinear logarithms is obtained via renormalization group arguments, in the form of the DGLAP equation [59, 90, 91] which (at LO) is given by:

$$\frac{d}{d \log \mu} b(x, \mu) = \frac{\alpha_s(\mu)}{\pi} \int_x^1 \frac{dz}{z} P_{qg}(z)\, g\left(\frac{x}{z}, \mu\right), \qquad (4.6)$$

therefore providing a potentially more stable perturbative expansion of the cross section.

With the use of a b-quark PDF, the 5FNS effectively reorders the perturbative expansion to be one in α_s and Λ_b^{-1}. To see how this works, let us consider the perturbative expansion of the inclusive process $b\bar{b} \to h$ (Fig. 4.3) which, according to what we just saw, is intrinsically of order $\alpha_s^2 \Lambda_b^2$. At NLO, the virtual and real corrections to the tree level process make contributions of $\mathcal{O}(\alpha_s^3 \Lambda_b^2)$. However, at NLO, we must also consider the contribution from $gb \to bh$ where the final state b is at high p_T. This process makes a contribution of order $\alpha_s^2 \Lambda_b$ and is, thus, a correction of $\mathcal{O}(\Lambda_b^{-1})$ to the tree level cross section. Similarly, at NNLO, besides the myriad of radiative corrections of $\mathcal{O}(\alpha_s^4 \Lambda_b^2)$, we must also include the contribution from the process $gg \to b\bar{b}h$, where both b and $\bar{b}$ are at high p_T. The contribution from these diagrams are of order α_s^2, and are, thus, $\mathcal{O}(\Lambda_b^{-2})$ (or NNLO) corrections to the tree level process $b\bar{b} \to h$ [83, 92].

The above discussion for $b\bar{b} \to h$ also applies to the perturbative expansion of $gb \to bh$. In this case, the tree level process is of order $\alpha_s^2 \Lambda_b$ and the contribution from $gg \to b\bar{b}h$ is a NLO correction of $\mathcal{O}(\Lambda_b^{-1})$ [87]. Moreover, the semi-inclusive

cross section is computed by requiring that at least one of the final state b quarks pass $p_{T,b}$ and η_b cuts, as in Section 4.1.1.

In contrast to the 4FNS calculation where the bottom quark masses are kept finite, all of the existing 5FNS calculations have been performed with the b mass set to zero, except in the overall Yukawa coupling. Finally, to obtain results for the MSSM Higgs boson from the NLO calculation of $gb \to bh$ [87], we follow the same rescaling procedure outlined in Section 4.1.1. The NNLO calculation for the inclusive process $b\bar{b} \to h$ does not contain any top-loop diagrams and results can be obtained from the SM results by simply replacing $g_{b\bar{b}h}^{SM}$ with $g_{b\bar{b}h}^{MSSM}$.

4.1.3 Definition of b quark mass

One potential source of theoretical uncertainty in the calculation of $p\bar{p}(pp) \to b\bar{b}h$ involves the renormalization of the b quark mass. Given the large sensitivity of the bottom quark mass to the renormalization scale and given the prominent role it plays in the $b\bar{b}h$ production cross section through the overall bottom quark Yukawa coupling, we have chosen to use two schemes for both the renormalization of the bottom quark mass and the renormalization constant of the external bottom quark field to investigate this renormalization scheme dependence: the $\overline{MS}$ scheme and an on-shell (OS) scheme [88].

When using the OS subtraction scheme, we fix the wave function renormalization constant of the external bottom quark field, $(\delta Z_2^{(b)})_{OS}$, and the mass renormalization constant, $(\delta m_b)_{OS}$, by requiring that

$$\hat{\Sigma}_b(\not{p} = m_b) = 0 \quad ; \quad \lim_{\not{p} \to m_b} \frac{\hat{\Sigma}_b(\not{p})}{\not{p} - m_b} = 0 \ , \tag{4.7}$$

where

$$\hat{\Sigma}_b = (\not{p} - m_b)\left(\Sigma_V + \delta Z_2^{(b)}\right) + m_b\left(\Sigma_S + \Sigma_V - \frac{\delta m_b}{m_b}\right) \tag{4.8}$$

denotes the renormalized bottom quark self-energy at 1-loop in QCD, expressed in terms of the vector, Σ_V, and scalar, Σ_S, parts of the unrenormalized self-energy,

and of the mass and wave function renormalization constants. Using Eq. (4.7) in $d = 4 - 2\epsilon$ dimensions one finds

$$\left(\delta Z_2^{(b)}\right)_{OS} = -\frac{\alpha_s}{4\pi} C_F \left(\frac{4\pi\mu^2}{m_b^2}\right)^{\epsilon} \Gamma(1+\epsilon) \left(\frac{1}{\epsilon_{UV}} + 4 + \frac{2}{\epsilon_{IR}}\right) , \qquad (4.9)$$

$$\left(\frac{\delta m_b}{m_b}\right)_{OS} = -\frac{\alpha_s}{4\pi} C_F \left(\frac{4\pi\mu^2}{m_b^2}\right)^{\epsilon} \Gamma(1+\epsilon) \left(\frac{3}{\epsilon_{UV}} + 4\right) , \qquad (4.10)$$

where we have explicitly distinguished between ultraviolet and infrared divergences. The infrared divergences are canceled between virtual and real soft and collinear contributions according to the pattern outlined in the last chapter, to which we refer for more details.

In the $\overline{MS}$ scheme, the bottom quark renormalization constants are fixed by requiring that they cancel the UV divergent parts of the bottom quark self energy $\hat{\Sigma}_b$ of Eq. (4.8), i.e.

$$\left(\delta Z_2^{(b)}\right)_{\overline{MS}} = -\frac{\alpha_s}{4\pi} C_F (4\pi)^{\epsilon} \Gamma(1+\epsilon) \frac{1}{\epsilon_{UV}} , \qquad (4.11)$$

$$\left(\frac{\delta m_b}{m_b}\right)_{\overline{MS}} = -\frac{\alpha_s}{4\pi} C_F (4\pi)^{\epsilon} \Gamma(1+\epsilon) \frac{3}{\epsilon_{UV}} . \qquad (4.12)$$

According to the LSZ prescription [93], one also needs to consider the insertion of the renormalized one-loop self-energy corrections on the external bottom quark legs. While these terms are zero in the OS scheme (see Eq. (4.7)), they are not zero in the $\overline{MS}$ scheme. Together with $(\delta Z_2^{(b)})_{\overline{MS}}$, their contribution to the NLO cross section equals the contribution of the wave function counterterm in the OS scheme, $(\delta Z_2^{(b)})_{OS}$, as expected from the LSZ prescription itself. The cross section does not depend on the renormalization of the external particle wave functions.

We therefore focus on the scheme dependence induced by the choice of different subtraction schemes for the bottom quark mass. We note that the bottom quark mass counterterm has to be used twice: once to renormalize the bottom quark mass appearing in internal propagators and once to renormalize the bottom quark Yukawa

128

coupling. Indeed, if one considers only QCD corrections, the counterterm for the bottom quark Yukawa coupling,

$$\delta g_{b\bar{b}h} = \frac{\delta m_b}{v} \ , \tag{4.13}$$

coincides with the counterterm for the bottom quark mass, since the SM Higgs vacuum expectation value v is not renormalized at 1-loop in QCD. This stays true when we generalize the $g_{b\bar{b}h}$ coupling from the SM to the case of the scalar Higgs bosons of the MSSM.

At 1-loop order in QCD, the relation between the pole mass, m_b, and the $\overline{MS}$ mass, $\overline{m}_b(\mu)$, is indeed determined by the difference between the OS and $\overline{MS}$ bottom mass counterterms, $\frac{\alpha_s}{4\pi}\delta CT$, since

$$\overline{m}_b(\mu) = m_b \left\{ 1 - \frac{\alpha_s(\mu)}{4\pi} C_F \left[3\ln\left(\frac{\mu^2}{m_b^2}\right) + 4 \right] \right\} \equiv m_b \left[1 - \frac{\alpha_s(\mu)}{4\pi}\delta CT(\mu) \right] \ . \tag{4.14}$$

Adopting the OS or $\overline{MS}$ prescription consists of using either Eq. (4.10) or Eq. (4.12) for the bottom mass counterterms while substituting m_b or $\overline{m}_b(\mu)$ respectively in both the bottom quark propagator and Yukawa coupling. At $\mathcal{O}(\alpha_s^3)$ the two prescriptions give identical results. Indeed, replacing m_b by $\overline{m}_b(\mu)$ in the Yukawa coupling adds a term

$$-\frac{\alpha_s(\mu)}{2\pi}\delta CT(\mu)\hat{\sigma}_{LO} + \mathcal{O}(\alpha_s^4) \tag{4.15}$$

to the NLO parton level cross section, which compensates exactly for the difference in the OS and $\overline{MS}$ counterterms. On the other hand, using the $\overline{MS}$ mass in the bottom quark propagator,

$$\frac{i}{\not{p} - \overline{m}_b(\mu)} = \frac{i}{\not{p} - m_b}\left[1 + im_b\frac{\alpha_s}{4\pi}\delta CT(\mu)\frac{i}{\not{p} - m_b} \right] + \mathcal{O}(\alpha_s^2) \ , \tag{4.16}$$

of the LO cross section leads to an extra contribution to the $\overline{MS}$ NLO cross section which, together with the $\overline{MS}$ mass counterterm insertions into the internal bottom quark propagators (see diagrams $S_1^{q\bar{q}}$ in Fig. 3.5 and S_2^{gg}, S_3^{gg}, and S_4^{gg} in Fig. 3.9 of

129

Chapter 3), coincides with the corresponding mass counterterm insertions in the OS scheme at $\mathcal{O}(\alpha_s^3)$.

Therefore, using OS or $\overline{MS}$ at $\mathcal{O}(\alpha_s^3)$ is perturbatively consistent, the difference between the two schemes being of higher order and hence, strictly speaking, part of the theoretical uncertainty of the NLO calculation. One notices however that some of the large logarithms involved in the renormalization procedure of the NLO cross section come from the renormalization of the bottom quark mass, and are nicely factored out by using the $\overline{MS}$ bottom mass in the bottom quark Yukawa coupling (see Eq. (4.14)). Therefore one should consider reorganizing the perturbative expansion in terms of leading logarithms (of the form $\alpha_s^n(\mu) \ln^n(\mu^2/m_b^2)$) or next-to-leading-logarithms (of the form $\alpha_s^n(\mu) \ln^{n-1}(\mu^2/m_b^2)$, for $\mu \simeq M_h$), as obtained by replacing the $\overline{MS}$ bottom mass in the Yukawa coupling by the corresponding 1-loop or 2-loop renormalization group improved $\overline{MS}$ masses:

$$\overline{m}_b(\mu)_{1l} = m_b \left[\frac{\alpha_s(\mu)}{\alpha_s(m_b)} \right]^{c_0/b_0} , \tag{4.17}$$

$$\overline{m}_b(\mu)_{2l} = m_b \left[\frac{\alpha_s(\mu)}{\alpha_s(m_b)} \right]^{c_0/b_0} \left[1 + \frac{c_0}{b_0}(c_1 - b_1) \frac{\alpha_s(\mu) - \alpha_s(m_b)}{\pi} \right] \left(1 - \frac{4}{3} \frac{\alpha_s(m_b)}{\pi} \right) , \tag{4.18}$$

where

$$b_0 = \frac{1}{4\pi} \left(\frac{11}{3}N - \frac{2}{3}n_{lf} \right) \quad , \quad c_0 = \frac{1}{\pi} \quad , \tag{4.19}$$

$$b_1 = \frac{1}{2\pi} \frac{51N - 19n_{lf}}{11N - 2n_{lf}} \quad , \quad c_1 = \frac{1}{72\pi}(101N - 10n_{lf}) \quad , \tag{4.20}$$

are the one and two loop coefficients of the QCD β-function and mass anomalous dimension γ_m, while $N=3$ is the number of colors and $n_{lf}=5$ is the number of light flavors.

In both Higgs boson decays to heavy quarks and Higgs boson production with heavy quarks in e^+e^- collisions, using Eq. (4.17) at LO and Eq. (4.18) at NLO in the Yukawa coupling proves to be a very powerful way to stabilize the perturbative

calculation of the cross section [94]. The difference between LO and NLO rates is reduced and the dependence on the renormalization and factorization scales at NLO is very mild, indicating a very small residual theoretical error or equivalently a very good convergence of the perturbative expansion of the corresponding rate. This is due to the fact that in these cases to a large extent the $\mathcal{O}(\alpha_s)$ QCD corrections amount to a renormalization of the heavy quark mass in the Yukawa coupling. In more complicated cases, like the case of the hadronic cross section discussed in this paper, the previous argument is not automatically true.

Using the OS or $\overline{MS}$ bottom quark mass mainly affects the Yukawa coupling. Therefore, in the hadronic case, we will look at the different behavior of the NLO cross section when the bottom quark Yukawa coupling is renormalized either in the OS or in the $\overline{MS}$ scheme, keeping the bottom quark pole mass everywhere else. For the purpose of illustration, let us consider the fully exclusive case. Fig. 4.5 of Section 4.2 shows the renormalization and factorization scale dependence of the LO and NLO cross sections for $p\bar{p}(pp) \to b\bar{b}h$ obtained using in the Yukawa coupling either the pole mass m_b or the $\overline{MS}$ running mass $\overline{m}_b(\mu)$ in Eq. (4.17) (at LO) and (4.18) (at NLO). The use of $\overline{m}_b(\mu)$ both at LO and NLO seems to improve the perturbative calculation of the cross section, since the NLO $\overline{MS}$ cross section is better behaved than the NLO OS cross section at low scales and since the difference between LO and NLO cross section is smaller when the bottom quark Yukawa coupling is renormalized in the $\overline{MS}$ scheme than in the OS scheme. For this reason, most of the numerical results in Section 4.2 are presented using the $\overline{MS}$ bottom quark mass in the Yukawa coupling.

However, both the OS and the $\overline{MS}$ cross sections have very well defined regions of minimum sensitivity to the variation of the renormalization/factorization scale and these regions do not quite overlap. The difference between the OS and $\overline{MS}$ results at the plateau should rather be interpreted, in the absence of a NNLO calculation, as an upper bound on the theoretical uncertainty.

131

The origin of the large difference between the OS and $\overline{MS}$ NLO cross sections illustrated in Fig. 4.5 can be understood by studying the numerical effect of the higher order terms that are included in the NLO $\overline{MS}$ cross section when $\overline{m}_b(\mu)$ is used in the Yukawa coupling. The parton level NLO cross sections for $ij \rightarrow b\bar{b}h$ ($ij = q\bar{q}, gg$) in the OS and $\overline{MS}$ prescription explained above can be written as:

$$
\hat{\sigma}^{ij}_{NLO,OS}(x_1, x_2, \mu) = m_b^2 \alpha_s^2(\mu) \Bigg\{ \; g^{ij}_{LO}(x_1, x_2)
$$
$$
+ \frac{\alpha_s(\mu)}{4\pi} \left[g^{ij}_{NLO}(x_1, x_2, \mu) - 2g^{ij}_{LO}(x_1, x_2)\delta CT(\mu) + \frac{m_t}{m_b} g^{ij}_{cl}(x_1, x_2) \right] \Bigg\} \; ,
\tag{4.21}
$$

$$
\hat{\sigma}^{ij}_{NLO,\overline{MS}}(x_1, x_2, \mu) = \overline{m}_b^2(\mu) \alpha_s^2(\mu) \Bigg\{ \; g^{ij}_{LO}(x_1, x_2)
$$
$$
+ \frac{\alpha_s(\mu)}{4\pi} \left[g^{ij}_{NLO}(x_1, x_2, \mu) + \frac{m_t}{\overline{m}_b(\mu)} g^{ij}_{cl}(x_1, x_2) \right] \Bigg\} \; ,
\tag{4.22}
$$

where the dependence on the renormalization scale is explicitly given. $\alpha_s(\mu)$ is the 2-loop strong coupling, m_b is the bottom pole mass, and $\overline{m}_b(\mu)$ is the bottom quark $\overline{MS}$ mass. g^{ij}_{LO}, g^{ij}_{NLO} and g^{ij}_{cl} have been defined in such a way that they are the same in the OS and the $\overline{MS}$ schemes. They correspond respectively to the $\mathcal{O}(\alpha_s^2)$ (g^{ij}_{LO}) and $\mathcal{O}(\alpha_s^3)$ (g^{ij}_{NLO}) contributions to the NLO QCD cross section, from which we have singled out the $\mathcal{O}(\alpha_s)$ virtual corrections where the Higgs boson couples to a top quark in a closed fermion loop (g^{ij}_{cl}, see, e.g., diagrams in Fig. 4.4) as well as $\delta CT(\mu)$, i.e. the difference between the OS and $\overline{MS}$ bottom mass counterterms defined in Eq. (4.14). Using Eqs. (4.21) and (4.22), one can easily verify that the difference between the parton level NLO cross sections obtained by using either the OS or the $\overline{MS}$ scheme for the bottom quark Yukawa coupling is, as expected, of higher order in α_s, i.e.:

$$
\hat{\Delta} = \hat{\sigma}^{ij}_{NLO,OS} - \hat{\sigma}^{ij}_{NLO,\overline{MS}}
$$
$$
= \alpha_s^2(\mu) g^{ij}_{LO}(x_1, x_2) \left[m_b^2 - \overline{m}_b^2(\mu) - m_b^2 \frac{\alpha_s(\mu)}{2\pi}\delta CT(\mu) \right]
$$
$$
+ \frac{\alpha_s^3(\mu)}{4\pi}(m_b^2 - \overline{m}_b^2(\mu)) \left[g^{ij}_{NLO}(x_1, x_2, \mu) + \frac{m_t}{m_b + \overline{m}_b(\mu)} g^{ij}_{cl}(x_1, x_2) \right] \; .
\tag{4.23}
$$

132

The term in the first bracket of Eq. (4.23) vanishes at $\mathcal{O}(\alpha_s^3)$, as can be easily verified by using Eq. (4.14). Hence all the terms in Eq. (4.23) only contribute at $O(\alpha_s^4)$ and higher. However, while the first term is in general quite small, the term proportional to $g_{NLO}^{ij}(x_1, x_2, \mu)$ can be large and has a non trivial scale dependence that we can formally write as:

$$g_{NLO}^{ij}(x_1, x_2, \mu) = g_1^{ij}(x_1, x_2) + \tilde{g}_1^{ij}(x_1, x_2) \ln\left(\frac{\mu^2}{s}\right) \ . \tag{4.24}$$

From renormalization group arguments one can see that $\tilde{g}_1^{ij}(x_1, x_2)$ is given by:

$$\tilde{g}_1^{ij}(x_1, x_2) = 2 \left\{ (4\pi b_0 + 4) g_{LO}^{ij}(x_1, x_2) - \sum_k \left[\int_\rho^1 dz_1 P_{ik}(z_1) g_{LO}^{kj}(x_1 z_1, x_2) \right.\right.$$
$$\left.\left. + \int_\rho^1 dz_2 P_{jk}(z_2) g_{LO}^{ik}(x_1, x_2 z_2) \right] \right\} \ , \tag{4.25}$$

where $\rho = (2m_b + M_h)^2/s$, $P_{ij}(z)$ denotes the lowest-order regulated Altarelli-Parisi splitting function [59] of parton i into parton j, when j carries a fraction z of the momentum of parton i, (see e.g. Section 3.4) and b_0 is given in Eq. (4.19). As a result, $\hat{\Delta}$, defined in Eq. (4.23), turns out to have a non trivial scale dependence and, thus, the difference between the NLO hadronic cross section calculated with the OS or with the $\overline{MS}$ definition of the bottom quark Yukawa coupling can be numerically quite significant for some values of the renormalization/factorization scale, as we will illustrate in Section 4.2 (see Figs. 4.5 and 4.6).

4.2 Numerical results

4.2.1 Higgs production with two high-p_T b jets

Our numerical results are obtained using CTEQ5M parton distribution functions for the calculation of the NLO cross section, and CTEQ5L parton distribution functions for the calculation of the lowest order cross section [79][2]. The NLO

---

[2]Since these PDF sets have been updated after the publication of this investigation, we have checked that using current PDF sets (CTEQ6) does not have a significant effect on the results presented here and hence we have not updated our plots.

Figure 4.5. σ_{NLO} and σ_{LO} for $p\bar{p} \to b\bar{b}h$ at $\sqrt{s} = 2$ TeV (top) and for $pp \to b\bar{b}h$ at $\sqrt{s} = 14$ TeV (bottom) as a function of the renormalization/factorization scale μ, for $M_h = 120$ GeV. The curves labeled $\sigma_{LO,OS}$ and $\sigma_{NLO,OS}$ use the OS renormalization scheme for the bottom quark Yukawa coupling, while the curves labeled $\sigma_{LO,MS}$ and $\sigma_{NLO,MS}$ use the $\overline{MS}$ scheme.
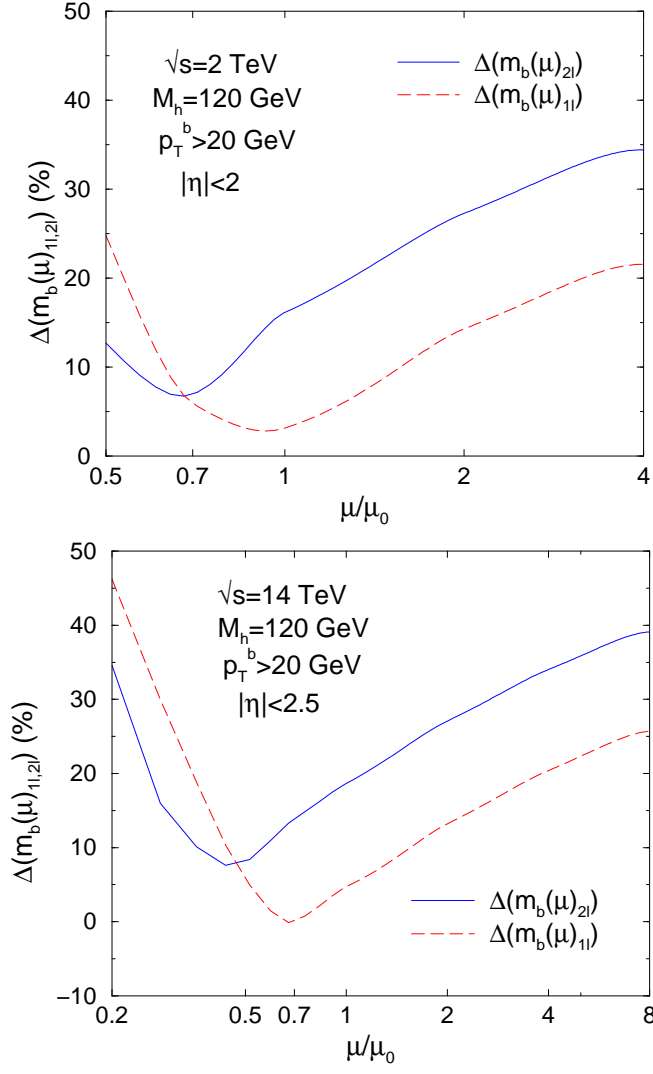
Figure 4.6. The absolute value of the percentage difference $\Delta(\%) = (\sigma_{NLO,OS} - \sigma_{NLO,\overline{MS}})/(\sigma_{NLO,OS} + \sigma_{NLO,\overline{MS}})$ for $p\bar{p} \to b\bar{b}h$ at $\sqrt{s} = 2$ TeV (top) and for $pp \to b\bar{b}h$ at $\sqrt{s} = 14$ TeV (bottom) as a function of the renormalization/factorization scale μ, for $M_h = 120$ GeV. The OS and $\overline{MS}$ labels refer to the renormalization scheme chosen for the bottom quark Yukawa coupling. The curves labeled as $\Delta(m_b(\mu)_{1l})$ and $\Delta(m_b(\mu)_{2l})$ use the $\overline{MS}$ bottom quark Yukawa coupling with the 1-loop running mass of Eq. (4.17) and the 2-loop running mass of Eq. (4.18), respectively.

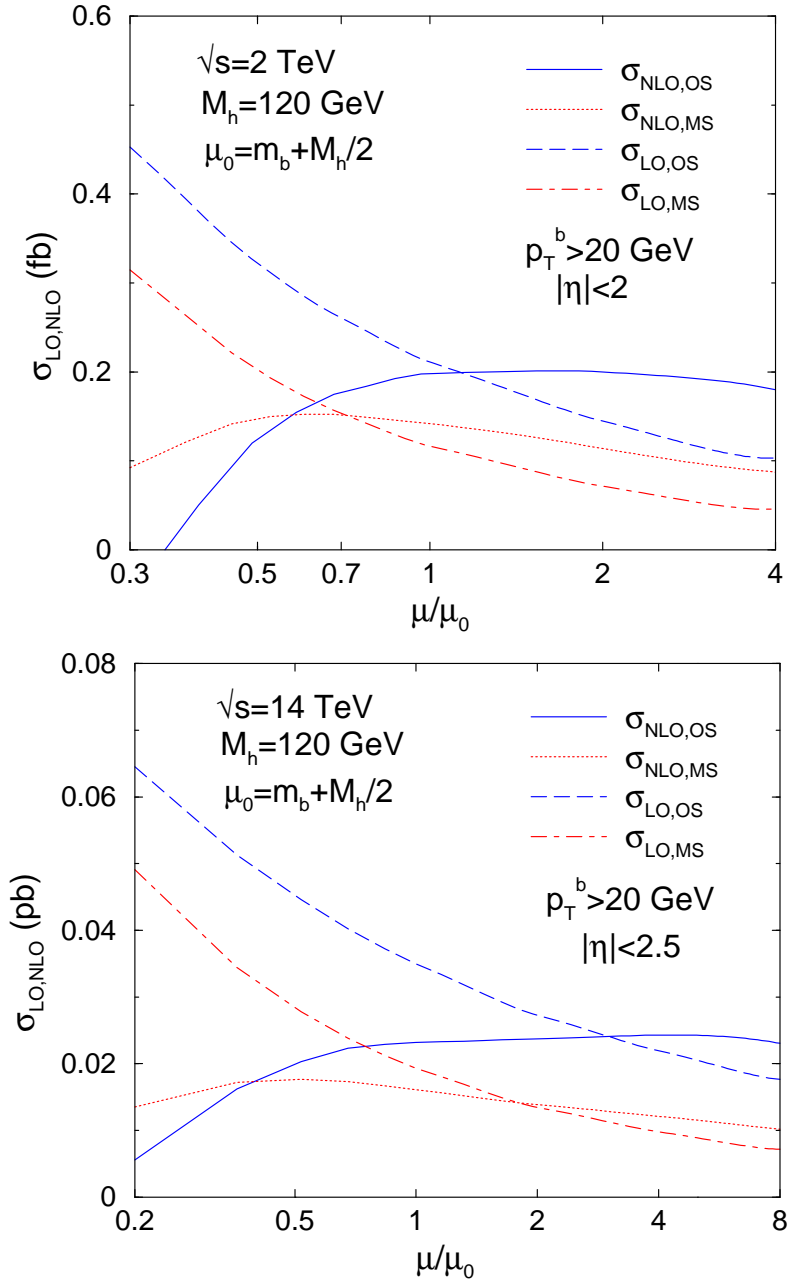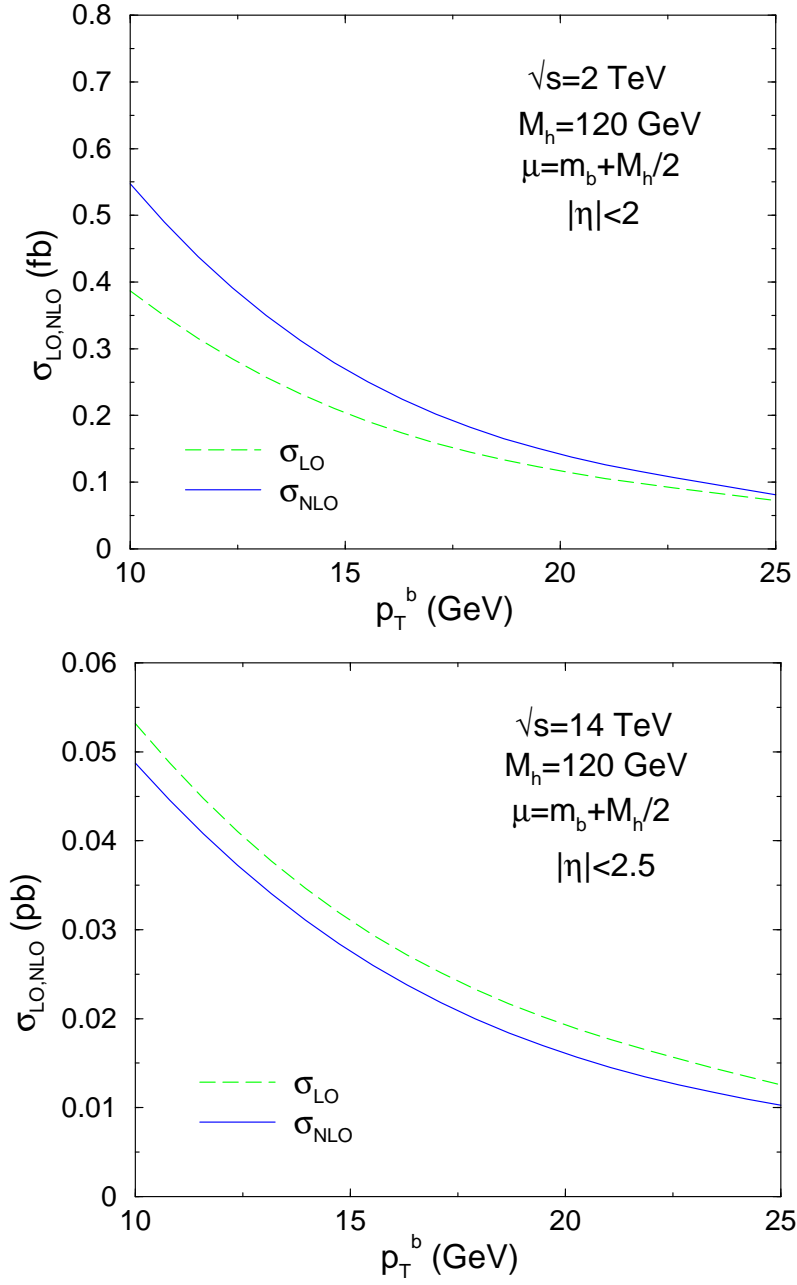**Figure 4.7.** $\sigma_{NLO,MS}$ and $\sigma_{LO,MS}$ for $p\bar{p} \rightarrow b\bar{b}h$ at $\sqrt{s} = 2$ TeV (top) and for $pp \rightarrow b\bar{b}h$ at $\sqrt{s} = 14$ TeV (bottom) as a function of the cut imposed on the final state bottom and anti-bottom transverse momentum (p_T^b), for $M_h = 120$ GeV and $\mu = \mu_0 = m_b + M_h/2$.

(LO) cross section is evaluated using the 2-loop (1-loop) evolution of $\alpha_s(\mu)$ with $\alpha_s^{NLO}(M_Z) = 0.118$. The bottom quark pole mass is taken to be $m_b = 4.6$ GeV. In the OS scheme the bottom quark Yukawa coupling is calculated as $g_{b\bar{b}h} = m_b/v$, while in the $\overline{MS}$ scheme as $g_{b\bar{b}h}(\mu) = \overline{m}_b(\mu)/v$, where we use $\overline{m}_b(\mu)_{1l}$ from Eq. (4.17) for σ_{LO} and $\overline{m}_b(\mu)_{2l}$ from Eq. (4.18) for σ_{NLO}.

We evaluate the fully exclusive LO and NLO cross sections for $b\bar{b}h$ production by requiring that the transverse momentum of both final state bottom and anti-bottom quarks be larger than 20 GeV ($p_T^b > 20$ GeV), and that their pseudorapidity satisfy the condition $|\eta_b| < 2$ for the Tevatron and $|\eta_b| < 2.5$ for the LHC. This corresponds to an experiment measuring the Higgs decay products along with two high p_T bottom quark jets that are clearly separated from the beam. Furthermore, we present LO and NLO transverse momentum and pseudorapidity distributions. In order to better simulate the detector response, the gluon and the bottom/anti-bottom quarks are treated as distinct particles only if the separation in the azimuthal angle-pseudorapidity plane is $\Delta R > 0.4$. For smaller values of ΔR, the four momentum vectors of the two particles are combined into an effective bottom/anti-bottom quark momentum four-vector.

4.2.1.1 Standard Model results

In Fig. 4.5 we show, for $M_h = 120$ GeV, the dependence of the LO and NLO cross sections for $p\bar{p} \to b\bar{b}h$ at the Tevatron (top) and for $pp \to b\bar{b}h$ at the LHC (bottom) on the unphysical factorization and renormalization scale, μ, when using either the OS or the $\overline{MS}$ renormalization schemes for the bottom quark Yukawa coupling. In both the OS and $\overline{MS}$ schemes the stability of the cross section is greatly improved at NLO, given the much milder scale dependence with respect to the corresponding LO cross section. The results presented in Fig. 4.5 are obtained by setting $\mu = \mu_r = \mu_f$, i.e. by identifying the renormalization (μ_r) and factorization (μ_f) scales. We have checked that varying them independently does not affect the results significantly. By varying the scale μ in the ranges $0.7\mu_0 < \mu < 4\mu_0$ (Tevatron) and $0.5\mu_0 < \mu < 8\mu_0$

(LHC), when using the OS scheme for the bottom quark Yukawa coupling, and in the ranges $0.4\mu_0 < \mu < 2\mu_0$ (Tevatron) and $0.2\mu_0 < \mu < 2\mu_0$ (LHC) when using the $\overline{MS}$ scheme, i. e. in the plateau regions, the value of the NLO cross section varies by at most 15-20% (where $\mu_0 = m_b + M_h/2$) .

As can be seen in Fig. 4.5, the cross section calculated with $g_{b\bar{b}h}$ in the $\overline{MS}$ scheme shows a better perturbative behavior, since the difference between σ_{LO} and σ_{NLO} is smaller. This is in part due to the fact that the LO cross section is calculated using $\overline{m}_b(\mu)_{1l}$ and therefore already contains some of the corrections from the renormalization of the bottom quark Yukawa coupling that appear in the NLO cross section as well as at higher order. This observation seems to justify the use of $\overline{m}_b(\mu)_{1l}$ at LO and $\overline{m}_b(\mu)_{2l}$ at NLO. One also observes that the $\overline{MS}$ NLO cross section is better behaved at low values of the renormalization/factorization scales. At the same time, both the OS and $\overline{MS}$ cross sections show well defined but distinct regions of least sensitivity to the renormalization/factorization scale. In both cases this happens in the region where the LO and NLO cross section are closer. The variation of the NLO cross section with μ about its point of least sensitivity to the renormalization/factorization scale is almost the same whether one uses the OS or $\overline{MS}$ schemes for the bottom quark Yukawa coupling. This indicates that the running of the Yukawa coupling is not the only important factor to determine the overall perturbative stability of the NLO cross section.

It is interesting to note that the $\overline{MS}$ calculation exhibits an area of least sensitivity to the renormalization/factorization scale in the vicinity of $\mu = 0.5\mu_0$, or $\mu \approx M_h/4$. It has been shown by the authors of [95] that this value of the factorization scale greatly improves the convergence of the perturbative calculation for the 5FNS process $b\bar{b} \rightarrow h$. This value of μ_f was extracted from kinematic studies of the behavior of the the bottom quark's p_T in the NLO correction, $gb \rightarrow bh$, to the tree-level process $b\bar{b} \rightarrow h$. In fact, the NNLO cross section for the inclusive mode also exhibited a plateau in this range of μ_f lending credence to the earlier claim of the *proper*

138

factorization scale for the calculation of higher-order corrections to the production of Higgs bosons in association with bottom quarks [85].

As discussed in Section 4.1.3, the numerical difference between the two renormalization schemes can be significant. This is illustrated in Fig. 4.6 where we plot the absolute values of the relative difference, $\Delta = (\sigma_{NLO,OS} - \sigma_{NLO,\overline{MS}})/(\sigma_{NLO,OS} + \sigma_{NLO,\overline{MS}})$, between the hadronic cross sections $\sigma_{NLO,OS}$ and $\sigma_{NLO,\overline{MS}}$ at both the Tevatron and the LHC. As discussed in detail at the parton level in Section 4.1.3 (see $\hat{\Delta}$ defined in Eq.(4.23)), the difference between the two schemes is scale dependent and can be very big for small and large scales. At the LHC, the relative difference can be well approximated by $\Delta = \frac{1}{2}AB$ with $A = \frac{\alpha_s}{4\pi}g_{NLO}/g_{LO}$ and $B = (1 - (\overline{m}_b/m_b)^2)$, where $g_{NLO,LO}$ correspond to the $g_{NLO,LO}^{ij}$ contributions of Eqs. (4.21) and (4.22) calculated at hadron level. For instance, at $\mu = 0.7\mu_0$, $A = 0.28$ and $B = 0.57$, while at $\mu = 4\mu_0$, $A = 0.92$ and $B = 0.66$, which shows that the difference between the $\overline{MS}$ and the OS schemes of the bottom quark is not dominated by the running of the bottom quark mass as it would be the case when the majority of the NLO corrections can be absorbed in the running of m_b.

From both the observed similar scale dependence of σ_{NLO} in both schemes and the large numerical difference due to the corrections that cannot be absorbed in the running of m_b, we conclude that the use of the $\overline{MS}$ bottom quark Yukawa coupling should probably not be overemphasized. It is probably a good approximation to take the difference between $\sigma_{NLO,OS}$ and $\sigma_{NLO,\overline{MS}}$ at their points of least scale sensitivity as an upper bound on the theoretical error of the NLO cross section, on top of the uncertainty due to the residual scale dependence. This would amount to an additional 15-20% uncertainty arising from the dependence on the bottom quark Yukawa coupling renormalization scheme.

In Fig. 4.7 we illustrate the dependence of the exclusive cross section on the p_T cut imposed on the final state bottom and anti-bottom quarks, at both the Tevatron (top) and the LHC (bottom). We plot the LO and NLO cross sections obtained

139

using the $\overline{MS}$ bottom quark Yukawa coupling. Reducing the p_T cut from 25 GeV to 10 GeV approximately increases the cross section by a factor of four. However, as the p_T cut is reduced, the theoretical calculation of the cross section becomes more unstable, because the integration over the phase space of the final state bottom quarks approaches more and more a region of collinear singularities.

Finally, in Figs. 4.8, 4.9, 4.10, and 4.11 we plot the LO and NLO transverse momentum (p_T) and pseudorapidity (η) distributions of the final state particles, the bottom and anti-bottom quarks and the Higgs boson, both for the Tevatron and for the LHC. Both LO and NLO differential cross sections are obtained in the SM and using the OS scheme for the bottom quark Yukawa coupling. For the renormalization/factorization scale we choose $\mu = 2m_b + M_h$ at the Tevatron and $\mu = 2(2m_b + M_h)$ at the LHC. These two scales are well within the plateau regions where the OS NLO cross sections vary the least with the value of μ. Similar results can be obtained using the $\overline{MS}$ bottom quark Yukawa coupling.

In Fig. 4.8 we show the LO and NLO p_T distributions of the bottom or anti-bottom quark with highest p_T, while Fig. 4.9 displays the p_T distributions of the SM Higgs boson. The pseudorapidity distributions of the bottom quark and the Higgs boson are shown in Fig. 4.10 and Fig. 4.11, respectively. The inclusion of the NLO corrections causes the cross sections to be more sharply peaked around low $p_T^{b,h}$ and around $\eta_{b,h} = 0$.

4.2.1.2   MSSM results

The rate for $b\bar{b}h$ production can be significantly enhanced in a supersymmetric model with large values of $\tan\beta$ (see Eqs. (1.26)-(1.31) in Section 1.2.2 for details on Yukawa couplings). By replacing the SM top and bottom quark Yukawa couplings with the corresponding MSSM ones, our calculation can then be straightforwardly generalized to the case of the scalar Higgs bosons of the MSSM.
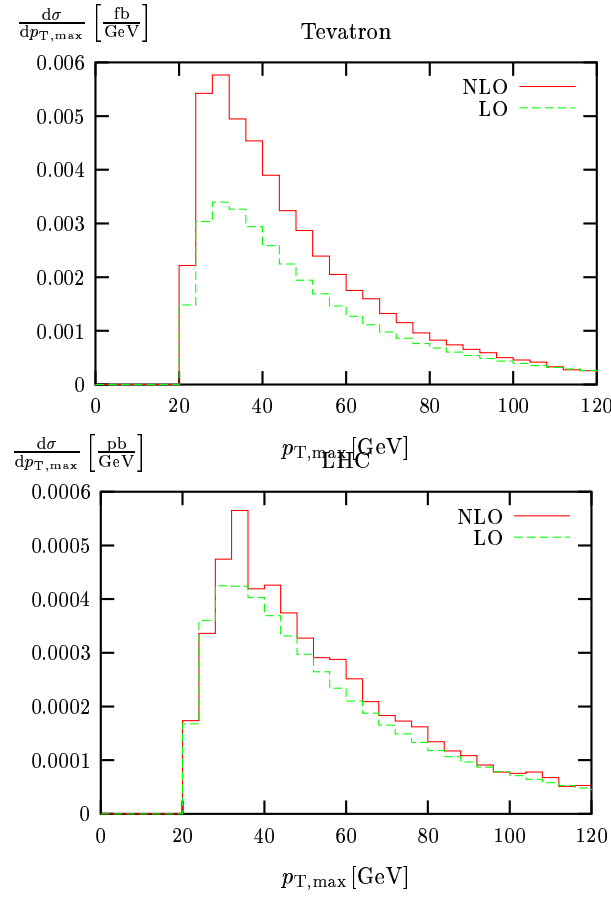
Figure 4.8. Transverse momentum distributions at LO and NLO of the bottom or anti-bottom quark with the largest p_T. Shown are the p_T^{max} distributions for $p\bar{p} \rightarrow b\bar{b}h$ production at $\sqrt{s} = 2$ TeV (left) and $pp \rightarrow b\bar{b}h$ production at $\sqrt{s} = 14$ TeV (right) in the SM and using the OS scheme for the bottom quark Yukawa coupling. At the Tevatron we choose $\mu = 2m_b + M_h$, while at the LHC we choose $\mu = 2(2m_b + M_h)$.

The MSSM Higgs boson masses and the mixing angle α have been computed up to two-loop order using the program FeynHiggs [1]. In Tables 4.2.1.2 and 4.2 we provide the values of the input parameters $((M_{h^0}, \tan\beta)$ or $(M_{H^0}, \tan\beta))$ and the resulting values of α used in the calculation of the top and bottom quark Yukawa couplings to the light and heavy neutral MSSM scalar Higgs bosons. This choice of MSSM parameters takes into account present experimental limits on the MSSM parameter space, but represents otherwise just one among many possible realizations
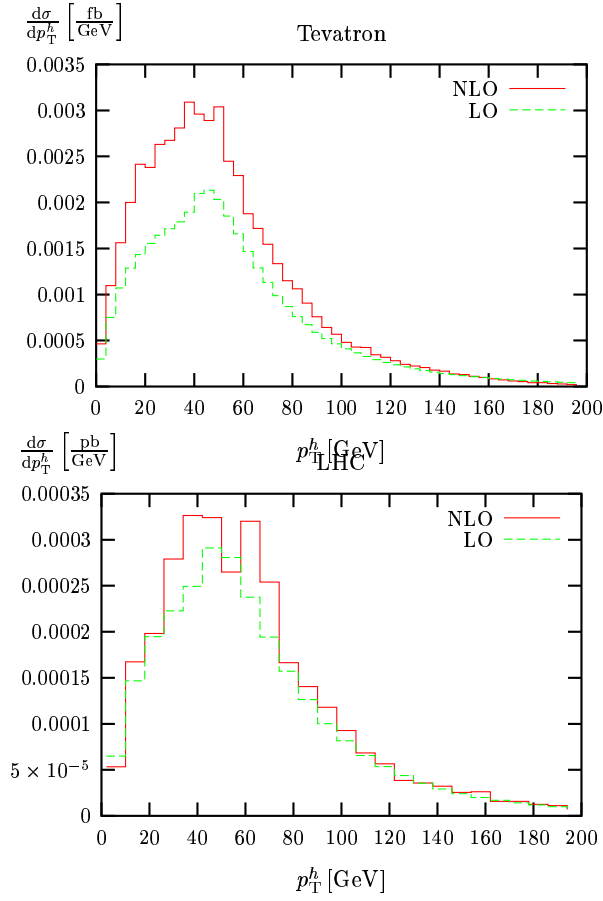
Figure 4.9. Transverse momentum distributions at LO and NLO of the SM Higgs boson. Shown are the p_T^h distributions for $p\bar{p} \to b\bar{b}h$ production at $\sqrt{s}=2$ TeV (left) and $pp \to b\bar{b}h$ production at $\sqrt{s}=14$ TeV (right) in the SM and using the OS scheme for the bottom quark Yukawa coupling. At the Tevatron we choose $\mu=2m_b + M_h$, while at the LHC we choose $\mu=2(2m_b + M_h)$.

of the MSSM parameter space. The results obtained with this choice of MSSM input parameters illustrate the typical enhancements over the SM results one can expect when considering the production of neutral scalar Higgs bosons in association with bottom quarks.

The top part of Fig. 4.12 compares the NLO $p\bar{p} \to b\bar{b}h$ SM cross section at the Tevatron with the corresponding cross section for production of the lightest neutral scalar Higgs boson in the MSSM for $\tan\beta = 10, 20$, and 40. A large enhancement
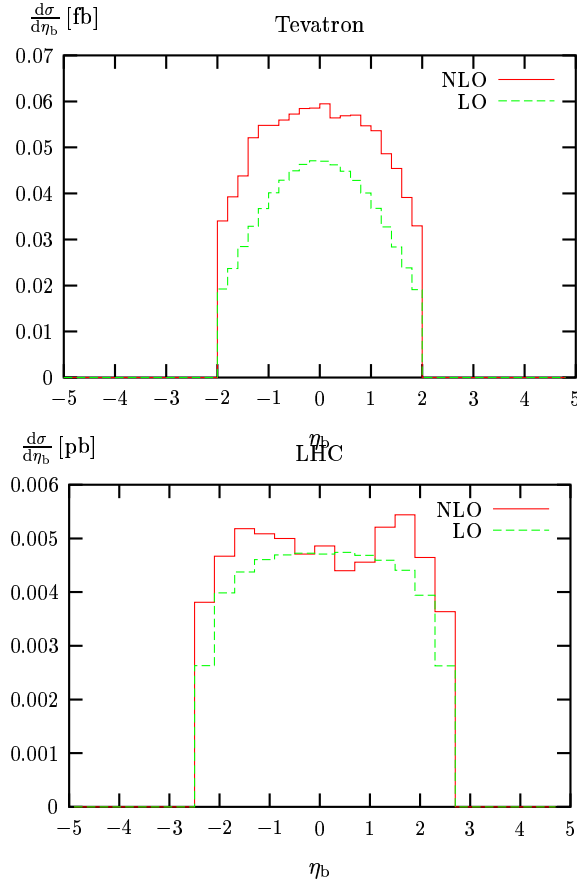
Figure 4.10. Pseudorapidity distributions at LO and NLO of the bottom quark. Shown are the η_b distributions for $p\bar{p} \to b\bar{b}h$ production at $\sqrt{s} = 2$ TeV (left) and $pp \to b\bar{b}h$ production at $\sqrt{s} = 14$ TeV (right) in the SM and using the OS scheme for the bottom quark Yukawa coupling. At the Tevatron we choose $\mu = 2m_b + M_h$, while at the LHC we choose $\mu = 2(2m_b + M_h)$.

of up to three orders of magnitude is observed. As the light neutral Higgs boson mass approaches its maximum value, the mixing angle α becomes very small, as can be clearly seen in Table 4.2.1.2. This has the effect of suppressing the $b\bar{b}h^0$ rates at this point. A similar effect can be observed in the production of a heavy neutral Higgs boson when M_{H^0} is approaching its minimum value (see Table 4.2), as shown in the bottom part of Fig. 4.12. Again, we compare the production of the SM Higgs

143
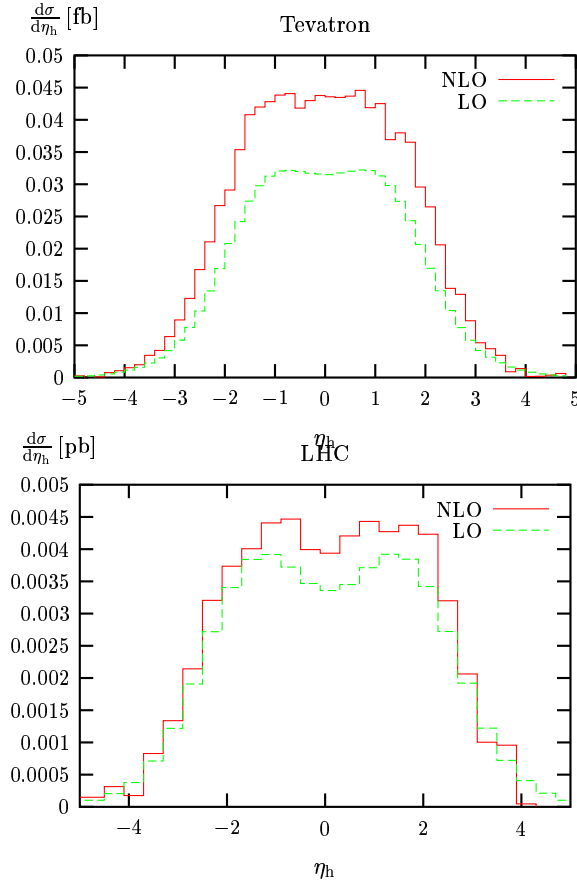
Figure 4.11. Pseudorapidity distributions at LO and NLO of the SM Higgs boson. Shown are the η_h distributions for $p\bar{p} \to b\bar{b}h$ production at $\sqrt{s} = 2$ TeV (left) and $pp \to b\bar{b}h$ production at $\sqrt{s} = 14$ TeV (right) in the SM and using the OS scheme for the bottom quark Yukawa coupling. At the Tevatron we choose $\mu = 2m_b + M_h$, while at the LHC we choose $\mu = 2(2m_b + M_h)$.

boson with that of the heavier neutral scalar Higgs boson of the MSSM and observe a significant enhancement of the rate in the MSSM for large $\tan\beta$.

4.2.2 Higgs production with one high-p_T b jet

Next, we consider the case in which a Higgs boson is produced with *at least* one high-p_T bottom quark, where the cross section can be calculated using either the 4FNS ($q\bar{q}, gg \to b(\bar{b})h + (b)\bar{b}h$) or the 5FNS ($gb \to bh$ and $g\bar{b} \to \bar{b}h$) as discussed
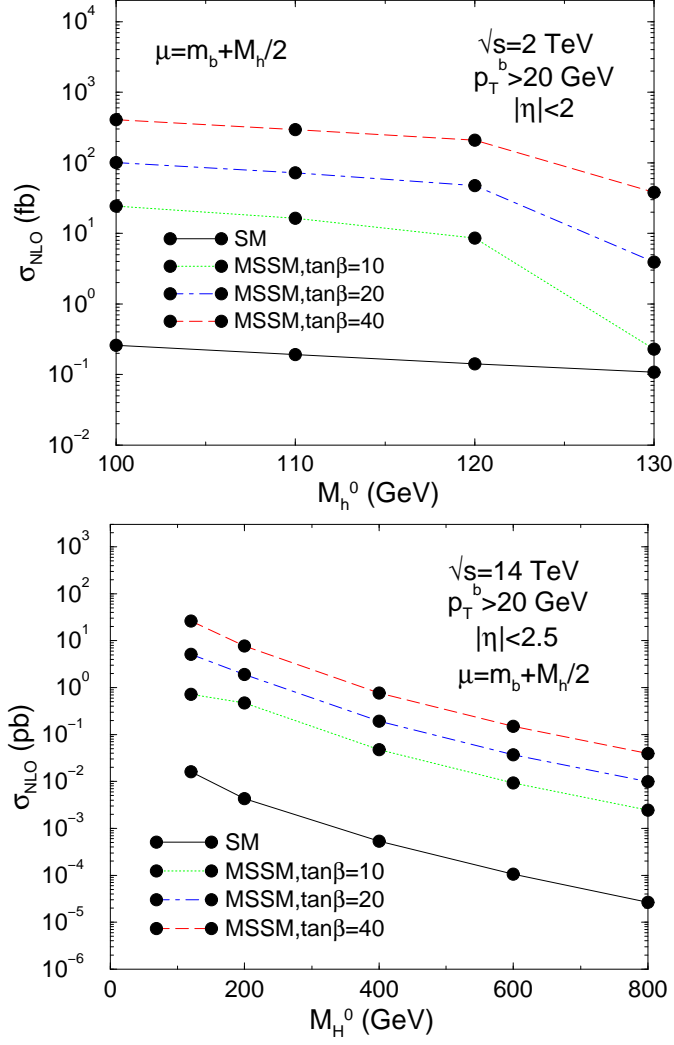
Figure 4.12. $\sigma_{NLO,MS}$ for $p\bar{p} \rightarrow b\bar{b}h$ production at $\sqrt{s} = 2$ TeV (top) and $pp \rightarrow b\bar{b}h$ production at $\sqrt{s} = 14$ TeV (bottom) in the SM and in the MSSM with $\tan\beta = 10, 20,$ and 40. For the Tevatron we considered $p\bar{p} \rightarrow b\bar{b}h^0$ with $M_{h^0} = 100, 110, 120,$ and 130 GeV, while for the LHC we considered $pp \rightarrow b\bar{b}H^0$ with $M_{H^0} = 120, 200, 400, 600,$ and 800 GeV. For each $(M_{h^0}, \tan\beta)$ and $(M_{H^0}, \tan\beta)$ point, the corresponding values of α and M_A are listed in Tables 4.2.1.2 and 4.2.

Table 4.1. Values of α and M_A, computed up to two-loop order by using the program FeynHiggs [1], corresponding to different choices of $\tan\beta$ and M_{h^0}. In the calculation of α and M_A we choose the genuine SUSY input parameters as follows: $M_{\tilde{g}} = M_{\tilde{t}_L} = M_{\tilde{t}_R} = M_{\tilde{b}_L} = M_{\tilde{b}_R} = 1$ TeV, $M_t^{LR} = 2$ TeV, $A_b = A_t = M_t^{LR} + \mu\cot\beta$, and $\mu = M_2 = 200$ GeV.

$\tan\beta = 10$				
M_{h^0} [GeV]	100	110	120	130
M_A [GeV]	102.42	113.86	127.95	264.72
α [rad]	-1.3249	-1.1963	-0.9054	-0.1463
$\tan\beta = 20$				
M_{h^0} [GeV]	100	110	120	130
M_A [GeV]	100.61	110.95	121.89	146.72
α [rad]	-1.4420	-1.3707	-1.1856	-0.3108
$\tan\beta = 40$				
M_{h^0} [GeV]	100	110	120	130
M_A [GeV]	100.15	110.23	120.46	133.71
α [rad]	-1.5007	-1.4601	-1.3444	-0.4999

Table 4.2. Values of α and M_A, computed up to two-loop order by using the program FeynHiggs [1], corresponding to different choices of $\tan\beta$ and M_{H^0}. In the calculation of α and M_A we choose the genuine SUSY input parameters as follows: $M_{\tilde{g}} = M_{\tilde{t}_L} = M_{\tilde{t}_R} = M_{\tilde{b}_L} = M_{\tilde{b}_R} = 1$ TeV, $M_t^{LR} = 0$, $A_b = A_t = M_t^{LR} + \mu\cot\beta$, and $\mu = M_2 = 1$ TeV.

$\tan\beta = 10$					
M_{H^0} [GeV]	120	200	400	600	800
M_A [GeV]	108.05	198.55	399.41	599.64	799.74
α [rad]	-0.9018	-0.1762	-0.1140	-0.1057	-0.1030
$\tan\beta = 20$					
M_{H^0} [GeV]	120	200	400	600	800
M_A [GeV]	116.45	199.56	399.81	599.89	799.91
α [rad]	-0.5785	-0.0901	-0.0574	-0.0531	-0.0517
$\tan\beta = 40$					
M_{H^0} [GeV]	120	200	400	600	800
M_A [GeV]	118.92	199.82	399.92	599.95	799.96
α [rad]	-0.3116	-0.0460	-0.0289	-0.0267	-0.0259

at the beginning of this chapter. In fact, assessing the validity and compatibility of the two schemes has recently been the subject of much theoretical interest, since early comparisons of the LO cross sections (using $\mu_h \approx M_h$) seemed to indicate that the 5FNS cross section prediction was much larger than that predicted by the 4FNS calculation (see Ref. [92]). This channel has also been the subject of much experimental interest, since requiring one final state b quark allows the unambiguous measurement of the bottom quark Yukawa coupling and significantly enhances the rate with respect to the case when both b quarks are identified (see Section 4.2.1). Higgs boson production with one b quark jet followed by $h \to b\bar{b}$ has been extensively studied by the CDF and D0 collaborations [34, 35] and is going to play a major role in the experimental searches for Higgs bosons beyond the SM at the Tevatron and at the LHC. Thus, a more dedicated effort aimed at refining the theoretical predictions for both total and differential cross sections is mandatory.

Recently, the first comparison of the NLO QCD total cross sections for $q\bar{q}, gg \to b(\bar{b})h$ [84, 88] and for $bg \to bh$ [87] processes has been presented in Ref. [96]. In this section, we concentrate on the comparison of total and differential cross sections at NLO QCD in the 4FNS and 5FNS schemes. This is the first comparison of differential cross sections in the two calculational schemes and it is important to assess the residual theoretical uncertainties in view of future experimental analyses. In particular, we discuss the effects of including the closed top quark loop diagram of Fig. 4.13, a contribution that had been previously neglected in the NLO 5FNS calculation of $bg \to bh$.

As in the last section, the NLO QCD corrections to $pp, p\bar{p} \to b(\bar{b})h$ production in the 4FNS consist of calculating the $\mathcal{O}(\alpha_s)$ virtual and real QCD corrections to the $q\bar{q}, gg \to b\bar{b}h$ tree level processes [84, 88], imposing identification cuts on the transverse momentum and pseudorapidity of either the b or $\bar{b}$ final state quark (antiquark). Results from the two existing calculations [84, 88] have been compared and found to be in good agreement (see Ref. [96]).
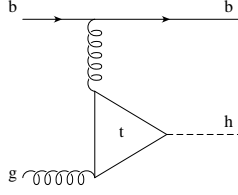
Figure 4.13. Feynman diagram for the closed top quark loop contribution to $gb \rightarrow bh$.

The NLO QCD corrections to $pp, p\bar{p} \rightarrow bh + \bar{b}h$ production in the 5FNS have been presented in Ref. [87] and are encoded in the Monte Carlo program MCFM [97]. In Ref. [87], the calculation of the cross sections for $gb \rightarrow bh$ is performed in the $m_b = 0$ approximation (except for the b quark Yukawa coupling), and for this reason the only virtual diagram containing a top quark loop (see Fig. 4.13) is neglected. Indeed, the contribution of this diagram to the virtual cross section is proportional to $g_{t\bar{t}h} g_{b\bar{b}h} m_b / m_t$ and therefore vanishes when the kinematic bottom quark mass is set to zero. At the same time, in the SM ($g_{b\bar{b}h}^{SM} = m_b/v$ and $g_{t\bar{t}h}^{SM} = m_t/v$) the contribution of this diagram is overall of order $g_{b\bar{b}h}^2$ as all other diagrams retained in the $m_b = 0$ approximation. So, it can play a relevant numerical role in the comparison between the 5FNS and the 4FNS, where diagrams with closed top quark loops are included (see Fig. 4.4). To investigate this issue we have added this contribution to the $gb \rightarrow bh$ NLO calculation of total and differential cross sections and implemented it into MCFM. All numerical results in the 5FNS presented here are obtained with this modified version of MCFM[3].

Our LO numerical results are obtained using CTEQ6L1 PDFs [89, 98] and the 1-loop evolution of α_s, while for NLO results we use CTEQ6M PDFs and the 2-loop

---

[3]It should be noted that the contribution from the top loop diagram is only important for the comparison performed using SM Yukawa couplings. Indeed, in the MSSM with large $\tan\beta$, the top quark Yukawa coupling is highly suppressed and the contribution from these diagrams is negligible. However, since the comparisons between 4FNS and 5FNS calculations have always been presented using SM Yukawa couplings [83, 92, 96], this is the case we discuss.
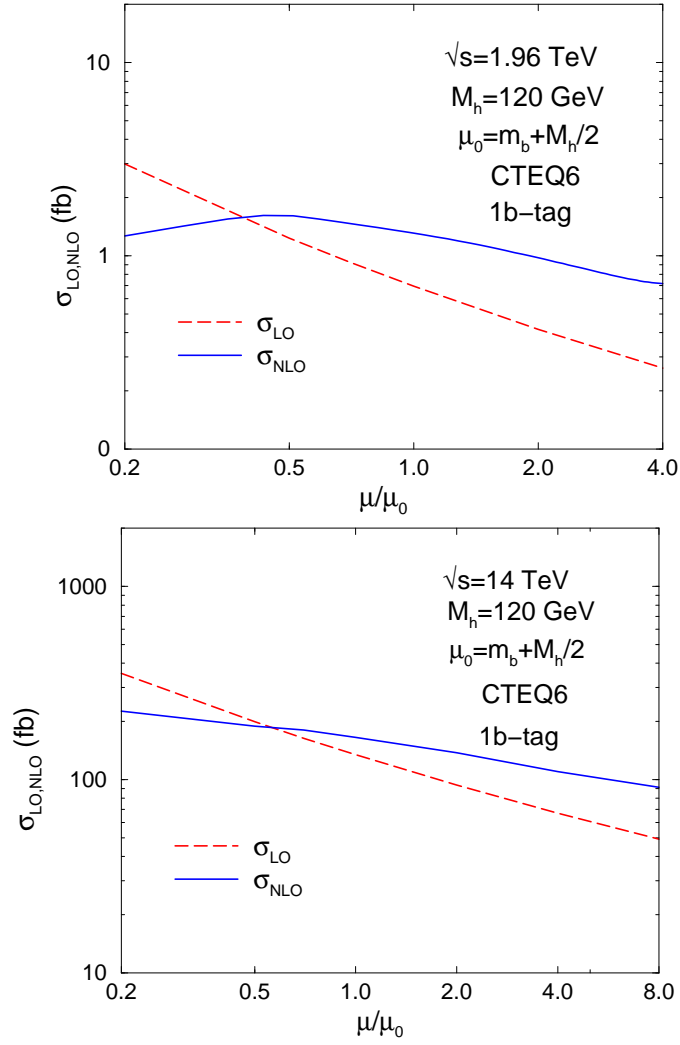
Figure 4.14. Total LO and NLO cross sections for $pp, p\bar{p} \to b(\bar{b})h$ production in the 4FNS as a function of $\mu = \mu_r = \mu_f$ for $M_h = 120$ GeV, at both the Tevatron (top) and the LHC (bottom).

evolution of α_s, with $\alpha_s(M_Z) = 0.118$. We use the $\overline{MS}$ running b quark mass in the b quark Yukawa coupling, evaluated at 1- and 2-loops respectively for LO and NLO results (with pole mass $m_b = 4.6$ GeV). Our renormalization scheme decouples the top quark from the running of $m_b(\mu)$ and $\alpha_s(\mu)$ and is explained in detail in Chapter 3 and Section 4.1.3. We work in the SM but the results can be straightforwardly
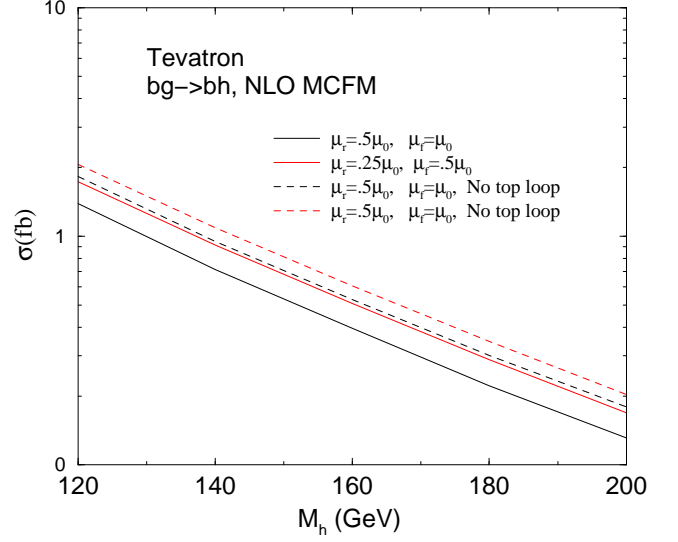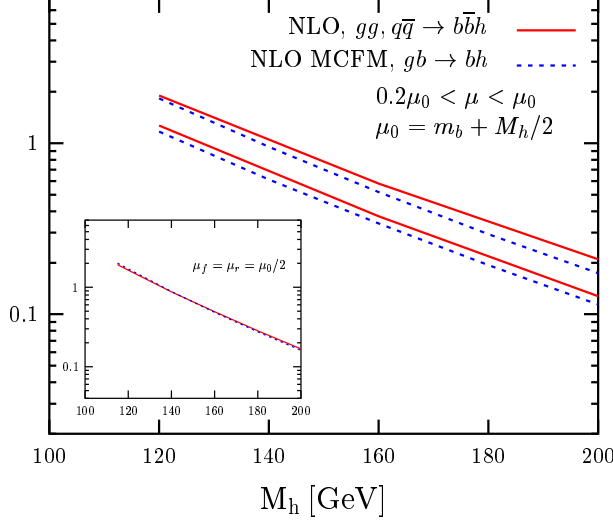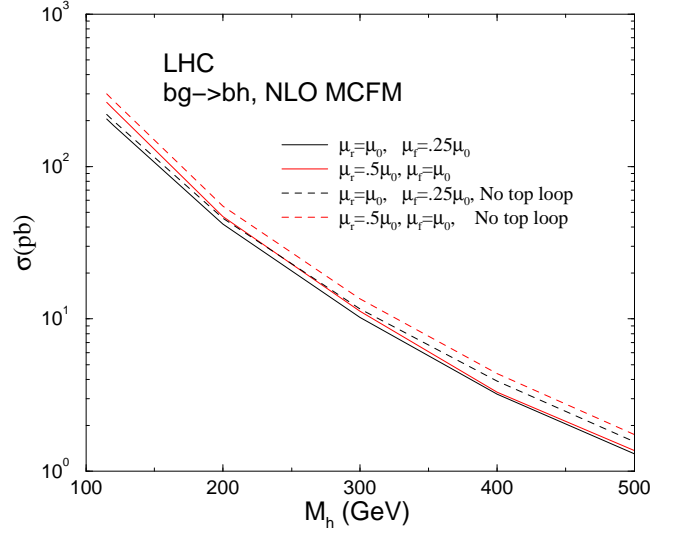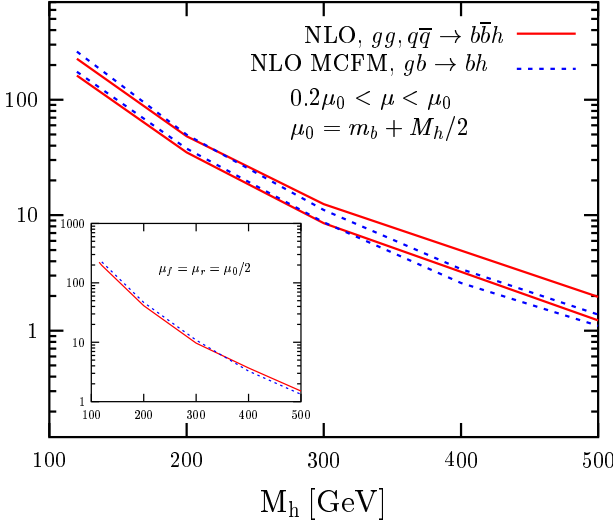
Figure 4.15. Total NLO cross section for $pp, p\bar{p} \rightarrow b(\bar{b})h$ production at the Tevatron and the LHC as a function of M_h. We have assumed $\mu_r = \mu_f = \mu_0/2$ for the central curves (see inlays) and varied μ_r and μ_f independently to obtain the uncertainty bands, as explained in the text. On the left, the solid curves correspond to the 4FNS, the dashed curves to the 5FNS. On the right, we show the 5FNS with (solid) and without (dashed) the top quark loop contribution.

generalized to the case of the scalar Higgs bosons of a supersymmetric extension of the SM as discussed in Section 4.1.1 (see Eq. (4.2)).

In order to simulate the experimental cuts, we require one of the final state b quarks to have $p_T > 20$ GeV and pseudo-rapidity $|\eta| < 2.0$ for the Tevatron and $|\eta| < 2.5$ for the LHC. In the NLO real gluon emission, the final state gluon and b quarks are considered as separate particles only if $\Delta R > 0.4$ ($\Delta R = \sqrt{(\Delta \eta)^2 + (\Delta \phi)^2}$ where ϕ is the azimuthal angle measured with respect to the beam axis).

In Fig. 4.14 we show, for $M_h = 120$ GeV, the dependence of the LO and NLO total cross sections, calculated in the 4FNS, on the arbitrary renormalization/factorization scale μ (with $\mu_r = \mu_f = \mu$). The NLO result has considerably less sensitivity to the scale choice, and the region around $\mu \approx \mu_0/2$ ($\mu_0 = m_b + M_h/2$) shows the least sensitivity to the variation of μ. For this reason we use $\mu_0/2$ as our reference scale in the following plots, whenever $\mu_r = \mu_f$. Analogous results for the 5FNS total cross sections have been presented in Ref. [87].

Fig. 4.15 shows the dependence of the NLO total cross sections on M_h, in both the 4FNS and 5FNS (left) and the effect of including the top loop diagram in the 5FNS calculation (right). The bands illustrate the theoretical uncertainty due to the independent variation of μ_r and μ_f about the central value $\mu_r = \mu_f = \mu_0/2$ (see inlays), between $0.2\mu_0$ and μ_0. From the left hand plots, it is extremely interesting to note that the 5FNS band is almost completely within the 4FNS band, and the corresponding central values are nearly identical at the Tevatron and very close at the LHC. The smaller scale dependence of the 5FNS calculation is a direct effect of resumming the collinear logarithms and the agreement between the central values (inlays), in particular, is direct evidence that the collinear logarithms are indeed the dominant contribution in the 4FNS calculation since these are the only pieces accounted for in the 5FNS. The right hand plots show that including the closed top quark loop diagrams lowers the 5FNS cross section (by $\approx 15\%$ at the Tevatron and $\approx 10\%$ at the LHC, when $M_h = 120$ GeV and $\mu_r = \mu_f = 0.5\mu_0$) and makes the

151

theoretical prediction in the 4FNS and 5FNS fully compatible (see for comparison Fig. 6 in Ref. [96]). Note that the bands only give an indication of the theoretical uncertainty of each approach due to the residual scale dependence. We shall examine the uncertainties coming from the PDFs in Section 4.3.

Figure 4.16. $d\sigma/dp_T^h$ at the Tevatron (top) and the LHC (bottom) for $M_h = 120$ GeV and $\mu_r = \mu_f = \mu_0/2$. We show the NLO results in the 4FNS (solid) and 5FNS (dashed), using two different bin sizes, 2 GeV (left) and 12 GeV (right).

Finally, in Figs. 4.16-4.18 we compare the results for the p_T and η distributions of the Higgs boson in both the 4FNS and 5FNS, at the Tevatron and the LHC. We see, in general, a good agreement between the two schemes, except in the region around $p_T^h \simeq p_T^{b,min}$. This is particularly dramatic in the p_T^h distributions where, around $p_T^h \simeq 20$ GeV, the 5FNS NLO calculation is highly unstable. This instability is a well-known effect (e.g. see Refs. [99] and [100]) and arises due to the fact that, in the region slightly above $p_T^{b,min}$, the NLO differential cross section $(d\sigma/dp_T^h)_{NLO}$ is a convolution of the LO differential cross section $(d\sigma/dp_T^h)_{LO}$ with a *soft gluon factor*, $K_{soft}(z)$, made up of the sum of the virtual and real contributions:

$$\left(\frac{d\sigma}{dp_T^h}\right)_{NLO} = \int dz \left(\frac{d\sigma}{dp_T^h}\right)_{NLO} K_{soft}(z) \tag{4.26}$$

Due to the kinematics of the two-body final state in the LO process, the cut on p_T^b translates into an effective cut on p_T^h, thus making $(d\sigma/dp_T^h)_{LO}$ a *non-smooth* function. Additionally, just above the threshold at $p_T^{b,min}$, the soft gluon factor takes the form of a *plus distribution*, which is defined under integration with a smooth function by:

$$\int_0^1 dz f(z)[g(z)]_+ = \int_0^1 dz (f(z) - f(1)) g(z) . \tag{4.27}$$

However, when a plus distribution is convoluted with a non-smooth function, such as $(d\sigma/dp_T^h)_{LO}$, *logarithmic divergences* result. These instabilities can be reabsorbed by using a larger bin size (see inlays), and could therefore be interpreted as a sort of theoretical *resolution* for the 5FNS. The instabilities could be removed by a systematic resummation of threshold corrections [101, 99], but this is not implemented in MCFM.

Fig. 4.18 illustrates the impact of NLO QCD corrections on p_T^h and η_h distributions in terms of a differential K-factor $(d\sigma_{NLO}/d\sigma_{LO})$. It is interesting to note that the 4FNS and 5FNS agree at large p_T^h but they differ substantially at low p_T^h. However, this difference is also due to the kinematics of the two-body final state of the LO process $gb \to bh$. Due to the effective cut on p_T^h mentioned above, in the

153

region below $p_T^{b,min}$, the distribution $(d\sigma/dp_T^h)_{LO}$ is zero and the ratio $(d\sigma_{NLO}/d\sigma_{LO})$ is undefined. Lastly, as can be seen in Fig. 4.18, there are regions of p_T^h and η_h where the NLO QCD corrections can considerably affect the shape of the distributions.
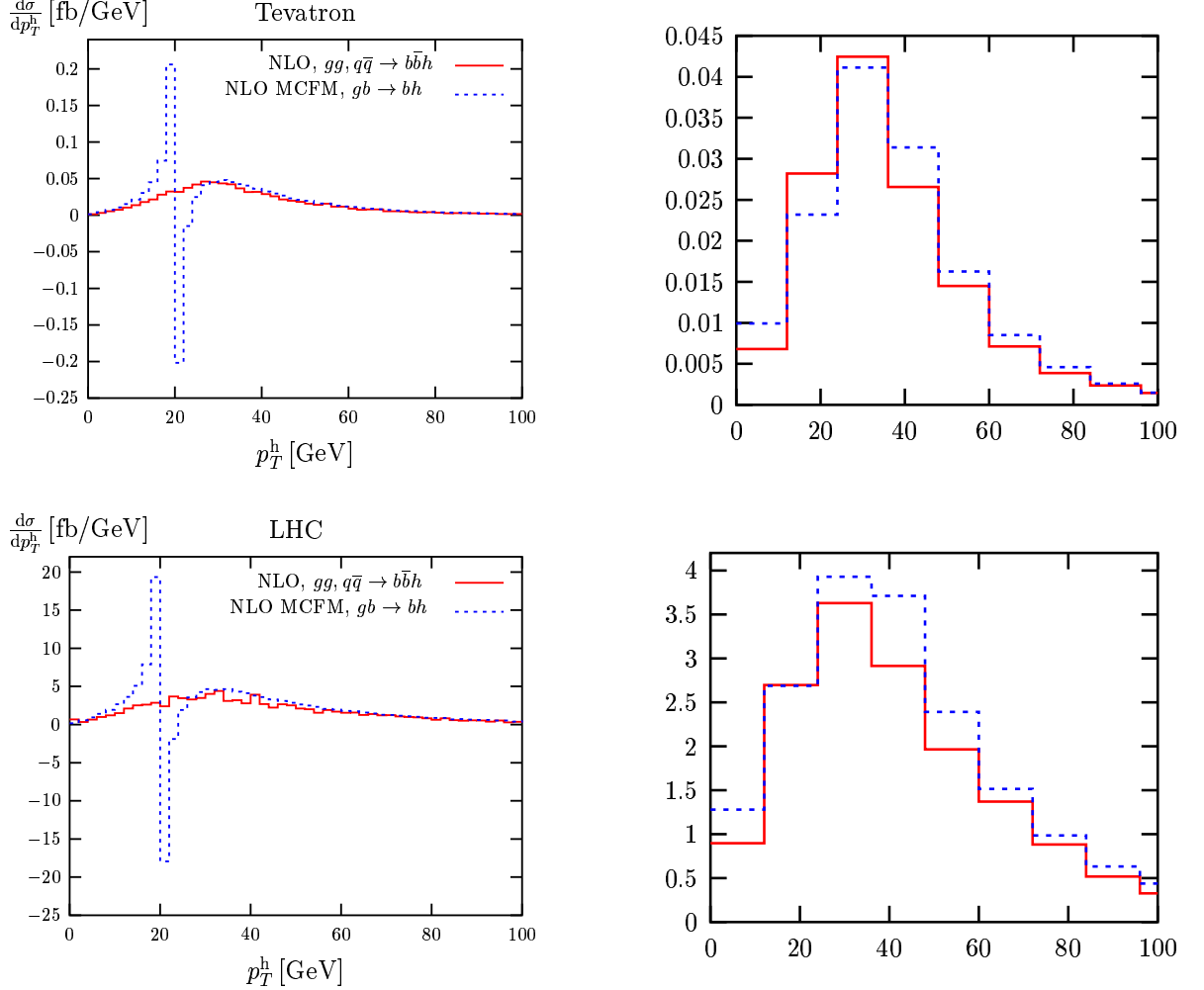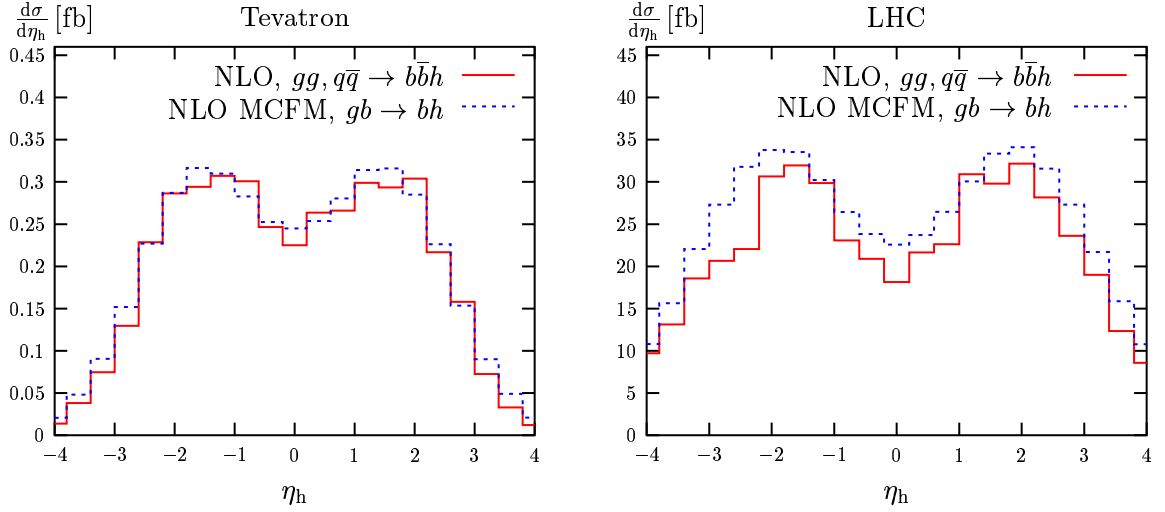

Figure 4.17. $d\sigma/d\eta_h$ at the Tevatron and the LHC for $M_h = 120$ GeV and $\mu_r = \mu_f = \mu_0/2$. We show the NLO results in the 4FNS (solid) and 5FNS (dashed).

4.2.3 Inclusive higgs production with bottom quarks

Finally, we consider the case where the bottom quarks which are produced in association with the Higgs boson are not observed. As mentioned earlier, the dominant 5FNS process in this situation is $b\bar{b} \to h$. Although the signal for this process will be swamped by large QCD backgrounds at the Tevatron, this mode could be among the Higgs discovery channels at the LHC for heavy MSSM Higgs bosons (H^0, A^0) by searching for the rare Higgs boson decay modes into $\mu^+\mu^-$ and $\tau^+\tau^-$.

154
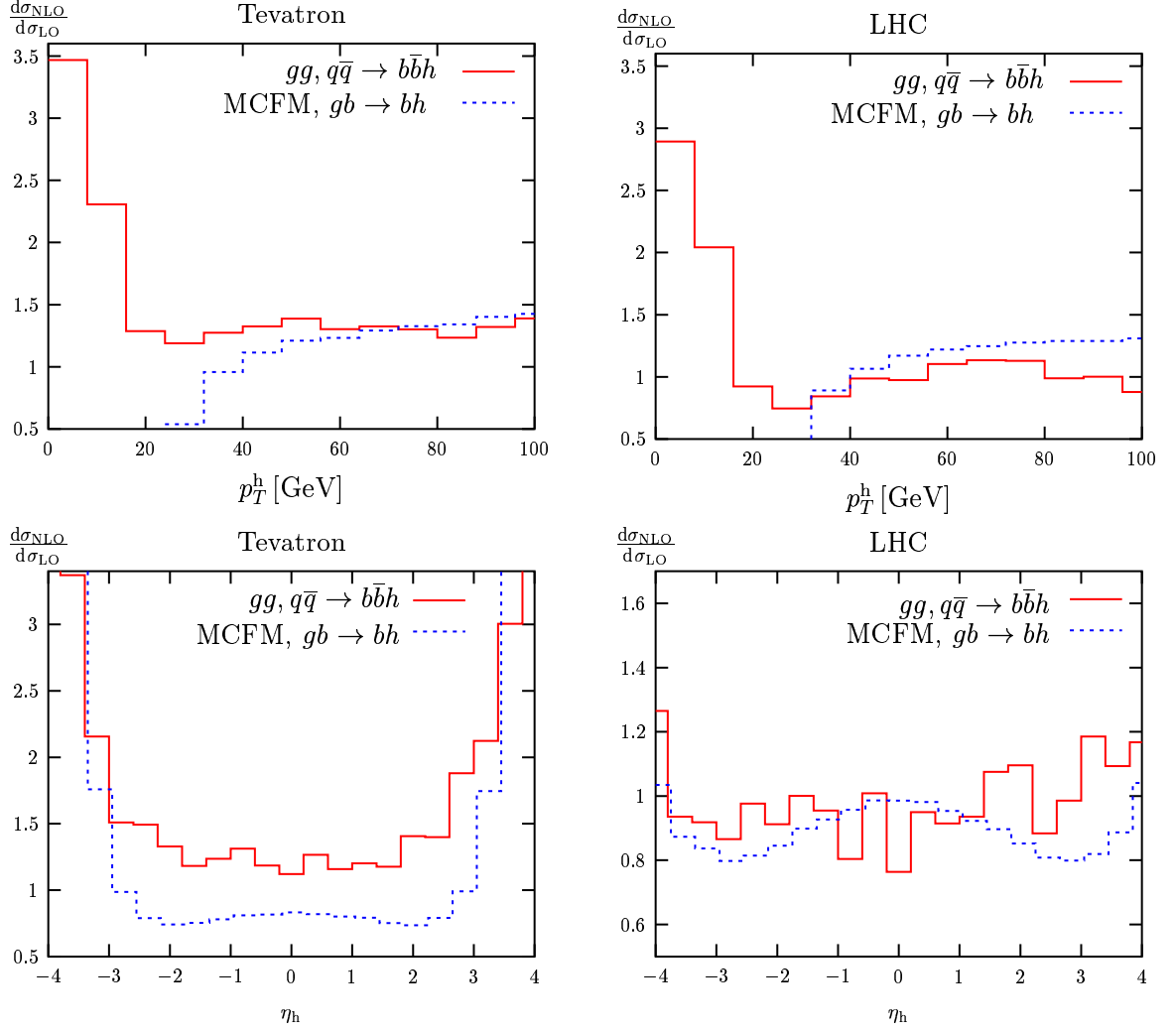
Figure 4.18. The ratios of the NLO and LO p_T^h and η_h distributions at the Tevatron and the LHC for $M_h = 120$ GeV and $\mu_r = \mu_f = \mu_0/2$. We show the ratios in the 4FNS (solid) and 5FNS (dashed).

155
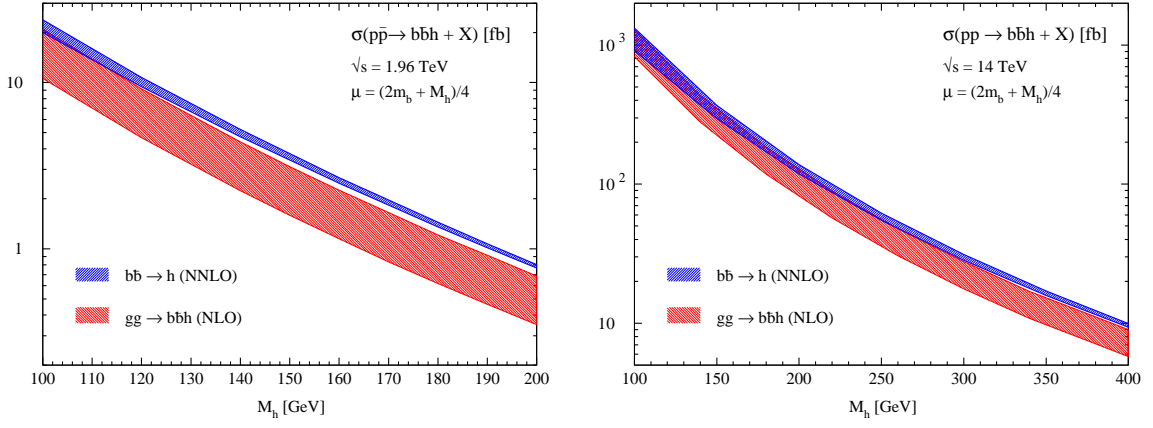
Figure 4.19. The total cross section as a function of M_h for $b\bar{b}h$ production when no b quarks are tagged in the final state for the Tevatron (left) and the LHC (right).

The 4FNS calculation of the NLO corrected process $pp, p\bar{p} \rightarrow (b\bar{b})h$ is identical to that discussed in the previous sections with the exception that, in this case, there are no restrictions placed on the p_T and η of the bottom quarks.

The higher-order corrections to the 5FNS process $b\bar{b} \rightarrow h$ involve corrections in both α_s and Λ_b^{-1}, as discussed at the beginning of this chapter. The NLO corrections have been known for quite some time [92], however, the scale dependence at NLO is still quite significant. Recently, the NNLO corrections to $b\bar{b} \rightarrow h$ have been computed and the results exhibit a drastically reduced scale dependence providing a very stable result [85].

In Fig. 4.19, we compare the NLO 4FNS and NNLO 5FNS calculations as a function of the Higgs boson mass at both the Tevatron and the LHC. The uncertainty bands are produced by varying the values of μ_r and μ_f about the central value $\mu_r = \mu_f = \mu_0/2$ between $0.2\mu_0$ and μ_0. These plots show that, for low Higgs masses, the calculations agree within their respective scale uncertainties. However, for larger Higgs masses, the 5FNS yields larger cross sections than those of the 4FNS [85]. It is worth noting, though, that top loop diagrams (similar to those discussed in the

156

last section) are not included in the 5FNS calculation. The top loop diagrams in the 4FNS calculation lower the cross sections by $\sim 4\%$ at the Tevatron and by $\sim 9\%$ at the LHC. In any case, at large $\tan\beta$, the top loop contributions become negligible and the agreement between the two calculational schemes should improve.

4.3   PDF uncertainties

Besides the residual renormalization/factorization scale dependence after higher-order corrections have been included, another major source of theoretical uncertainty for cross section predictions at Hadron colliders comes from the Parton Distribution Functions. Unfortunately, PDFs are plagued by uncertainties which arise either from the non-perturbative, initial starting distributions used to fit the available data or from the DGLAP scale evolution to the higher energies relevant at hadron colliders [59, 90, 91].

Recently, several collaborations have provided automatic methods to estimate the theoretical uncertainty on physical observables due to the uncertainty in the PDFs. Here, we focus on the method introduced by the CTEQ collaboration (see Ref. [89]), since we have used CTEQ PDFs in our work. The details of this method are beyond the scope of this thesis, however, we give a brief explanation below. First, the nominal set of PDFs (e.g. CTEQ6) is constructed by fitting a *non-perturbative core equation* to data from low-energy experiments designed to measure PDFs. The core equation, in the method used by CTEQ, is parameterized by 20 independent parameters which are dialed to fit the data. Once the nominal set is fixed, the 20 parameters are then varied in a well-defined manner to produce an additional 40 sets of PDFs. These sets serve as a *map* of the neighborhood around the nominal fit to the data. Indeed, one can then use the 40 sets to estimate the uncertainty from the PDFs on a physical observable in the following way [4]: first, the central value cross section

---

[4]We have also performed this analysis using the PDF sets of the MRST collaboration [102]. These sets are made up of 30 sets in addition to the nominal fit and, hence, map less of the neighborhood

157

σ_0 is calculated using the global minimum PDF (i.e. CTEQ6M). The calculation of the cross section is then performed with the additional 40 PDFs to produce 40 different predictions, σ_i. For each of these, the deviation from the central value is calculated to be $\Delta\sigma_i^\pm = |\sigma_i - \sigma_0|$ when $\sigma_i \gtrless \sigma_0$. Finally, to obtain the uncertainties due to the PDFs the deviations are summed quadratically as $\Delta\sigma^\pm = \sqrt{\sum_i \Delta\sigma_i^{\pm 2}}$ and the cross section including the theoretical uncertainties arising from the PDFs is quoted as $\sigma_0|_{-\Delta\sigma^-}^{+\Delta\sigma^+}$. Recently, a similar analysis has been performed for other SM Higgs production modes [103].

For the light partons (i.e. gluons and light quarks), there are three distinct regions of the uncertainties as a function of the momentum fraction carried by the parton, x: decreasing uncertainties at low x, constant or oscillating ones at intermediate x, and increasing uncertainties at high x. The magnitude of these uncertainties depends on the parton considered and the CM energy Q^2. For light quarks at high Q^2, the three regions are clearly observed with uncertainties typically in the 10-20% range in the low and high x regions and, in the intermediate region, they are typically less than a few percent. For the gluons, the three regions are not as distinct and the uncertainties are typically higher than that of light quarks (see Fig. 4.20).

However, the heavy quarks, in particular the bottom quark, are treated in a different manner. As we have seen, bottom quarks inside protons (or antiprotons) arise from gluon splitting $g \to b\bar{b}$ and are not believed to be *intrinsic* partons. Indeed, the b-quark PDF is not fit from data, but is instead derived from measurements of the gluon PDF using the perturbative expression in Eq. (4.4). Therefore, the uncertainty in the b PDF is intimately linked to the uncertainty of the gluon PDF as shown in Fig. 4.20. The fact that the b PDF uncertainty curve appears to be a shifted version of the gluon curve at higher values of x can be explained in a simple, physical way: gluons at higher values of x split into bottom quarks which carry smaller values of x.

around the global minimum. This results in smaller spread uncertainties than the CTEQ analysis. Therefore, we only show results using the CTEQ sets and quote these results as an upper limit of the uncertainty from PDFs.
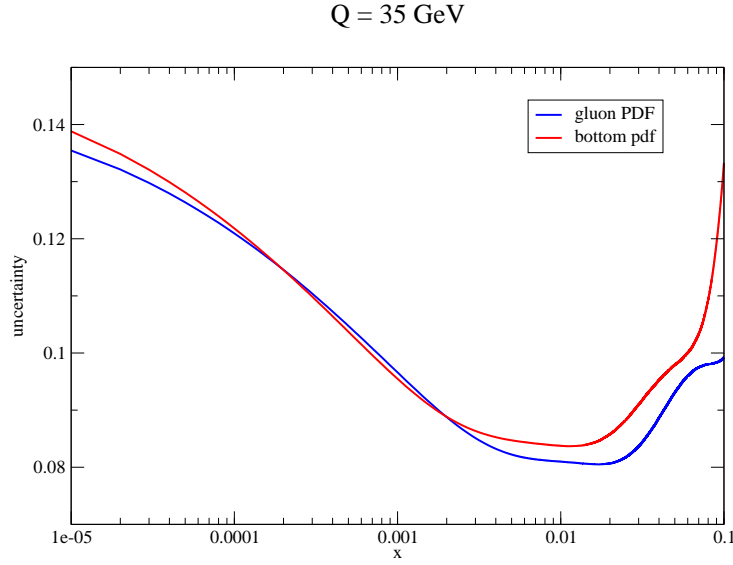
Figure 4.20. The uncertainties for the bottom quark and gluon PDFs at $Q = 35$ GeV as a function of x.

In other words, the uncertainties of gluons at high values of x *feed down* to bottom quarks at smaller x, hence explaining the shifted appearance of the bottom quark PDF with respect to that of the gluon [104].

In Figures 4.21 and 4.22 we plot the total NLO cross section for $gb \rightarrow bh$ obtained with MCFM [97] at the Tevatron and LHC respectively. Here, we compare the uncertainties due to the residual scale dependence and due to the PDF uncertainty, both for the total cross section (top) and the total cross section normalized to the central value calculated with CTEQ6M (bottom). From Figure 4.22 one can see that, at the LHC, the theoretical uncertainty is dominated by the residual scale dependence. Due to the large CM energy at the LHC, the gluons and bottom quarks in the initial state have small x values and, hence, small PDF uncertainties typically in the 5-10% range.
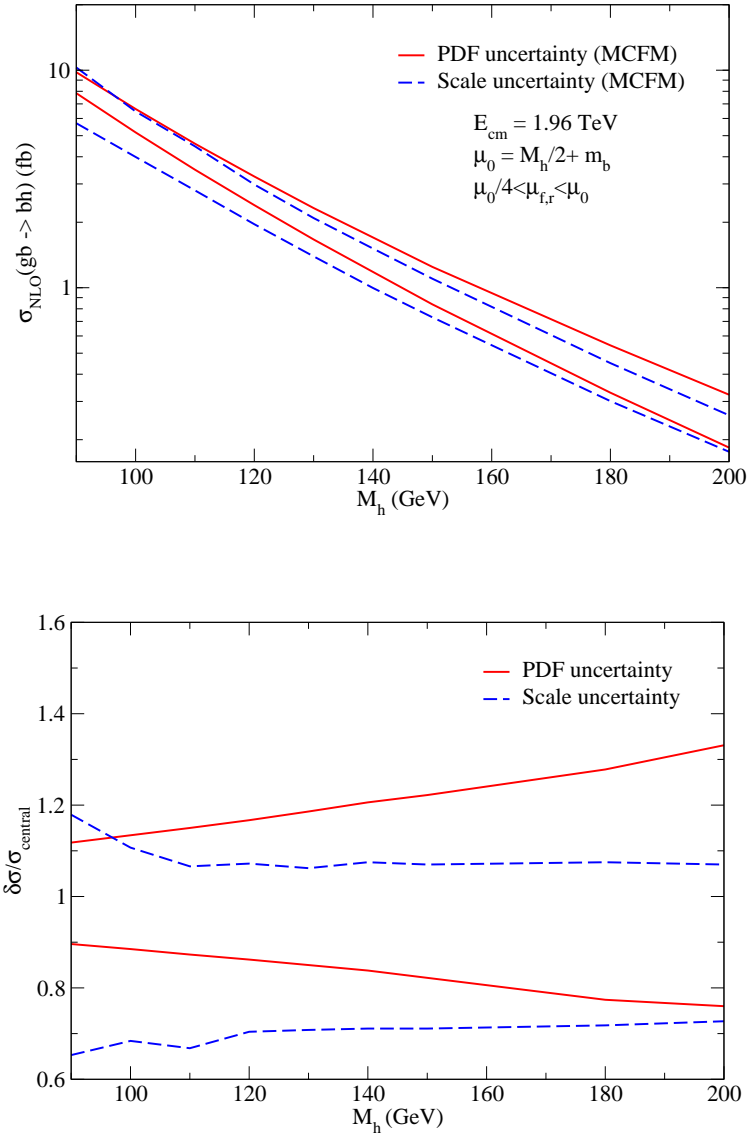
Figure 4.21. Comparison between theoretical uncertainties due to scale dependence and uncertainties arising from the PDFs at the Tevatron (top). In the bottom plot, both uncertainty bands have been normalized to the central value of the total cross section σ_0.
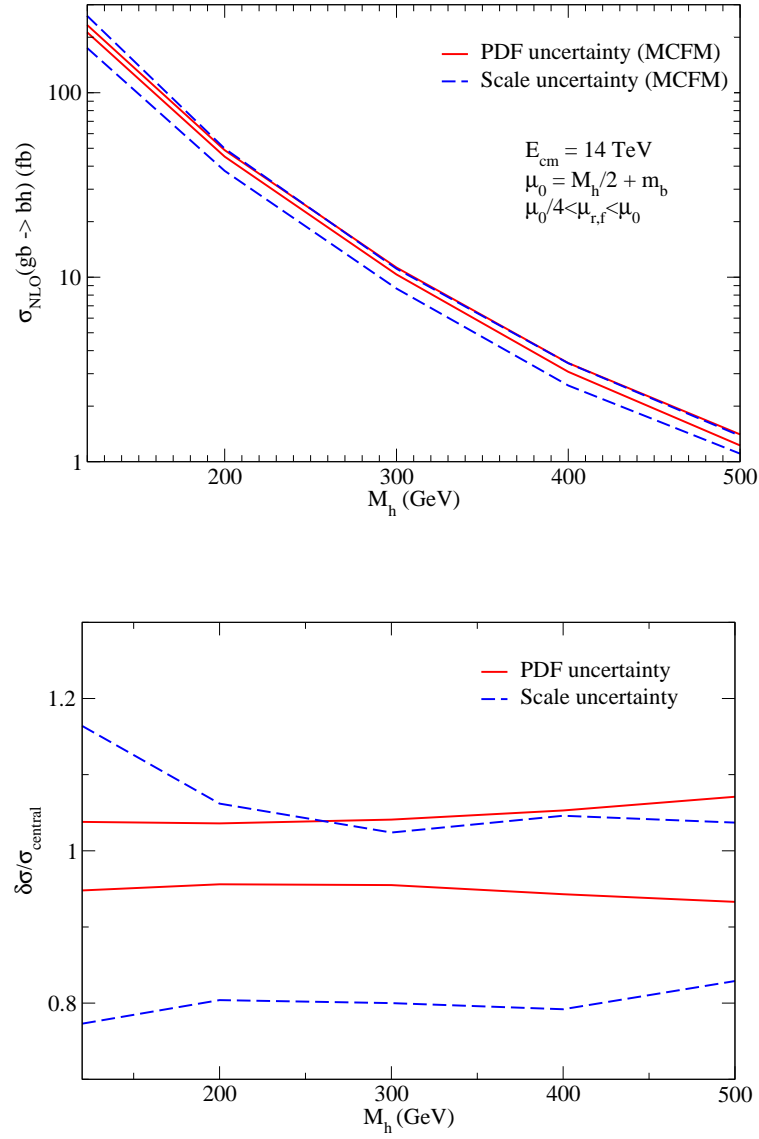
Figure 4.22. Comparison between theoretical uncertainties due to scale dependence and uncertainties arising from the PDFs at the LHC (top). In the bottom plot, both uncertainty bands have been normalized to the central value of the total cross section σ_0.

In contrast, due to the smaller CM energy, the uncertainty from the PDFs at the Tevatron (Figure 4.21) are comparable and even larger than the uncertainty due to the residual scale dependence over the full Higgs mass range. The smaller CM energy results in higher-x gluons and bottom quarks in the initial state, for which the PDF uncertainties can be in the 10-30% range.

Finally, in Figure 4.23, we plot the normalized total cross sections of $gb \to bh$ and $gg \to b(\bar{b})h$ and compare their respective uncertainties due to the PDFs. We see that, at both the Tevatron and the LHC, the PDF uncertainties are almost identical for both the gg and gb initial states. This can be understood since most of the reactions take place at a value of x where the bottom quark and gluon PDF uncertainties are similar.

4.4   Summary

The production of a non-SM Higgs boson in association with bottom quarks can play an extremely important role at both the Tevatron and the LHC. For the case of the MSSM with large $\tan\beta$, this channel dominates over all other Higgs production processes and could provide the first signal of supersymmetry at Run II of the Tevatron.

The cross sections for inclusive and exclusive $b\bar{b}h$ production have different analytical properties and need to be considered separately. In this chapter, we have discussed in detail how to approach both inclusive and exclusive calculations and we have shown how the NLO calculation of $q\bar{q}, gg \to b\bar{b}h$ presented in this thesis has been instrumental to solving the outstanding issue of comparing 4FNS and 5FNS approaches to the calculation of inclusive cross sections. We have compared the 4FNS prediction for the semi-inclusive (inclusive) process with the NLO (NNLO) 5FNS calculations of $gb \to bh$ ($b\bar{b} \to h$). For the semi-inclusive process, we showed that by including a previously neglected top quark loop diagram in the 5FNS calculation, the two approaches (i.e. 4FNS and 5FNS) agree spectacularly. Although this is
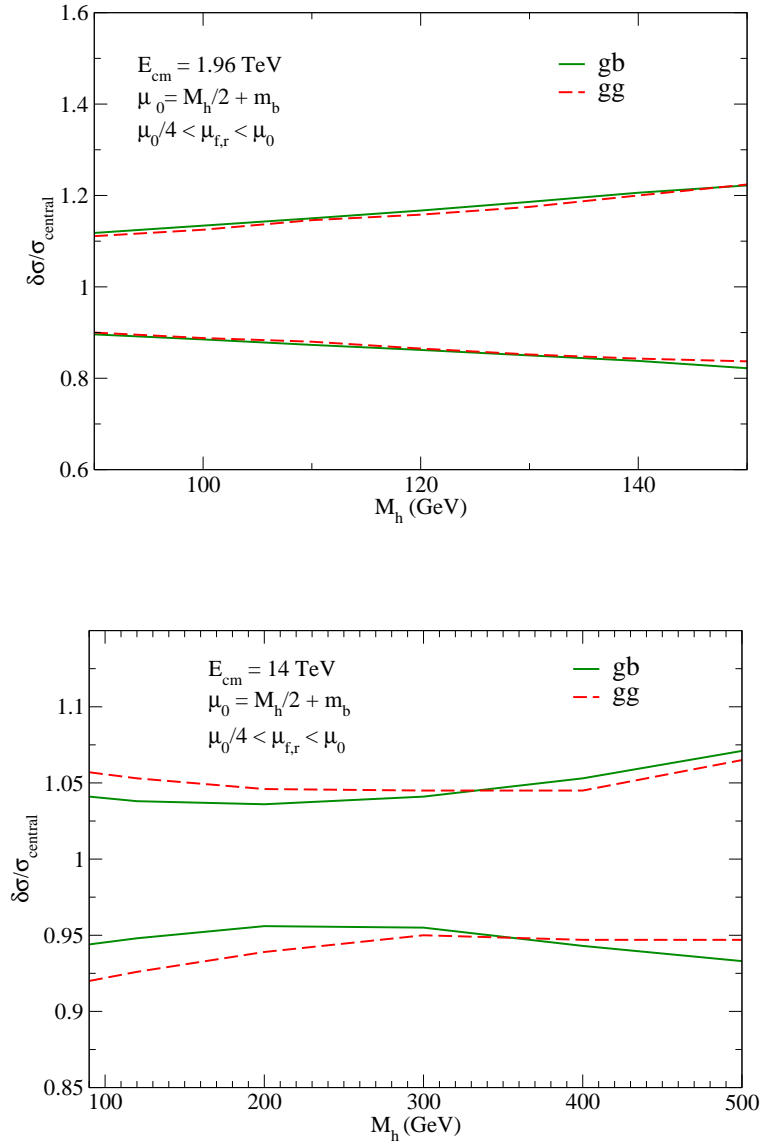
Figure 4.23. Normalized cross sections for Higgs production with one b jet at the Tevatron (top) and the LHC (bottom) showing the uncertainty from PDFs for both the gg and gb initial states.

a purely academic exercise, since the top quark loops in both calculations become negligible for large $\tan\beta$ where $b\bar{b}h$ production is important, this solved a decade old puzzle concerning the largeness of 5FNS predictions compared to the corresponding 4FNS predictions. Comparing the NLO cross section for $gg, q\bar{q} \to (b\bar{b})h$ where the b quarks are unobserved with the NNLO calculation of $b\bar{b} \to h$, we showed that these calculations agree within their theoretical uncertainties, but overall, the 5FNS cross section was slightly larger over most of the Higgs mass range. However, the 5FNS calculation does not include any top quark loop diagrams which could well explain the small discrepancy between the two calculations. Both the inclusive and exclusive NLO cross sections show a much reduced renormalization/factorization scale dependence, leading to much more stable theoretical predictions. Our investigation has also pointed to a residual renormalization scheme dependence in the definition of the bottom quark mass appearing in the overall Yukawa coupling. We have used both OS and $\overline{MS}$ schemes for m_b, checked that, as expected, their difference is higher-order in the perturbative expansion, and conservatively concluded that at most 15-20% uncertainty should be expected from renormalization scheme dependence.

Finally, we investigated the theoretical uncertainty in $b\bar{b}h$ production coming from the parton distribution functions. We showed that, at the Tevatron, the uncertainties coming from PDFs can be comparable or even larger than the uncertainties associated with scale dependence. At the LHC, however, the uncertainties from the PDFs are quite small compared to the residual scale dependence.

APPENDIX A

BOX AND PENTAGON INTEGRALS

We label the various one-loop box and pentagon scalar and tensor integrals appearing in the calculations of the $\mathcal{O}(\alpha_s)$ virtual corrections to

$$q(q_1) + \bar{q}(q_2) \rightarrow t(p_t) + \bar{t}(p'_t) + h(p_h)$$

and

$$g(q_1) + g(q_2) \rightarrow t(p_t) + \bar{t}(p'_t) + h(p_h)$$

according to the diagram where they are encountered. Moreover, we denote by $D0$, $D1^\mu$, $D2^{\mu\nu}$, and $D3^{\mu\nu\rho}$ the scalar and tensor box integrals with one, two, and three tensor indices, and by $E0$, $E1^\mu$, $E2^{\mu\nu}$, and $E3^{\mu\nu\rho}$ the analogous scalar and tensor pentagon integrals. With this convention $D0_{D_i^{(k),q\bar{q}}}$ and $D0_{D_{i,j}^{(k),gg}}$, for instance, are the scalar box integrals appearing in box diagrams $D_i^{(k),q\bar{q}}$ and $D_{i,j}^{(k),gg}$, as labeled in Figs. 3.7 and 3.11. The external momenta are labeled as shown above, where q_1, q_2 are incoming and p_t, p'_t, p_h are outgoing momenta with $q_1 + q_2 = p_t + p'_t + p_h$. It is convenient to express our results in terms of the kinematic invariants of Eq. (3.36) and:

$$\omega_1 = (p_t + p_h)^2 - m_t^2 \ ,$$
$$\omega_2 = (p'_t + p_h)^2 - m_t^2 \ . \tag{A.1}$$

These kinematic invariants do not form a linearly independent set, but are related by:

$$\tau_3 = \sigma - \tau_1 - \omega_2 \quad \text{and} \quad \tau_4 = \sigma - \tau_2 - \omega_1 \ . \tag{A.2}$$

We also make frequent use of the shorthand notation $\Lambda_a \equiv \ln(a/m_t^2)$ with $a = \sigma, \tau_i, \omega_i$.

165

In the following, we explicitly give only the box and pentagon integrals that contain IR divergences. The IR divergences are extracted using dimensional regularization with $d = 4 - 2\epsilon$. All of the box and pentagon integrals appearing in the $q\bar{q} \to t\bar{t}h$ calculation are a subset of the integrals appearing in the $gg \to t\bar{t}h$ calculation, hence, for convenience we present them together and note when an integral appears in both calculations. For the case of $gg \to t\bar{t}h$, we only give results for integrals arising from the $s-$channel and $t-$channel diagrams. The integrals for the $u-$channel diagrams can be obtained from the integrals of the corresponding $t-$channel diagrams by exchanging $q_1 \leftrightarrow q_2$, i.e. by exchanging $\tau_1 \leftrightarrow \tau_3$ and $\tau_2 \leftrightarrow \tau_4$. Finally, the IR finite scalar integrals are evaluated by implementing the method described in Ref. [54] and are cross checked against the FF package [66].

A.0.1 Box integrals

The scalar and tensor box integrals arising in the computation of box diagram $D_{i,(j)}^{(k),q\bar{q}(gg)}$ are of the following form:

$$
D0_{D_{i,(j)}^{(k),q\bar{q}(gg)}}, D1_{D_{i,(j)}^{(k),q\bar{q}(gg)}}^{\mu}, D2_{D_{i,(j)}^{(k),q\bar{q}(gg)}}^{\mu\nu}, D3_{D_{i,(j)}^{(k),q\bar{q}(gg)}}^{\mu\nu\rho} = \mu^{4-d} \int \frac{d^d k}{(2\pi)^d} \frac{1, k^\mu, k^\mu k^\nu, k^\mu k^\nu k^\rho}{N_1 N_2 N_3 N_4} ,
$$
(A.3)

where

$$
N_1 = (k^2 - m_0^2) \ , \quad N_2 = (k + p_1)^2 - m_1^2 \ ,
$$
$$
N_3 = (k + p_1 + p_2)^2 - m_2^2 \ , \quad N_4 = (k + p_1 + p_2 + p_3)^2 - m_3^2 \ ,
$$
(A.4)

p_1, p_2, p_3, and $p_4 = -p_1 - p_2 - p_3$ are the external (incoming) momenta connected to the box topology, and m_0, m_1, m_2, and m_3 are the masses of the propagators in the box loop. We write the tensor integrals as a linear combination of the linearly independent tensor structures built of the independent external momenta p_1^μ, p_2^μ, and p_3^μ plus the metric tensor $g^{\mu\nu}$. Our notation for the box tensor integrals is as follows:

166

$$D1^\mu = D_1^{(1)} p_1^\mu + D_1^{(2)} p_2^\mu + D_1^{(3)} p_3^\mu \;,$$

$$D2^{\mu\nu} = D_2^{(0)} g^{\mu\nu} + D_2^{(11)} p_1^\mu p_1^\nu + D_2^{(22)} p_2^\mu p_2^\nu + D_2^{(33)} p_3^\mu p_3^\nu$$
$$+ D_2^{(12)} (p_1^\mu p_2^\nu + p_1^\nu p_2^\mu) + D_2^{(13)} (p_1^\mu p_3^\nu + p_1^\nu p_3^\mu) + D_2^{(23)} (p_2^\mu p_3^\nu + p_2^\nu p_3^\mu) \;,$$

$$D3^{\mu\nu\rho} = D_3^{(01)} (g^{\mu,\nu} p_1^\rho + \text{perm}) + D_3^{(02)} (g^{\mu,\nu} p_2^\rho + \text{perm}) + D_3^{(03)} (g^{\mu,\nu} p_3^\rho + \text{perm})$$
$$+ D_3^{(111)} p_1^\mu p_1^\nu p_1^\rho + D_3^{(222)} p_2^\mu p_2^\nu p_2^\rho + D_3^{(333)} p_3^\mu p_3^\nu p_3^\rho$$
$$+ D_3^{(112)} (p_1^\mu p_1^\nu p_2^\rho + \text{perm}) + D_3^{(113)} (p_1^\mu p_1^\nu p_3^\rho + \text{perm})$$
$$+ D_3^{(221)} (p_2^\mu p_2^\nu p_1^\rho + \text{perm}) + D_3^{(223)} (p_2^\mu p_2^\nu p_3^\rho + \text{perm})$$
$$+ D_3^{(331)} (p_3^\mu p_3^\nu p_1^\rho + \text{perm}) + D_3^{(332)} (p_3^\mu p_3^\nu p_2^\rho + \text{perm}) + D_3^{(123)} (p_1^\mu p_2^\nu p_3^\rho + \text{perm}) \;,$$

$$\text{(A.5)}$$

where "+perm" indicates that the sum over all possible permutations of the tensor indices is understood. In the following we will give the full structure of the scalar box integrals, including both pole and finite parts, while for the corresponding tensor integrals we will only give the IR pole parts, since they can be of interest in checking the IR structure of the virtual cross section. We will write the pole part of each tensor integral coefficient as

$$D_i^{(j)}|_{IR-pole} = \frac{i}{16\pi^2} \mathcal{N}_t \Delta_{IR}(D_i^{(j)}) \;,$$
$$D_i^{(jk)}|_{IR-pole} = \frac{i}{16\pi^2} \mathcal{N}_t \Delta_{IR}(D_i^{(jk)}) \;,$$
$$D_i^{(jkl)}|_{IR-pole} = \frac{i}{16\pi^2} \mathcal{N}_t \Delta_{IR}(D_i^{(jkl)}) \;, \tag{A.6}$$

where $\mathcal{N}_t$ is defined in Eq. (3.26), and give for each box integral the non zero $\Delta_{IR}(D_i^{(j)})$, $\Delta_{IR}(D_i^{(jk)})$, and $\Delta_{IR}(D_i^{(jkl)})$ coefficients.

A.0.1.1 Box scalar integrals $D0_{B_2^{(1,2),q\bar{q}}}$ and $D0_{B_{2,s}^{(1,2),gg}}$

The scalar integrals appearing in diagrams $B_2^{(1),q\bar{q}}$ and $B_{2,s}^{(1),gg}$ can be parameterized according to Eq. (A.3) with:

$$N_1 = k^2 \ , \quad N_2 = (k + p_t)^2 - m_t^2 \ ,$$

$$N_3 = (k + p_t + p_h)^2 - m_t^2 \ , \quad N_4 = (k - p_t')^2 - m_t^2 \ . \qquad (A.7)$$

$D0_{B_{2,s}^{(2),q\bar{q}}}$ $(D0_{B_{2,s}^{(2),gg}})$ is obtained from $D0_{B_{2,s}^{(1),q\bar{q}}}$ $(D0_{B_{2,s}^{(1),gg}})$ by exchanging $p_t \leftrightarrow p_t'$.

The part of $D0_{B_{2,s}^{(1)}}$ which contributes to the amplitude squared is of the form:

$$D0_{B_2^{(1),q\bar{q}}} \left(D0_{B_{2,s}^{(1),gg}}\right) = \frac{i}{16\pi^2} \mathcal{N}_t \frac{1}{\omega_1(\sigma - \omega_1 - \omega_2 + M_h^2)} \left(\frac{X_{-1}}{\epsilon} + X_0\right) \ , \quad (A.8)$$

where $\mathcal{N}_t$ is defined in Eq. (3.26). The pole part X_{-1} is:

$$X_{-1} = -\frac{1}{\beta_{t\bar{t}}} \ln \left(\frac{1 + \beta_{t\bar{t}}}{1 - \beta_{t\bar{t}}}\right) \ , \qquad (A.9)$$

where $\beta_{t\bar{t}}$ is given in Eq. (3.37). The finite part X_0 can be calculated using Ref. [105]. All tensor box integrals associated to $B_{2,s}^{(1)}$ and $B_{2,s}^{(2)}$ are IR finite.

A.0.1.2 Box scalar integral $D0_{B_{7,t}^{(1,2),gg}}$

The scalar integral appearing in diagram $B_{7,t}^{(1),gg}$, $D0_{B_{7,t}^{(1),gg}}$, can be parameterized according to Eq. (A.3) with:

$$N_1 = k^2 \ , \quad N_2 = (k + q_1)^2 \ ,$$

$$N_3 = (k + q_1 - p_t)^2 - m_t^2 \ , \quad N_4 = (k + q_1 - p_t - p_h)^2 - m_t^2 \ . \qquad (A.10)$$

The part of $D0_{B_{7,t}^{(1),gg}}$ which contributes to the virtual amplitude squared is of the form:

$$D0_{B_{7,t}^{(1),gg}} = \frac{i}{16\pi^2} \mathcal{N}_t \left(-\frac{1}{\omega_1\tau_1}\right) \left(\frac{X_{-2}}{\epsilon^2} + \frac{X_{-1}}{\epsilon} + X_0\right) \ , \qquad (A.11)$$

where the coefficients X_{-2}, X_{-1}, and X_0 are given by:

$$X_{-2} = \frac{1}{2} \ ,$$

$$X_{-1} = \ln \left(\frac{\tau_2 m_t^2}{\omega_1 \tau_1}\right) \ ,$$

$$X_0 = Re \left\{ -\frac{5}{6}\pi^2 + \ln^2 \left(\frac{\omega_1}{m_t^2}\right) + \ln^2 \left(\frac{\tau_1}{m_t^2}\right) - \ln^2 \left(\frac{\tau_2}{m_t^2}\right) \right.$$

$$
+ 2 \ln \left(\frac{\omega_1 + \tau_2}{\tau_1} \right) \ln \left(\frac{\tau_2}{\omega_1} \right) + 2 \ln \left(\frac{\tau_1 - \tau_2}{\omega_1} \right) \ln \left(\frac{\tau_2}{\tau_1} \right)
$$

$$
- 2 \operatorname{Li}_2 \left(\frac{\tau_1 - \tau_2 - \omega_1}{\tau_1} \right) - 2 \operatorname{Li}_2 \left(\frac{\omega_1 + \tau_2 - \tau_1}{\omega_1} \right) + 2 \operatorname{Li}_2 \left(\frac{\tau_2 (\omega_1 + \tau_2 - \tau_1)}{\omega_1 \tau_1} \right) - I_0 \Bigg\} \ ,
$$

$$(A.12)$$

with

$$
I_0 = \ln \left(\frac{\tau_1}{\tau_2} \right) \ln \left(\frac{M_h^2}{m_t^2} \right) + \Bigg\{ -\operatorname{Li}_2 \left(\frac{1}{\lambda_+} \right) + \ln \left(\frac{\tau_1}{\tau_2} \right) \ln \left(\frac{-\tau_2 - \lambda_+ (\tau_1 - \tau_2)}{\tau_1 - \tau_2} \right)
$$

$$
- \operatorname{Li}_2 \left(\frac{\tau_1}{\lambda_+ (\tau_1 - \tau_2) + \tau_2} \right) + \operatorname{Li}_2 \left(\frac{\tau_2}{\lambda_+ (\tau_1 - \tau_2) + \tau_2} \right) + (\lambda_+ \leftrightarrow \lambda_-) \Bigg\} \ ,
$$

$$(A.13)$$

and

$$
\lambda_\pm = \frac{1}{2} \left(1 \pm \sqrt{1 - \frac{4 m_t^2}{M_h^2}} \right) \ . \tag{A.14}
$$

The tensor integrals associated with $B_{7,t}^{(1),gg}$ also contain IR divergences. Using the notation introduced in Eqs. (A.5) and (A.6), only the following coefficients of $D1_{B_{7,t}^{(1),gg}}^{\mu}$:

$$
\Delta_{IR}(D_1^{(1)}) = \frac{1}{2} \frac{1}{\tau_1 \omega_1} \frac{1}{\epsilon^2} + \frac{1}{\tau_1 \omega_1} \left[-\Lambda_{\tau_1} + \frac{\tau_2}{\tau_2 + \omega_1} (\Lambda_{\tau_2} - \Lambda_{\omega_1}) \right] \frac{1}{\epsilon} \ , \tag{A.15}
$$

and of $D2_{B_{7,t}^{(1),gg}}^{\mu\nu}$:

$$
\Delta_{IR}(D_2^{(11)}) = -\frac{1}{2} \frac{1}{\tau_1 \omega_1} \frac{1}{\epsilon^2} + \frac{1}{\tau_1 \omega_1} \left[\Lambda_{\tau_1} - \frac{\tau_2^2}{(\tau_2 + \omega_1)^2} (\Lambda_{\tau_2} - \Lambda_{\omega_1}) - \frac{\omega_1}{\tau_2 + \omega_1} \right] \frac{1}{\epsilon} \ ,
$$

$$(A.16)$$

are IR divergent.

$D0_{B_{7,t}^{(2),gg}}$ and the corresponding tensor integrals are obtained from $D0_{B_{7,t}^{(1),gg}}$ by exchanging $q_1 \leftrightarrow q_2$ and $p_t \leftrightarrow p_t'$, i.e. by exchanging $\tau_1 \leftrightarrow \tau_2$ and $\omega_1 \leftrightarrow \omega_2$ in Eqs. (A.11)-(A.16).

A.0.1.3 Box scalar integrals $D0_{B_3^{(1-4),q\bar{q}}}$ and $D0_{B_{8,t}^{(1,2),gg}}$

The scalar box integrals appearing in diagrams $B_3^{(1),q\bar{q}}$ and $B_{8,t}^{(1),gg}$, $D0_{B_3^{(1),q\bar{q}}}$ and $D0_{B_{8,t}^{(1)}}$, can be parameterized according to Eq. (A.3) with:

$$N_1 = k^2 \ , \quad N_2 = (k+q_1)^2 \ ,$$

$$N_3 = (k+q_1+q_2)^2 \ , \quad N_4 = (k+q_1+q_2-p_t')^2 - m_t^2 \ . \tag{A.17}$$

The part of $D0_{B_3^{(1),q\bar{q}}}$ $(D0_{B_{8,t}^{(1),gg}})$ which contributes to the virtual amplitude squared is given by:

$$D0_{B_3^{(1),q\bar{q}}} \, (D0_{B_{8,t}^{(1),gg}}) = \frac{i}{16\pi^2} \mathcal{N}_t \left(-\frac{1}{\sigma\tau_2}\right) \left(\frac{X_{-2}}{\epsilon^2} + \frac{X_{-1}}{\epsilon} + X_0\right) \ , \tag{A.18}$$

where $\mathcal{N}_t$ is defined in Eq. (3.26), and the coefficients X_{-2}, X_{-1}, and X_0 are given by:

$$X_{-2} = \frac{3}{2} \ ,$$

$$X_{-1} = \ln\left(\frac{\omega_1 m_t^4}{\sigma\tau_2^2}\right) \ ,$$

$$X_0 = 2\ln\left(\frac{\tau_2}{m_t^2}\right)\ln\left(\frac{\sigma}{m_t^2}\right) - \ln^2\left(\frac{\omega_1}{m_t^2}\right) - 2\,\mathrm{Li}_2\left(1+\frac{\omega_1}{\tau_2}\right) + \frac{\pi^2}{3} \ . \tag{A.19}$$

The tensor integrals associated with $B_3^{(1),q\bar{q}}$ $(B_{8,t}^{(1),gg})$ also contain IR divergences. Using the notation introduced in Eqs. (A.5) and (A.6), only the following tensor coefficients of $D1^\mu_{B_3^{(1),q\bar{q}}}$ $(D1^\mu_{B_{8,t}^{(1),gg}})$:

$$\Delta_{IR}(D_1^{(1)}) = \frac{3}{2}\frac{1}{\sigma\tau_2}\frac{1}{\epsilon^2} - \frac{1}{\sigma\tau_2}\left[\Lambda_\sigma + \Lambda_{\tau_2} + \frac{\omega_1}{\tau_2+\omega_1}(\Lambda_{\tau_2}-\Lambda_{\omega_1})\right]\frac{1}{\epsilon} \ ,$$

$$\Delta_{IR}(D_1^{(2)}) = \frac{1}{2}\frac{1}{\sigma\tau_2}\frac{1}{\epsilon^2} - \frac{1}{\sigma\tau_2}\Lambda_{\tau_2}\frac{1}{\epsilon} \ , \tag{A.20}$$

of $D2^{\mu\nu}_{B_3^{(1),q\bar{q}}}$ $(D2^{\mu\nu}_{B_{8,t}^{(1),gg}})$:

$$\Delta_{IR}(D_2^{(11)}) = -\frac{3}{2}\frac{1}{\sigma\tau_2}\frac{1}{\epsilon^2} + \frac{1}{\sigma\tau_2}\left[-\frac{\tau_2}{\tau_2+\omega_1} + \Lambda_\sigma + \Lambda_{\tau_2} + \frac{\omega_1^2}{(\tau_2+\omega_1)^2}(\Lambda_{\tau_2}-\Lambda_{\omega_1})\right]\frac{1}{\epsilon} \ ,$$

$$\Delta_{IR}(D_2^{(12)}) = -\frac{1}{2}\frac{1}{\sigma\tau_2}\frac{1}{\epsilon^2} + \frac{1}{\sigma\tau_2}\Lambda_{\tau_2}\frac{1}{\epsilon} \ ,$$

$$\Delta_{IR}(D_2^{(22)}) = -\frac{1}{2}\frac{1}{\sigma\tau_2}\frac{1}{\epsilon^2} + \frac{1}{\sigma\tau_2}(-1+\Lambda_{\tau_2})\frac{1}{\epsilon} \ , \tag{A.21}$$

and of $D3^{\mu\nu\rho}_{B_3^{(1),q\bar{q}}}$ $(D3^{\mu\nu\rho}_{B_{8,t}^{(1),gg}})$:

$$\Delta_{IR}(D_3^{(111)}) = \frac{3}{2}\frac{1}{\sigma\tau_2}\frac{1}{\epsilon^2} + \frac{1}{2\sigma\tau_2}\left[\frac{3\tau_2}{\tau_2+\omega_1} + \frac{2\tau_2\omega_1}{(\tau_2+\omega_1)^2} - 2\Lambda_\sigma - 2\Lambda_{\tau_2}\right.$$
$$\left. - \frac{2\omega_1^2}{(\tau_2+\omega_1)^3}(\Lambda_{\tau_2} - \Lambda_{\omega_1})\right]\frac{1}{\epsilon} \ ,$$

$$\Delta_{IR}(D_3^{(112)}) = \frac{1}{2}\frac{1}{\sigma\tau_2}\frac{1}{\epsilon^2} - \frac{1}{\sigma\tau_2}\Lambda_{\tau_2}\frac{1}{\epsilon} \ ,$$

$$\Delta_{IR}(D_3^{(221)}) = \frac{1}{2}\frac{1}{\sigma\tau_2}\frac{1}{\epsilon^2} + \frac{1}{\sigma\tau_2}(1-\Lambda_{\tau_2})\frac{1}{\epsilon} \ ,$$

$$\Delta_{IR}(D_3^{(222)}) = \frac{1}{2}\frac{1}{\sigma\tau_2}\frac{1}{\epsilon^2} + \frac{1}{\sigma\tau_2}\left(\frac{3}{2}-\Lambda_{\tau_2}\right)\frac{1}{\epsilon} \ , \tag{A.22}$$

are IR divergent.

We note that $D0_{B_3^{(2),q\bar{q}}}$ as well as the corresponding tensor integrals are obtained from $D0_{B_3^{(1),q\bar{q}}}$ by exchanging $q_1 \leftrightarrow q_2$, while $D0_{B_3^{(3),q\bar{q}}}$ $(D0_{B_{8,t}^{(2),gg}})$ can be obtained from $D0_{B_3^{(1),q\bar{q}}}$ $(D0_{B_{8,t}^{(1),gg}})$ by exchanging $q_1 \leftrightarrow q_2$ and $p_t' \leftrightarrow p_t$, i.e. by exchanging $\tau_1 \leftrightarrow \tau_2$ and $\omega_1 \leftrightarrow \omega_2$ in Eqs. (A.18)-(A.22). Finally, $D0_{B_3^{(4),q\bar{q}}}$ is obtained from $D0_{B_3^{(3),q\bar{q}}}$ by exchanging $q_1 \leftrightarrow q_2$.

A.0.1.4 Box scalar integral $D0_{B_{10,t}^{(1,2),gg}}$

The scalar box integral appearing in diagram $B_{10,t}^{(1),gg}$, $D0_{B_{10,t}^{(1),gg}}$, can be parameterized according to Eq. A.3 with:

$$N_1 = k^2 \ , \quad N_2 = (k+q_1)^2 \ ,$$
$$N_3 = (k+q_1-p_t')^2 - m_t^2 \ , \quad N_4 = (k+q_1+q_2-p_t')^2 - m_t^2 \ . \tag{A.23}$$

The part of $D0_{B_{10,t}^{(1),gg}}$ which contributes to the virtual amplitude squared is given by:

$$D0_{B_{10,t}^{(1),gg}} = \frac{i}{16\pi^2}\mathcal{N}_t\left(\frac{1}{\tau_2\tau_4}\right)\left(\frac{X_{-2}}{\epsilon^2} + \frac{X_{-1}}{\epsilon} + X_0\right) \ , \tag{A.24}$$

where the coefficients X_{-2}, X_{-1}, and X_0 are given by:

$$X_{-2} = \frac{1}{2} \ ,$$

$$X_{-1} = \ln\left(\frac{\omega_1}{\tau_4}\right) - \ln\left(\frac{\tau_2}{m_t^2}\right) \ ,$$

$$X_0 = \mathcal{R}e\left\{\ln^2\left(\frac{\tau_2}{m_t^2}\right) + \ln^2\left(\frac{\tau_4}{m_t^2}\right) - \ln^2\left(\frac{\omega_1}{m_t^2}\right) + \frac{3}{2}\pi^2\right.$$

$$+ 2\ln\left(\frac{\tau_2 + \omega_1}{\tau_4}\right)\ln\left(\frac{\tau_4}{\tau_2 + \tau_4 + \omega_1}\right) + 2\ln\left(\frac{\tau_4 + \omega_1}{\tau_2}\right)\ln\left(\frac{\tau_2}{\tau_2 + \tau_4 + \omega_1}\right)$$

$$\left. - 2\,\mathrm{Li}_2\left(\frac{\tau_2 + \tau_4 + \omega_1}{\tau_4}\right) - 2\,\mathrm{Li}_2\left(\frac{\tau_2 + \tau_4 + \omega_1}{\tau_2}\right) - 2\,\mathrm{Li}_2\left(\frac{(\tau_2 + \omega_1)(\tau_4 + \omega_1)}{\tau_2\tau_4}\right)\right\} \ .$$

$$(A.25)$$

The tensor integrals associated with $B_{10,t}^{(1),gg}$ also contain IR divergences. Using the notation introduced in Eqs. (A.5) and (A.6), the only IR divergent tensor coefficients of $D1^\mu_{B_{10,t}^{(1),gg}}$:

$$\Delta_{IR}(D_1^{(1)}) = -\frac{1}{2}\frac{1}{\tau_2\tau_4}\frac{1}{\epsilon^2} + \frac{1}{\tau_2\tau_4(\tau_2 + \omega_1)}\left[(\tau_2 + \omega_1)\Lambda_{\tau_4} + \omega_1(\Lambda_{\tau_2} - \Lambda_{\omega_1})\right]\frac{1}{\epsilon} \ ,$$

$$(A.26)$$

of $D2^{\mu\nu}_{B_{10,t}^{(1),gg}}$:

$$\Delta_{IR}(D_2^{(11)}) = \frac{1}{2}\frac{1}{\tau_2\tau_4}\frac{1}{\epsilon^2} + \frac{1}{\tau_2\tau_4(\tau_2 + \omega_1)^2}\left[\tau_2(\tau_2 + \omega_1) - (\tau_2 + \omega_1)^2\Lambda_{\tau_4} - \omega_1^2(\Lambda_{\tau_2} - \Lambda_{\omega_1})\right]\frac{1}{\epsilon} \ ,$$

$$(A.27)$$

and of $D3^{\mu\nu\rho}_{B_{10,t}^{(1),gg}}$:

$$\Delta_{IR}(D_3^{(111)}) = -\frac{1}{2}\frac{1}{\tau_2\tau_4}\frac{1}{\epsilon^2} - \frac{1}{2}\frac{1}{\tau_2\tau_4(\tau_2 + \omega_1)^3}\left[-2\omega_1^2(\Lambda_{\tau_2} - \Lambda_{\omega_1}) - 2(\tau_2 + \omega_1)^3\Lambda_{\tau_4}\right.$$

$$\left. + 3\tau_2(\tau_2 + \omega_1)^2 + 2\tau_2\omega_1(\tau_2 + \omega_1)\right]\frac{1}{\epsilon} \ , \qquad (A.28)$$

are IR divergent.

$D0_{B_{10,t}^{(2),gg}}$ can be obtained from $D0_{B_{10,t}^{(1),gg}}$ by exchanging $p_t' \leftrightarrow p_t$, i.e. by exchanging $\tau_1 \leftrightarrow \tau_4$, $\tau_2 \leftrightarrow \tau_3$, and $\omega_1 \leftrightarrow \omega_2$ in Eqs (A.24) and (A.28).

172

A.0.2 Pentagon integrals

The scalar and tensor pentagon integrals originating from the generic pentagon diagrams $P_i^{q\bar{q}}$ and $P_{i,j}^{gg}$ in Figs. 3.8 and 3.12 are of the form:

$$E0_{P_{i,(j)}^{q\bar{q}(gg)}}, E1^{\mu}_{P_{i,(j)}^{q\bar{q}(gg)}}, E2^{\mu\nu}_{P_{i,(j)}^{q\bar{q}(gg)}}, E3^{\mu\nu\rho}_{P_{i,(j)}^{q\bar{q}(gg)}} = \mu^{4-d} \int \frac{d^d k}{(2\pi)^d} \frac{1, k^{\mu}, k^{\mu}k^{\nu}, k^{\mu}k^{\nu}k^{\rho}}{N_1 N_2 N_3 N_4 N_5} \quad , \quad \text{(A.29)}$$

where

$$N_1 = (k^2 - m_0^2) \ , \quad N_2 = (k + p_1)^2 - m_1^2 \ ,$$

$$N_3 = (k + p_1 + p_2)^2 - m_2^2 \ , \quad N_4 = (k + p_1 + p_2 + p_3)^2 - m_3^2 \ ,$$

$$N_5 = (k + p_1 + p_2 + p_3 + p_4)^2 - m_4^2 \ , \tag{A.30}$$

p_1, p_2, p_3, p_4, and $p_5 = -p_1 - p_2 - p_3 - p_4$ are the external (incoming) momenta connected to the pentagon topology, while m_0, m_1, m_2, m_3, and m_4 are the masses of the propagators in the pentagon loop.

The scalar pentagon integrals are evaluated as a linear combination of five scalar box integrals, using the technique originally proposed in Ref. [52, 53] that we generalize here to the case of several massive particles. In particular, we use:

$$E0_{P_{i,j}} = -\frac{1}{2} \sum_{k=1}^{5} c_k D0^{(k)}_{P_{i,j}} \ , \tag{A.31}$$

where each scalar box integral $D0^{(k)}_{P_{i,j}}$ can be obtained from the scalar pentagon integral $E0_{P_{i,j}}$ in Eq. (A.29) by dropping one of the internal propagators. The coefficients c_k are given by:

$$c_k = \sum_{l=1}^{5} S_{kl}^{-1} \ , \tag{A.32}$$

where S_{kl} is the symmetric matrix:

$$S_{kl} = \frac{1}{2} \left(M_k^2 + M_l^2 - p_{kl}^2 \right) \ , \tag{A.33}$$

built out of the internal propagator masses M_k and M_l and the linear combination of external momenta $p_{kl}^{\mu} = p_k^{\mu} + \ldots + p_{l-1}^{\mu}$ ($k, l = 1, \ldots, 5$). A thorough explanation

173

of this method is given in Section A.0.2.1 and in Refs. [52, 53], to which we refer for more details.

We write the tensor pentagon integrals as a linear combination of the linearly independent tensor structures built of the external momenta p_1^μ, p_2^μ, p_3^μ, and p_4^μ, which in $d = 4$ constitute a complete basis. Our notation for the pentagon tensor integrals is as follows:

$$
\begin{aligned}
E1^\mu &= E_1^{(1)} p_1^\mu + E_1^{(2)} p_2^\mu + E_1^{(3)} p_3^\mu + E_1^{(4)} p_4^\mu \ , \\
E2^{\mu\nu} &= E_2^{(11)} p_1^\mu p_1^\nu + E_2^{(22)} p_2^\mu p_2^\nu + E_2^{(33)} p_3^\mu p_3^\nu + E_2^{(44)} p_4^\mu p_4^\nu \\
&\quad + E_2^{(12)} (p_1^\mu p_2^\nu + p_1^\nu p_2^\mu) + E_2^{(13)} (p_1^\mu p_3^\nu + p_1^\nu p_3^\mu) + E_2^{(14)} (p_1^\mu p_4^\nu + p_1^\nu p_4^\mu) \\
&\quad + E_2^{(23)} (p_2^\mu p_3^\nu + p_2^\nu p_3^\mu) + E_2^{(24)} (p_2^\mu p_4^\nu + p_2^\nu p_4^\mu) + E_2^{(34)} (p_3^\mu p_4^\nu + p_3^\nu p_4^\mu) \ , \\
E3^{\mu\nu\rho} &= E_3^{(111)} p_1^\mu p_1^\nu p_1^\rho + E_3^{(222)} p_2^\mu p_2^\nu p_2^\rho + E_3^{(333)} p_3^\mu p_3^\nu p_3^\rho + E_3^{(444)} p_4^\mu p_4^\nu p_4^\rho \\
&\quad + E_3^{(112)} (p_1^\mu p_1^\nu p_2^\rho + \text{perm}) + E_3^{(113)} (p_1^\mu p_1^\nu p_3^\rho + \text{perm}) + E_3^{(114)} (p_1^\mu p_1^\nu p_4^\rho + \text{perm}) \\
&\quad + E_3^{(221)} (p_2^\mu p_2^\nu p_1^\rho + \text{perm}) + E_3^{(223)} (p_2^\mu p_2^\nu p_3^\rho + \text{perm}) + E_3^{(224)} (p_2^\mu p_2^\nu p_4^\rho + \text{perm}) \\
&\quad + E_3^{(331)} (p_3^\mu p_3^\nu p_1^\rho + \text{perm}) + E_3^{(332)} (p_3^\mu p_3^\nu p_2^\rho + \text{perm}) + E_3^{(334)} (p_3^\mu p_3^\nu p_4^\rho + \text{perm}) \\
&\quad + E_3^{(441)} (p_4^\mu p_4^\nu p_1^\rho + \text{perm}) + E_3^{(442)} (p_4^\mu p_4^\nu p_2^\rho + \text{perm}) + E_3^{(443)} (p_4^\mu p_4^\nu p_4^\rho + \text{perm}) \\
&\quad + E_3^{(123)} (p_1^\mu p_2^\nu p_3^\rho + \text{perm}) + E_3^{(124)} (p_1^\mu p_2^\nu p_4^\rho + \text{perm}) + E_3^{(134)} (p_1^\mu p_3^\nu p_4^\rho + \text{perm}) \\
&\quad + E_3^{(234)} (p_2^\mu p_3^\nu p_4^\rho + \text{perm}) \ .
\end{aligned}
$$

(A.34)

The calculation of $q\bar{q} \to t\bar{t}h$ involves two pentagon structures (see Fig. 3.8) which are a subset of the six pentagon structures of $gg \to t\bar{t}h$ illustrated in Fig. 3.12. As in the case of the box integrals, we present them together and note when an integral appears in both calculations. For each of the pentagon structures, we will give in the following the IR pole parts of the corresponding scalar integrals, as well as the coefficient c_k (in terms of the S_{kl} matrix) and the IR singular box scalar integrals $D0_{P_{i,(j)}}^{(k),q\bar{q}(gg)}$ out of which they can be calculated. We will moreover list the IR pole parts of the corresponding tensor integral coefficients, since they may be of interest

174

in checking the IR structure of the virtual cross section. We will write the pole part of each tensor integral coefficient as

$$E_i^{(j)}|_{IR-pole} = \frac{i}{16\pi^2}\mathcal{N}_t\Delta_{IR}(E_i^{(j)}) \ ,$$

$$E_i^{(jk)}|_{IR-pole} = \frac{i}{16\pi^2}\mathcal{N}_t\Delta_{IR}(E_i^{(jk)}) \ ,$$

$$E_i^{(jkl)}|_{IR-pole} = \frac{i}{16\pi^2}\mathcal{N}_t\Delta_{IR}(E_i^{(jkl)}) \ , \tag{A.35}$$

where $\mathcal{N}_t$ is defined in Eq. (3.26), and give for each pentagon integral the non zero $\Delta_{IR}(E_i^{(j)})$, $\Delta_{IR}(E_i^{(jk)})$, and $\Delta_{IR}(E_i^{(jkl)})$ coefficients.

As in Section A.0.1 we express our results in terms of the kinematic invariants σ, τ_i, ω_i of Eqs. (3.48) and (3.36), and $\beta_{t\bar{t}}$ of Eq. (3.37).

A.0.2.1 Pentagon scalar integral $E0_{P_{1,t}}$

The pentagon scalar integrals arising from diagrams $P_1^{q\bar{q}}$ and $P_{1,t}^{gg}$, $E0_{P_1^{q\bar{q}}}$ and $E0_{P_{1,t}^{gg}}$, coincide and can be parameterized according to Eq. (A.29) with:

$$N_1 = k^2 \ , \quad N_2 = (k + q_1)^2 \ , \quad N_3 = (k + q_1 + q_2)^2 \ ,$$

$$N_4 = (k + q_1 + q_2 - p_t')^2 - m_t^2 \ , \quad N_5 = (k + q_1 + q_2 - p_t' - p_h)^2 - m_t^2 \ . \tag{A.36}$$

We note that the pentagon scalar integral originating from diagram $P_2^{q\bar{q}}$, $E0_{P_2^{q\bar{q}}}$, can be obtained from $E0_{P_1^{q\bar{q}}}$ by exchanging $q_1 \leftrightarrow q_2$. In addition, to simplify the notation, we only present the results for the case $P_{1,t}^{gg}$ below; however, the results for $P_1^{q\bar{q}}$ are identical.

We calculate these integrals following the method introduced by the authors of Ref. [52]. To make contact with their notation, we denote by k_i the external momenta (such that $k_i^2 = m_i^2$), by M_i the internal masses, by p_i the sum of the first i external momenta, $p_i^\mu = \sum_{j=1}^i k_j^\mu$, by p_{ij} the difference $p_{ij}^\mu = p_{j-1}^\mu - p_{i-1}^\mu = k_i^\mu + k_{i+1}^\mu + \cdots + k_{j-1}^\mu$ (for $i < j$), and finally by $\bar{s}_{ij}$ the invariant masses $\bar{s}_{ij} = (k_i + k_j)^2$.
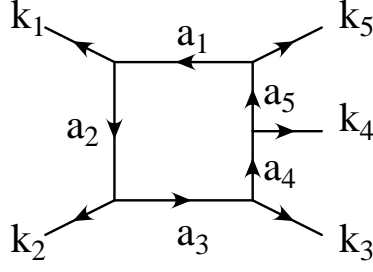
Figure A.1. Topology of the pentagon scalar integral.

The topology of the generic pentagon scalar integral is illustrated in Fig. A.1, which can be specified to our case by identifying:

$$
\begin{aligned}
k_1 &\longrightarrow -q_1 \quad \text{(incoming } q) \\
k_2 &\longrightarrow -q_2 \quad \text{(incoming } \bar{q}) \\
k_3 &\longrightarrow p'_t \quad \text{(outgoing } \bar{t}) \\
k_4 &\longrightarrow p_h \quad \text{(outgoing } h) \\
k_5 &\longrightarrow p_t \quad \text{(outgoing } t) \, .
\end{aligned}
\tag{A.37}
$$

Using the standard Feynman parameterization technique, the pentagon integral in Eq.(A.29) can be written as:

$$
E0_{P_{1,t}^{gg}} = -\frac{i}{16\pi^2}(4\pi\mu^2)^\epsilon \Gamma(3+\epsilon) \int_0^1 \frac{\Pi_{k=1}^5 da_k \delta(1 - \Sigma_{k=1}^5 a_k)}{[\mathcal{D}_{P_{1,t}^{gg}}(a_k)]^{3+\epsilon}} \, ,
\tag{A.38}
$$

where the denominator $\mathcal{D}_{P_{1,t}^{gg}}(a_k)$ is:

$$
\mathcal{D}_{P_{1,t}^{gg}}(a_k) = \sum_{k,l=1}^5 S_{kl} a_k a_l - i\eta \, ,
\tag{A.39}
$$

and the symmetric matrix S_{kl} is given by:

$$
S_{kl} = \frac{1}{2}(M_k^2 + M_l^2 - p_{kl}^2) \, .
\tag{A.40}
$$

176

For our particular process, the matrix S_{kl} has the following explicit form:

$$S = \frac{1}{2} \begin{pmatrix} 0 & 0 & -\bar{s}_{12} & (m_t^2 - \bar{s}_{45}) & 0 \\ 0 & 0 & 0 & (m_t^2 - \bar{s}_{23}) & (m_t^2 - \bar{s}_{15}) \\ -\bar{s}_{12} & 0 & 0 & 0 & (m_t^2 - \bar{s}_{34}) \\ (m_t^2 - \bar{s}_{45}) & (m_t^2 - \bar{s}_{23}) & 0 & 2m_t^2 & (2m_t^2 - M_h^2) \\ 0 & (m_t^2 - \bar{s}_{15}) & (m_t^2 - \bar{s}_{34}) & (2m_t^2 - M_h^2) & 2m_t^2 \end{pmatrix} .$$

$$(A.41)$$

Following Ref. [52], $E0_{p1}$ can then be written as the linear combination of five scalar box integrals $D0_{p1}^{(k)}$:

$$E0_{P_{1,t}^{gg}} = -\frac{1}{2} \sum_{k=1}^{5} c_k D0_{P_{1,t}^{gg}}^{(k)} , \qquad (A.42)$$

where each $D0_{P_{1,t}^{gg}}^{(k)}$ scalar box integral can be obtained from the scalar pentagon integral $E0_{p1}$ of Eq. (A.38) in the limit where one of the Feynman parameters a_k of the internal propagators goes to zero (i.e. $D0_{p1}^{(k)}$ is obtained when $a_k \to 0$). The five box scalar integrals we need are presented in the following. The coefficients c_k in Eq. (A.42) are given by:

$$c_k = \sum_{l=1}^{5} S_{kl}^{-1} . \qquad (A.43)$$

Using Eq. (A.41) we can easily obtain them in terms of m_t, M_h, and the kinematic invariants $\bar{s}_{kl}$.

The final result for the pentagon scalar integral $E0_{p1}$ can be written as:

$$E0_{p1} = \frac{i}{16\pi^2} \mathcal{N}_t \left[\frac{X_{-2}}{\epsilon^2} + \frac{X_{-1}}{\epsilon} + X_0 \right] , \qquad (A.44)$$

where $\mathcal{N}_t$ is given in Eq. (3.26), while X_{-2}, X_{-1} and X_0 are obtained using Eqs. (A.42)-(A.41), and the results below for the $D0_{P_{1,t}}^{(1-5)}$ scalar integrals. The expression for X_0 is too lengthy to be given explicitly in this appendix, while X_{-2} and X_{-1} have the following compact form:

$$X_{-2} = \frac{1}{2\sigma} \left(-\frac{1}{\omega_1 \tau_1} - \frac{1}{\omega_2 \tau_2} + \frac{2}{\tau_1 \tau_2} \right) , \qquad (A.45)$$

$$X_{-1} = \frac{1}{\sigma \tau_1 \tau_2} \left(-\Lambda_\sigma + \Lambda_{\omega_1} + \Lambda_{\omega_2} - \Lambda_{\tau_1} - \Lambda_{\tau_2} \right) + \frac{1}{\sigma \tau_2 \omega_2} \left(\Lambda_{\tau_2} - \Lambda_{\tau_1} + \Lambda_{\omega_2} \right) +$$

$$+ \frac{1}{\sigma \tau_1 \omega_1} \left(\Lambda_{\tau_1} - \Lambda_{\tau_2} + \Lambda_{\omega_1} \right) .$$

177

The tensor integrals associated with $P_{1,t}^{gg}$ contain IR divergences. Using the notation introduce in Eqs. (A.34) and (A.35), only the following coefficients of $E1_{P_{1,t}^{gg}}^{\mu}$:

$$\Delta_{IR}(E_1^{(1)}) = \frac{1}{2\sigma\tau_2}\left(\frac{1}{\omega_2} - \frac{2}{\tau_1}\right)\frac{1}{\epsilon^2} + \frac{1}{\sigma}\left[\frac{1}{\tau_1\tau_2}(\Lambda_\sigma + \Lambda_{\tau_1} + \Lambda_{\tau_2} - \Lambda_{\omega_1} - \Lambda_{\omega_2})\right.$$
$$\left. + \frac{1}{\omega_2\tau_2}(\Lambda_{\tau_1} - \Lambda_{\tau_2} - \Lambda_{\omega_2})\right]\frac{1}{\epsilon}\ ,$$
$$\Delta_{IR}(E_1^{(2)}) = \frac{1}{2\sigma\tau_2\omega_2}\frac{1}{\epsilon^2} + \frac{1}{\sigma\tau_2\omega_2}(\Lambda_{\tau_1} - \Lambda_{\tau_2} - \Lambda_{\omega_2})\frac{1}{\epsilon}\ ,$$

$$(A.46)$$

of $E2_{P_{1,t}^{gg}}^{\mu\nu}$:

$$\Delta_{IR}(E_2^{(11)}) = -\frac{1}{2\sigma\tau_2}\left(\frac{1}{\omega_2} - \frac{2}{\tau_1}\right)\frac{1}{\epsilon^2} + \frac{1}{\sigma}\left[\frac{1}{\tau_1\tau_2}(\Lambda_{\omega_2} - \Lambda_{\tau_1} - \Lambda_\sigma) + \frac{1}{\tau_2\omega_2}(\Lambda_{\tau_2} + \Lambda_{\omega_2} - \Lambda_{\tau_1})\right.$$
$$\left. + \frac{\omega_1}{\tau_1\tau_2(\tau_2 + \omega_1)}(\Lambda_{\omega_1} - \Lambda_{\tau_2})\right]\frac{1}{\epsilon}\ ,$$
$$\Delta_{IR}(E_2^{(12)}) = -\frac{1}{2\sigma\tau_2\omega_2}\frac{1}{\epsilon^2} - \frac{1}{\sigma\tau_2\omega_2}(\Lambda_{\tau_1} - \Lambda_{\tau_2} - \Lambda_{\omega_2})\frac{1}{\epsilon}\ ,$$
$$\Delta_{IR}(E_2^{(22)}) = -\frac{1}{2\sigma\tau_2\omega_2}\frac{1}{\epsilon^2} + \frac{1}{\sigma\tau_2\omega_2}\left[\Lambda_{\tau_2} + \frac{\tau_1}{(\tau_2 + \omega_1)}(\Lambda_{\omega_2} - \Lambda_{\tau_1})\right]\frac{1}{\epsilon}\ ,$$

$$(A.47)$$

and of $E3_{P_{1,t}^{gg}}^{\mu\nu\rho}$:

$$\Delta_{IR}(E_3^{(111)}) = \frac{1}{2\sigma\tau_2}\left(\frac{1}{\omega_2} - \frac{2}{\tau_1}\right)\frac{1}{\epsilon^2} - \left[\frac{1}{\tau_1\tau_2}(\Lambda_{\omega_2} - \Lambda_{\tau_1} - \Lambda_\sigma) + \frac{1}{\tau_2\omega_2}(\Lambda_{\tau_2} + \Lambda_{\omega_2} - \Lambda_{\tau_1})\right.$$
$$\left. + \frac{\omega_1^2}{\tau_1\tau_2(\tau_2 + \omega_1)^2}(\Lambda_{\omega_1} - \Lambda_{\tau_2}) + \frac{1}{\tau_1(\tau_2 + \omega_1)}\right]\frac{1}{\epsilon}\ ,$$
$$\Delta_{IR}(E_3^{(112)}) = \frac{1}{2\sigma\tau_2\omega_2}\frac{1}{\epsilon^2} + \frac{1}{\sigma\tau_2\omega_2}(\Lambda_{\tau_1} - \Lambda_{\tau_2} - \Lambda_{\omega_2})\frac{1}{\epsilon}\ ,$$
$$\Delta_{IR}(E_3^{(221)}) = \frac{1}{2\sigma\tau_2\omega_2}\frac{1}{\epsilon^2} - \frac{1}{\sigma\tau_2\omega_2}\left[\Lambda_{\tau_2} + \frac{\tau_1}{(\tau_2 + \omega_1)}(\Lambda_{\omega_2} - \Lambda_{\tau_1})\right]\frac{1}{\epsilon}\ ,$$
$$\Delta_{IR}(E_3^{(222)}) = \frac{1}{2\sigma\tau_2\omega_2}\frac{1}{\epsilon^2} - \frac{1}{\sigma}\left[\frac{1}{\tau_2\omega_2}\Lambda_{\tau_2} + \frac{\tau_1^2}{\tau_2\omega_2(\tau_1 + \omega_2)^2}(\Lambda_{\omega_2} - \Lambda_{\tau_1}) - \frac{1}{\tau_2(\tau_1 + \omega_2)}\right]\frac{1}{\epsilon}\ ,$$

$$(A.48)$$

are IR divergent.

We present in the following the IR singular box scalar integrals $D0^{(k)}_{P^{gg}_{1,t}}$, which are used in Eq. (A.31) to calculate $E0_{P^{gg}_{1,t}}$. $D0^{(2)}_{P^{gg}_{1,t}}$ is finite and we will not discuss it further.

Box scalar integral $\boldsymbol{D0^{(1)}_{P_{1,t}}}$

$D0^{(1)}_{P_{1,t}}$ can be parameterized according to Eq. (A.3) with:

$$N_1 = k^2 \ , \quad N_2 = (k + q_2)^2 \ ,$$

$$N_3 = (k + q_2 - p'_t)^2 - m_t^2 \ , \quad N_4 = (k + q_2 - p'_t - p_h)^2 - m_t^2 \ . \qquad (A.49)$$

and can be obtained from $D0_{B^{(1)}_{7,t}}$ in Section A.0.1.2 by exchanging $q_1 \leftrightarrow q_2$ and $p_t \leftrightarrow p'_t$, i.e. by exchanging $\tau_1 \leftrightarrow \tau_2$, and $\omega_1 \leftrightarrow \omega_2$.

Box scalar integral $\boldsymbol{D0^{(3)}_{P_{1,t}}}$

$D0^{(3)}_{P_{1,t}}$ can be parameterized according to Eq. (A.3) with:

$$N_1 = k^2 \ , \quad N_2 = (k + q_1)^2 \ ,$$

$$N_3 = (k + q_1 - p_t)^2 - m_t^2 \ , \quad N_4 = (k + q_1 - p_t - p_h)^2 - m_t^2 \ . \qquad (A.50)$$

and is equal to $D0_{B^{(1)}_{7,t}}$ in Section A.0.1.2.

Box scalar integral $\boldsymbol{D0^{(4)}_{P_{1,t}}}$

$D0^{(4)}_{P_{1,t}}$ can be parameterized according to Eq. (A.3) with:

$$N_1 = k^2 \ , \quad N_2 = (k + q_2)^2 \ ,$$

$$N_3 = (k + q_1 + q_2)^2 \ , \quad N_4 = (k + q_1 + q_2 - p_t)^2 - m_t^2 \ . \qquad (A.51)$$

and is equal to $D0^{(2)}_{B_{8,t}}$ in Section A.0.1.3.

Box scalar integral $\boldsymbol{D0^{(5)}_{P_{1,t}}}$

$D0^{(5)}_{P_{1,t}}$ can be parameterized according to Eq. (A.3) with:

$$N_1 = k^2 \ , \quad N_2 = (k + q_1)^2 \ ,$$

$$N_3 = (k + q_1 + q_2)^2 \ , \quad N_4 = (k + q_1 + q_2 - p'_t)^2 - m_t^2 \ , \qquad (A.52)$$

and coincides with $D0_{B^{(1)}_{8,t}}$ in Section A.0.1.3.

179

A.0.2.2 Pentagon scalar integral $E0_{P_{2,t}}$

The pentagon scalar integral arising from diagram $P_{2,t}$ can be parameterized according to Eq. (A.29) with:

$$N_1 = k^2 \ , \quad N_2 = (k - p'_t)^2 - m_t^2 \ , \quad N_3 = (k - p'_t + q_2)^2 - m_t^2 \ ,$$

$$N_4 = (k - p'_t + q_1 + q_2)^2 - m_t^2 \ , \quad N_5 = (k - p'_t + q_1 + q_2 - p_h)^2 - m_t^2 \ . \quad \text{(A.53)}$$

The c_k $(k=1,\ldots,5)$ coefficients of Eq. (A.31) are obtained, according to Eq. (A.32), as:

$$c_k = \sum_{l=1}^{5} [S(P_{2,t})]_{kl}^{-1} \ , \quad \text{(A.54)}$$

where

$$S(P_{2,t}) = \frac{1}{2} \begin{pmatrix} 0 & 0 & \tau_2 & -\omega_1 & 0 \\ 0 & 2m_t^2 & 2m_t^2 & 2m_t^2 - \sigma & a_1 \\ \tau_2 & 2m_t^2 & 2m_t^2 & 2m_t^2 & a_2 \\ -\omega_1 & 2m_t^2 - \sigma & 2m_t^2 & 2m_t^2 & 2m_t^2 - M_h^2 \\ 0 & a_1 & a_2 & 2m_t^2 - M_h^2 & 2m_t^2 \end{pmatrix} \ , \quad \text{(A.55)}$$

and we have defined

$$a_1 = 2m_t^2 - (p_t + p'_t)^2 = 2m_t^2 - \sigma + \omega_1 + \omega_2 - M_h^2 \ ,$$

$$a_2 = 2m_t^2 - (q_1 - p_h)^2 = 2m_t^2 + \omega_1 - \tau_1 + \tau_2 - M_h^2 \ . \quad \text{(A.56)}$$

The part of $E0_{P_{2,t}}$ that contributes to the virtual amplitude squared can be written as:

$$E0_{P_{2,t}} = \frac{i}{16\pi^2} \mathcal{N}_t \left[\frac{X_{-1}}{\epsilon} + X_0 \right] \ , \quad \text{(A.57)}$$

where X_{-1} and X_0 are obtained using Eqs. (A.31), (A.54)-(A.56), and the results for the $D0_{P_{2,t}}^{(k)}$ integrals presented in the following. The expression for X_{-1} has the following form:

$$X_{-1} = \frac{1}{\tau_2 \omega_1 (\sigma - \omega_1 - \omega_2 + M_h^2)} \frac{1}{\beta_{t\bar{t}}} \ln \left(\frac{1 + \beta_{t\bar{t}}}{1 - \beta_{t\bar{t}}} \right) \ . \quad \text{(A.58)}$$

All tensor pentagon integrals associated with $P_{2,t}$ are IR finite.

We present in the following the IR singular box scalar integrals $D0^{(k)}_{P_{2,t}}$ which are used in Eq. (A.31) to calculate $E0_{P_{2,t}}$. $D0^{(1)}_{P_{2,t}}$, $D0^{(2)}_{P_{2,t}}$, and $D0^{(5)}_{P_{2,t}}$ are finite and we will not discuss them further.

Box scalar integral $\boldsymbol{D0^{(3)}_{P_{2,t}}}$

$D0^{(3)}_{P_{2,t}}$ can be parameterized according to Eq. (A.3) with:

$$N_1 = k^2 \ , \quad N_2 = (k - p'_t)^2 - m_t^2 \ ,$$

$$N_3 = (k - p'_t + q_1 + q_2)^2 - m_t^2 \ , \quad N_4 = (k + p_t)^2 - m_t^2 \ , \tag{A.59}$$

and is equal to $D0_{B^{(1)}_{2,s}}$ in Section A.0.1.1.

Box scalar integral $\boldsymbol{D0^{(4)}_{P_{2,t}}}$.

$D0^{(4)}_{P_{2,t}}$ can be parameterized according to Eq. (A.3) with:

$$N_1 = k^2 \ , \quad N_2 = (k - p'_t)^2 - m_t^2 \ ,$$

$$N_3 = (k - p'_t + q_2)^2 - m_t^2 \ , \quad N_4 = (k + p_t)^2 - m_t^2 \ , \tag{A.60}$$

and can be written as

$$D0^{(4)}_{P_{2,t}} = \frac{i}{16\pi^2} \mathcal{N}_t \left(\frac{X_{-1}}{\epsilon} + X_0 \right) \ , \tag{A.61}$$

where the pole part X_{-1} is given by:

$$X_{-1} = \frac{1}{\tau_2 (\sigma - \omega_1 - \omega_2 + M_h^2)} \frac{1}{\beta_{t\bar{t}}} \ln \left(\frac{1 + \beta_{t\bar{t}}}{1 - \beta_{t\bar{t}}} \right) \ , \tag{A.62}$$

while the finite part X_0 can be found from Eq. (2.9) of Ref. [105] with the identifications:

$$m_0^2 = m_1^2 = m_4^2 \rightarrow m_t^2 \ , \tag{A.63}$$

$$s \rightarrow (p_t + p'_t)^2 = \sigma - \omega_1 - \omega_2 + M_h^2 \ ,$$

$$t \rightarrow (q_2 - p'_t)^2 = m_t^2 - \tau_2 \ .$$

181

A.0.2.3 Pentagon scalar integral $E0_{P_{3,t}}$

The pentagon scalar integral arising from diagram $P_{3,t}$ can be parameterized according to Eq. (A.29) with:

$$N_1 = k^2 \ , \quad N_2 = (k - p'_t)^2 - m_t^2 \ , \quad N_3 = (k - p'_t + q_2)^2 - m_t^2 \ ,$$

$$N_4 = (k - p'_t + q_2 - p_h)^2 - m_t^2 \ , \quad N_5 = (k + p_t)^2 - m_t^2 \ . \tag{A.64}$$

The c_k $(k=1,\ldots,5)$ coefficients of Eq. (A.31) are obtained, according to Eq. (A.32), as:

$$c_k = \sum_{l=1}^{5} [S(P_{3,t})]_{kl}^{-1} \ , \tag{A.65}$$

where

$$S(P_{3,t}) = \frac{1}{2} \begin{pmatrix} 0 & 0 & \tau_2 & \tau_1 & 0 \\ 0 & 2m_t^2 & 2m_t^2 & a_3 & a_1 \\ \tau_2 & 2m_t^2 & 2m_t^2 & 2m_t^2 - M_h^2 & a_2 \\ \tau_1 & a_3 & 2m_t^2 - M_h^2 & 2m_t^2 & 2m_t^2 \\ 0 & a_1 & a_2 & 2m_t^2 & 2m_t^2 \end{pmatrix} \ , \tag{A.66}$$

and we have defined

$$a_3 = 2m_t^2 - (q_2 - p_h)^2 = 2m_t^2 - M_h^2 + \omega_2 + \tau_1 - \tau_2 \ , \tag{A.67}$$

while a_1 and a_2 are given in Eq. (A.56).

The part of $E0_{P_{3,t}}$ that contributes to the virtual amplitude squared can be written as:

$$E0_{P_{3,t}} = \frac{i}{16\pi^2} \mathcal{N}_t \left[\frac{X_{-1}}{\epsilon} + X_0 \right] \ , \tag{A.68}$$

where X_{-1} and X_0 are obtained using Eqs. (A.31), (A.65)-(A.67), and the results for $D0_{P_{3,t}}^{(k)}$ given in the following. The expression for X_{-1} has the following form:

$$X_{-1} = -\frac{1}{\tau_1 \tau_2 (\sigma - \omega_1 - \omega_2 + M_h^2)} \frac{1}{\beta_{t\bar{t}}} \ln \left(\frac{1 + \beta_{t\bar{t}}}{1 - \beta_{t\bar{t}}} \right) \ . \tag{A.69}$$

All tensor pentagon integrals associated with $P_{3,t}$ are IR finite.

We present in the following the box scalar integrals $D0_{P_{3,t}}^{(k)}$, which are used in Eq. (A.31) to calculate $E0_{P_{3,t}}$. $D0_{P_{3,t}}^{(1)}$, $D0_{P_{3,t}}^{(2)}$, and $D0_{P_{3,t}}^{(5)}$ are finite and we will not discuss them further.

Box scalar integral $\boldsymbol{D0_{P_{3,t}}^{(3)}}$

$D0_{P_{3,t}}^{(3)}$ can be parameterized according to Eq. (A.3) with:

$$N_1 = k^2 \ , \ \ N_2 = (k - p_t')^2 - m_t^2 \ ,$$
$$N_3 = (k - p_t' + q_2 - p_h)^2 - m_t^2 \ , \ \ N_4 = (k + p_t)^2 - m_t^2 \ , \tag{A.70}$$

and can be written as

$$D0_{P_{3,t}}^{(3)} = \frac{i}{16\pi^2}\mathcal{N}_t \left(\frac{X_{-1}}{\epsilon} + X_0 \right) \ , \tag{A.71}$$

where the pole part X_{-1} is:

$$X_{-1} = \frac{1}{\tau_1(\sigma - \omega_1 - \omega_2 + M_h^2)} \frac{1}{\beta_{t\bar{t}}} \ln\left(\frac{1 + \beta_{t\bar{t}}}{1 - \beta_{t\bar{t}}} \right) \ , \tag{A.72}$$

while the finite part X_0 can be found from Eq. (2.9) of Ref. [105] with the identifications:

$$m_0^2 = m_1^2 = m_4^2 \to m_t^2 \ ,$$
$$s \to (p_t + p_t')^2 = \sigma + m_h^2 - \omega_1 - \omega_2 \ ,$$
$$t \to (q_1 - p_t)^2 = m_t^2 - \tau_1 \ . \tag{A.73}$$

Box scalar integral $\boldsymbol{D0_{P_{3,t}}^{(4)}}$.

$D0_{P_{3,t}}^{(4)}$ can be parameterized according to Eq. (A.3) with:

$$N_1 = k^2 \ , \ \ N_2 = (k - p_t')^2 - m_t^2 \ ,$$
$$N_3 = (k - p_t' + q_2)^2 - m_t^2 \ , \ \ N_4 = (k + p_t)^2 - m_t^2 \ , \tag{A.74}$$

and is equal to $D0_{P_{2,t}}^{(4)}$ in Section A.0.2.2.

A.0.2.4   Pentagon scalar integral $E0_{P_{4,t}}$

The pentagon scalar and tensor integrals arising from diagram $P_{4,t}$ can be found from the corresponding integrals for diagram $P_{2,t}$ by exchanging $q_1 \leftrightarrow q_2$ and $p_t \leftrightarrow p'_t$, i.e. by exchanging $\tau_1 \leftrightarrow \tau_2$, $\tau_3 \leftrightarrow \tau_4$, and $\omega_1 \leftrightarrow \omega_2$.

A.0.2.5   Pentagon scalar integral $E0_{P_{5,t}}$

The pentagon scalar integral arising from diagram $P_{5,t}$ can be parameterized according to Eq. (A.29) with:

$$N_1 = k^2 \ , \ \ N_2 = (k + q_1)^2 \ , \ \ N_3 = (k + q_1 - p'_t)^2 - m_t^2 \ ,$$

$$N_4 = (k + q_1 + q_2 - p'_t)^2 - m_t^2 \ , \ \ N_5 = (k + q_1 + q_2 - p'_t - p_h)^2 - m_t^2 \ . \ \text{(A.75)}$$

The c_k $(k=1,\ldots,5)$ coefficients of Eq. (A.31) are obtained, according to Eq. (A.32), as:

$$c_k = \sum_{l=1}^{5} [S(P_{5,t})]_{kl}^{-1} \ , \tag{A.76}$$

where

$$S(P_{5,t}) = \frac{1}{2}\begin{pmatrix} 0 & 0 & \tau_4 & -\omega_1 & 0 \\ 0 & 0 & 0 & \tau_2 & \tau_1 \\ \tau_4 & 0 & 2m_t^2 & 2m_t^2 & a_3 \\ -\omega_1 & \tau_2 & 2m_t^2 & 2m_t^2 & 2m_t^2 - M_h^2 \\ 0 & \tau_1 & a_3 & 2m_t^2 - M_h^2 & 2m_t^2 \end{pmatrix} \ , \tag{A.77}$$

with a_3 as defined in Eq. (A.67).

The part of $E0_{P_{5,t}}$ that contributes to the virtual amplitude squared can be written as:

$$E0_{P_{5,t}} = \frac{i}{16\pi^2}\mathcal{N}_t \left[\frac{X_{-2}}{\epsilon^2} + \frac{X_{-1}}{\epsilon} + X_0\right] \ , \tag{A.78}$$

where X_{-2}, X_{-1} and X_0 are obtained using Eqs. (A.31), (A.76), (A.77), and the results for $D0_{P_{5,t}}^{(k)}$ given below. The expressions for X_{-2} and X_{-1} have the following form:

$$X_{-2} = \frac{1}{2\tau_1\tau_4}\left(\frac{1}{\omega_1} - \frac{1}{\tau_2}\right) \ ,$$

$$X_{-1} = \frac{1}{\tau_1\tau_4}\left[\frac{1}{\omega_1}\left(\Lambda_{\tau_2} - \Lambda_{\tau_1} - \Lambda_{\omega_1}\right) + \frac{1}{\tau_2}\left(\Lambda_{\tau_2} + \Lambda_{\tau_4} - \Lambda_{\omega_1}\right)\right] \ . \tag{A.79}$$

The tensor integrals associated with $P_{5,t}$ also contain IR divergences. Only the following tensor coefficients of $E1^{\mu}_{P_{5,t}}$:

$$\Delta_{IR}(E_1^{(1)}) = \frac{1}{2\tau_1\tau_2\tau_4}\frac{1}{\epsilon^2} + \frac{1}{\tau_1\tau_2\tau_4}(\Lambda_{\omega_1} - \Lambda_{\tau_2} - \Lambda_{\tau_4})\frac{1}{\epsilon} \quad ,$$
(A.80)

of $E2^{\mu\nu}_{P_{5,t}}$:

$$\Delta_{IR}(E_2^{(11)}) = -\frac{1}{2\tau_1\tau_2\tau_4}\frac{1}{\epsilon^2} + \frac{1}{\tau_1\tau_2\tau_4(\tau_2 + \omega_1)}[(\tau_2 + \omega_1)\Lambda_{\tau_4} - \omega_1(\Lambda_{\omega_1} - \Lambda_{\tau_2})]\frac{1}{\epsilon} \quad ,$$
(A.81)

and of $E3^{\mu\nu\rho}_{P_{5,t}}$:

$$\Delta_{IR}(E_3^{(111)}) = \frac{1}{2\tau_1\tau_2\tau_4}\frac{1}{\epsilon^2} - \frac{1}{\tau_1\tau_2\tau_4(\tau_2 + \omega_1)^2}\left[-\tau_2(\tau_2 + \omega_1) + (\tau_2 + \omega_1)^2\Lambda_{\tau_4}\right.$$
$$\left. +\omega_1^2(\Lambda_{\tau_2} - \Lambda_{\omega_1})\right]\frac{1}{\epsilon}$$
(A.82)
(A.83)

are IR divergent.

We present in the following the IR singular box scalar integrals $D0^{(k)}_{P_{5,t}}$, which are used in Eq. (A.31) to calculate $E0_{P_{5,t}}$. $D0^{(1)}_{P_{5,t}}$ and $D0^{(2)}_{P_{5,t}}$ are finite and we will not discuss them further.

Box scalar integral $\boldsymbol{D0^{(3)}_{P_{5,t}}}$

$D0^{(3)}_{P_{5,t}}$ can be parameterized according to Eq. (A.3) with:

$$N_1 = k^2 \, , \, , \quad N_2 = (k + q_1)^2 \quad ,$$
$$N_3 = (k + q_1 + q_2 - p'_t)^2 - m_t^2 \, , \quad N_4 = (k + p_t)^2 - m_t^2 \quad ,$$
(A.84)

and coincides with $D0^{(3)}_{P_{1,t}}$ in Section A.0.2.1, after shifting $k \to -k - q_1$.

Box scalar integral $\boldsymbol{D0^{(4)}_{P_{5,t}}}$.

185

$D0_{P_{5,t}}^{(4)}$ can be parameterized according to Eq. (A.3) with:

$$N_1 = k^2 \; , \;\; N_2 = (k + q_1)^2 \; ,$$

$$N_3 = (k + q_1 - p_t')^2 - m_t^2 \; , \;\; N_4 = (k + p_t)^2 - m_t^2 \; . \tag{A.85}$$

The part of $D0_{P_{5,t}}^{(4)}$ which contributes to the virtual amplitude squared is given by:

$$D0_{P_{5,t}}^{(4)} = \frac{i}{16\pi^2} \mathcal{N}_t \left(\frac{1}{\tau_1 \tau_4} \right) \left(\frac{X_{-2}}{\epsilon^2} + \frac{X_{-1}}{\epsilon} + X_0 \right) \; , \tag{A.86}$$

where the coefficients X_{-2}, X_{-1}, and X_0 are given by:

$$X_{-2} = 1 \; ,$$

$$X_{-1} = -\ln\left(\frac{\tau_1}{m_t^2} \right) - \ln\left(\frac{\tau_4}{m_t^2} \right) \; ,$$

$$X_0 = \mathcal{R}e \left\{ \ln^2\left(\frac{\tau_1}{m_t^2} \right) + \ln^2\left(\frac{\tau_4}{m_t^2} \right) - \ln^2\left(\frac{\tau_4}{\tau_1} \right) - \frac{2}{3}\pi^2 + 2\mathrm{Li}_2\left(\frac{1}{z_+} \right) + 2\mathrm{Li}_2\left(\frac{1}{z_-} \right) \right\} \; ,$$

$$\tag{A.87}$$

with

$$z_\pm = \frac{1}{2}(1 \pm \Delta) \; , \;\; \Delta = \sqrt{1 - \frac{4m_t^2}{2m_t^2 - a_3}} \; , \tag{A.88}$$

and a_3 defined in Eq. (A.67).

<u>Box integral $\boldsymbol{D0_{P_{5,t}}^{(5)}}$</u>.

$D0_{P_{5,t}}^{(5)}$ can be parameterized according to Eq. (A.3) with:

$$N_1 = k^2 \; , \;\; N_2 = (k + q_1)^2 \; ,$$

$$N_3 = (k + q_1 - p_t')^2 - m_t^2 \; , \;\; N_4 = (k + q_1 + q_2 - p_t')^2 - m_t^2 \; , \tag{A.89}$$

and is equal to $D0_{B_{10,t}^{(1)}}$ in Section A.0.1.4.

186

A.0.2.6 Pentagon scalar integral $E0_{P_{6,t}}$

The pentagon scalar integral arising from diagram $P_{6,t}$ can be parameterized according to Eq. (A.29) with:

$$N_1 = k^2 \ , \quad N_2 = (k + q_1)^2 \ , \quad N_3 = (k + q_1 - p'_t)^2 - m_t^2 \ ,$$

$$N_4 = (k + q_1 - p'_t - p_h)^2 - m_t^2 \ , \quad N_5 = (k + q_1 - p'_t - p_h + q_2)^2 - m_t^2 \ . \, \text{(A.90)}$$

We note that $E0_{P_{6,t}}$ can be obtained from $E0_{P_{5,t}}$ by shifting $k \to -k - q_1$ and exchanging $p_t \leftrightarrow p'_t$, or equivalently by exchanging $\tau_1 \leftrightarrow \tau_4$, $\tau_2 \leftrightarrow \tau_3$, and $\omega_1 \leftrightarrow \omega_2$. The same applies to the tensor pentagon integrals $E1^{\mu}_{P_{6,t}}$, $E2^{\mu\nu}_{P_{6,t}}$, and $E3^{\mu\nu\rho}_{P_{6,t}}$.

APPENDIX B

TENSOR INTEGRAL REDUCTIONS

In this Appendix, we give a simple example of the reduction of a tensor integral to a linear combination of scalar integrals. We will also make explicit the dependence of the tensor coefficients on the inverse of the Gram determinant. For more details, we refer the reader to the original works in Refs. [64, 65].

For simplicity, we consider a three-point function, e.g. the vertex corrections encountered in $q\bar{q}, gg \rightarrow t\bar{t}h$. We write the scalar integral and the first-rank and second-rank tensor integrals as:

$$C_0, C_1^\mu, C_2^{\mu\nu} = \mu^{4-d} \int \frac{d^d k}{(2\pi)^d} \frac{1, k^\mu, k^\mu k^\nu}{N_1 N_2 N_3} \ , \qquad (B.1)$$

where the denominators are given by:

$$N_1 = (k^2 - m^2) \ , \ \ N_2 = (k + p_1)^2 - m^2 \ , \ \ N_3 = (k + p_1 + p_2)^2 - m^2 \ , \quad (B.2)$$

where p_1 and p_2 are two of the external momenta connected with the three-point function and m is the mass which, we assume for simplicity, is the same for all denominators.

We can write the tensor integrals, C_1^μ and $C_2^{\mu\nu}$, as linear combinations of the linearly-independent tensor structures built of the independent external momenta p_1^μ, p_2^μ plus the metric tensor, $g^{\mu\nu}$:

$$C_1^\mu = C_{11} \, p_1^\mu + C_{12} \, p_2^\mu \qquad (B.3)$$

and

$$C_2^{\mu\nu} = p_1^\mu p_1^\nu \, C_{21} + p_2^\mu p_2^\nu \, C_{22} + (p_1^\mu p_2^\nu + p_1^\nu p_2^\mu) \, C_{23} + g^{\mu\nu} \, C_{24} \ . \qquad (B.4)$$

188

where the C_{ij} are the *tensor coefficients*.

First, let us consider the rank-one tensor integral. Replacing C_1^μ in Eq. (B.1) with the expression in Eq. (B.3) and saturating each side with the external momenta, we can construct the following system of equations:

$$C_{11}\, p_1^2 + C_{12}\, (p_1 \cdot p_2) = \mu^{4-d} \int \frac{d^d k}{(2\pi)^d} \frac{(p_1 \cdot k)}{N_1 N_2 N_3}$$

$$C_{11}\, (p_1 \cdot p_2) + C_{12}\, p_2^2 = \mu^{4-d} \int \frac{d^d k}{(2\pi)^d} \frac{(p_2 \cdot k)}{N_1 N_2 N_3} \ , \tag{B.5}$$

where we can write:

$$
\begin{aligned}
(p_1 \cdot k) &= \frac{1}{2}\left[(k + p_1)^2 - m^2 - (k^2 - m^2) - p_1^2 \right] \\
&= \frac{1}{2}\left[N_2 - N_1 - p_1^2 \right] \tag{B.6}
\end{aligned}
$$

$$
\begin{aligned}
(p_2 \cdot k) &= \frac{1}{2}\left[(k + p_1 + p_2)^2 - m^2 - ((k + p_1)^2 - m^2) - p_1^2 \right] \\
&= \frac{1}{2}\left[N_3 - N_2 - (p_2^2 + 2 p_1 \cdot p_2) \right] . \tag{B.7}
\end{aligned}
$$

Using Eqs. (B.6) and (B.7), we can write the system of equations in Eq. (B.5) as a matrix equation:

$$X \begin{pmatrix} C_{11} \\ C_{12} \end{pmatrix} = \begin{pmatrix} R_1 \\ R_2 \end{pmatrix} \tag{B.8}$$

where we have defined:

$$R_1 = \frac{1}{2}\left(B_0(1,3) - B_0(2,3) - p_1^2\, C_0 \right) \tag{B.9}$$

$$R_2 = \frac{1}{2}\left(B_0(1,2) - B_0(1,3) - (p_2^2 + 2 p_1 \cdot p_2)\, C_0 \right) , \tag{B.10}$$

with the two-point scalar integral, $B_0(i, j)$ given by:

$$B_0(i, j) = \mu^{4-d} \int \frac{d^d k}{(2\pi)^d} \frac{1}{N_i N_j} \ , \tag{B.11}$$

and the matrix X is defined as:

$$X = \begin{pmatrix} p_1^2 & (p_1 \cdot p_2) \\ (p_1 \cdot p_2) & p_2^2 \end{pmatrix} . \tag{B.12}$$

Then, solving for the C_{11}, C_{12} coefficients in Eq. (B.8), we find:

$$\begin{pmatrix} C_{11} \\ C_{12} \end{pmatrix} = X^{-1} \begin{pmatrix} R_1 \\ R_2 \end{pmatrix} . \tag{B.13}$$

With the inverse of the matrix given by:

$$X^{-1} = \frac{1}{|X|} \begin{pmatrix} p_2^2 & -(p_1 \cdot p_2) \\ -(p_1 \cdot p_2) & p_1^2 \end{pmatrix} \tag{B.14}$$

Hence, we see the explicit dependence of the tensor coefficients C_{11}, C_{12} on the inverse of the Gram determinant, $|X|$, which is defined to be:

$$|X| = p_1^2 p_2^2 - (p_1 \cdot p_2)^2 . \tag{B.15}$$

Next, we consider the rank-two tensor integral $C_2^{\mu\nu}$. Using Eq. (B.4) in Eq. (B.1) and saturating both sides with the momenta p_1^μ, p_2^μ and the metric tensor $g^{\mu\nu}$, we can solve for the coefficients using the same procedure outlined above. In this case, we arrive at two matrix equations:

$$\begin{pmatrix} C_{21} \\ C_{23} \end{pmatrix} = X^{-1} \begin{pmatrix} R_3 \\ R_5 \end{pmatrix} \tag{B.16}$$

and:

$$\begin{pmatrix} C_{22} \\ C_{23} \end{pmatrix} = X^{-1} \begin{pmatrix} R_4 \\ R_6 \end{pmatrix} , \tag{B.17}$$

along with an independent expression for C_{24}:

$$C_{24} = \frac{1}{4} + \frac{1}{2} m^2 C_0 + \frac{1}{4} \left(B_0(2,3) + p_1^2 C_{11} + (p_2^2 + 2p_1 \cdot p_2) C_{12} \right) . \tag{B.18}$$

The inverse matrix X^{-1} is that given in Eq. (B.14) and we have defined:

$$R_3 = \frac{1}{2} \left(p_1^2 C_{11} + B_1(1,3) + B_0(2,3) \right) - C_{24} \tag{B.19}$$

$$R_4 = \frac{1}{2} \left(p_1^2 C_{12} + B_1(1,3) - B_1(2,3) \right) \tag{B.20}$$

$$R_5 = \frac{1}{2} \left((p_2^2 + 2p_1 \cdot p_2) C_{11} + B_1(1,2) - B_1(1,3) \right) \tag{B.21}$$

$$R_6 = \frac{1}{2} \left((p_2^2 + 2p_1 \cdot p_2) C_{12} - B_1(1,3) \right) - C_{24} , \tag{B.22}$$

190

where $B_1(i,j)$ is the tensor coefficient defined through the two-point tensor integral, i.e.:

$$B_1^\mu = \mu^{4-d} \int \frac{d^d k}{(2\pi)^d} \frac{k^\mu}{N_i N_j} = p_j^\mu B_1(i,j) \ . \tag{B.23}$$

From Eqs. (B.16) and (B.17), it appears that the C_{ij} coefficients have the same dependence on the inverse Gram determinant as the rank-one tensor coefficients C_i. However, given the fact that the latter carry an implicit dependence on $|X|^{-1}$, we actually see that the C_{ij} coefficients depend on *two powers* of the inverse Gram determinant. In fact, a general feature of this reduction method is that higher-rank coefficients depend on higher powers of the inverse Gram determinant.

Finally, the reduction technique outlined above is also applicable to box and pentagon tensor integrals. However, as one can imagine, the situation becomes more complicated due to the additional momenta connected to the box and pentagon topologies.

APPENDIX C

PHASE SPACE INTEGRALS FOR THE EMISSION OF A SOFT GLUON IN THE TWO-CUTOFF PSS METHOD.

In this Appendix we collect the phase space integrals for a final state soft gluon that are used in calculating the results reported in Eq. (3.66). We parameterize the soft gluon d-momentum in the $q\bar{q}$ (gg) rest frame as:

$$k = E_g(1, \ldots, \sin\theta_1 \sin\theta_2, \sin\theta_1 \cos\theta_2, \cos\theta_1) \ , \tag{C.1}$$

such that the phase space of the soft gluon in $d = 4 - 2\epsilon$ dimensions can be written as:

$$d(PS_g)_{soft} = \frac{\Gamma(1-\epsilon)}{\Gamma(1-2\epsilon)} \frac{\pi^\epsilon}{(2\pi)^3} \int_0^{\delta_s \sqrt{s}/2} dE_g E_g^{1-2\epsilon} \times$$
$$\int_0^\pi d\theta_1 \sin^{1-2\epsilon}\theta_1 \int_0^\pi d\theta_2 \sin^{-2\epsilon}\theta_2 \ . \tag{C.2}$$

Then, all the integrals we need are of the form:

$$I_n^{(k,l)} = \int_0^\pi d\theta_1 \sin^{d-3}\theta_1 \int_0^\pi d\theta_2 \sin^{d-4}\theta_2 \frac{(a + b\cos\theta_1)^{-k}}{(A + B\cos\theta_1 + C\sin\theta_1 \cos\theta_2)^l} \ . \tag{C.3}$$

In particular we need the following four cases. When $A^2 \neq B^2 + C^2$, and $b = -a$, we use (dropping terms of order $\mathcal{O}\left((d-4)^2\right)$):

$$I_n^{(1,1)} = \frac{\pi}{a(A+B)} \left\{ \frac{2}{d-4} + \ln\left[\frac{(A+B)^2}{A^2 - B^2 - C^2}\right] \right. \tag{C.4}$$
$$+ \frac{1}{2}(d-4)\left[\ln^2\left(\frac{A - \sqrt{B^2 + C^2}}{A+B}\right) - \frac{1}{2}\ln^2\left(\frac{A + \sqrt{B^2 + C^2}}{A - \sqrt{B^2 + C^2}}\right)\right.$$
$$\left.\left. + \ 2\,\mathrm{Li}_2\left(-\frac{B + \sqrt{B^2 + C^2}}{A - \sqrt{B^2 + C^2}}\right) - 2\,\mathrm{Li}_2\left(\frac{B - \sqrt{B^2 + C^2}}{A+B}\right)\right]\right\} \ ,$$

while when $b \neq -a$ we use:

$$I_n^{(0,1)} = \frac{\pi}{\sqrt{B^2 + C^2}} \left\{ \ln\left(\frac{A + \sqrt{B^2 + C^2}}{A - \sqrt{B^2 + C^2}} \right) \right.$$

$$\left. -(d-4)\left[\mathrm{Li}_2\left(\frac{2\sqrt{B^2 + C^2}}{A + \sqrt{B^2 + C^2}} \right) + \frac{1}{4}\ln^2\left(\frac{A + \sqrt{B^2 + C^2}}{A - \sqrt{B^2 + C^2}} \right) \right] \right\} \quad , \tag{C.5}$$

$$I_n^{(0,2)} = \frac{2\pi}{A^2 - B^2 - C^2}\left[1 - \frac{1}{2}(d-4)\frac{A}{\sqrt{B^2 + C^2}}\ln\left(\frac{A + \sqrt{B^2 + C^2}}{A - \sqrt{B^2 + C^2}} \right) \right] \quad . \tag{C.6}$$

Additionally, when $A^2 = B^2 + C^2$, and $b = -a$, we have:

$$I_n^{(1,1)} = 2\pi \frac{1}{aA}\frac{1}{d-4}\left(\frac{A+B}{2A} \right)^{d/2-3}\left[1 + \frac{1}{4}(d-4)^2\mathrm{Li}_2\left(\frac{A-B}{2A} \right) \right] \quad . \tag{C.7}$$

Finally, all the integrals we need are the following four:

$$\int d(PS_g)_{soft}\frac{(q_1 \cdot q_2)}{(q_1 \cdot k)(q_2 \cdot k)} = \frac{1}{(4\pi)^2}\mathcal{N}_t\, 2\left[\frac{1}{\epsilon^2} - \frac{2}{\epsilon}\ln(\delta_s) - \frac{1}{\epsilon}\Lambda_\sigma \right.$$

$$\left. -\frac{\pi^2}{3} + \frac{1}{2}\left(\Lambda_\sigma^2 + 4\Lambda_\sigma\ln(\delta_s) + 4\ln^2(\delta_s) \right) \right] \quad ,$$

$$\int d(PS_g)_{soft}\frac{(q_1 \cdot p_t)}{(q_1 \cdot k)(p_t \cdot k)} = \frac{1}{(4\pi)^2}\mathcal{N}_t\left[\frac{1}{\epsilon^2} - \frac{2}{\epsilon}\Lambda_{\tau_1} - \frac{2}{\epsilon}\ln(\delta_s) - \frac{\pi^2}{3} \right.$$

$$\left. -\frac{1}{2}\Lambda_\sigma^2 + 2\Lambda_{\tau_1}\Lambda_\sigma + 2\ln^2(\delta_s) + 4\Lambda_{\tau_1}\ln(\delta_s) + F(q_1, p_t) \right] \quad ,$$

$$\int d(PS_g)_{soft}\frac{(p_t \cdot p_t')}{(p_t \cdot k)(p_t' \cdot k)} = \frac{1}{(4\pi)^2}\mathcal{N}_t\left(\frac{\bar{s}_{t\bar{t}} - 2m_t^2}{\bar{s}_{t\bar{t}}} \right)\left[\left(-\frac{2}{\epsilon} + 2\Lambda_\sigma + 4\ln(\delta_s) \right)\frac{1}{\beta_{t\bar{t}}}\Lambda_{t\bar{t}} \right.$$

$$\left. -\frac{1}{\beta_{t\bar{t}}}\Lambda_{t\bar{t}}^2 - \frac{4}{\beta_{t\bar{t}}}\mathrm{Li}_2\left(\frac{2\beta_{t\bar{t}}}{1 + \beta_{t\bar{t}}} \right) \right] \quad ,$$

$$\int d(PS_g)_{soft}\frac{p_t^2}{(p_t \cdot k)^2} = \frac{1}{(4\pi)^2}\mathcal{N}_t\left[-\frac{2}{\epsilon} + 2\Lambda_\sigma + 4\ln(\delta_s) - 2\frac{1}{\beta_{t\bar{t}}}\Lambda_{t\bar{t}} \right] \quad , \tag{C.8}$$

where $\bar{s}_{t\bar{t}}$ is given in Eq. (3.47), while $\beta_{t\bar{t}}$ and $\Lambda_{t\bar{t}}$ are defined in Eq. (3.37). Moreover we have denoted by $F(p_i, p_f)$ the function:

$$F(p_i, p_f) = \ln^2\left(\frac{1 - \beta_f}{1 - \beta_f\cos\theta_{if}} \right) - \frac{1}{2}\ln^2\left(\frac{1 + \beta_f}{1 - \beta_f} \right)$$

$$+2\mathrm{Li}_2\left(-\frac{\beta_f(1 - \cos\theta_{if})}{1 - \beta_f} \right) - 2\mathrm{Li}_2\left(-\frac{\beta_f(1 + \cos\theta_{if})}{1 - \beta_f\cos\theta_{if}} \right) \quad , \tag{C.9}$$

193

where $\cos\theta_{if}$ is the angle between partons i and f in the center-of-mass frame of the initial state partons, and

$$\beta_f = \sqrt{1 - \frac{m_t^2}{(p_f^0)^2}} \quad , \quad 1 - \beta_f \cos\theta_{if} = \frac{s_{if}}{p_f^0 \sqrt{s}} \quad . \tag{C.10}$$

All the quantities in Eq. (C.9) can be expressed in terms of kinematical invariants, once we use $s_{if} = 2p_i \cdot p_f$ and:

$$p_t^0 = \frac{s - \bar{s}_{\bar{t}h} + m_t^2}{2\sqrt{s}} \quad \text{and} \quad p_{\bar{t}}^0 = \frac{s - \bar{s}_{th} + m_t^2}{2\sqrt{s}} \quad , \tag{C.11}$$

with $\bar{s}_{fh} = (p_f + p_h)^2$.

APPENDIX D

COLOR ORDERED AMPLITUDES FOR
$H \to Q\bar{Q}T\bar{T} + G$

The tree-level amplitude for $h \to q(q_1)\bar{q}(q_2)t(p_t)\bar{t}(p_t')$ is explicitly given by:

$$
\mathcal{A}_{LO}^{h\to q\bar{q}t\bar{t}} = i\,\frac{m_t}{v}g_s^2\delta_{f_q f_{\bar{q}}}\delta_{f_t f_{\bar{t}}}\left[\bar{u}(q_1)\gamma^\nu T^a_{c_q c_{\bar{q}}}v(q_2)\right]\frac{1}{(p_h - p_t - p_t')^2}\times \tag{D.1}
$$

$$
\left[\bar{u}(p_t)\left(\gamma_\nu\frac{\not{p}_h - \not{p}_t' + m_t}{(p_h - p_t')^2 - m_t^2} + \frac{-\not{p}_h + \not{p}_t + m_t}{(p_h - p_t)^2 - m_t^2}\gamma_\nu\right)T^a_{c_t c_{\bar{t}}}v(p_t')\right]
$$

$$
= \frac{1}{2}\left(\delta_{c_t c_{\bar{q}}}\delta_{c_q c_{\bar{t}}} - \frac{1}{N}\delta_{c_t c_{\bar{t}}}\delta_{c_q c_{\bar{q}}}\right)\delta_{f_q f_{\bar{q}}}\delta_{f_t f_{\bar{t}}}\mathcal{A}_0 \ ,
$$

where p_h is taken as incoming, while all the other momenta are outgoing. Using the color decomposition given in Eq. (3.82), we have rewritten $\mathcal{A}_{LO}^{h\to q\bar{q}t\bar{t}}$ in terms of a leading color and a sub-leading color ordered amplitude. Both amplitudes are given by:

$$
\mathcal{A}_0 = i\,\frac{m_t}{v}g_s^2\left[\bar{u}(q_1)\gamma^\nu v(q_2)\right]\frac{1}{(p_h - p_t - p_t')^2}\times \tag{D.2}
$$

$$
\left[\bar{u}(p_t)\left(\gamma_\nu\frac{\not{p}_h - \not{p}_t' + m_t}{(p_h - p_t')^2 - m_t^2} + \frac{-\not{p}_h + \not{p}_t + m_t}{(p_h - p_t)^2 - m_t^2}\gamma_\nu\right)v(p_t')\right]
$$

$$
= i\,\frac{m_t}{v}g_s^2\mathcal{A}_{q\bar{q}}^{0,\nu}\frac{1}{(p_h - p_t - p_t')^2}\mathcal{A}_{t\bar{t},\nu}^0 \ ,
$$

where, for future purposes, we have introduced the $\mathcal{A}_{q\bar{q}}^{0,\nu}$ and $\mathcal{A}_{t\bar{t}}^{0,\nu}$ tree-level partial amplitudes:

$$
\mathcal{A}_{q\bar{q}}^{0,\nu} = \bar{u}(q_1)\gamma^\nu v(q_2) \ , \tag{D.3}
$$

$$
\mathcal{A}_{t\bar{t}}^{0,\nu} = \bar{u}(p_t)\left(\gamma^\nu\frac{\not{p}_h - \not{p}_t' + m_t}{(p_h - p_t')^2 - m_t^2} + \frac{-\not{p}_h + \not{p}_t + m_t}{(p_h - p_t)^2 - m_t^2}\gamma^\nu\right)v(p_t') \ .
$$

The $\mathcal{O}(\alpha_s)$ real corrections to the Born amplitude consist of the process $h \to q\bar{q}t\bar{t} + g$, where the gluon can be emitted either from the external quark legs or from the internal gluon propagator. Therefore we can write $\mathcal{A}^{h \to q\bar{q}t\bar{t}g}$ as follows:

$$
\mathcal{A}^{h \to q\bar{q}t\bar{t}g} = (ig_s)\delta_{f_q f_{\bar{q}}}\delta_{f_t f_{\bar{t}}}\left[\mathcal{A}_q^\mu \left(T^a T^b\right)_{c_q c_{\bar{q}}}T^b_{c_t c_{\bar{t}}} + \mathcal{A}_{\bar{q}}^\mu \left(T^b T^a\right)_{c_q c_{\bar{q}}}T^b_{c_t c_{\bar{t}}} \right. \tag{D.4}
$$
$$
\left. + \mathcal{A}_t^\mu T^b_{c_q c_{\bar{q}}}\left(T^a T^b\right)_{c_t c_{\bar{t}}} + \mathcal{A}_{\bar{t}}^\mu T^b_{c_q c_{\bar{q}}}\left(T^b T^a\right)_{c_t c_{\bar{t}}} + \mathcal{A}_g^\mu \left(if^{abc}T^b_{c_t c_{\bar{t}}}T^c_{c_q c_{\bar{q}}}\right)\right] \cdot \epsilon_\mu(k) \ ,
$$

where $\epsilon^\mu(k)$ is the polarization vector of the emitted gluon and we have defined by $\mathcal{A}_i^\mu$ the part of the real amplitude corresponding to the emission of the gluon from $i = q, \bar{q}, t, \bar{t}, g$. More explicitly, the $\mathcal{A}_i^\mu$ amplitudes are given by:

$$
\mathcal{A}_q^\mu = \left(g_s^2 \frac{m_t}{v}\right)\left(\bar{u}(q_1)\gamma^\mu \frac{\slashed{q}_1 + \slashed{k}}{2q_1 \cdot k}\gamma_\nu v(q_2)\right)\frac{1}{(p_h - p_t - p_t')^2}\mathcal{A}_{t\bar{t}}^{0,\nu} \ , \tag{D.5}
$$

$$
\mathcal{A}_{\bar{q}}^\mu = \left(g_s^2 \frac{m_t}{v}\right)\left(\bar{u}(q_1)\gamma_\nu \frac{-\slashed{q}_2 - \slashed{k}}{2q_2 \cdot k}\gamma^\mu v(q_2)\right)\frac{1}{(p_h - p_t - p_t')^2}\mathcal{A}_{t\bar{t}}^{0,\nu} \ ,
$$

$$
\mathcal{A}_g^\mu = \left(g_s^2 \frac{m_t}{v}\right)\mathcal{A}_{q\bar{q},\rho}^0 \frac{1}{(p_h - p_t - p_t')^2}\left(V_{3g}^{\mu\rho\nu}(k, q_1, q_2)\right)\frac{1}{(q_1 + q_2)^2}\mathcal{A}_{t\bar{t},\nu}^0 \ ,
$$

$$
\mathcal{A}_t^\mu = \left(g_s^2 \frac{m_t}{v}\right)\mathcal{A}_{q\bar{q}}^{0,\nu}\bar{u}(p_t)\left(\gamma^\mu \frac{\slashed{p}_t + \slashed{k} + m_t}{2p_t \cdot k}\gamma_\nu \frac{\slashed{p}_h - \slashed{p}_t' + m_t}{(p_h - p_t')^2 - m_t^2}\right.
$$
$$
+ \frac{-\slashed{p}_h + \slashed{p}_t + m_t}{(p_h - p_t)^2 - m_t^2}\gamma^\mu \frac{-\slashed{p}_h + \slashed{p}_t + \slashed{k} + m_t}{(p_h - p_t - k)^2 - m_t^2}\gamma_\nu
$$
$$
\left. + \gamma^\mu \frac{\slashed{p}_t + \slashed{k} + m_t}{2p_t \cdot k}\frac{-\slashed{p}_h + \slashed{p}_t + \slashed{k} + m_t}{(p_h - p_t - k)^2 - m_t^2}\gamma_\nu\right)\frac{1}{(q_1 + q_2)^2}v(p_t') \ ,
$$

$$
\mathcal{A}_{\bar{t}}^\mu = \left(g_s^2 \frac{m_t}{v}\right)\mathcal{A}_{q\bar{q}}^{0,\nu}\bar{u}(p_t)\left(\frac{-\slashed{p}_h + \slashed{p}_t + m_t}{(p_h - p_t)^2 - m_t^2}\gamma_\nu \frac{-\slashed{p}_t' - \slashed{k} + m_t}{2p_t' \cdot k}\gamma^\mu\right.
$$
$$
+ \gamma_\nu \frac{\slashed{p}_h - \slashed{p}_t' - \slashed{k} + m_t}{(p_h - p_t' - k)^2 - m_t^2}\gamma^\mu \frac{\slashed{p}_h - \slashed{p}_t' + m_t}{(p_h - p_t')^2 - m_t^2}
$$
$$
\left. + \gamma_\nu \frac{\slashed{p}_h - \slashed{p}_t' - \slashed{k} + m_t}{(p_h - p_t' - k)^2 - m_t^2}\frac{-\slashed{p}_t' - \slashed{k} + m_t}{2p_t' \cdot k}\gamma^\mu\right)\frac{1}{(q_1 + q_2)^2}v(p_t') \ ,
$$

where

$$
V_{3g}^{\mu\rho\nu}(k, q_1, q_2) = (-2k^\rho - q^\rho)g^{\mu\nu} + (2q^\mu + k^\mu)g^{\nu\rho} + (-q^\nu + k^\nu)g^{\mu\rho} \ . \tag{D.6}
$$

Using the color decomposition given in Eq. (3.82), we can also rewrite $\mathcal{A}^{h \to q\bar{q}t\bar{t}g}$ as a linear combination of four color ordered amplitudes, as already given in Eq. (3.83).

196

By matching the color factors in Eq. (D.4) to the color factors in Eq. (3.83), we see that the color ordered amplitudes $\mathcal{A}_i(q_1, q_2, p_t, p'_t, k)$ (for $i = 1, \ldots, 4$) are given by [72]:

$$\mathcal{A}_1(q_1, q_2, p_t, p'_t, k) = \left(\mathcal{A}^\mu_q + \mathcal{A}^\mu_t - \mathcal{A}^\mu_g\right) \cdot \epsilon_\mu(k) \ , \tag{D.7}$$

$$\mathcal{A}_2(q_1, q_2, p_t, p'_t, k) = \left(\mathcal{A}^\mu_{\bar{q}} + \mathcal{A}^\mu_t + \mathcal{A}^\mu_g\right) \cdot \epsilon_\mu(k) \ ,$$

$$\mathcal{A}_3(q_1, q_2, p_t, p'_t, k) = \left(\mathcal{A}^\mu_q + \mathcal{A}^\mu_{\bar{q}}\right) \cdot \epsilon_\mu(k) \ ,$$

$$\mathcal{A}_4(q_1, q_2, p_t, p'_t, k) = \left(\mathcal{A}^\mu_t + \mathcal{A}^\mu_{\bar{t}}\right) \cdot \epsilon_\mu(k) \ .$$

APPENDIX E

EXTRACTING COLLINEAR LOGARITHMS

In this Appendix, we provide a detailed calculation which illustrates the origin of the collinear logarithms, Λ_b, in Eq. (4.1) and the form of the b PDF given in Eq. (4.4). As explained in Chapter 4, Λ_b-type collinear logarithms arise in the integration over the phase space of final state b quarks emitted at low transverse momentum with respect to the incoming partons. Fig. E.1 illustrates a prototype case: one of the final state b quarks is directly originating from the $g \to b\bar{b}$ splitting of an initial state gluon, while the shaded blob represents all possible non-collinear configurations of the remaining particles (one in this case, corresponding to the emission of a Higgs boson from the external $\bar{b}$ antiquark leg). In the $m_b \to 0$ limit, the $g \to b\bar{b}$ configuration gives origin to collinear singularities where the two b quarks are emitted in the same direction of the splitting gluon. In our case, these singularities will appear in the $p_T^b \to 0$ phase space region, and, if we take $m_b \neq 0$, will be regulated by the b-quark mass, leaving behind logarithms of m_b, as we will see in the following.
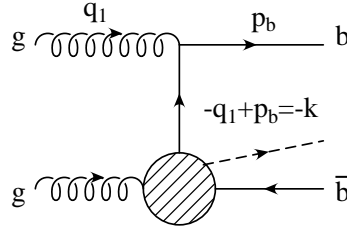

Figure E.1. Tree-level Feynman diagram for $gg \to b\bar{b}h$ depicting the almost collinear emission of a bottom quark (upper leg).

The contribution to the total partonic cross section from this diagram can be written as:

$$d\hat{\sigma}_{gg\to b\bar{b}h} = \frac{1}{(2)2E_1 2E_2} \frac{d^3 p_b}{(2\pi)^3} \frac{1}{2E_b} \frac{d^3 p_{\bar{b}}}{(2\pi)^3} \frac{1}{2E_{\bar{b}}} \frac{d^3 p_h}{(2\pi)^3} \frac{1}{2E_h} \overline{\sum} |\mathcal{M}_{gg\to b\bar{b}h}|^2$$
$$\cdot (2\pi)^4 \delta^{(4)}(q_1 + q_2 - p_b - p_{\bar{b}} - p_h) \ . \qquad \text{(E.1)}$$

where $E_{1,2}$ are the energies of the initial state gluons, while $E_{b,\bar{b},h}$ are the energies of the final state particles. The amplitude for this process is given by $\mathcal{M}_{gg\to b\bar{b}h}$. To investigate the origin of the collinear logarithms, we write the amplitude of this diagram as (neglecting mass terms):

$$\mathcal{M}_{gg\to b\bar{b}h} = g_s T^a \bar{u}(p_b) \gamma_\mu \frac{(\slashed{q}_1 - \slashed{p}_b)}{(q_1 - p_b)^2} \mathcal{M}'_{g\bar{b}\to\bar{b}h} \epsilon^\mu \ , \qquad \text{(E.2)}$$

where $\mathcal{M}'_{g\bar{b}\to\bar{b}h}$ is related to the full $g\bar{b}\to\bar{b}h$ amplitude by:

$$\mathcal{M}_{g\bar{b}\to\bar{b}h} = \bar{v}(-q_1 + p_b) \mathcal{M}'_{g\bar{b}\to\bar{b}h} \qquad \text{(E.3)}$$

For the sum over the gluon polarizations, we introduce a light-like vector n^μ which satisfies $n \cdot q_1 \neq 0$ and write:

$$\sum \epsilon^\mu(q_1) \epsilon^{\nu*}(q_1) = -g^{\mu\nu} + \frac{q_1^\mu n^\nu + q_1^\nu n^\mu}{q_1 \cdot n} \ . \qquad \text{(E.4)}$$

The amplitude squared then takes the form:

$$|\mathcal{M}_{gg\to b\bar{b}h}|^2 = g_s^2 C_F Tr \left\{ \mathcal{M}'^*_{g\bar{b}\to\bar{b}h} \frac{(\slashed{q}_1 - \slashed{p}_b)}{(q_1 - p_b)^2} [\gamma_\nu \slashed{p}_b \gamma_\mu] \frac{(\slashed{q}_1 - \slashed{p}_b)}{(q_1 - p_b)^2} \right.$$
$$\cdot \mathcal{M}'_{g\bar{b}\to\bar{b}h} \left\} \left(-g^{\mu\nu} + \frac{q_1^\mu n^\nu + q_1^\nu n^\mu}{q_1 \cdot n} \right) \right.$$
$$= g_s^2 C_F Tr \left\{ \mathcal{M}'^*_{g\bar{b}\to\bar{b}h} \frac{(\slashed{q}_1 - \slashed{p}_b)}{(q_1 - p_b)^2} \left[-\gamma^\mu \slashed{p}_b \gamma_\mu \right. \right.$$
$$\left. \left. + \frac{1}{n \cdot q_1} (\slashed{n} \slashed{p}_b \slashed{q}_1 + \slashed{q}_1 \slashed{p}_b \slashed{n}) \right] \frac{(\slashed{q}_1 - \slashed{p}_b)}{(q_1 - p_b)^2} \mathcal{M}'_{g\bar{b}\to\bar{b}h} \right\} \qquad \text{(E.5)}$$

199

Commuting gamma matrices and contracting like indices, we find:

$$|\mathcal{M}_{gg\to b\bar{b}h}|^2 = g_s^2 C_F \frac{2}{(2q_1 \cdot p_b)^2 (n \cdot q_1)} Tr\left\{ \mathcal{M}'^*_{g\bar{b}\to\bar{b}h}(\slashed{q}_1 - \slashed{p}_b)\right.$$

$$\left. \cdot \left[((n \cdot p_b)\ \slashed{q}_1 + (p_b \cdot q_1)\ \slashed{n})\right](\slashed{q}_1 - \slashed{p}_b)\mathcal{M}'_{g\bar{b}\to\bar{b}h}\right\}\ , \tag{E.6}$$

and commuting the first factor of $(\slashed{q}_1 - \slashed{p}_b)$ to the right and contracting it with the other factor of $(\slashed{q}_1 - \slashed{p}_b)$, we get:

$$|\mathcal{M}_{gg\to b\bar{b}h}|^2 = g_s^2 C_F \frac{2}{(2q_1 \cdot p_b)(n \cdot q_1)} Tr\left\{ \mathcal{M}'^*_{g\bar{b}\to\bar{b}h} \cdot \left[(n \cdot p_b)\ \slashed{p}_b \right.\right.$$

$$\left.\left. +n \cdot (q_1 - p_b)(\slashed{q}_1 - \slashed{p}_b) + (q_1 \cdot p_b)\ \slashed{n}\right]\mathcal{M}'_{g\bar{b}\to\bar{b}h}\right\}\ . \tag{E.7}$$

Now we wish to specialize to the *near collinear limit,* i.e. to the limit when the b quark has small transverse momentum. To do this, we use the following decomposition for the four-momenta of the b quark:

$$k^\mu = zq_1^\mu + \beta n^\mu + k_\perp^\mu\ , \tag{E.8}$$

where $k = q_1 - p_b$ is the momentum of the virtual b and z is the fraction of the initial gluon's energy carried by the b quark. In addition, the external quark's momentum can be written as:

$$p_b^\mu = q_1^\mu - k^\mu$$

$$= (1 - z)q_1^\mu - \beta n^\mu - k_\perp^\mu\ . \tag{E.9}$$

Note that $k_\perp^\mu$ is transverse to both q_1^μ and n^μ and $k_\perp^\mu k_{\mu\perp} = -k_T^2$.

Requiring the external b quark to be on-shell ($p_b^2 = 0$), we find:

$$\beta = -\frac{k_T^2}{2(1 - z)(q_1 \cdot n)}\ . \tag{E.10}$$

With this parameterization, the matrix-element-squared simplifies to:

$$|\mathcal{M}_{gg\to b\bar{b}h}|^2 = 2g_s^2 C_F \frac{(1 - z)}{k_T^2} Tr\left\{ \mathcal{M}'^*_{g\bar{b}\to\bar{b}h}\left[(1 - z)\ \slashed{p}_b + z(\slashed{q}_1 - \slashed{p}_b) - \beta\ \slashed{n}\right]\mathcal{M}'_{g\bar{b}\to\bar{b}h}\right\}\ , \tag{E.11}$$

We can now rewrite the amplitude squared for the two-to-three process ($gg \to b\bar{b}h$) as the convolution of the $g \to b\bar{b}$ splitting function with the amplitude squared of the two-to-two process ($g\bar{b} \to \bar{b}h$), plus corrections that vanish in the small k_T limit. To achieve this, we rewrite the $\not{p}_b$ appearing in the first term of the trace in terms of ($\not{q}_1 - \not{p}_b$) plus terms of higher order in k_T. From the definition of $\not{p}_b$, we find:

$$\not{p}_b = \left(\frac{1-z}{z}\right)\left[(\not{q}_1 - \not{p}_b) - \not{k}_T - \beta\,\not{n}\right] - \not{k}_T - \beta\,\not{n} \ , \tag{E.12}$$

and using this in Eq. (E.11) we have:

$$
\begin{aligned}
|\mathcal{M}_{gg\to b\bar{b}h}|^2 &= 2g_s^2 C_F \frac{(1-z)}{k_T^2} Tr\Bigg\{ \mathcal{M}'^*_{g\bar{b}\to\bar{b}h}\Bigg[\left(\frac{z^2+(1-z)^2}{z}\right)(\not{q}_1 - \not{p}_b) \\
&\qquad + \mathcal{O}(k_T)\Bigg]\mathcal{M}'_{g\bar{b}\to\bar{b}h}\Bigg\} \\
&\simeq g_s^2 C_F \frac{4}{k_T^2}\left(\frac{1-z}{z}\right)\left(\frac{(1-z)^2+z^2}{2}\right)Tr\Bigg\{\mathcal{M}'^*_{g\bar{b}\to\bar{b}h}(\not{q}_1 - \not{p}_b) \\
&\qquad \cdot \mathcal{M}'_{g\bar{b}\to\bar{b}h}\Bigg\} \\
&\equiv g_s^2 C_F \frac{4}{k_T^2}\left(\frac{1-z}{z}\right)P_{qg}(z)|\mathcal{M}_{g\bar{b}\to\bar{b}h}|^2 \ . \tag{E.13}
\end{aligned}
$$

In the small k_T limit, the phase space for the external b quark can be written as:

$$\frac{d^3p_b}{(2\pi)^3}\frac{1}{2E_b} \simeq \frac{1}{16\pi^2}\frac{dz\,dk_T^2}{(1-z)} \tag{E.14}$$

Inserting Eqs. (E.13) and (E.14) into Eq. (E.1), we find:

$$
\begin{aligned}
d\hat{\sigma}_{gg\to b\bar{b}h} &= \frac{1}{16\pi^2}\frac{dz\,dk_T^2}{k_T^2}\left(16\pi\alpha_s C_F P_{qg}(z)\right)\Bigg[\frac{1}{(2)2zE_1 2E_2}\frac{d^3p_{\bar{b}}}{(2\pi)^3}\frac{1}{2E_{\bar{b}}} \\
&\qquad \frac{d^3p_h}{(2\pi)^3}\frac{1}{2E_h}\left(\frac{2N_c}{2(N_c^2-1)}\right)\overline{\sum}|\mathcal{M}_{g\bar{b}\to\bar{b}h}|^2(2\pi)^4\delta^{(4)}(k+q_2-p_{\bar{b}}-p_h)\Bigg] \\
&\equiv \frac{dk_T^2}{k_T^2}dz\frac{\alpha_s}{2\pi}P_{qg}(z)d\hat{\sigma}_{g\bar{b}\to\bar{b}h} \tag{E.15}
\end{aligned}
$$

where the factor $\left(\frac{2N_c}{2(N_c^2-1)}\right)$ comes from rescaling the spin/color average of $gg \to b\bar{b}h$ to that of $g\bar{b} \to \bar{b}h$. The integration over k_T^2, with upper and lower bounds of μ_h^2

201

and m_b^2, respectively, gives rise to the collinear logarithm Λ_b. Finally, to obtain the hadronic cross section, we convolute Eq. (E.15) with the gluon PDFs, whereupon the form of the b PDF (Eq. (4.4)) becomes apparent.

REFERENCES

[1] S. Heinemeyer, W. Hollik, and G. Weiglein. *Comput. Phys. Commun.*, 124:76–89, 2000. hep-ph/9812320.

[2] S. Weinberg. *Phys. Rev. Lett.*, 19:1264–1266, 1967.

[3] S.L. Glashow. *Nucl. Phys.*, 22:579, 1961.

[4] A. Salam, 1968. in *Elementary Particle Theory*, the Nobel Symposium no 8, edited by N. Svartholm (Almqzist and Wiksell, Stockholm, 1968), p. 367.

[5] P.W. Higgs. *Phys. Rev. Lett.*, 12:132, 1964.

[6] P.W. Higgs. *Phys. Rev.*, 145:1156, 1966.

[7] F. Englert and R. Brout. *Phys. Rev. Lett.*, 13:321, 1964.

[8] T.W.B. Kibble. *Phys. Rev.*, 155:1554, 1967.

[9] M. Carena and H.E. Haber. *Prog. Part. Nucl. Phys.*, 50:63–152, 2003. hep-ph/0208209.

[10] A. Djouadi. 2005. hep-ph/0503172.

[11] T. Hambye and K. Riesselmann. *Phys. Rev.*, D55:7255–7262, 1997. hep-ph/9610272.

[12] G. Altarelli and G. Isidori. *Phys. Lett.*, B337:141–144, 1994.

[13] L.E. Ibanez and G.G. Ross. *Phys. Lett.*, B110:215–220, 1982.

[14] L.E. Ibanez. *Phys. Lett.*, B118:73, 1982.

[15] J.R. Ellis, D. V. Nanopoulos, and K. Tamvakis. *Phys. Lett.*, B121:123, 1983.

[16] L. Alvarez-Gaume, J. Polchinski, and Mark B. Wise. *Nucl. Phys.*, B221:495, 1983.

[17] M. Carena, S. Mrenna, and C. E. M. Wagner. *Phys. Rev.*, D60:075010, 1999. hep-ph/9808312.

[18] LEPEWWG. webpage: http://lepewwg.web.cern.ch/LEPEWWG/.

[19] The LEP Collaboration. *Phys. Lett.*, B565:61, 2003.

[20] LHWG/2001-04, 2001. arXiv:hep-ex/0107030.

[21] A. Djouadi, M. Spira, and P. M. Zerwas. *Phys. Lett.*, B264:440–446, 1991.

[22] S. Dawson. *Nucl. Phys.*, B359:283–300, 1991.

[23] D. Graudenz, M. Spira, and P. M. Zerwas. *Phys. Rev. Lett.*, 70:1372–1375, 1993.

[24] M. Spira, A. Djouadi, D. Graudenz, and P. M. Zerwas. *Nucl. Phys.*, B453:17–82, 1995.

[25] M. Kramer, E. Laenen, and M. Spira. *Nucl. Phys.*, B511:523–549, 1998.

[26] C. Balazs and C. P. Yuan. *Phys. Lett.*, B478:192–198, 2000.

[27] M. Spira. *Fortsch. Phys.*, 46:203–284, 1998.

[28] T. Han, G. Valencia, and S. Willenbrock. *Phys. Rev. Lett.*, 69:3274–3277, 1992.

[29] S. Dawson, C. Jackson, L. H. Orr, L. Reina, and D. Wackeroth. *Phys. Rev.*, D68:034022, 2003. hep-ph/0305087.

[30] L. Reina, S. Dawson, and D. Wackeroth. *Phys. Rev. D*, 65:053017, 2002. arXiv:hep-ph/0109066.

[31] W. Beenakker, S. Dittmaier, M. Kramer, B. Plumber, M. Spira, and P.M. Zerwas. *Phys. Rev. Lett.*, 87:201805, 2001. arXiv:hep-ph/0107081.

[32] R.V. Harlander and W.B. Kilgore. *Phys. Rev. Lett.*, 88:201801, 2002. hep-ph/0201206.

[33] O. Brein, A. Djouadi, and R. Harlander. *Phys. Lett.*, B579:149–156, 2004. hep-ph/0307206.

[34] T. Affolder et al. *Phys. Rev. Lett.*, 86:4472–4478, 2001. hep-ex/0010052.

[35] V. M. Abazov et al. 2005. hep-ex/0504018.

[36] M. Carena et al. 2000. hep-ph/0010338.

[37] S. Asai et al. *Eur. Phys. J.*, C32S2:19–54, 2004. hep-ph/0402254.

[38] S. Abdullin et al. *CMS Note 2003/13.*

[39] CERN-LHCC-99-15.

[40] F. Gianotti et al. *Eur. Phys. J.*, C39:293–333, 2005. hep-ph/0204087.

[41] W.J. Marciano and F.E. Paige. *Phys. Rev. Lett.*, 66:2433, 1991.

[42] Technical Report CERN/LHCC/94-38, CERN, 1994.

[43] Technical Report CERN/LHCC/99-15, CERN, 1999.

[44] J. Goldstein et al. *Phys. Rev. Lett.*, 86:1694, 2001. arXiv:hep-ph/0006311.

[45] M. Beneke et al.

[46] D. Zeppenfeld et al. *Phys. Rev. D*, 62:013009, 2000.

[47] D. Zeppenfeld. arXiv:hep-ph/0203123.

[48] A. Belyaev and L. Reina. *JHEP*, 08:041, 2002. arXiv:hep-ph/0205270.

[49] F. Maltoni, D. Rainwater, and S. Willenbrock. *Phy. Rev.*, D66:034022, 2002. arXiv:hep-ph/0202205.

[50] Z. Kunszt. *Phys.*, B247:339, 1984.

[51] J.N. Ng and P. Zakarauskas. *Phys. Rev.*, D29:876, 1984.

[52] Z. Bern, L.J. Dixon, and D.A. Kosower. *Phys. Rev. Lett.*, B302:299, 1993.

[53] Z. Bern, L.J. Dixon, and D.A. Kosower. *Nucl. Phys.*, B412:751, 1994.

[54] A. Denner. *Fortschr. Phys.*, 41:307, 1993.

[55] B. Harris and J. Owens. *Phys. Rev.*, D65:094032, 2002.

[56] W.T. Giele and E.W.N. Glover. *Phys. Rev.*, D46:1980, 1992.

[57] W.T. Giele, E.W.N. Glover, and D.A. Kosower. *Nucl. Phys.*, B403:633, 1993. arXiv:hep-ph/9302225.

[58] S. Keller and E. Laenen. *Phys. Rev.*, D59:114004, 1999. arXiv:hep-ph/9812415.

[59] G. Altarelli and G. Parisi. *Nucl. Phys.*, B126:298, 1977.

[60] J.A.M. Vermaseren.

[61] M. Jamin and M.E. Lautenbacher. *Comput. Phys. Commun.*, 74:265, 1993.

[62] T. Stelzer and W.F. Long. *Comput. Phys. Commun.*, 81:357, 1994. arXiv:hep-ph/9401258.

[63] K. J. F. Gaemers and G. J. Gounaris. *Phys. Lett.*, B77:379, 1978.

[64] G. 't Hooft and M.J.G. Veltman. *Nucl. Phys.*, B153:365, 1979.

[65] G. Passarino and M.J.G. Veltman. *Nucl. Phys.*, B160:151, 1979.

[66] G.J. van Oldenborgh and J.A.M. Vermaseren. *Z. Phys.*, C46:425, 1990.

205

[67] J.C. Collins, F. Wilczek, and A. Zee. *Phys. Rev.*, D18:242, 1978.

[68] P. Nason, S. Dawson, and R.K. Ellis. *Nucl. Phys.*, B327:49, 1989.

[69] L. Bergmann, 1989. Ph.D. Thesis, Florida State University.

[70] W. Beenakker, H. Kuijf, W. L. van Neerven, and J. Smith. *Phys. Rev.*, D40:54–82, 1989.

[71] U. Baur, S. Keller, and D. Wackeroth. *Phys. Rev.*, D59:013002, 1999.

[72] F.A. Berends, W. T. Giele, and H. Kuijf. *Nucl. Phys.*, B321:39, 1989.

[73] G.P. Lepage. *J. Comput. Phys.*, 27:192, 1978.

[74] F.A. Berends, P.H. Daverveldt, and R. Kleiss. *Nucl. Phys.*, B253:441, 1985.

[75] J. Hilgart, R. Kleiss, and F. Le Diberder. *Comput. Phys. Commun.*, 75:191, 1993.

[76] A. Denner, S. Dittmaier, M. Roth, and D. Wackeroth. *Nucl. Phys.*, B560:33, 1999. arXiv:hep-ph/9904472.

[77] H.L. Lai et al. *Phys. Rev.*, D59:1280, 1997.

[78] R. Bonciani, S. Catani, M.L. Mangano, and P. Nason. *Nucl. Phys.*, B529:424–450, 1998.

[79] H.L. Lai et al. *Eur. Phys. J.*, C12:375, 2000. arXiv:hep-ph/9903282.

[80] K. A. Assamagan et al. 2004. hep-ph/0406152.

[81] R.M. Barnett, H.E. Haber, and D.E. Soper. *Nucl. Phys.*, B306:697, 1988.

[82] F.I. Olness and W-K Tung. *Nucl. Phys.*, B308:813, 1988.

[83] D.A. Dicus and S. Willenbrock. *Phys. Rev.*, D39:751, 1989.

[84] S. Dittmaier, M. Kramer, and M. Spira. *Phys. Rev.*, D70:074010, 2004. hep-ph/0309204.

[85] R.V. Harlander and W.B. Kilgore. *Phys. Rev.*, D68:013001, 2003. hep-ph/0304035.

[86] S. Dawson, C. B. Jackson, L. Reina, and D. Wackeroth. *Phys. Rev. Lett.*, 94:031802, 2005. hep-ph/0408077.

[87] J. Campbell, R. K. Ellis, F. Maltoni, and S. Willenbrock. *Phys. Rev.*, D67:095002, 2003. hep-ph/0204093.

[88] S. Dawson, C. B. Jackson, L. Reina, and D. Wackeroth. *Phys. Rev.*, D69:074027, 2004. hep-ph/0311067.

[89] J. Pumplin et al. *JHEP*, 07:012, 2002. hep-ph/0201195.

[90] V. N. Gribov and L. N. Lipatov. *Sov. J. Nucl. Phys.*, 15:438–450, 1972.

[91] Y.L. Dokshitzer. *Sov. Phys. JETP*, 46:641–653, 1977.

[92] D. Dicus, T. Stelzer, Z. Sullivan, and S. Willenbrock. *Phys. Rev.*, D59:094016, 1999. hep-ph/9811492.

[93] H. Lehmann, K. Symanzik, and W. Zimmermann. *Nuovo Cim.*, 1:205–225, 1955.

[94] E. Braaten and J. P. Leveille. *Phys. Rev.*, D22:715, 1980.

[95] F. Maltoni, Z. Sullivan, and S. Willenbrock. *Phys. Rev.*, D67:093005, 2003. hep-ph/0301033.

[96] J. Campbell et al. 2004. hep-ph/0405302.

[97] J. Campbell and R.K. Ellis. webpage: mcfm.fnal.gov.

[98] Daniel Stump et al. *JHEP*, 10:046, 2003. hep-ph/0303013.

[99] S. Catani and B. R. Webber. *JHEP*, 10:005, 1997. hep-ph/9710333.

[100] N. Kidonakis. *Int. J. Mod. Phys.*, A19:1793–1821, 2004. hep-ph/0303186.

[101] V. Del Duca, F. Maltoni, Z. Nagy, and Z. Trocsanyi. *JHEP*, 04:059, 2003. hep-ph/0303012.

[102] A. D. Martin, R. G. Roberts, W. J. Stirling, and R. S. Thorne. *Eur. Phys. J.*, C28:455–473, 2003. hep-ph/0211080.

[103] A. Djouadi and S. Ferrag. *Phys. Lett.*, B586:345–352, 2004. hep-ph/0310209.

[104] J. Owens. Private communication.

[105] W. Beenakker and A. Denner. *Nucl. Phys.*, B338:349, 1990.

BIOGRAPHICAL SKETCH

Christopher B. Jackson

Education

- BS in Physics (summa cum laude)

  April, 2000

  Dept. of Natural Sciences, University of North Florida, Jacksonville, FL

- MS in High Energy Physics

  April, 2002

  Dept. of Physics, Florida State University

Graduate Assistantships and Teaching Experience

- 2001-2004: Research Assistant (High Energy Physics), Dept. of Physics, Florida State University.

- 2004: Co-director of Independent Study Group "Compact Stars for Undergraduates", Dept. of Physics, Florida State University.

- 2000-2001: Teaching Assistant, Astronomy lab instructor, Dept. of Physics, Florida State University.

Undergraduate Fellowships and Assistantships

- 1998-2000: Tutor of math and physics, Academic Center for Excellence, University of North Florida.

- 1999: Lab Instructor, first semester calculus-based introductory physics lab, Dept. of Natural Sciences, University of North Florida.

- 1999: Research Experience for Undergraduates Junior Fellow, Experimental Nuclear Physics, Dept. of Physics, Florida State University.

Awards and Honors

- 2005: Dirac-Hellman Award for Theoretical Physics, Excellence in theoretical physics by a graduate student or post-doctoral researcher, Florida State University.

- 2000: Outstanding Senior in Physics, University of North Florida.

- 1999: Outstanding Sophomore in Physics, University of North Florida

- 1999: Research Experience for Undergraduates Junior Fellow, Experimental Nuclear Physics, Dept. of Physics, Florida State University.

Publications

- Higgs Boson Production with Bottom Quarks at Hadron Colliders, (with S. Dawson, L. Reina and D. Wackeroth), to appear in proceedings of the Meeting of the Division of Particles and Fields (DPF 04), hep-ph/0409345.

- Compact Objects for Everyone: A Real Experiment, (with J. Taruna, S.L. Pouliot, B.W. Ellison, D.D. Lee, and J. Piekarewicz), astro-ph/0409348, submitted to Am. J. Phys.

- Higgs Boson Production with One Bottom Quark Jet at Hadron Colliders, (with S. Dawson, L. Reina and D. Wackeroth), hep-ph/0408077, Phys. Rev. Lett. **94**, 031802 (2004).

- The Higgs Working Group: Summary Report 2003, (with K.A. Assamagan et al.), in proceedings of the 3rd Les Houches Workshop: Physics at TeV Colliders; hep-ph/0406152.

- Higgs Boson Production in Association with Bottom Quarks, (with J. Campbell et al.), in proceedings of the 3rd Les Houches Workshop: Physics at TeV Colliders; hep-ph/0405302.

- Theoretical Progress for the Associated Production of a Higgs Boson with Heavy Quarks at Hadron Colliders, (with S. Dawson, L.H. Orr, L. Reina and D. Wackeroth), in proceedings of the International Europhysics Conference on High-Enery Physics (HEP 2003), hep-ph/0311216.

- NLO QCD Corrections to Hadronic Higgs Production with Heavy Quarks, (with S. Dawson, L.H. Orr, L. Reina and D. Wackeroth), in proceedings of the 10th International QCD Conference (QCD 03), hep-ph/0311105.

- Exclusive Higgs Boson Production with Bottom Quarks at Hadron Colliders, (with S. Dawson, L. Reina and D. Wackeroth), hep-ph/0311067, Phys. Rev. **D69**, 074027 (2004).

- Associated Higgs Production with Top Quarks at the Large Hadron Collider: NLO QCD Corrections, (with S. Dawson, L.H. Orr, L. Reina and D. Wackeroth), hep-ph/0305087, Phys. Rev. **D68**, 034022 (2003).

- Transition Strengths and Band Determinations in Zr-86, (with M. Wiedeking, S.L. Tabor, F. Cristancho, M. Devlin, J. Doring, G.D. Johns, R.A. Kaye, I.Y. Lee, F. Lerma, A.O. Machiavelli, M. Naidu, I. Ragnarsson, D.G. Sarantites, and G.Z. Solomon), Phys. Rev. **C67**, 034320 (2003).

Talks

- Theoretical Status of Higgs Production with Bottom Quarks, Meeting of the American Physical Society, Tampa, FL, Apr. 18, 2005.

- Bottom Quark PDF Uncertainties and $h + b$ Production, Tev4LHC Workshop, Higgs Working Group, Brookhaven National Lab, Upton, NY, Feb. 3-5, 2005.

- Status of Theoretical Predictions for the Associated Production of Higgs Bosons with Bottom Quarks, UF-FSU Symposium on High Energy Phenomenology,Tallahassee, FL, Dec. 1, 2004.

- Higgs Boson Production with a Single Bottom Quark at Hadron Colliders, Tev4LHC Workshop, Higgs Working Group, Fermilab, Batavia, IL, Sep. 16-18, 2004.

- Higgs Boson Production with Bottom Quarks at Hadron Colliders, Meeting of the Division of Particles and Fields (DPF 04), UCR, Riverside, CA, Aug. 27, 2004.

- Higgs Boson Production with Bottom Quarks at Hadron Colliders, Dept. of Physics, Florida State Univ., Tallahassee, FL, Aug. 24, 2004.

- The Muon Anomalous Magnetic Dipole Moment: A Search for New Physics, Dept. of Physics, Florida State Univ., Tallahassee, FL, Mar. 2001.

Schools and Conferences

- Meeting of the American Physical Society, Tampa, FL, Apr. 15-19, 2005.

- Tev4LHC Workshop at Brookhaven National Lab, Upton, NY, Feb. 3-5, 2005.

- UF-FSU Symposium on High Energy Phenomenology, Florida State University, Tallahassee, FL, Dec. 1, 2004.

- Meeting of the Division of Particles and Fields (DPF 04), UCR, Riverside, CA, Aug. 26-31, 2004.

- PierreFest, Univ. of Florida, Gainsville, FL, Feb. 1-2, 2003.

- Dirac Symposium, Florida State Univ., Tallahassee, FL, Dec. 6-7, 2002.

- Theoretical Advanced Study Institute (TASI) in Elementary Particle Physics, University of Colorado at Boulder, Boulder, CO, Jun. 2-29, 2002.

- Conference Experience for Undergraduates, Division of Nuclear Physics of the American Physical Society, Asilomar, Pacific Grove, CA, Oct. 20-23, 1999.